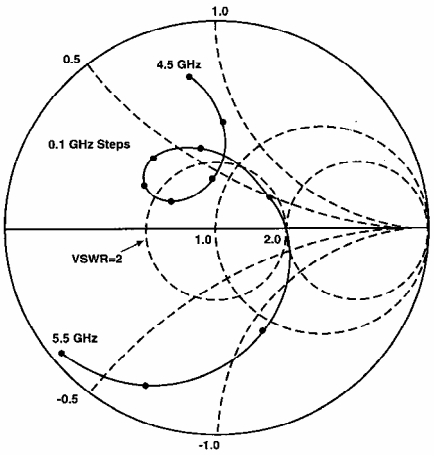

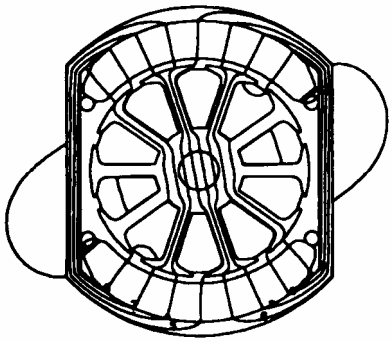

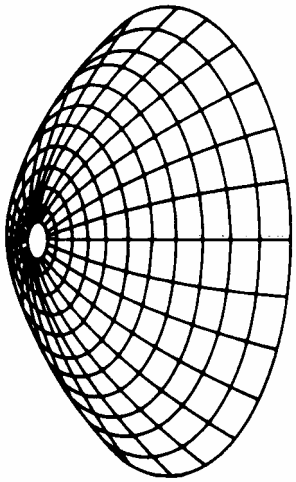

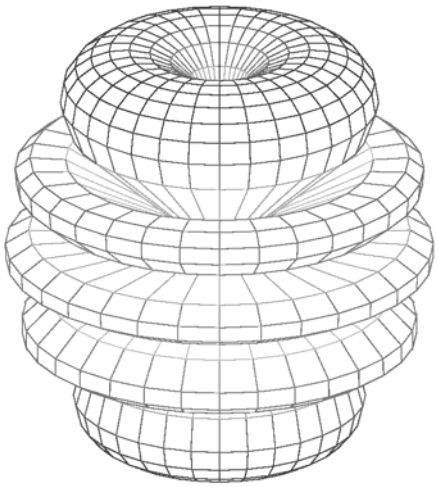

Applied Computational Electromagnetics Society Journal

Special Issue on

ACES 2007 Conference

Part I

Editor-in-Chief

Atef Z. Elsherbeni

March 2008

Vol. 23 No. 1

ISSN 1054-4887

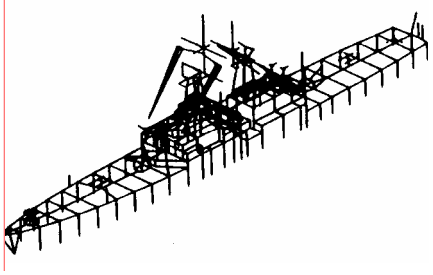

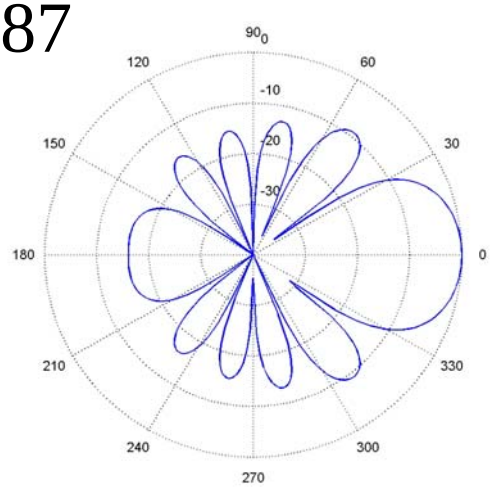

GENERAL PURPOSE AND SCOPE: The Applied Computational Electromagnetics Society ***(ACES)*** Journal hereinafter known as the ***ACES Journal*** is devoted to the exchange of information in computational electromagnetics, to the advancement of the state-of-the art, and the promotion of related technical activities. A primary objective of the information exchange is the elimination of the need to "re-invent the wheel" to solve a previously-solved computational problem in electrical engineering, physics, or related fields of study. The technical activities promoted by this publication include code validation, performance analysis, and input/output standardization; code or technique optimization and error minimization; innovations in solution technique or in data input/output; identification of new applications for electromagnetics modeling codes and techniques; integration of computational electromagnetics techniques with new computer architectures; and correlation of computational parameters with physical mechanisms.

SUBMISSIONS: The ***ACES Journal*** welcomes original, previously unpublished papers, relating to applied computational electromagnetics. Typical papers will represent the computational electromagnetics aspects of research in electrical engineering, physics, or related disciplines. However, papers which represent research in applied computational electromagnetics itself are equally acceptable.

Manuscripts are to be submitted through the upload system of ***ACES*** web site http://aces.ee.olemiss.edu See "Information for Authors" on inside of back cover and at ***ACES*** web site. For additional information contact the Editor-in-Chief:

Dr. Atef Elsherbeni
Department of Electrical Engineering
The University of Mississippi
University, MS 386377 USA
Phone: 662-915-5382 Fax: 662-915-7231
Email: atef@olemis.edu

SUBSCRIPTIONS: All members of the Applied Computational Electromagnetics Society are entitled to download any published journal article available at http://aces.ee.olemiss.edu . Printed copies of the Journal are also available to members with institutional subscription level.

Back issues, when available, are $15 each. Subscriptions to ***ACES*** is through the web site. Orders for back issues of the ***ACES Journal*** and changes of addresses should be sent directly to ***ACES*** Executive Officer:

Dr. Richard W. Adler
ECE Department, Code ECAB
Naval Postgraduate School
833 Dyer Road, Room 437
Monterey, CA 93943-5121 USA
Fax: 831-649-0300
Email: *rwa@attglobal.net*

Allow four week's advance notice for change of address. Claims for missing issues will not be honored because of insufficient notice or address change or loss in mail unless the Executive Officer is notified within 60 days for USA and Canadian subscribers or 90 days for subscribers in other countries, from the last day of the month of publication. For information regarding reprints of individual papers or other materials, see "Information for Authors".

LIABILITY. Neither ***ACES***, nor the ***ACES Journal*** editors, are responsible for any consequence of misinformation or claims, express or implied, in any published material in an ***ACES Journal*** issue. This also applies to advertising, for which only camera-ready copies are accepted. Authors are responsible for information contained in their papers. If any material submitted for publication includes material which has already been published elsewhere, it is the author's responsibility to obtain written permission to reproduce such material.

APPLIED COMPUTATIONAL ELECTROMAGNETICS SOCIETY JOURNAL

Special Issue on
ACES 2007 Conference
Part I

Editor-in-Chief
Atef Z. Elsherbeni

March 2008
Vol. 23 No. 1
ISSN 1054-4887

The ACES Journal is abstracted in INSPEC, in Engineering Index, DTIC, Science Citation Index Expanded, the Research Alert, and to Current Contents/Engineering, Computing & Technology.

The first, fourth, and sixth illustrations on the front cover have been obtained from the Department of Electrical Engineering at the University of Mississippi.

The third and fifth illustrations on the front cover have been obtained from Lawrence Livermore National Laboratory.

The second illustration on the front cover has been obtained from FLUX2D software, CEDRAT S.S. France, MAGSOFT Corporation, New York.

THE APPLIED COMPUTATIONAL ELECTROMAGNETICS SOCIETY

JOURNAL

SPECIAL ISSUE ON
ACES 2007 CONFERENCE
Part I

Vol. 23 No. 1 March 2008

TABLE OF CONTENTS

An Improved Time-Domain Near-Field to Far-Field Transform in Two Dimensions

J. A. Roden, S. L. Johns, and J. Sacchini

The Aerospace Corporation
Chantilly, VA

Abstract – Computing the far-field transient response of a two-dimensional geometry requires a convolution of near-field currents with a two-dimensional far-field impulse response. In this work, a purely time domain implementation is derived and its accuracy is demonstrated. This method is applicable to EMI, radiation, and scattering problems.

I. INTRODUCTION

The finite difference time domain technique (FDTD) is a robust and proven technique for full-wave electromagnetic analysis of complex microwave, antenna, and scattering geometries. Often, the quantity of interest is not near-field quantities, which are directly computed by the time marching scheme. Instead, far-field radiation or scattering quantities are desired.

In order to compute these far-field quantities, various transform techniques have been successfully applied in both three dimensions [1-4] and two dimensions [5-6]. When angular patterns at a few discrete frequencies are of interest, a single frequency transform is appropriate and easily computed in either two or three dimensions using a running Fourier transform and proper weightings. Far-field patterns are then computed using a post processing operation.

When a broadband or transient far-field result is desired at a few discrete angles, a purely time-domain near-field to far-field transform is appropriate. In three dimensions, this process is straight forward in theory, though implementation requires a bit of bookkeeping. In two dimensions, the time-domain near-field to far-field transform is complicated by the two-dimensional Green's function which is no longer of a simple exponential form.

In [6], a hybrid time/frequency domain approach is derived for the two-dimensional time-domain transform. In this hybrid method, post processing accomplishes the complex Green's function convolution. Specifically, a multi-step procedure consisting of a Fourier transform, a frequency domain multiplication, and finally an inverse Fourier transform produces the final time-domain result.

In this paper, a more elegant approach is formulated which is accomplished entirely in the time domain. Efficiency is gained by using an extremely accurate approximation of the Green's function's time-domain impulse response and subsequent application of an efficiently implemented convolution sum. The accuracy of the method is proven against known analytic solutions. Furthermore, the discrete impulse response derived in this work has applications in other FDTD applications where $1/\sqrt{j\omega}$ type impulse responses are present.

II. FREQUENCY DOMAIN FORMULATION

It is widely known that if a radiator or scatterer is surrounded by a closed surface *S*, the far-fields may be computed from vector magnetic and electric surface currents $\vec{\mathbf{M}}_s$ and $\vec{\mathbf{J}}_s$ defined along the enclosing surface by $-\hat{\mathbf{n}}\times\vec{\mathbf{E}}$ and $\hat{\mathbf{n}}\times\vec{\mathbf{H}}$, respectively. The fields are most easily defined in terms of the intermediate radiation vectors defined as follow,

$$\vec{\mathbf{N}} = \oint_S \vec{\mathbf{J}} e^{-jk\left(\vec{\mathbf{r}}'\cdot\vec{\mathbf{r}}\right)} ds\,, \tag{1}$$

$$\vec{\mathbf{L}} = \oint_S \vec{\mathbf{M}} e^{-jk\left(\vec{\mathbf{r}}'\cdot\vec{\mathbf{r}}\right)} ds \tag{2}$$

where $\vec{\mathbf{r}}'$ is the vector from the origin to the surface current, and $\vec{\mathbf{r}}$ is the unit vector to the far-field point.

The vector components of the electric field in the far-field are then given by,

$$E_\theta^{3D} = \frac{-j}{2\lambda R} e^{-jkR}\left(\eta N_\theta + L_\phi\right), \tag{3}$$

$$E_\phi^{3D} = \frac{j}{2\lambda R} e^{-jkR}\left(-\eta N_\phi + L_\theta\right) \tag{4}$$

where λ is the wavelength, k is the wave number $\omega\sqrt{\mu\varepsilon}$, and η is the free-space wave impedance.

III. HYBRID TIME 2D FORMULATION

In a three-dimensional FDTD code the implementation of equations (3) and (4) is typically accomplished by introducing the temporary summation variables $\vec{W}, \vec{U}$ defined as,

$$\vec{\mathbf{W}}^{3D} = j e^{-jkR}\,\vec{\mathbf{N}} \Big/ 2\lambda R \tag{5}$$

$$\vec{\mathbf{U}}^{3D} = j e^{-jkR}\,\vec{\mathbf{L}} \Big/ 2\lambda R\,. \tag{6}$$

Applying the Laplace transform, these become

$$\vec{\mathbf{W}}^{3D}(t)=\left(\frac{1}{4\pi Rc}\right)\frac{\partial}{\partial t}\left\{\int_S \vec{\mathbf{J}}\left[t+\left(\vec{r}'\bullet\hat{r}\right)\Big/c-R\Big/c\right]ds'\right\}, \quad (7)$$

$$\vec{\mathbf{U}}^{3D}(t)=\left(\frac{1}{4\pi Rc}\right)\frac{\partial}{\partial t}\left\{\int_S \vec{\mathbf{M}}\left[t+\left(\vec{r}'\bullet\hat{r}\right)\Big/c-R\Big/c\right]ds'\right\} \quad (8)$$

$\vec{\mathbf{W}}$ and $\vec{\mathbf{U}}$ result in a discrete binning operation whereas contributions from each surface patch on the far-field transform surface is time-delayed and added appropriately to the appropriate time bin. At the end of the FDTD computation, the far-field components of the electric field are then simply given as,

$$E_\theta^{3D}=-\eta W_\theta^{3D}-U_\phi^{3D} \quad (9)$$

$$E_\phi^{3D}=-\eta W_\phi^{3D}+U_\theta^{3D}. \quad (10)$$

In [6] it was shown that a simple relation exists between equations (9), (10), and their two dimensional counterparts,

$$\vec{E}^{2D}(\omega)=\sqrt{\frac{2\pi c\rho}{j\omega}}\vec{E}^{3D}(\omega) \quad . \quad (11)$$

The implementation of equation (11) in conjunction with equations (9) and (10) was accomplished in [6] as a three-step post processing operation. Specifically, once the far-field components $E_z(t)$ and $E_\phi(t)$ are computed for all times of interest, a Fourier transform is applied to the time waveforms rendering a discrete frequency spectrum for the fields. Next, equation (11) is applied to each frequency component of interest. If a frequency spectrum alone is needed, no further processing is necessary. However, if the time-domain far-field is the quantity of interest, equation (11) must be applied to the entire frequency spectrum of the signal. Subsequently, the weighted frequency spectrum is transformed back to the time domain using the inverse Fourier transform.

IV. A FULLY TIME-DOMAIN FORMULATION

While the hybrid approach presented in the last section is simple and effective, a fully time-domain approach can be beneficial, particularly if the time-domain far-field is of interest. To this end, consider the time-domain representation of equation (11),

$$E_z^{2D}(t)=\int_0^T\sqrt{\frac{2c\rho}{\tau}}E_\theta^{3D}(t-\tau)\,d\tau$$
$$E_\phi^{2D}(t)=\int_0^T\sqrt{\frac{2c\rho}{\tau}}E_\phi^{3D}(t-\tau)\,d\tau \quad . \quad (12)$$

These convolutions are quite costly in the present form which of course is the reason this form has been avoided. To minimize this cost, the impulse response of $1/\sqrt{\tau}$ is required in a form amenable to a more efficient implementation. Specifically, an accurate exponential representation of the discrete impulse response is needed. In [2], Prony's method was used to approximate this time domain discrete impulse response. However, in the course of the present work, it was found that this published expansion was not adequate. Therefore, a new expansion was generated using the TLS (total least squares) Prony method [7-8]. Using this approximation, equation (12) is accomplished in discrete form as,

$$E_{z,\phi}^{(n+1)2D}=2\sqrt{2\Delta_t c_0}E_{\theta,\phi}^{(n+1)3D}+\sum_{i=1}^{10}\psi_i^{(n+1)} \quad (13)$$

where

$$\psi_i^{(n+1)}=e^{\omega_i}\psi_i^{(n)}+a_i E_{\theta,\phi}^{(n)3D}, \quad (14)$$

$$a_i=\sqrt{2\Delta_t c_0}C_i \quad (15)$$

the variables C_i and ω_i are defined in Table 1 and Δ_t is the time step used in the FDTD computation

Equation (13) is applicable to each field component with the summation variable of equation (14) is executed in tandem. Note that this operation is accomplished after the simulation has been completed and does not add additional cost to the FDTD time stepping algorithm.

Table 1. Time domain approximate expansion coefficients for the discrete impulse response.

C_i	w_i
2.8127012947e-002	-1.5342833368e-004
3.0430608890e-002	-1.4566027270e-003
3.6162010199e-002	-4.5530898790e-003
4.7669826308e-002	-1.0919385763e-002
6.7935155570e-002	-2.4433346192e-002
9.8433658984e-002	-5.4569291616e-002
1.3696192243e-001	-1.2389528094e-001
1.6810710585e-001	-2.8723727545e-001
1.5152191381e-001	-6.8432281745e-001
6.3077757874e-002	-1.7514471961e+000

The accuracy of this technique is directly impacted by the accuracy of this rational approximation. This accuracy is demonstrated in Fig. 1 where the impulse response for the time domain expression $1/\sqrt{\tau}$ is demonstrated. This formulation is independent of time step. Note that the late time response (large n) is much improved over previously published approximations of the underlying discrete impulse response.

V. RESULTS

Initially, the accuracy of this method was proven by computing the monostatic scattering from a two-dimensional perfectly conducting cylinder with a radius

of 0.25 meters. The FDTD problem size was 500 by 500 cells and the cell size was 1.25 mm. These results were validated against a Mie series solution for the geometry. The accuracy of the method in this paper is demonstrated in Figs. 2 and 3. Note that the new formulation and the previous combined frequency/time domain method give near identical results. Figure 4 demonstrates the accuracy of the method across the entire bistatic angular sweep at 300 MHz for the TM_z polarization. Again the agreement is excellent.

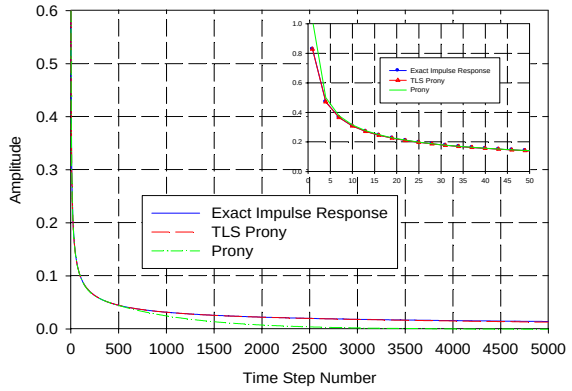

Fig. 1. Discrete impulse response for far-field convolution.

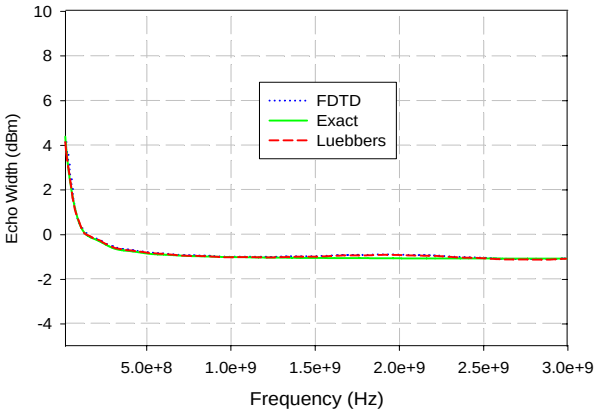

Fig. 2. TM_z monostatic backscatter for 0.25 meter PEC cylinder.

Finally, the far-field radiation from an infinitely thin wire was computed. This geometry has an analytic solution also which is well known. Figure 5 demonstrates the accuracy of the present method for this practical geometry.

VI. CONCLUSION

In this paper, an efficient and compact method for computing the two-dimensional far-fields from an FDTD simulation was presented. The accuracy was demonstrated for a simple canonical test case. The coefficients generated for the time-domain solution of this problem are also applicable to commonly used high frequency surface impedance formulations and provide an accurate alternative to previously published approximations.

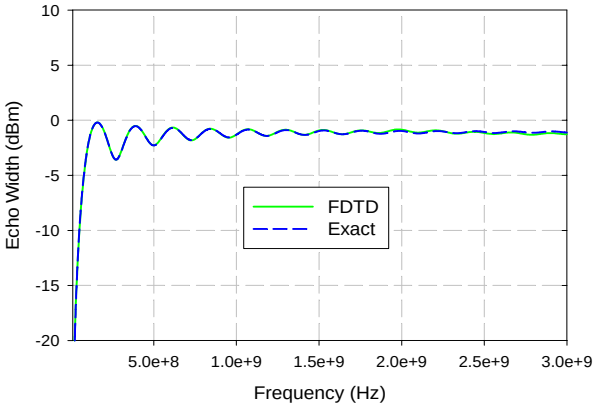

Fig. 3. TE_z monostatic backscatter for 0.25 meter PEC cylinder.

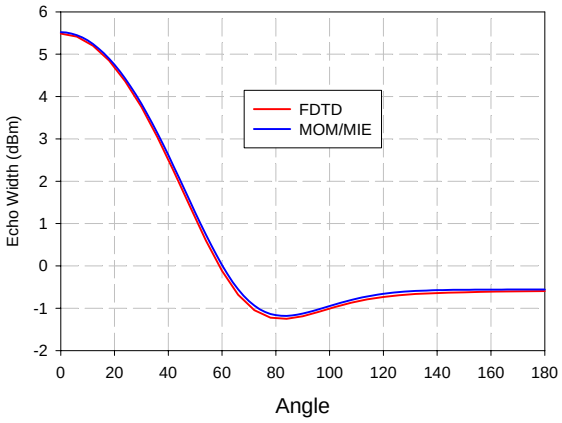

Fig. 4. Bistatic TM_z scattering from a PEC cylinder.

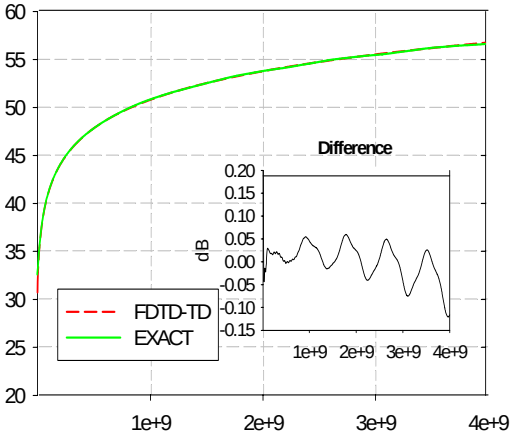

Fig. 5. Far-field of a long thin wire.

REFERENCES

[1] A. Taflove and K. R. Umashankar, "Radar cross section of general three-dimensional structures," *IEEE Trans. Electromagnetic Compatibility*, vol. 25, pp. 433-440, Nov. 1983.

[2] J. H. Beggs, R. J. Luebbers, K. S. Yee, and K. S. Kunz, "Finite-difference time-domain implementation of surface impedance boundary conditions," *IEEE Trans. Antennas and Propagation*, vol. 40, no. 1, Jan. 1992.

[3] R. J. Luebbers, K. S. Kunz, M. Schneider, and F. Hundsberger, "A finite-difference time-domain near zone to far zone transformation," *IEEE Trans. Antennas Propagation*, vol. 39, pp. 429-33, Apr. 1991.

[4] A. Taflove and S. C. Hagness, *Computational Electrodynamics: The Finite Difference Time-Domain Method, 3rd ed.* , Norwood, MA, Artech House, 2005.

[5] K. R. Umashankar and A. Taflove, "A novel method to analyze electromagnetic scattering of complex objects," *IEEE Trans. Electromagnetic Compatibility*, vol. 24, pp. 397-405, Nov. 1982.

[6] R. Luebbers, D. Ryan, and J. Beggs, "A two-dimensional time-domain near-zone to far-zone transformation," *IEEE Trans. Antennas and Prop*agation, vol. 40, no. 7, July 1992.

[7] J. J. Sacchini, W. M. Steedly, and R. L. Moses, "Two-dimensional prony modeling and parameter estimation," *IEEE Trans. Signal Processing*, vol. 41, no. 11, Nov. 1993.

[8] M. A. Rahman and K. B. Yu, "Total least squares approach for frequency estimation using linear prediction," *IEEE Trans. Acoust. Speech Signal Processing*, vol. ASSP-35, pp. 1440-1454, Oct. 1987.

Alan Roden is a Senior Project Leader with The Aerospace Corporation where his responsibilities include electromagnetic analysis and design for satellite systems. Previously, Dr. Roden worked with The Georgia Tech Research Institute in Atlanta Georgia, and the IBM Corporation in Research Triangle Park, NC. He received his Ph.D. in Electrical Engineering from the University of Kentucky, Lexington, KY in 1997, his master's degree in electrical engineering from North Carolina State University in 1989, and his B.S. from the University of Tennessee at Chattanooga in 1984. Dr. Roden is a senior member of the IEEE and has published over 30 journal and conference papers.

Steven L Johns was born in Spencer, Iowa, in 1966. He received his B.S. degree in 1987, M.S. degree in 1989, and Ph.D. degree in 1999, all from the University of Southern California, and all in electrical engineering. From 1985 to the present he has been employed by The Aerospace Corporation and involved in the design and analysis of microwave, antenna, and radar systems. He is currently a Senior Project Engineer working in the Advanced Programs Office in Colorado Springs, Colorado. He is a member of Tau Beta Pi and Eta Kappa Nu.

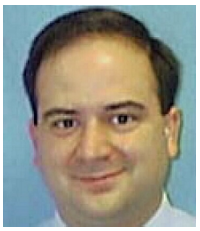

Joseph J. Sacchini is currently a Senior Project Leader for The Aerospace Corporation, Chantilly, Virginia where he works on a variety of programs involving signal processing, radar, digital communications, and electromagnetics. Prior to joining The Aerospace Corporation, Dr. Sacchini worked for SAIC and The Analytical Sciences Corporation, both in Chantilly, Virginia. He received the B.E. degree from Youngstown State University in 1984, the M.S. degree in electrical engineering from the University of Dayton in 1988, and the Ph.D. degree in electrical engineering from The Ohio State University in 1992. He was on active duty with The US Air Force from 1983 to 1998. He retired from the Air Force in 1998. During his Air Force career, Dr. Sacchini was a Program Manager and Engineer on various programs involving radar, signal processing, digital communications, electronic warfare, automatic target recognition, and electromagnetics. He also was an Assistant Professor of Electrical Engineering at the Air Force Institute of Technology from 1992 to 1996. His primary research interests are in radar signal processing, radar target identification, digital communications, and electromagnetics. Dr. Sacchini is a senior member of the IEEE, and a member of Tau Beta Pi, Phi Kappa Phi, and is registered in Ohio as a professional engineer.

Efficient Time-domain Sensitivity Analysis using Coarse Grids

Y. Song, N. K. Nikolova, and M. H. Bakr

Department of Electrical and Computer Engineering
McMaster University, Hamilton, ON L8S 4K1, Canada
songyp@grads.ece.mcmaster.ca, talia@mail.ece.mcmaster.ca, mbakr@mail.ece.mcmaster.ca

Abstract ─ We propose an efficient coarse-grid approach to the sensitivity analysis with full-wave electromagnetic (EM) time-domain simulations. In order to compute the response sensitivity using an adjoint approach, waveforms at all perturbation grid points need to be saved and post-processed. Therefore, the memory requirements of the response sensitivity analysis may become excessive for electrically large objects or problems with a large number of optimizable parameters. The use of coarse grids can reduce these memory requirements drastically and improve the computational efficiency of the sensitivity analysis while maintaining good accuracy. In this paper, we show that the discretization step size used in the sensitivity computation can be many times larger than the step size used in the finite-difference time-domain (FDTD) simulation. The effects of the coarseness of the grid on the accuracy of the sensitivity analysis are investigated. Verification is carried out through 1-D, 2-D and 3-D lossy dielectric structures using commercial FDTD solvers.

Keywords**:** Time-domain analysis, sensitivity analysis, Jacobian computation, and adjoint-variable method.

I. INTRODUCTION

The sensitivity analysis of microwave problems is important in gradient-based computer-aided design [1-4] and inverse-problem solutions [5]. It yields the response gradients (Jacobians) with respect to the optimizable shape and material parameters. Jacobians are widely used for efficient optimization, modeling, tolerance and yield analyses.

Jacobians are usually computed using response-level finite differences (FDs). For a problem with n design parameters, such an approach requires n additional simulations if forward or backward differences are used. The optimization cycle can easily become prohibitively slow due to the computational demand of the full-wave simulations. Beside its inefficiency, it is also shown in [6] to [7] that the FD approaches are unreliable, i.e. they may be prone to numerical noise [6].

In contrast, the Jacobian computation using adjoint-based methods is efficient and reliable. Over the last several years, the adjoint variable method has been studied extensively in the sensitivity analysis of transient electromagnetic (EM) systems. An adjoint approach needs at most two system analyses to compute the response Jacobians regardless of the number of the optimizable parameters. In [1-3], Chung *et al.* have proposed an exact adjoint-variable expression for high-frequency problems. This exact approach is only applicable to unstructured-grid solvers since analytical system matrix derivatives are needed. Later, Nikolova *et al.* [8] and Bakr and Nikolova [9] proposed a new adjoint-based time-domain approach based on finite-difference time-domain (FDTD) and transmission-line matrix simulations. A discrete sensitivity expression of second-order accuracy is derived based on the **E**-field vector wave equation [8]. This approach does not need analytical system matrix derivatives and allows sensitivity computation on structured grids.

Recently, we proposed a self-adjoint approach to compute responses, such as network parameters or point-wise response functions, and their Jacobian matrices use only one EM system analysis [7, 10-11]. Our approach is efficient, accurate and versatile. The adjoint field solution is obtained directly from the original field solution by some simple mathematical transformations. Adjoint simulations are not needed. Thus, this self-adjoint formulation reduces in half the computational cost in comparison with the existing adjoint methods [1-3] and [8-9]. More importantly, it is applicable with commercial EM solvers, since the Jacobian computation is reduced to a post-process of the EM field solution. In contrast, currently existing adjoint approaches [1-3] and [8-9] are only applicable to in-house codes. This is because the excitation distribution of the adjoint simulations is response dependent, which is difficult to set up in a commercial solver.

In our original self-adjoint approach, the sensitivity solver adopts the grid of the FDTD simulation for the computation of the response gradient. For this computation, at each perturbation grid point, the waveforms of all three **E**-field components need to be stored. However, this may increase the memory requirements, especially in the case of electrically large regions whose permittivity or conductivity distribution is being optimized. For some time-domain solvers, the speed of the overall simulation may be affected as well. This happens if the simulator stores on the hard disk the requested **E**-field solution at each iteration [12]. Slow-down due to recording the field solution is insignificant if the latter is exported after the simulation is over [13]. Even in this case, when the time-domain simulation is very long and the number of required field points is large, the memory requirements may become excessive.

In order to alleviate the problems described above, we propose the use of an independent coarse FD grid for the sensitivity analysis. We show that this grid can be many times coarser than the one used in the FDTD simulation. Recommendations are given for a proper choice of its step size.

We start with a brief overview of the time-domain self-adjoint sensitivity analysis. Then, we describe the implementation of the coarse-grid in inhomogeneous structures containing lossy dielectric objects. We investigate the accuracy of the proposed coarse grid approach through 1-D, 2-D and 3-D examples.

II. BACKGROUND

A. Self-adjoint S-parameter Sensitivities

The S-parameters of a multi-port structure can be expressed as [7],

$$S_{pq}^{\omega_0} = \sqrt{\frac{Z_q^{\omega_0}}{Z_p^{\omega_0}}} \cdot \frac{\tilde{F}_{pq}^{\omega_0}}{\tilde{F}_q^{\omega_0}} \tag{1}$$

where

$$\tilde{F}_{pq}^{\omega_0} = \int_0^{T_{\max}} \iint_{S_{p-port}} \mathbf{E}_q^{out}(x_p', y_p', t) \cdot \mathbf{M}_p(x_p', y_p') dx_p' dy_p' \cdot e^{-j\omega_0 t} dt \,, \tag{2}$$

$$\tilde{F}_q^{\omega_0} = \int_0^{T_{\max}} \iint_{S_{q-port}} \mathbf{E}_q^{in}(x_q', y_q', t) \cdot \mathbf{M}_q(x_q', y_q') dx_q' dy_q' \cdot e^{-j\omega_0 t} dt. \tag{3}$$

Here, T_{max} is the simulation time; the subscript q in $\mathbf{E}_q$ denotes the field solution when port q is excited, and the superscripts *out* and *in* denote the outgoing (scattered) and incoming (incident) wave, respectively; $\mathbf{M}_\xi$ ($\xi = p, q$) is the field modal (orthonormal) vector at port ξ [14]; x_ξ' and y_ξ' ($\xi = p, q$) are the coordinates at the ξ^{th} port plane; $Z_\xi^{\omega_0}$ ($\xi = p, q$) is the wave impedance of the ξ^{th} port; and ω_0 is the frequency at which the *S*-parameters are computed. For brevity, the superscript ω_0 will be omitted but implied in all formulas hereafter.

Consider a set of N optimizable parameters p_n, $n = 1, ..., N$, which represent the shape and constitutive parameters of the structure. Assuming that the parameter changes do not affect the port waveguides, the derivative of the *S*-parameter with respect to p_n is,

$$\frac{\partial S_{pq}}{\partial p_n} = \sqrt{\frac{Z_q}{Z_p}} \cdot \frac{1}{\tilde{F}_q} \cdot \frac{\partial \tilde{F}_{pq}}{\partial p_n}, \quad n = 1, ..., N \,. \tag{4}$$

The complex response $\tilde{F}_{pq}$ whose derivative is needed in equation (4) allows for a self-adjoint formulation of the sensitivity problem. This means that the associated adjoint-field solutions $(\hat{\mathbf{E}}_p)_R$ and $(\hat{\mathbf{E}}_p)_I$ [9] can be obtained from the original-field solution $\mathbf{E}_p$ where port p is excited. Here, $(\hat{\mathbf{E}}_p)_R$ and $(\hat{\mathbf{E}}_p)_I$ are the adjoint fields needed to compute the real and imaginary parts of $\partial \tilde{F}_{pq} / \partial p_n$, respectively. Thus, in our self-adjoint formulation, adjoint simulations are not needed. The computation of $(\hat{\mathbf{E}}_p)_R$ and $(\hat{\mathbf{E}}_p)_I$ from $\mathbf{E}_p$ is briefly explained below.

The adjoint current density $\hat{\mathbf{J}}_{pq}$ is the derivative of the local response $f(\mathbf{E}, \boldsymbol{p})$ with respect to the field $\mathbf{E}$ at the p^{th} port [8]. Its distribution across the port is the same as that of the current density $\mathbf{J}$. In the case of the S_{pq} derivatives, the real and imaginary parts of $\hat{\mathbf{J}}_{pq}$ are [7],

$$(-\hat{\mathbf{J}}_{pq})_R(x_p', y_p', t) = \mathbf{M}_{p\perp}(x_p', y_p') \cdot \hat{g}_R^{\omega_0}(t) \tag{5}$$

$$(-\hat{\mathbf{J}}_{pq})_I(x_p', y_p', t) = \mathbf{M}_{p\perp}(x_p', y_p') \cdot \hat{g}_I^{\omega_0}(t) \,, \tag{6}$$

where

$$\hat{g}_R^{\omega_0}(t) = \frac{\sin(\omega_0 t)}{\omega_0 \beta \Delta t \Delta z_p}, \; \hat{g}_I^{\omega_0}(t) = \frac{\cos(\omega_0 t)}{\omega_0 \beta \Delta t \Delta z_p} \,. \tag{7}$$

When the adjoint problem is excited by $-\hat{\mathbf{J}}_{pq}$ and runs backwards in time, i.e. $\tau = T_{\max} - t$, it is equivalent to the original problem [8]. To make the adjoint simulation in the backward running τ-time identical to the original one in forward *t*-time, we assume that the adjoint problem is excited by the reversed pulse $\hat{g}(\tau) = g(t)$, where $g(t)$ is the time waveform of the original excitation. The ω_0 spectral component of $\hat{g}(t)$ is related to that of $g(t)$ as [7],

$$\hat{g}^{\omega_0}(t) = G_m \cos(\omega_0 t - \varphi_g - \omega_0 T_{\max}) \tag{8}$$

where G_m and φ_g are the magnitude and phase of the ω_0 spectral component of $g(t)$. Due to the equivalence between the original and the backward-running adjoint problem, the adjoint field is related to the original one at a point *P* as,

$$\hat{\mathbf{E}}_p(P, T_{\max} - t) = \mathbf{E}_p(P, t) \tag{9}$$

and its ω_0 spectral component is

$$\hat{E}^{\omega_0}_{\zeta p}(P,t) = |E^{\omega_0}_{\zeta p(P)}| \cos(\omega_0 t - \varphi_{e\zeta p(P)} - \omega_0 T_{\max}),\ \zeta = x, y, z. \tag{10}$$

Here, ζ denotes the vector component; $|E^{\omega_0}_{\zeta p(P)}|$ and $\varphi_{e\zeta p(P)}$ are the magnitude and the phase of the ω_0 spectral component of the original $E_{\zeta p}$ waveform at *P*.

By comparing the desired adjoint excitation waveform in equation (7) with that in equation (8), the adjoint field of equation (10) should be adjusted both in magnitude and phase in order to obtain $(\hat{\mathbf{E}}_p)_R$ and $(\hat{\mathbf{E}}_p)_I$ as [7],

$$(\hat{E}^{\omega_0}_{\zeta p})_R(P,t) = \frac{|E^{\omega_0}_{\zeta p(P)}|}{J_{0p} G_m \omega_0 \beta \Delta t \Delta z} \cos\left(\omega_0 t - \varphi_{e\zeta p(P)} + \varphi_g - \pi/2\right) \tag{11}$$

$$(\hat{E}^{\omega_0}_{\zeta p})_I(P,t) = \frac{|E^{\omega_0}_{\zeta p(P)}|}{J_{0p} G_m \omega_0 \beta \Delta t \Delta z} \cos\left(\omega_0 t - \varphi_{e\zeta p(P)} + \varphi_g\right),\ \varsigma = x, y, z. \tag{12}$$

Here, G_m and φ_g are the magnitude and phase of the ω_0 spectral component of the original excitation waveform $g(t)$; $|E^{\omega_0}_{\zeta p(P)}|$ and $\varphi_{e\zeta p(P)}$ are the magnitude and phase of the ω_0 spectral component of the ζ-component of the original **E**-field at point *P*; Δz is the longitudinal cell size at the port; Δt is the discretization step in time; β is a constant defined as $\beta = \mu_0 \Delta h^2 / \Delta t$, where $\Delta h = \min(\Delta x, \Delta y, \Delta z)$; J_{0p} is the scaling factor determining the strength of the original excitation (usually set to 1).

B. Sensitivity of a Response at a Point

In open problems with a point excitation at point *Q* and a field observation at point *P*, there are no waveguide ports and the definition in equation (1) is simplified as follows: (i) the modal wave impedances are replaced by the intrinsic impedances Z_P and Z_Q of the media at which point *P* and point *Q* are located; (ii) the incoming phasor $\tilde{F}_q$ is replaced by the ω_0 spectral component $\tilde{E}_Q$ of the incident field $E_Q(t)$ at point *Q*, (iii) the outgoing phasor $\tilde{F}_{pq}$ is replaced by the ω_0 spectral component $\tilde{E}_{PQ}$ of the observed scattered field $E_{PQ}(t)$ at *P*. The response then becomes,

$$F_{PQ} = \sqrt{\frac{Z_Q}{Z_P}} \cdot \frac{\tilde{E}_{PQ}}{\tilde{E}_Q}. \tag{13}$$

Here, the scalar scattered field response $\tilde{E}_{PQ}$ and the incident field response $\tilde{E}_Q$ are defined as,

$$\tilde{E}_{PQ} = \tilde{\mathbf{E}}_{PQ} \cdot \tilde{\mathbf{M}}_P \tag{14}$$

$$\tilde{E}_Q = \tilde{\mathbf{E}}_Q \cdot \tilde{\mathbf{M}}_Q, \tag{15}$$

where $\tilde{\mathbf{E}}_{PQ}$ is the ω_0 spectral component of the scattered vector field $\mathbf{E}_{PQ}(t)$ at point *P* when point *Q* is excited and $\tilde{\mathbf{E}}_Q$ is the ω_0 spectral component of the incident vector field $\mathbf{E}_Q(t)$ at point *Q* when point *Q* is excited. $\mathbf{E}_Q(t)$ is obtained through a reference simulation where point *Q* is excited in an infinite uniform medium of the same electrical properties as the medium at point *Q* and the field $\mathbf{E}_Q(t)$ is recorded at the point of excitation. $\tilde{\mathbf{M}}_\xi$ ($\xi = P, Q$) is the desired polarization vector [14] at point ξ, which is a complex vector in general.

The derivative of F_{PQ} with respect to the *n*th parameter can be expressed as,

$$\frac{\partial F_{PQ}}{\partial p_n} = \sqrt{\frac{Z_Q}{Z_P}} \cdot \frac{1}{\tilde{E}_Q} \cdot \frac{\partial \tilde{E}_{PQ}}{\partial p_n} \tag{16}$$

where the derivative of $\tilde{E}_{PQ}$ is computed as that of $\tilde{F}_{pq}$ in the case of the *S*-parameters. The adjoint fields are derived as before.

C. Sensitivity Formula

The conventional sensitivity expressions rely on analytical derivatives of the system coefficients, i.e., the coefficients of the governing equations, with regard to the parameter of interest p_n. However, on structured grids, as those used by finite-difference methods or transmission-line methods, the system coefficients are not analytical functions of the structure's shape parameters. Consequently, their derivatives are not available analytically. To deal with such cases, a second-order accurate sensitivity formula was proposed in [8-9], which is specifically developed for discrete parameter spaces. It allows the use of a stepwise perturbation of a shape parameter equal to that of the local cell size Δh, i.e. $\Delta p_n = \pm \Delta h$. Such a perturbation results in well defined changes in the system coefficients, which yield accurate results when used in the discrete sensitivity formula. Later, we discuss the possibility of using much larger cell sizes, which are multiples of Δh.

In the case of the complex response $\tilde{F}_{pq}$ in equation (4), the discrete sensitivity formula for the real and imaginary parts of its derivative is [7],

$$\left(\frac{\partial \tilde{F}_{pq}}{\partial p_n}\right)_{R,I} \approx \int_0^{T_{\max}} \iiint_{\Omega} (\hat{\mathbf{E}}_p)_{n\,R,I} \cdot \frac{\Delta_n R(\mathbf{E}_q)}{\Delta p_n} d\Omega dt,\ n = 1,...,N \quad (17)$$

where

$$\frac{\Delta_n R(\mathbf{E}_q)}{\Delta p_n} = \frac{\Delta_n \mathcal{C}^2}{\Delta p_n}\mathbf{E}_q - \frac{\Delta_n \alpha}{\Delta p_n}\cdot D_{tt}\mathbf{E}_q - \frac{\Delta_n s}{\Delta p_n}\cdot D_{t2}\mathbf{E}_q - \frac{\Delta_n(\beta D_t \mathbf{J})}{\Delta p_n}. \quad (18)$$

Here, the subscripts *R* and *I* denote the real and the imaginary part of a complex quantity, respectively, and Δ_n denotes a stepwise change occurring in a system coefficient as a result of the perturbation Δp_n of the *n*th parameter; Ω is the computational volume; $\mathbf{E}_q$ is the original field solution of the nominal structure when port *q* is excited, and $(\hat{\mathbf{E}}_p)_{nR,I}$ are the field solutions of the adjoint problems in the *n*th perturbed state when port *p* is excited. Note that the adjoint field solutions for the real and the imaginary parts of the complex derivative are different and obtained from the original field solution $\mathbf{E}_p$ (when port *p* is excited) using equations (11) and (12) Note also that the adjoint solutions must correspond to the n^{th} perturbed state, i.e. the structure where p_n is perturbed by the smallest on-grid perturbations. However, no actual simulations of the perturbed structures are performed since their respective field solutions are approximated by a simple mapping procedure [8], which involves a one-cell shift in the direction of the respective perturbations. These approximations use the available field solution of the unperturbed structure only.

With a further regard to equation (18), the system coefficients α, β and s are,

$$\alpha = \varepsilon_r \left(\frac{\Delta h}{c\Delta t}\right)^2,\ \beta = \mu_0 \frac{\Delta h^2}{\Delta t},\ s = \frac{\sigma \mu_0 \Delta h^2}{2\Delta t}. \quad (19)$$

They correspond to a central finite-difference discretization of the **E**-field vector wave equation. The operators D_{tt}, D_{t2} and D_t are respective second- and first-order finite-difference operators with respect to time. $\mathcal{C}^2$ is the FD double-curl operator of the **E**-field vector wave equation. Points, at which the expression (18) is non-zero, are referred to as perturbation grid points.

In the case when the optimizable parameter p_n is a material parameter, the derivatives of the system coefficients can be computed analytically. Also, $\Delta_n \mathcal{C}^2$ and $\Delta_n(\beta D_t \mathbf{J})$ in equation (18) are equal to zero since the system coefficients $\mathcal{C}^2$ and $\beta D_t \mathbf{J}$ are independent of variations in the material parameters in the case of dielectric structures. Thus, equation (18) can be written in an analytical form as,

$$\frac{dR(\mathbf{E}_q)}{dp_n} = -\frac{d\alpha}{dp_n}\cdot D_{tt}\mathbf{E}_q - \frac{ds}{dp_n}\cdot D_{t2}\mathbf{E}_q \quad (20)$$

where

$$\frac{d\alpha}{dp_n} = \begin{cases} \left(\dfrac{\Delta h}{c\Delta t}\right)^2, & p_n = \varepsilon_r \\ 0, & p_n = \sigma \end{cases} \quad (21)$$

$$\frac{ds}{dp_n} = \begin{cases} 0, & p_n = \varepsilon_r \\ \dfrac{\mu_0 \Delta h^2}{2\Delta t}, & p_n = \sigma. \end{cases} \quad (22)$$

Also, in this case, there is no need for the mapping approximation of the adjoint fields. The adjoint solutions correspond to the unperturbed structure and $(\hat{\mathbf{E}}_p)_{nR,I}$ in equation (17) are replaced simply by $(\hat{\mathbf{E}}_p)_{R,I}$.

Further details of the self-adjoint sensitivity computations are given in [11] with regard to acquiring the excitation waveform, the incident-field waveform, and the de-embedding required in the case of *S*-parameter sensitivities.

III. SENSITIVITY SOLVER GRID

In our discrete self-adjoint sensitivity analysis method, the computational domain is discretized into rectangular cells as in a FD grid. Figure 1 illustrates the FD 2-D grid for a lossy dielectric rectangular object, which is modeled with constitutive parameters ε_{r2} and σ_2. The host medium is modeled with ε_{r1} and σ_1. The vertical **E**-field component of a 2-D TM mode is computed at the nodes of the grid. In original approach [7, 10-11], the sensitivity solver adopts the grid of the FDTD simulation. In order to compute the response Jacobians, the field at all perturbation grid points is stored and post-processed. For example, if the response derivatives with respect to ε_{r2} and σ_2 are needed, the waveforms of all nodes marked with black dots in Fig.1(a) must be stored.

The grid of the sensitivity solver can be independent of the simulation grid because it is nothing more than a discrete means of calculating the sensitivity integral equation (17). Note that the spatial discretization defined by the step size $\Delta\chi$ can be many times larger than the

step size Δh used by the FDTD simulation. While Δh relates to Δt through the Courant stability condition, $\Delta\chi$ is limited only by the smoothness of the integrated field quantity in the perturbation region. We emphasize that a coarse grid for the sensitivity calculation does not imply in any way a possibility to use a coarse grid in the FDTD analysis. The accuracy of the sensitivity calculation depends crucially on the accuracy of the field solution and, therefore, the grid of the EM simulation must remain fine enough to ensure convergent numerical analysis.

To illustrate the coarse sensitivity grid, three different grids are shown in Fig. 1(b): the black crosses are used for the case $\Delta\chi = 2\Delta h$; the red squares for $\Delta\chi = 4\Delta h$; and the blue circles for $\Delta\chi = 8\Delta h$. We note that the number of stored field waveforms decreases as $3k^3$ in a 3-D simulation and as k^2 in a 2-D simulation when the grid is made coarser by a factor $k = \Delta\chi / \Delta h$.

The coarse sensitivity-solver grid may be applied to shape parameters as well although the savings in memory are not as dramatic since perturbation grid points exist only at the object's interfaces instead of its whole volume. For instance, when the response gradient with respect to w is computed, the nodes where the field is saved are shown in Figs. 2(a-b). The black dots in Fig. 2(a) are the perturbation nodes for our original approach. Figure 2(b) shows the perturbation nodes for the three coarse grids: black crosses for $\Delta\chi = 2\Delta h$ (12 nodes), red squares for $\Delta\chi = 4\Delta h$ (6 nodes), and blue circles for $\Delta\chi = 8\Delta h$ (3 nodes).

Coarse grids are needed for computationally large objects, i.e., objects which are more than several Δh in size, due to the excessive memory requirements. For computationally small objects, we suggest that the sensitivity solver adopts the simulation grid, i.e. $\Delta\chi = \pm\Delta h$. In the case of computationally large objects, we investigate the limits of the factor $k = \Delta\chi / \Delta h$, below which the Jacobian computation is of acceptable accuracy. We consider 1-D, 2-D and 3-D examples and give recommendation.

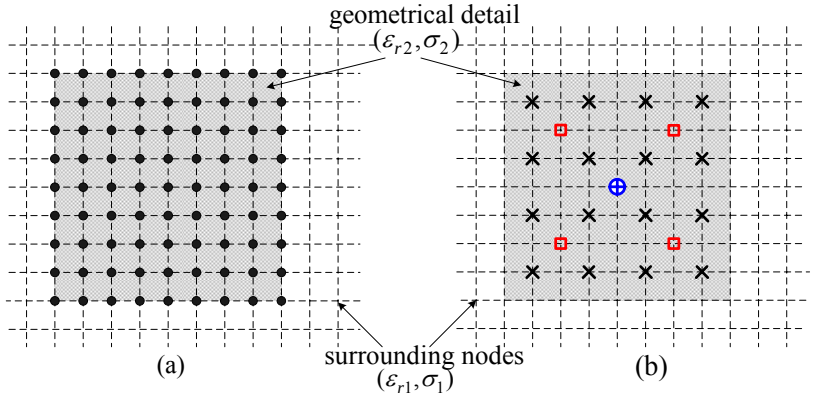

Fig. 1. Sensitivity solver grid: (a) the fine simulation grid; (b) the coarse sensitivity-analysis grids.

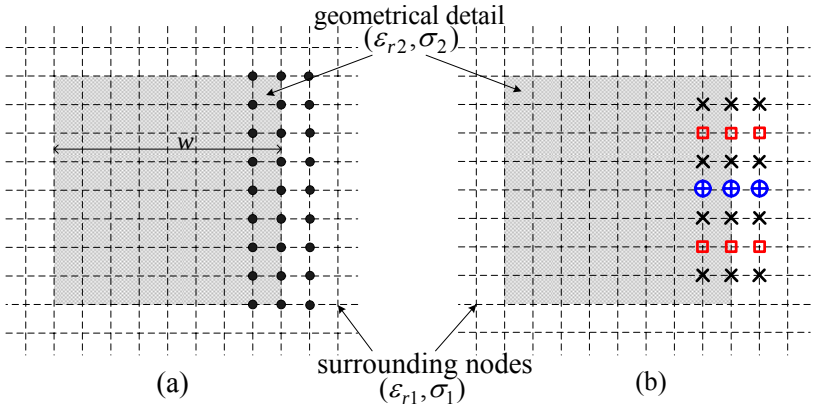

Fig. 2. Sensitivity solver grid: (a) the fine simulation grid (b) the coarse sensitivity-analysis grids.

IV. NUMERICAL RESULTS AND DISCUSSION

Our approach is verified through 1-D, 2-D and 3-D dielectric lossy inhomogeneous examples. We compute the *S*-parameter derivatives and the derivatives of a point-wise response function with respect to both constitutive and shape parameters for electrically large and small objects. Field analyses are carried out in the time domain with the commercial FDTD-based solvers XFDTD [12] and QW-3D [13]. Mesh convergence is checked for all examples. The convergence error formula is,

$$e = \left|\tilde{E}_\zeta^{(k+1)} - \tilde{E}_\zeta^{(k)}\right| / \left|\tilde{E}_\zeta^{(k+1)}\right|, \qquad \zeta = x,\ y,\ z. \tag{23}$$

Here, the superscripts denote two consecutive mesh sizes. $\tilde{E}_\zeta^{(k+1)}$ and $\tilde{E}_\zeta^{(k)}$ are the phasors of the field solutions for two consecutive mesh sizes at the highest frequency of interest. This error is usually monitored at the ports for *S*-parameter analysis or at the observation points *P* and *Q*.

In all plots, the results obtained using the original approach of self-adjoint sensitivity analysis are marked as 'FDTD-SASA'. The results obtained using coarse-grid schemes of the self-adjoint sensitivity analysis are marked as ' $\Delta\chi = k\Delta h$ ', which means that the sensitivity-solver grid is *k* times coarser than the FDTD grid. The results estimated using the forward, central and backward finite differences are marked as 'FFD', 'CFD' and 'BFD', respectively. For shape parameter derivatives, the FD estimates use parameter perturbation of $1\Delta h$ unless specified otherwise in brackets in the plot's legend. For material parameters derivatives, the amount of parameter perturbation is shown in brackets as a percentage of the nominal value. Where available, analytical results are marked as 'Analytical'. All analyses are performed over a frequency range from 3.0 GHz to 5.0 GHz, which is the bandwidth of the excitation pulse.

A. Parallel-Plate Waveguide with an Electrically Thick Layer

We first illustrate the approach with a parallel-plate waveguide (see the insert in Fig. 3) with an electrically thick inhomogeneity (shown in shade). Both media are lossy. Uniform mesh ($\Delta h = 0.25$ mm) is used in the FDTD simulation with a mesh convergence error less than 5 %. The excitation is a modulated Gaussian pulse. It has a uniform distribution across the port conforming to a TEM plane wave.

The optimizable parameters $\boldsymbol{p}^T = [\varepsilon_{r2}, \sigma_2, w]$ are the constitutive parameters of the central layer. Figure 3 shows the derivative of $|S_{11}|^2$ with respect to σ_2. It is noted that the results obtained using all coarse schemes except the one using $\Delta\chi = 20\Delta h$, which is the Nyquist limit at 5 GHz, show good agreement with the analytical, the FDTD-SASA and the CFD results.

For electrically large objects in a 1-D problem, if the optimizable parameters are material parameters, we recommend to choose the step size of the sensitivity solver as $\Delta\chi \le \lambda_{\min}/4$ in order to maintain good accuracy. Here, $\lambda_{\min}$ is the minimum wavelength of interest in the medium of the optimized object.

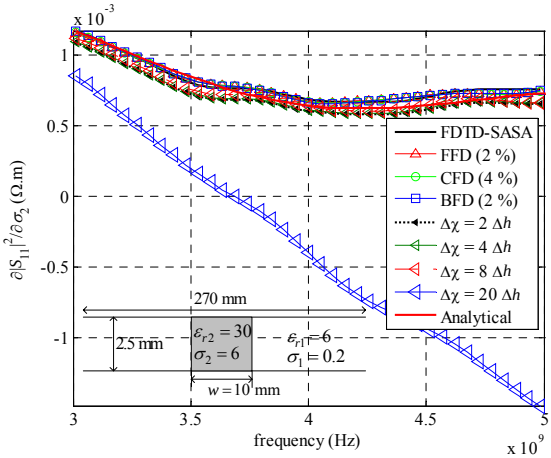

Fig. 3. Derivative of $|S_{11}|^2$ with respect to σ_2 in the 1-D example with electrically thick layer.

Figures 4 and 5 show the derivatives of the real and imaginary parts of S_{11} with respect to the shape parameter *w*. It is observed that all curves obtained using coarse grids except the one with $\Delta\chi = 2\Delta h$ show substantial discrepancies in comparison with the FDTD-SASA ($\Delta\chi = \Delta h$) as well as the FD curves. For 1-D problems, if the shape parameter is optimized, we recommend to choose the step size of the sensitivity solver as that of the simulation grid in order to maintain good accuracy. This is also because the memory requirements in this case are small.

B. Parallel-Plate Waveguide with a Thin Layer

A parallel-plate waveguide with an electrically thin central layer is shown in the insert of Fig. 6. Uniform mesh ($\Delta h = 0.125$ mm) with a mesh convergence error less than 4 % is used in the FDTD simulation. The excitation and the optimizable parameters are the same as in the first example.

Figure 6 shows the derivative of the real part of S_{21} with respect to ε_{r2}. It is observed that all curves obtained using different coarse-grid schemes are in good agreement. There is very small discrepancy between the

curves obtained using coarse grids and all the other curves. We conclude that for an electrically small object in a 1-D problem, the step size $\Delta\chi$ of the sensitivity solver can be chosen as large as the size of the object when derivatives with respect to material parameters are computed.

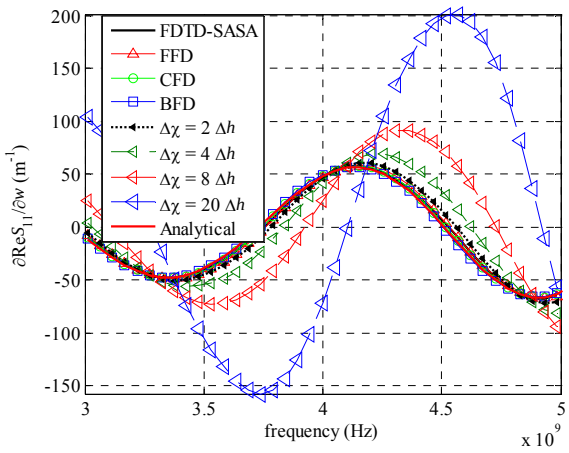

Fig. 4. Derivative of $\mathrm{Re}(S_{11})$ with respect to w in the 1-D example with electrically thick layer.

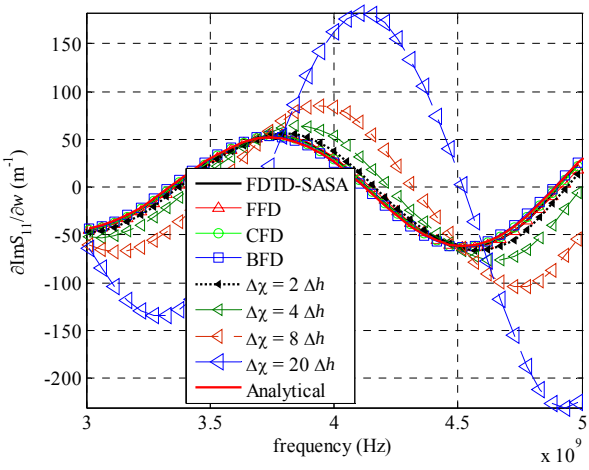

Fig. 5. Derivative of $\mathrm{Im}(S_{11})$ with respect to w in the 1-D example with electrically thick layer.

C. Electrically Large Object in a Lossy Medium

Figure 7(a) shows a 2-D structure with an electrically large object immersed in a host medium. Both the host medium and the object are lossy. Uniform mesh ($\Delta h = 0.25$ mm) with a mesh convergence error below 4 % is used. We use the same excitation waveform as in the above examples.

The design parameters are $\boldsymbol{p}^T = [\varepsilon_{r2}, \sigma_2, w]$. We use the normalized point-wise response function F_{PQ} in equation (13). In Fig. 7(a), Q is the excitation point while P is the observation point. The sensitivity of $|F_{QQ}|$ with respect to ε_{r2} and the sensitivity of $|F_{PQ}|$ with respect to w are plotted in Fig. 8 and 9, respectively. We notice that the step size of sensitivity solver can be 8 times coarser than that of the FDTD simulation. A sensitivity-grid cell size of $\Delta\chi = 16\Delta h$ corresponds to the Nyquist limit at 5 GHz for the medium of the obstacle and the respective curves show significant departure from all other results. For electrically large object in a 2-D problem, we recommend to choose the step size of the sensitivity solver as $\Delta\chi \le \lambda_{\min}/4$ in order to maintain good accuracy.

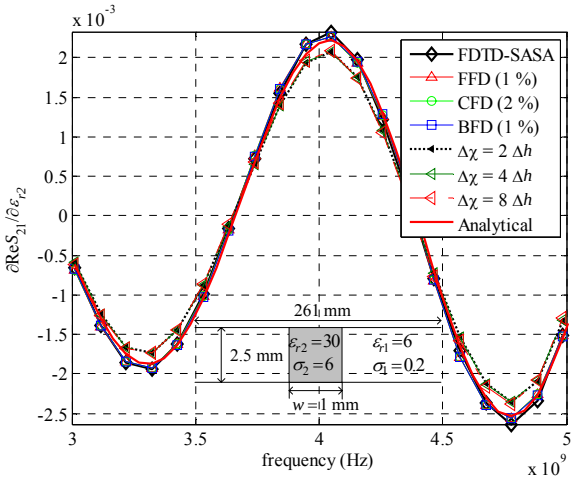

Fig. 6. Derivative of $\mathrm{Re}(S_{21})$ with respect to ε_{r2} in the 1-D example with electrically thin layer.

D. Electrically Small Object in a Lossy Medium

Figure 7(b) shows a 2-D structure with an electrically small inhomogeneity in a host medium. Both the host medium and the inhomogeneity are lossy. A uniform mesh ($\Delta h = 0.125$ mm) with a mesh convergence error below 3 % is used. The excitation, design parameters, and the response functions are the same as those in the example in subsection *C*.

In Fig. 7(b), Q is the excitation point while P is the observation point. The sensitivities of $|F_{PQ}|$ with respect to σ_2 and w are plotted in Fig. 10 and 11, respectively. We notice that the step size of the sensitivity solver needs to be the same as the step size of the FDTD simulation in order to achieve good accuracy. For electrically small objects in 2-D problems, we recommend to choose the step size of the sensitivity solver as that of the FDTD simulation for both shape and material parameters in order to maintain good accuracy.

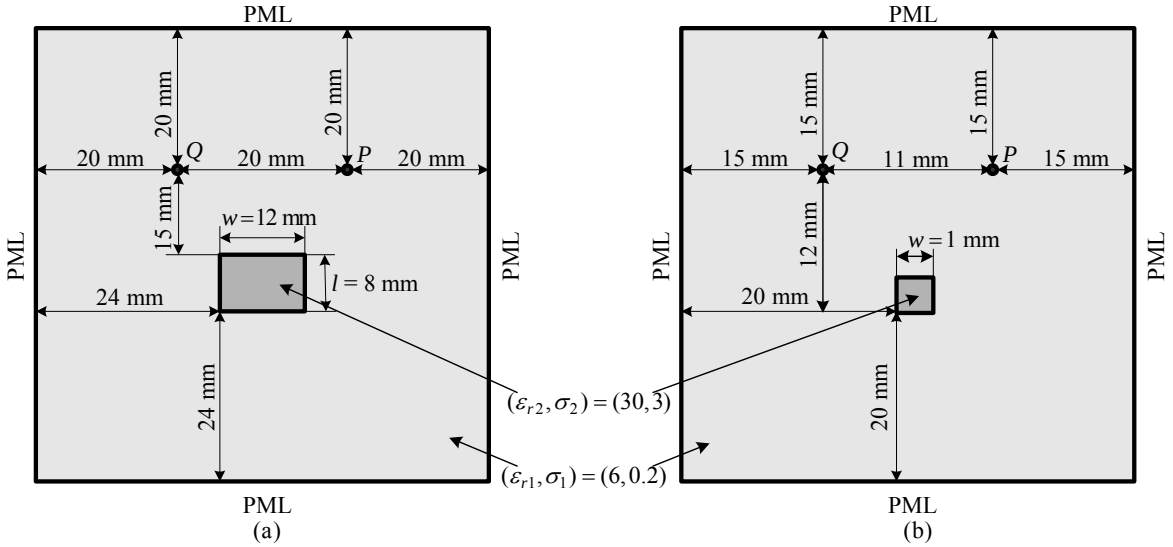

Fig. 7. Geometry of 2-D examples: (a) electrical large and (b) electrical small objects in lossy medium.

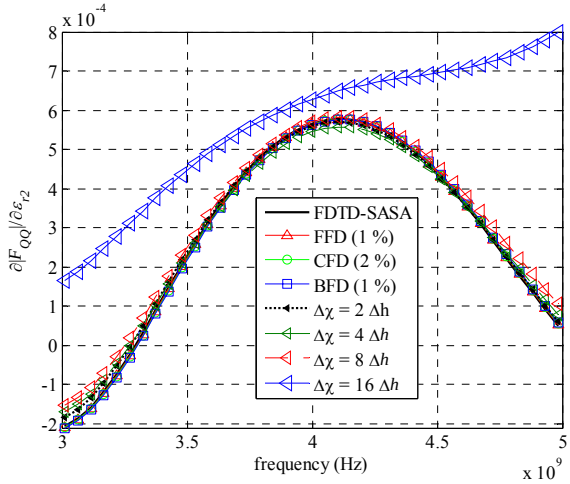

Fig. 8. Derivative of $|F_{QQ}|$ with respect to ε_{r2} in the 2-D example with a large object.

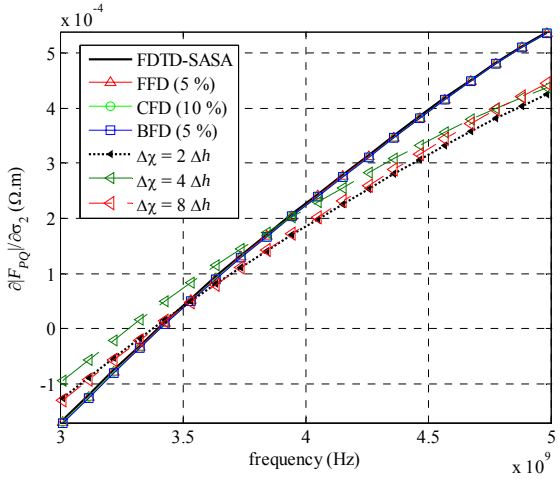

Fig. 10. Derivative of $|F_{PQ}|$ with respect to σ_2 in the 2-D example with a small object.

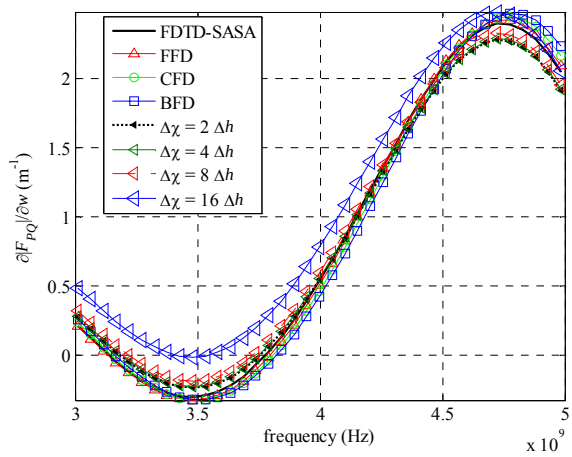

Fig. 9. Derivative of $|F_{PQ}|$ with respect to w in the 2-D example with a large object.

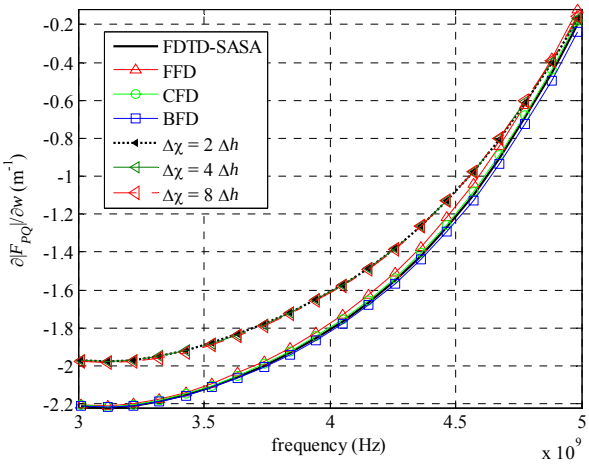

Fig. 11. Derivative of $|F_{PQ}|$ with respect to w in the 2-D example with a small object.

E. 3-D Object in a Lossy Medium

Figure 12 shows a 2-D cross-section of the 3-D structure and its parameters. The host medium and the immersed object are lossy. The host medium is a rectangular box with a corner at (0, 0, 0) mm. It extends 40 mm along the *x*-axis and the *z*-axis, and 44 mm along the *y*-axis. The immersed object is a small rectangular object with a corner at (18, 15, 18) mm, and an extent of w = 4 mm along the *x*-axis, h = 4 mm along the *y*-axis and l = 4 mm along the *z*-axis. Uniform mesh ($\Delta h = 0.25$ mm) with a mesh convergence error below 5 % is used.

The design parameters are $\boldsymbol{p}^T = [\varepsilon_{r2}, \sigma_2, w, h, l]$. The excitation and the response functions are the same as those of the example in subsection *C*. In Fig. 12, *Q* is the excitation point located at (15, 29, 17) mm while *P* is the observation point located at (25, 29, 17) mm. Figure 13 shows the derivative of $|F_{QQ}|^2$ with respect to w. It is noted that all curves obtained using coarse grids except the one with $\Delta\chi = 16\Delta h$, which approaches the Nyquist limit of the object medium at 5 GHz, have good agreement with the curves computed using our original self-adjoint approach. These curves are in close agreement, i.e., they are convergent. In contrast, the curves computed using response-level FDs are not convergent. Different shape parameter perturbations have been tried. The best FD estimates are shown here obtained with $\Delta w = 2\Delta h$.

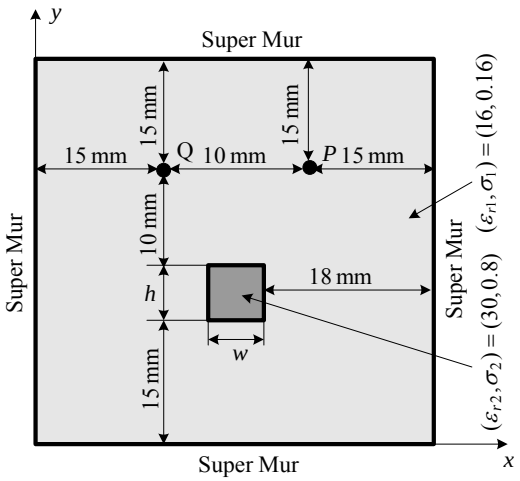

Fig. 12. A 2-D cross-section of the 3-D example.

Figure 14 shows the derivative of $|F_{QQ}|^2$ with respect to ε_{r2}, where similar results are obtained. Figure 15 shows the derivative of $|F_{PQ}|^2$ with respect to ε_{r2}. All curves except the one with $\Delta\chi = 16\Delta h$ are in good agreement. We recommend that in a 3-D problem, the step size of the sensitivity solver is chosen as $\Delta\chi \le \lambda_{\min}/4$ for both material and shape parameters in order to maintain good accuracy.

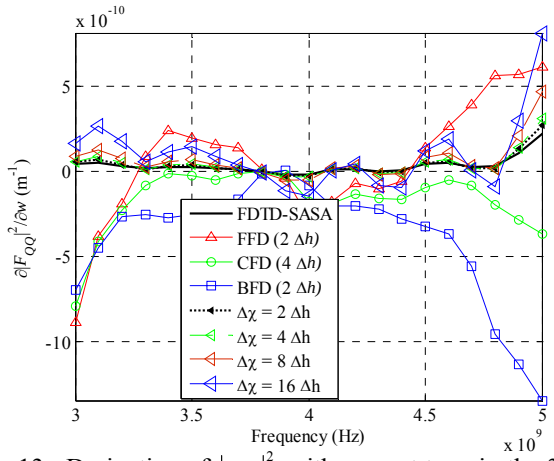

Fig. 13. Derivative of $|F_{QQ}|^2$ with respect to w in the 3-D example.

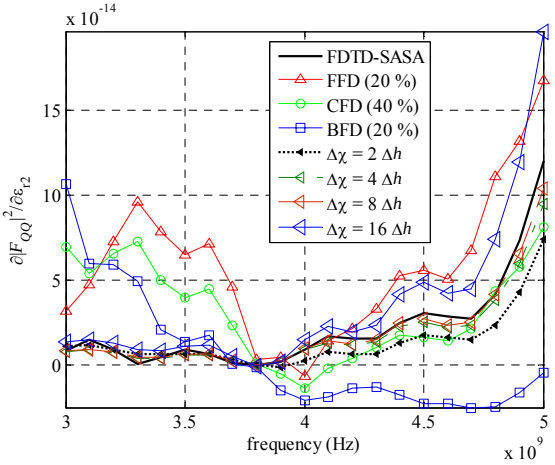

Fig. 14. Derivative of $|F_{QQ}|^2$ with respect to ε_{r2} in the 3-D example.

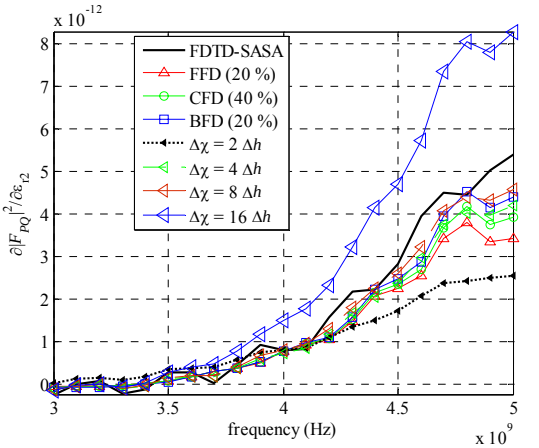

Fig. 15. Derivative of $|F_{PQ}|^2$ with respect to ε_{r2} in the 3-D example.

V. CONCLUSIONS

We propose a coarse-grid approach for the efficient computation of response Jacobians using the self-adjoint sensitivity analysis method. The sensitivity-analysis grid can be many times coarser than the grid used by the EM simulation. We emphasize that the accuracy of the sensitivity result is dependent on the accuracy of the field solution and, therefore, the grid of the EM simulation must remain fine enough to ensure convergent solution. Yet, the sensitivity grid can be as coarse as a quarter wavelength for the highest frequency of interest. This is because it is nothing more than a discrete means of calculating the sensitivity integral. It is limited only by the requirement that the local field solution is a sufficiently smooth function of space at the given frequency.

The coarse-grid approach reduces the memory requirements drastically. It is especially useful in the case of electrically large regions whose permittivity or conductivity distribution is being optimized, since the memory requirement of our original self-adjoint approach, which uses the FDTD simulation grid directly, may become excessive. The coarse-grid Jacobian computations are verified through 1-D, 2-D and 3-D examples. We find that they maintain very good accuracy as long as the step size of the sensitivity solver is below the Nyquist limit. Recommendations about the step size of the sensitivity solver are given for both electrically large and small objects.

Our new grid scheme is independent of the simulation grid and is simple to implement. The approach can be realized as standalone software to compute response Jacobians, which can be used in gradient-based computer-aided design and inverse-problem solutions. Applications focus on lossy dielectric media as those used to model high-frequency problems arising in biomedical applications of microwave imaging.

REFERENCES

[1] Y. Chung, C. Cheon, I. Park, and S. Hann, "Optimal shape design of microwave device using FDTD and design sensitivity analysis," *IEEE Trans. Microw. Theory Tech.*, vol. 48, no. 12, pp. 2289-2296, Dec. 2000.

[2] Y. Chung, J. Ryu, C. Cheon, I. Park, and S. Hahn, "Optimal design method for microwave device using time domain method and design sensitivity analysis-Part I: FETD case," *IEEE Trans. Magn.*, vol. 37, no. 9, pp. 3289-3293, Sep. 2001.

[3] Y. Chung, J. Ryu, C. Cheon, I. Park, and S. Hahn, "Optimal design method for microwave device using time domain method and design sensitivity analysis-Part II: FDTD case," *IEEE Trans. Magn.*, vol. 37, no. 9, pp. 3255–3259, Sep. 2001.

[4] N. K. Nikolova, J. W. Bandler, and M. H. Bakr, "Adjoint techniques for sensitivity analysis in high-frequency structure CAD," *IEEE Trans. Microw. Theory Tech.*, vol. 52, no. 1, pp. 403-419, Jan. 2004.

[5] Q. Fang, P. M. Meaney, S. D. Geimer, K. D. Paulsen, and A. V. Streltsov, "Microwave image reconstruction from 3-D fields coupled to 2-D parameter estimation," *IEEE Trans. Med. Imag.*, vol. 23, pp. 475-484, Apr. 2004.

[6] Y. Song and N. K. Nikolova, "Sensitivity analysis of electrically small objects in lossy inhomogeneous structures," *IEEE AP-S Int. Symp.*, pp. 4453-4456, June 2006.

[7] N. K. Nikolova, Ying Li, Yan Li, and M. H. Bakr, "Sensitivity analysis of scattering parameters with electromagnetic time-domain simulators," *IEEE Trans. Microw. Theory Tech.*, vol. 54, pp. 1589-1610, April 2006.

[8] N. K. Nikolova, H. W. Tam, and M. H. Bakr, "Sensitivity analysis with the FDTD method on structured grids," *IEEE Trans. Microw. Theory Tech.*, no. 52, pp. 1207–1216, 2004.

[9] M. H. Bakr and N. K. Nikolova, "An adjoint variable method for time domain TLM with fixed structured grids," *IEEE Trans. Microw. Theory Tech.*, vol. 52, pp. 554-559, Feb. 2004.

[10] Yang Li, Yan Li, N. K. Nikolova, and M. H. Bakr, "Time domain sensitivity analysis of lossy dielectric structures," *Frontiers of Applied Computation Electromagnetics (FACE) 2006 CDROM* (Victoria, BC), June 2006.

[11] Y. Song, Y. Li, N. K. Nikolova and M. H. Bakr, "Self-adjoint sensitivity analysis of lossy dielectric structures with electromagnetic time-domain simulators," *Int. J. of Numerical Modelling: Electronic Networks, Devices and Fields* (accepted).

[12] XFDTD v. 6.2, *Reference Manual*, Remcom, 2004, http://www.recom.com/xfdtd6/.

[13] QuickWave-3D v. 6.0, *Reference Manual*, QWED, 2006, http://www.qwed.com.pl/index.htm.

[14] N. Marcuvitz, *Waveguide Handbook*, Chapter 2, London, UK: Peter Peregrinus Ltd., 1993 reprint.

[15]C. A. Balanis, *Antenna Theory: Analysis and Design*, 3rd ed., New Jersey, USA: John Willey & Sons, Inc., 2005

Yunpeng Song received the M. Sc. Degree in electrical engineering from Concordia University, Montreal, Canada, in 2005, and is currently working toward the Ph. D degree in electrical engineering at McMaster University, Hamilton, ON, Canada. His research interests include computational electromagnetics, inverse-scattering problems, optimization methods, computer-aided analysis and design in microwave engineering and antennas.

Natalia K. Nikolova received the Dipl. Eng. degree from the Technical University of Varna, Bulgaria, in 1989, and the Ph.D. degree from the University of Electro-Communications, Tokyo, Japan, in 1997. From 1998 to 1999, she held a Postdoctoral Fellowship of the Natural Sciences and Engineering Research Council of Canada (NSERC), during which time she was initially with the Microwave and Electromagnetics Laboratory, DalTech, Dalhousie University, Halifax, Canada, and, later, for a year, with the Simulation Optimization Systems Research Laboratory, McMaster University, Hamilton, ON, Canada. In July 1999, she joined the Department of Electrical and Computer Engineering, McMaster University, where she is currently an Associate Professor. Her research interests include theoretical and computational electromagnetism, inverse problems and microwave imaging, as well as CAD methods for high-frequency structures and antennas. Prof. Nikolova was the recipient of a University Faculty Award of NSERC from 2000 to 2005. She is a senior member of the IEEE and a member of the Applied Computational Electromagnetics Society (ACES) and the International Union of Radio Science (URSI). Prof. Nikolova was the representative of Commission D in the Canadian National Committee of URSI from 2002 till 2007. She is currently a member of the ACES Board of Directors. She is a registered professional engineer in the province of Ontario, Canada.

Mohamed H. Bakr received a B.Sc. degree in Electronics and Communications Engineering from Cairo University, Egypt in 1992 with distinction (honors). In June 1996, he received a Master's degree in Engineering Mathematics from Cairo University. In 1997, he was a student intern with Optimization Systems Associates (OSA), Inc. From 1998 to 2000, he worked as a research assistant with the Simulation Optimization Systems (SOS) research laboratory, McMaster University, Hamilton, Ontario, Canada. He earned the Ph.D. degree in September 2000 from the Department of Electrical and Computer Engineering, McMaster University. In November 2000, he joined the Computational Electromagnetics Research Laboratory (CERL), University of Victoria, Victoria, Canada as an NSERC Post Doctoral Fellow. His research areas of interest include optimization methods, computer-aided design and modeling of microwave and photonic circuits, neural network applications, smart analysis of microwave circuits, efficient optimization using time/frequency domain methods, and bio-electromagnetism. He is currently an associate professor with the Department of Electrical and Computer Engineering, McMaster University. Dr. Bakr was a recipient of a Premier's Research Excellence Award (PREA) from the province of Ontario, Canada, in 2003.

Practical Implementation of a CPML Absorbing Boundary for GPU Accelerated FDTD Technique

[1]M. J. Inman, [1]A. Z. Elsherbeni, [2]J. G. Maloney, and [2]B. N. Baker

[1] Department of Electrical Engineering
University of Mississippi, University, MS 38677-1848, USA
atef@olemiss.edu , mjinman@olemiss.edu

[2] Georgia Tech Research Institute
Georgia Institute of Technology, Atlanta, GA 30332, USA
jim.maloney@gtri.gatech.edu , brad.baker@gtri.gatech.edu

Abstract – The use of graphical processing units (GPU) has been recently documented for the implementation of the FDTD technique; however, little has been reported about the necessary additions to three dimensional FDTD codes to make the technique more useful for fast antenna analysis and design. This paper details the addition of a convolutional perfectly matched layer absorbing boundary (CPML) to a three dimensional GPU accelerated FDTD code.

Keywords: FDTD, PML, CPML, and GPU.

I. INTRODUCTION

The use of a graphical processing unit (GPU) to accelerate the nested loops for updating the field of a three dimensional FDTD code has been documented in literature over the past few years [1-3]. What has been absent is the implementation of all the additional features of electromagnetic simulation that allow the FDTD technique to be so useful to the antenna engineer. These features include, but are not limited to, a functioning absorbing boundary, a plane wave injection method, discrete feeds for driven antennas, sub-cell models, linear and non-linear circuit element models, and near to far-field transformation for radar cross-section (RCS) and antenna pattern analysis. The goal of this paper is to add the first item in the list, a PML absorbing boundary, to a GPU-accelerated code without giving up too much of the speed advantage provided by the use of the GPUs. Since the convolutional PML [4] relies on the same triple-nested loops as the standard 3D FDTD, as well as having several other benefits [5], it seemed to be a promising candidate to implement in a GPU FDTD code. This paper addresses the benefits of implementing the CPML in a 3D FDTD code executed on a GPU. The details of how to construct a GPU FDTD code is not within the scope of this paper as this can be found in [1-3].

II. CPML FORMULATION

The CPML formulation was chosen both for its simplicity, as well as the straightforward nature of its implementation [5]. Both the standard PML [6] and its Uniaxial [7] formulation require the PML region to be updated separately from the rest of the computational domain. These formulations also possess a two-step update procedure and a complicated set of coefficients to allow general materials to be present in the PML region. The CFS-PML is favorable due to the fact that all cells in the PML are updated in the normal FDTD loop, so all general materials are handled. After the normal loop of updating the field components, the convolutional term is added to the appropriate fields for each face that has PML present on it. This is also a two step process, but the first step is simply the normal FDTD update process.

For the sake of completeness, this section will detail the formulation of CPML used in the GPU accelerated code described in this paper. The derivations for all equations, as well as a much better descriptions of both the CFS-PML and the CPML, are given in [8]. The first step in building the CPML is to set the field updating coefficients correctly. The coefficients are scaled spatially from the edge of the computational domain. All of the following equations describe a CPML that attenuates waves traveling toward the lower z boundary. The two important terms are the complex frequency shifted term, a, and the PML conductivity term, σ which are given as,

$$a_z(u) = a_{\max}\left(\frac{iPML-(u-1)}{iPML}\right)^m \qquad (1)$$

$$\sigma_z(u) = \sigma_{\max}\left(\frac{u}{iPML}\right)^m. \qquad (2)$$

In equations (1) and (2), *u* is the integer representing the location from the lower z boundary, and *iPML* is the number of PML cells (which is set to 10 for the results presented here). The term *m* is the order of the polynomial taper, which was set to 4. The polynomial tapers are applied to a maximum values for *a* and σ, which are defined as,

$$a_{\max} = 2\pi\varepsilon_o F_o / 10 \tag{3}$$

$$\sigma_{\max} = \frac{0.8(\mathrm{m}+1)}{\Delta_z \sqrt{\mu_o / \varepsilon_o}}. \tag{4}$$

Equation (3) is taken directly from [7], while equation (4) is chosen as a good fit for most problems. The F_o term is the center frequency of the excitation pulse in the frequency domain. For this case, a derivative of a Gaussian is used as the source waveform. The spatially scaled terms are then used to create the b_z and c_z coefficients such that,

$$b_z(u) = e^{-\Delta_t\left(\frac{\sigma_z(u)}{\varepsilon_o \kappa_z(u)} + \frac{a_z(u)}{\varepsilon_o}\right)} \tag{5}$$

$$c_z(u) = \left(\frac{\sigma_z(u)}{\sigma_z(u)\kappa_z(u) + \kappa_z(u)^2 a_z(u)}\right) b_z(u). \tag{6}$$

As mentioned previously, all cells in the computational domain, the PML cells included, are updated with the standard FDTD update equations. For the lower z boundary example, the *Ex* and *Ey* terms are then modified by a convolutional "correction" term to apply the PML. These terms are given in equations (7) and (8). They are then added into the *Ex* and *Ey* terms as given in equations (9) and (10). The *CEXH* term in equations (9) is the usual magnetic coefficient for the Ex update equation. Likewise for the *CEYH* term in equations (10). These terms are defined in equations (11) and (12) as a function of the permittivity and conductivity of the material at individual points and are separated by direction,

$$\Psi E_{xz}(i,j,u) = b_z(u)\Psi E_{xz}(i,j,u) + c_z(u)\left(Hy(i,j,u) - Hy(i,j,u-1)\right) \tag{7}$$

$$\Psi E_{yz}(i,j,u) = b_z(u)\Psi E_{yz}(i,j,u) + c_z(u)\left(Hx(i,j,u) - Hx(i,j,u-1)\right), \tag{8}$$

$$E_x(i,j,u) = E_x(i,j,u) - CEXH(i,j,u)\Psi E_{xz}(i,j,u), \tag{9}$$

$$E_y(i,j,u) = E_y(i,j,u) + CEYH(i,j,u)\Psi E_{yz}(i,j,u), \tag{10}$$

$$CEXH(i,j,u) = \frac{\Delta t}{\varepsilon_{rx}(i,j,u)\varepsilon_0 + \frac{\Delta t \sigma_{ex}(i,j,u)}{\varepsilon_0}}, \tag{11}$$

$$CEYH(i,j,u) = \frac{\Delta t}{\varepsilon_{ry}(i,j,u)\varepsilon_0 + \frac{\Delta t \sigma_{ey}(i,j,u)}{\varepsilon_0}}. \tag{12}$$

The magnetic CPML update process proceeds similarly. The one difference that should be noted is that the spatially scaled coefficients are shifted by the usual ½ cell characteristic of the Yee cell [9]. The update equations for the magnetic field are given by,

$$\Psi H_{xz}(i,j,u) = b_z(u)\Psi H_{xz}(i,j,u) + c_z(u)\left(Ey(i,j,u+1) - Ey(i,j,u)\right) \tag{13}$$

$$\Psi H_{yz}(i,j,u) = b_z(u)\Psi H_{yz}(i,j,u) + c_z(u)\left(Ex(i,j,u+1) - Ex(i,j,u)\right), \tag{14}$$

$$H_x(i,j,u) = H_x(i,j,u) - CHXE\left(\Psi H_{xz}(i,j,u)\right), \tag{15}$$

$$H_y(i,j,u) = H_y(i,j,u) + CHYE\left(\Psi H_{yz}(i,j,u)\right), \tag{16}$$

$$CHXE(i,j,u) = \frac{\Delta t}{\mu_{rx}(i,j,u)\mu_0 + \frac{\Delta t \sigma_{mx}(i,j,u)}{\mu_0}}, \tag{17}$$

$$CHYE(i,j,u) = \frac{\Delta t}{\mu_{ry}(i,j,u)\mu_0 + \frac{\Delta t \sigma_{my}(i,j,u)}{\mu_0}}. \tag{18}$$

III. GPU IMPLEMENTATION OF THE CPML

Efficient implementations of basic FDTD technique on GPU's have been documented in the past, however, including absorbing boundary conditions can present a few challenges. Certain common boundary types such as Mur or Liao may not have easy implementation due to the nature of the time and spatial dependency of their updating equations, especially for higher orders absorbing boundaries. Furthermore, this problem gets to be more complicated for three dimensional problems where the 3D to 2D translation [3] is necessary for storage inside the GPU card as seen in Fig. 1. Because of this translation, the various x, y, and z boundaries inside the domain are scattered amongst the various tiles. Thus applying the boundary conditions on the individual boundaries becomes very complicated.

On the contrary, the CMPL boundary condition can be implemented with a much easier procedure since CPML can be represented by FDTD-like arrays. In most efficient C and FORTRAN implementations of CPML, the coefficients (ψ, b, c) and the processing loops operate only on the boundary locations, however since the coefficients in non-boundary areas would be zero, the coefficients and processing loops can be extended to cover the entire domain. While unnecessary in C and FORTRAN implementations, this becomes necessary in the GPU code as the boundaries are scattered throughout the 2D translated arrays. This allows for a much simpler updating function as it can be applied over the entire domain without having to worry in the GPU section where exactly the boundary locations are. Figure 2 shows the location of the various boundaries once the 3D domain has been decomposed into a 2D tiled domain. The program will calculate and populate the various coefficients necessary to implement the CPML boundary in these regions only.

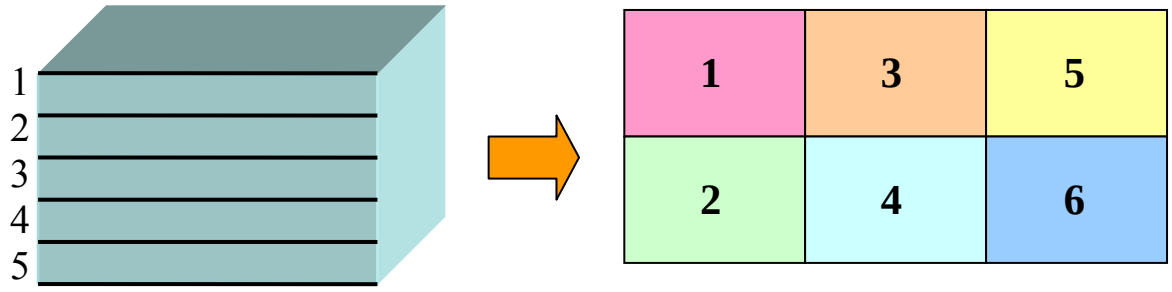

Fig. 1. 3D to 2D translation via tiling.

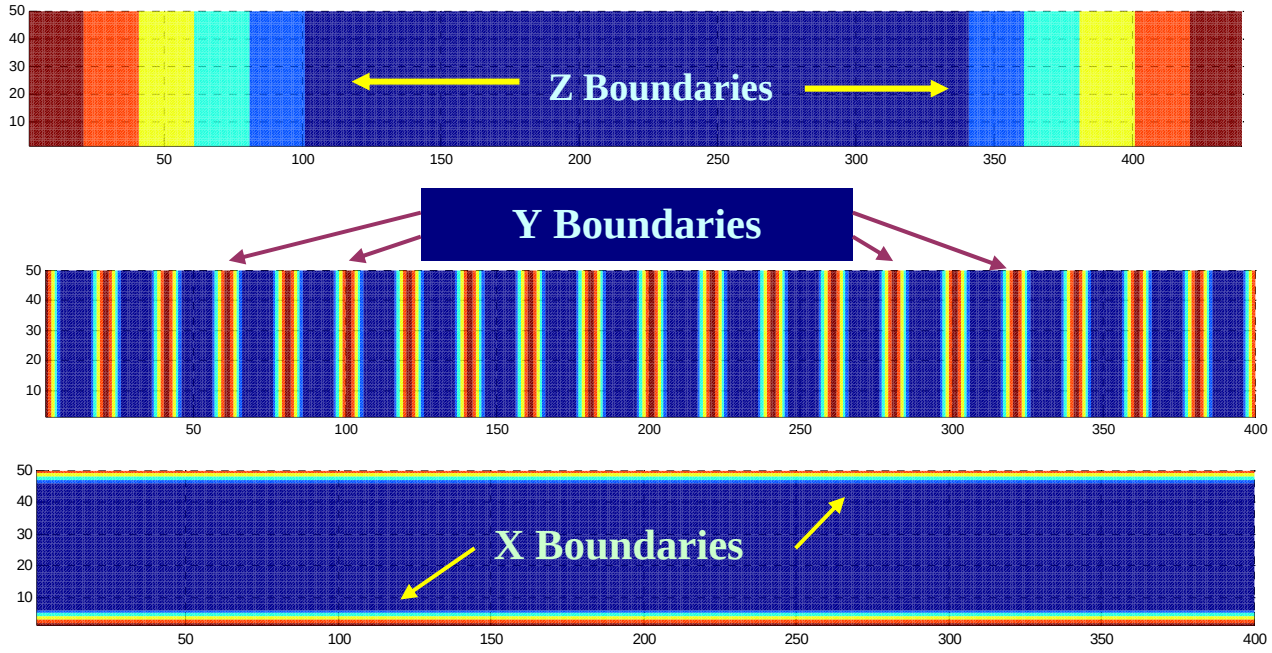

Fig. 2. Locations of the boundaries in the 2D texture.

The updating equations were implemented in GPU kernels as simple functions that would first calculate the necessary ψ terms, then apply the correcting terms to the E and H field components. The entire process is integrated easily into the GPU program with only minor changes in the precalculation of the *b* and *c* terms before the GPU performs the time steps.

IV. RESULTS

The GPU program was tested against a known FORTRAN based FDTD code with CPML to insure accuracy and proper operation. Both the GPU and CPU based codes were run on Intel Dual-Core 2.8 GHz systems with an Nvidia 8800 GTX video card with 768M of RAM. In the progression of time steps a derivative of a Gaussian waveform is injected from a point source at the center of the domain and progresses outward before being absorbed by the CPML layers and finally only very small reflections of the CPML remains. The source waveform is defined as,

$$s(t) = \frac{2}{\tau^2}\left(t_0 - t\right) e^{\frac{(t-t_0)^2}{\tau^2}} \tag{19}$$

where

$$\tau = \frac{2.1c}{40\pi \min(\Delta x, \Delta y, \Delta z)}, \tag{20}$$

$$t_0 = 4.5\tau . \tag{21}$$

Figure 3 shows the Ez field component at a plane cut containing the source point for various time steps to show proper operation of the GPU based program.

Figure 4 shows the Ez field component at an observation point 10 cells from the source point over 500 time steps. The wave is injected from approximately 40 to 150 time steps while the reflection of the CPML boundary can be seen at approximately 225 time steps into the simulation. The maximum magnitude of this reflection was calculated to be less than 0.3%. This reflection is higher than standard FORTRAN codes due to the numerical precision of the GPU.

With the PML having been verified, several test cases were run to present the full functionality and verify real simulation results. The two cases presented here are the well known microstrip patch antenna and filter [10]. Figure 5 shows the layout for the simple microstrip patch antenna.

The patch was simulated on both the GPU and CPU based systems for 3000 time steps. Figure 6 shows both the time domain and frequency domain results. The results show good comparison overall to the reference data [10] with minor difference due to the actual implementation of the codes and the numerical precision of the GPU.

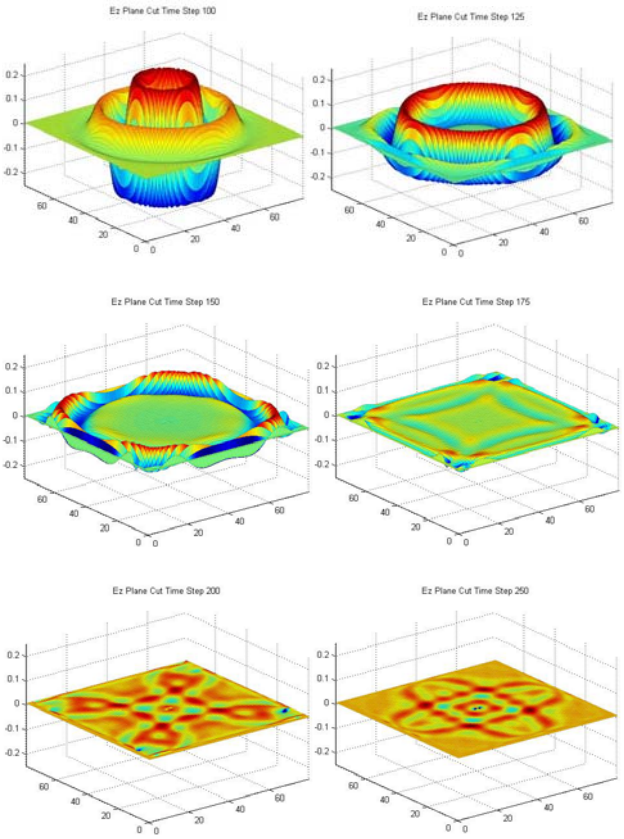

Fig. 3. Ez plane cuts at various time steps.

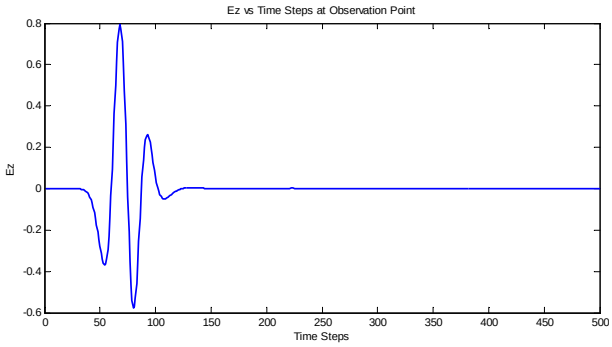

Fig. 4. The Ez field component at the observation point over 500 time steps.

The second test case simulates a microstrip filter. The simulation was also run on the GPU systems for 3000 time steps. Figure 7 shows the layout of the simple microstrip filter while Fig. 8 shows the results from this filter. Again good agreement is shown between the GPU results and the reference data [10].

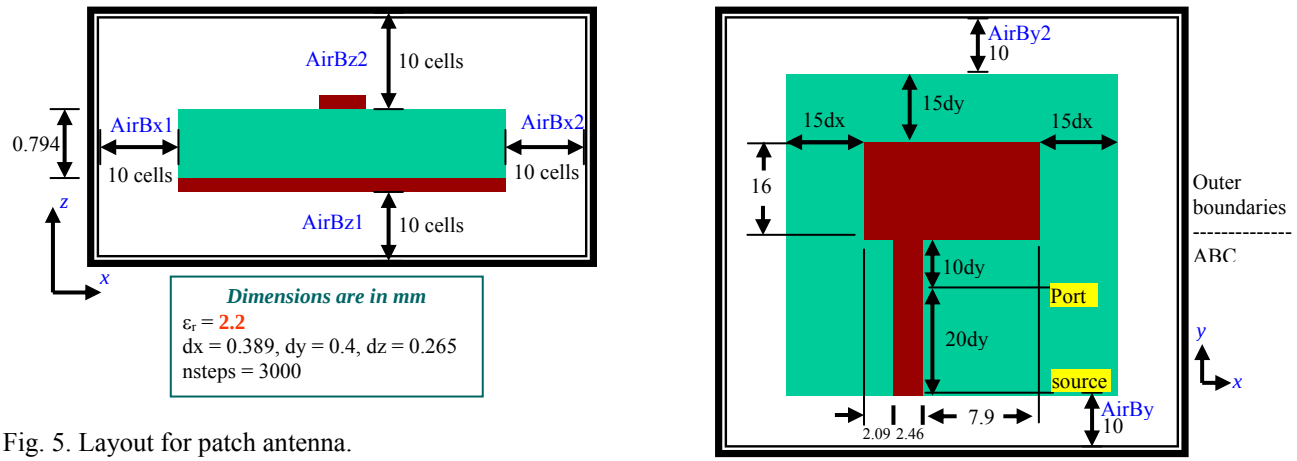

Fig. 5. Layout for patch antenna.

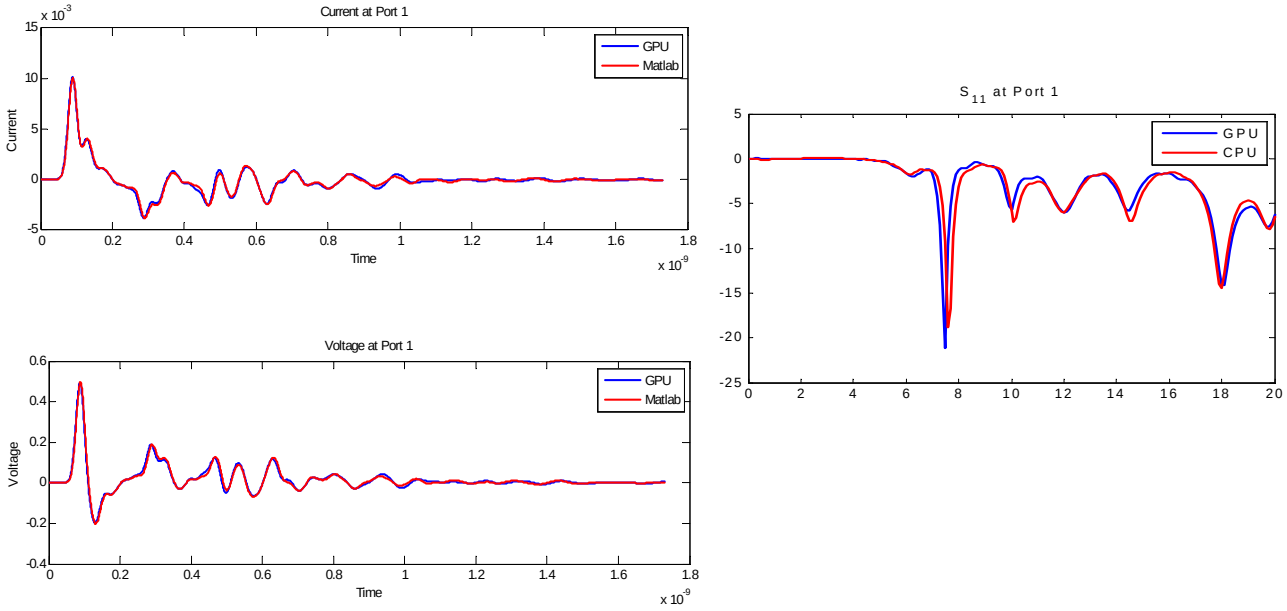

Fig. 6. Patch antenna verification results.

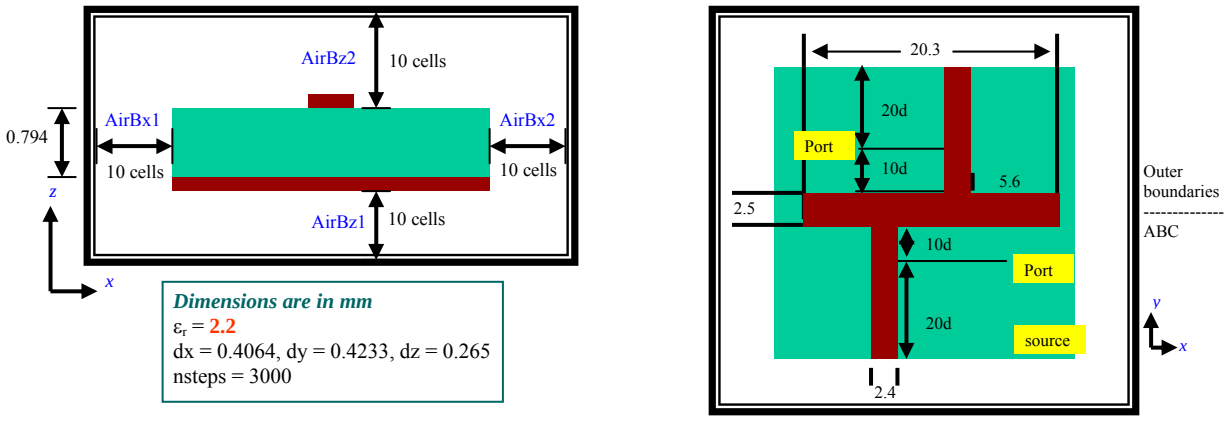

Fig. 7. Microstrip filter layout.

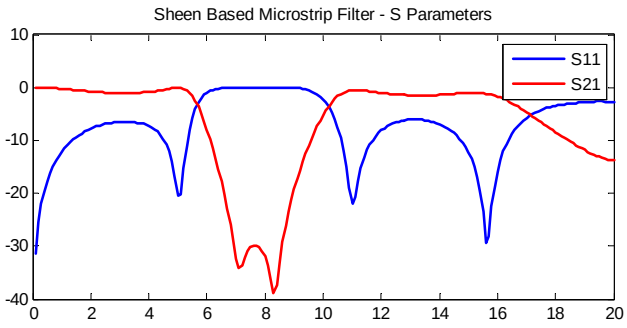

Fig. 8. Microstrip filter results.

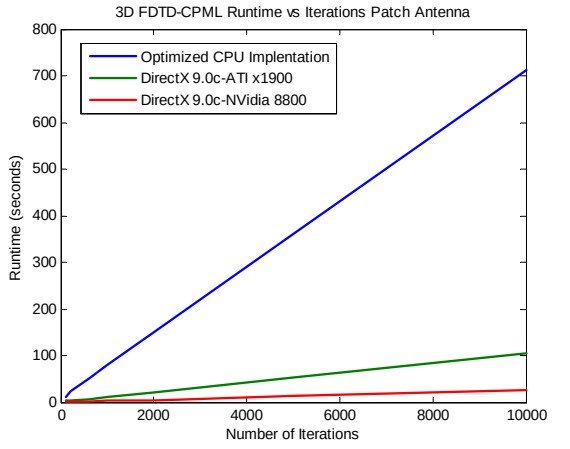

(a)

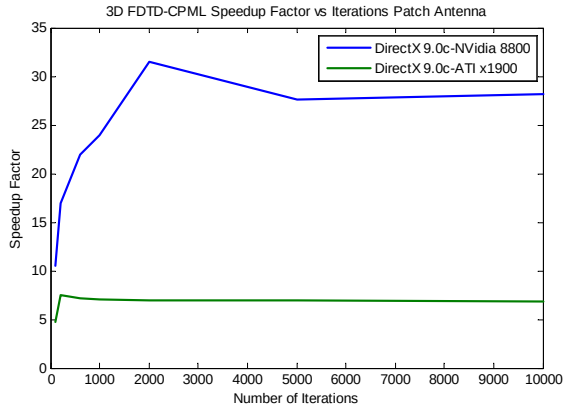

(b)

Fig. 9. Fortran CMPL vs. GPU CPML implementation results for various time steps with 500000 cell configuration, (a) run time; (b) speed up factor.

Figure 9 shows runtime and speedup results for both an optimized CPU and GPU code for the patch antenna test configuration of approximately 500000 cells. The GPU code was run on both an ATI x1900 and NVidia 8800 GPUs, while the CPU code was run on a Dual Core Pentium 2.8 GHz processor. The runtime results show a near linear trend for this case as the number of time steps is increased. The speedup factors for this case show that as the number of time steps is increased the maximum speedup factor asymptotically approaches a limit of 26 for the GPU on the NVidia 8800 and 6.4 for the ATI x1900.

V. CONCLUSIONS

The GPU based code outlined in this paper has shown good performance compared to a known FORTRAN code in implementing a three dimensional FDTD simulation with a CPML boundary condition. While the speedup factors gained in this GPU code is less than that has been shown without a boundary condition, it still offers a significant gain in speed over purely CPU based FDTD solvers. As the domain size is increased, the speedup factor slightly decreases due to the fact that the CPML coefficients and updates has to be implemented over the entire domain rather than in sections as it is in the FORTRAN code. It is expected that the current implementation would yield higher speed factor when new generation of GPUs are used.

REFERENCES

[1] M. J. Inman, A. Z. Elsherbeni, and C. E. Smith "GPU programming for FDTD calculations," *The Applied Computational Electromagnetics Society (ACES) Conference*, Honolulu, Hawaii, 2005.

[2] M. J. Inman and A. Z. Elsherbeni, "3D FDTD acceleration using graphical processing units," *The Applied Computational Electromagnetics Society (ACES) Conference*, Miami, Florida, 2006.

[3] M. J. Inman and A. Z. Elsherbeni, "Programming video cards for computational electromagnetics applications," *IEEE Antennas Propagation Mag*., vol. 47, no. 6, pp. 71-78, 2005.

[4] J. A. Roden, and S. D. Gedney, "Convolutional PML (CPML): An efficient FDTD implementation of the CFS-PML for arbitrary media," *Microwave Optical Tech. Let*., vol. 27, pp. 334-339, 2000.

[5] S. D. Gedney, "Scaled CFS-PML: It is more accurate, more efficient, and simple to implement. why aren't you using it?," *IEEE Antennas and Propagation Society International Symposium*, vol. 4B, pp. 364-367, July 2005.

[6] J. P. Berenger, "A perfectly matched layer for the absorption of electromagnetic waves," *Journal of Computational Physics*, vol. 114, pp. 195-200, 1994.

[7] S. D. Gedney, "The perfectly matched layer absorbing medium," *Advances in Computational Electrodynamics: The Finite Difference Time Domain*, A. Taflove, Editor, Artech House, New York, pp. 263-340, 1998.

[8] S. D. Gedney, "Perfectly Matched Layer Absorbing Boundary Conditions," in *Computational Electrodynamics: The Finite Difference Time Domain*, third edition, A. Taflove, and Susan C. Hagness, Editors, Artech House, Norwood, MA, pp. 295-313, 2005.

[9] K. S. Yee, "Numerical solution of initial boundary value problems involving Maxwell's equations in isotropic media," *IEEE Trans. Antenna Propagation*, vol. AP-14, pp. 302-307, May 1966.

[10] D. M. Sheen, S. M. Ali, M. D. Abouzahra, and J. A. Kong, "Application of three-dimensional finite-difference time-domain method to the analysis of planar microstrip circuits," *IEEE Trans. Microwave Theory and Techniques*, vol. 37, no. 7, pp. 849-857, July 1990.

Matthew Joseph Inman received his B.S. in Electrical Engineering in 2000 and his Masters in Electromagnetics in 2003 from the University of Mississippi. He currently is currently pursuing Ph. D. studies in electromagnetics there. He is currently employed at the University as a research assistant and graduate instructor. His interests involve electromagnetic theories, numerical techniques, antenna design and visualization, as well as teaching a number of undergraduate courses.

Atef Z. Elsherbeni – Biography can be found on page 61

Broad-band Characterization of Wire Interconnects Using a Surface Integral Formulation with a Surface Effective Impedance

A. Maffucci[1], G. Rubinacci[2], S. Ventre[1], F. Villone[1], and W. Zamboni[1]

[1] Ass. EURATOM/ENEA/CREATE, DAEIMI
Università degli Studi di Cassino, I-03043 Cassino (FR), Italy
{maffucci, ventre, villone, zamboni}@unicas.it

[2] Ass. EURATOM/ENEA/CREATE, DIEL
Università degli Studi di Napoli "Federico II", I-80125 Napoli, Italy
rubinacci@unina.it

Abstract – A surface integral formulation is used for a broad-band characterization of wire interconnects. A suitable definition of effective impedance accounts for the penetration of currents and charges inside lossy conductors. The results are successfully compared to a volumetric integral approach.

Keywords**:** Surface integral equation, effective surface impedance, and interconnects.

I. INTRODUCTION

The high-frequency operating conditions in digital high-speed circuits require an accurate electromagnetic modeling of all the physical components of the overall system, such as interconnects, packages, discontinuities, and devices. Effects related to the three-dimensional (3D) nature and finite size of the interconnects, are less and less negligible as frequency goes up. For this reason several efforts are made in literature to propose efficient full-wave simulators able to model adequately the high-frequency behavior of such structures. Efficient full-wave models may be obtained starting from integral formulations of the electromagnetic problem: a typical example is the popular EFIE (Electric Field Integral Equation) approach [1]. All the integral approaches benefit from the possibility to reduce the mesh to the conducting regions only and to impose rigorously the boundary conditions at infinity. When dealing with high-conductivity materials or when characterizing high-frequency behavior we can assume that the sources lie only on the conductor surfaces. In this case it is useful to introduce a surface integral formulation.

The most common way of discretizing a surface integral formulation is based on the use of the so-called RGW basis functions [2]. This approach suffers from the so-called low-frequency breakdown problem [1], *i.e.*, an ill-conditioning of the problem at frequencies low enough to make the conductors size small as compared to the wavelength. To overcome this problem, a loop-star or loop-tree decompositions are commonly used [3], able to decouple the solenoidal component of the current density from the non-solenoidal one. This cannot be automatically done for multiconnected domain or in the presence of electrodes. This point has been stressed since the very early applications [4], and has received considerable attention in the last years [5-6]. The Authors have recently proposed a surface integral formulation able to deal with arbitrary topologies thanks to a null-pinv decomposition of the basis functions that can be seen as a generalization of the loop-star and loop-tree decompositions [7-11].

This paper deals with the inclusion in such a formulation of a suitable surface impedance for broad-band characterization of lossy interconnects. A correct evaluation of the broad-band behaviour of ohmic conductors is essential to accurately predict the overall performances of high-speed digital circuits. When testing the signal integrity, for example, the signalling system is forced by a random sequence of bits and the quality is checked by observing the corresponding "eye-diagram". This requires a time-domain analysis performed by representing the interconnects through equivalent circuits, often extracted from a frequency domain characterization (*e.g.*, in terms of *S* parameters). The equivalent circuits have to be able to reproduce accurately fast transients as well as the DC response, hence the frequency characterization should be accurate for a wide range, from DC to microwave.

The surface approach for perfect conductors is fully consistent at any frequency. On the contrary, when dealing with ohmic conductors the electrical charges and currents do not necessarily lie on the conductor surfaces. This hypothesis is a good approximation when the skin effect is strong (high frequency and or high conductivity). In this case a suitable surface impedance can often be

used [12]. On the contrary, the definition of such an impedance should be changed to account for the penetration of sources at low frequency [13-14]. In this work we derive a consistent definition of the surface impedance, able to describe correctly both the low and high frequency behaviour, by solving analytically the axial diffusion problem in ohmic conductors of circular cross section.

The paper is organized as follows. In Section II the surface integral formulation is briefly reviewed and in Section III the theory for the equivalent surface impedance is described for cylindrical conductors. Section IV presents some results with particular reference to Unshielded Twisted Pairs (UTPs). This demonstrates the potentiality of the approach in broad-band modelling of conducting structures of arbitrary topology. Finally, Section V draws the conclusions.

II. MATHEMATICAL AND NUMERICAL FORMULATION

This section briefly illustrates the features of the 3D surface integral formulation used in this paper, and the related code SURFCODE. A more detailed derivation can be found in [9].

We solve Maxwell's equations in the frequency domain, assuming that some good conductors are present in the free space. The formulation can be extended to stratified dielectric media, as illustrated in [11]. Let Σ be the external surface of the conductors (see Fig. 1); we assume that $\partial\Sigma$ is made of N_E linear equipotential electrodes l_j, through which the current can flow.

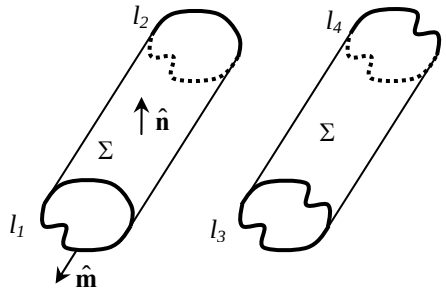

Fig. 1. Reference geometry.

Assuming that the current density lies on the surface Σ, we must satisfy the condition,

$$\mathbf{E}\times\hat{\mathbf{n}}\big|_{\Sigma} = \zeta_S\,\mathbf{J}_s\times\hat{\mathbf{n}}\big|_{\Sigma} \tag{1}$$

where **E** is the electric field, $\hat{\mathbf{n}}$ is the unit vector normal to Σ, ζ_S is the surface impedance of the conducting body, and $\mathbf{J}_s$ is the surface current density. The above assumption is rigorously satisfied in case of perfect conductors ($\zeta_S \to \infty$) at any frequency. It can be considered as a good approximation at sufficiently high frequencies due to the skin effect. At very low frequencies as well as in intermediate range condition. Equation (1) may still be imposed, provided that a suitable definition of the surface impedance is adopted.

Introducing the magnetic vector potential **A** and the scalar electric potential φ, we express **E** as follows,

$$\mathbf{E} = -i\omega\mathbf{A} - \nabla\varphi\,. \tag{2}$$

Using equation (2), we impose equation (1) in weak form using the weighted residual approach and the surface divergence theorem,

$$\begin{aligned} &i\omega\iint_{\Sigma}\mathbf{A}\cdot\mathbf{p}\,dS + \iint_{\Sigma}\zeta_M\,\mathbf{J}_s\cdot\mathbf{p}\,dS + \\ &+\iint_{\Sigma}\varphi\,\nabla_s\cdot\mathbf{p}\,dS = -\sum_{j=1}^{N_E}\varphi_j\int_{l_j}\mathbf{p}\cdot\hat{\mathbf{m}}\,dl = 0 \quad \forall\mathbf{p} \end{aligned} \tag{3}$$

where **p** is a vector weighting function tangent to Σ, $\hat{\mathbf{m}}$ is the normal to $\partial\Sigma$ over Σ (exiting from Σ), and the operator $\nabla_s = \nabla - \hat{\mathbf{n}}\,\partial/\partial n$. Using Lorenz gauge, the potentials are related to the surface current density $\mathbf{J}_s$ and the surface charge density σ through the Green function *G* as follows,

$$\begin{aligned} \mathbf{A}(\mathbf{r}) &= \frac{\mu_0}{4\pi}\iint_{\Sigma} G\left(|\mathbf{r}-\mathbf{r}'|\right)\mathbf{J}_s(\mathbf{r}')\,dS', \\ \varphi(\mathbf{r}) &= \frac{1}{4\pi\varepsilon_0}\iint_{\Sigma} G\left(|\mathbf{r}-\mathbf{r}'|\right)\sigma(\mathbf{r}')\,dS'. \end{aligned} \tag{4}$$

The sources must further satisfy the charge conservation law,

$$\nabla_s\cdot\mathbf{J}_s\big|_{\Sigma} = -i\omega\sigma\big|_{\Sigma}\,. \tag{5}$$

To solve the problem numerically, we give a triangular finite elements discretization of Σ, with *e* edges, *n* nodes, and *t* triangles. We expand the surface current density $\mathbf{J}_s$ in terms of div-conforming basis functions $\mathbf{w}_k$, having a continuous normal component all over the mesh [9]. The resulting degrees of freedom (DoF) I_k are the currents flowing across the edges. The surface charge density σ is expanded in terms of piecewise constant functions q_m, so that the resulting DoF Q_m are the charges in the triangles. It can be easily seen that

$$\begin{bmatrix} \nabla_s\cdot\mathbf{w}_1 \\ \vdots \\ \nabla_s\cdot\mathbf{w}_e \end{bmatrix} = \underline{\underline{\mathrm{D}}}^T \begin{bmatrix} q_1 \\ \vdots \\ q_t \end{bmatrix}, \tag{6}$$

where $\underline{\underline{\mathrm{D}}}$ is a suitable sparse matrix, which can be seen as the discrete divergence. Using equation (6), equation (5) becomes,

$$\underline{\underline{\mathrm{D}}}\,\underline{\mathrm{I}} = -i\omega\,\underline{\mathrm{Q}}\,, \tag{7}$$

where $\underline{\mathrm{I}}$ and $\underline{\mathrm{Q}}$ are the vectors of the DoF I_k and Q_m. Assuming that Σ is an open surface, the rank of $\underline{\underline{\mathrm{D}}}$ is full, hence we can automatically satisfy equation (7) by writing,

$$\underline{\mathrm{I}} = \underline{\underline{\mathrm{K}}}\,\underline{\mathrm{I}}_{\mathrm{s}} - i\omega\,\underline{\underline{\mathrm{R}}}\,\underline{\mathrm{Q}}\,, \tag{8}$$

where $\underline{\underline{\mathrm{K}}}$ is a matrix whose columns are a basis for the null space of $\underline{\underline{\mathrm{D}}}$, $\underline{\underline{\mathrm{R}}}$ is a pseudoinverse matrix of $\underline{\underline{\mathrm{D}}}$, and $\underline{\mathrm{I}}_{\mathrm{s}}$ are unknowns which give no contribution to the current density divergence (and hence to the charge). We are in fact using the following "null-pinv" basis functions [9],

$$\begin{aligned} \boldsymbol{\alpha}_h &= \sum_{k=1}^{e} K(k,h)\mathbf{w}_k\,, \quad h = 1,\ldots,n_x\,, \\ \boldsymbol{\beta}_h &= \sum_{k=1}^{e} R(k,h)\mathbf{w}_k\,, \quad h = 1,\ldots,t \end{aligned} \tag{9}$$

where n_x is a number depending on the topology of the solution domain. The null-pinv decomposition of equation (9) is a generalization of the loop-star decomposition [3], hence, it allows avoiding the so-called "low-frequency breakdown". Furthermore, the proposed decomposition also provides the possibility to deal with topologically complex geometries (via holes, bends, and electrodes).

Using equation (9) as weighting functions in equation (2), we have,

$$\begin{aligned} i\omega\begin{bmatrix} \underline{\underline{\mathrm{L}}}_{\alpha\alpha} & \underline{\underline{\mathrm{L}}}_{\alpha\beta} \\ \underline{\underline{\mathrm{L}}}_{\beta\alpha} & \underline{\underline{\mathrm{L}}}_{\beta\beta} \end{bmatrix}\begin{bmatrix} \underline{\mathrm{I}}_{\mathrm{s}} \\ -i\omega\underline{\mathrm{Q}} \end{bmatrix} + \begin{bmatrix} \underline{\underline{\mathrm{R}}}_{\alpha\alpha} & \underline{\underline{\mathrm{R}}}_{\alpha\beta} \\ \underline{\underline{\mathrm{R}}}_{\beta\alpha} & \underline{\underline{\mathrm{R}}}_{\beta\beta} \end{bmatrix}\begin{bmatrix} \underline{\mathrm{I}}_{\mathrm{s}} \\ -i\omega\underline{\mathrm{Q}} \end{bmatrix} + \\ -\begin{bmatrix} \underline{\underline{0}} \\ \underline{\underline{\mathrm{S}}} \end{bmatrix}\underline{\mathrm{Q}} = -\begin{bmatrix} \underline{\underline{\mathrm{F}}}_{\alpha} \\ \underline{\underline{\mathrm{F}}}_{\beta} \end{bmatrix}\underline{\varphi} = -\underline{\underline{\mathrm{F}}}\,\underline{\varphi} \end{aligned} \tag{10}$$

where $\underline{\varphi}$ is a vector containing N_E electrode potentials and the other elements are defined as follows,

$$\begin{aligned} L_{\gamma\delta}(i,j) &= \frac{\mu_0}{4\pi}\iint_\Sigma\iint_\Sigma G\left(|\mathbf{r}-\mathbf{r}'|\right)\boldsymbol{\gamma}_j(\mathbf{r}')\cdot\boldsymbol{\delta}_i(\mathbf{r})\,dS'\,dS\,, \\ S(i,j) &= \frac{1}{4\pi\varepsilon_0}\iint_\Sigma\iint_\Sigma G\left(|\mathbf{r}-\mathbf{r}'|\right)q_j(\mathbf{r}')q_i(\mathbf{r})\,dS'\,dS\,, \\ R_{\gamma\delta}(i,j) &= \iint_\Sigma \zeta_S\boldsymbol{\gamma}_j(\mathbf{r}')\cdot\boldsymbol{\delta}_i(\mathbf{r})dS\,, \\ F_\gamma(h,j) &= \int_{l_j}\boldsymbol{\gamma}_h\cdot\hat{\mathbf{m}}\,dl\,. \end{aligned} \tag{11}$$

Equation (10) can be rewritten in a compact form as,

$$\underline{\underline{\mathrm{Z}}}\,\underline{\mathrm{T}} = -\underline{\underline{\mathrm{F}}}\,\underline{\varphi}\,, \tag{12}$$

with a suitable definition of the matrices $\underline{\underline{\mathrm{Z}}}$, $\underline{\mathrm{T}}$. From this point, simple algebraic manipulations [9] allow the computation of any matrix describing the behavior of the interconnect at its terminals. For instance the admittance matrix $\underline{\underline{\mathrm{Y}}}$ is simply given by,

$$\underline{\underline{\mathrm{Y}}} = \underline{\underline{\mathrm{F}}}^T\,\underline{\underline{\mathrm{Z}}}^{-1}\,\underline{\underline{\mathrm{F}}}\,. \tag{13}$$

III. EQUIVALENT SURFACE IMPEDANCE FOR CYLINDRICAL CONDUCTORS OF CIRCULAR CROSS SECTION

Let us consider cylindrically-shaped straight conductors with circular cross section of radius a. In order to derive a possible expression for the surface impedance ζ_S, for each conductor we consider a single straight cylindrical wire with a volumetric current density $\mathbf{J}_{vol}$ directed along the conductor axis. In ohmic conductors of resistivity η the amplitude of the electric field E is related to the volumetric current density J_{vol} through,

$$E = \eta J_{vol} \tag{14}$$

in the whole conductor domain, including its surface Σ. Neglecting the displacement current in the conductor, the amplitude of the magnetic field on Σ is related to the total current I flowing in the wire by,

$$H\big|_\Sigma = \frac{I}{2\pi a}\,. \tag{15}$$

It is possible to prove that the volumetric current density depends on the radial coordinate r as follows [15],

$$J_{vol}(r) = \frac{\sqrt{2}\,I}{i^{5/2}\,2\pi\,a\,\delta}\,\frac{J_0\left(i^{3/2}\sqrt{2}\,r/\delta\right)}{J_1\left(i^{3/2}\sqrt{2}\,a/\delta\right)}, \tag{16}$$

where δ is the penetration depth,

$$\delta = \sqrt{\frac{2\eta}{\omega\mu}}\,, \tag{17}$$

and J_α is the Bessel function of order α. On the surface Σ this volumetric current density is equal to,

$$J_{vol}\big|_\Sigma = \frac{\sqrt{2}\,I}{i^{5/2}\,2\pi\,a\,\delta}\,\frac{J_0\left(i^{3/2}\sqrt{2}\,a/\delta\right)}{J_1\left(i^{3/2}\sqrt{2}\,a/\delta\right)} = T\,I\,, \tag{18}$$

where the quantity T can be approximated as,

$$T = \frac{\sqrt{2}}{i^{5/2}\,2\pi\,a\,\delta}\,\frac{J_0\left(i^{3/2}\sqrt{2}\,\dfrac{a}{\delta}\right)}{J_1\left(i^{3/2}\sqrt{2}\,\dfrac{a}{\delta}\right)} \cong \begin{cases} \dfrac{1}{\pi a^2} & \delta >> a \\ \dfrac{(1+i)}{2\pi a\delta} & \delta << a \end{cases}. \tag{19}$$

Consequently, the relation between the electric and magnetic fields on Σ becomes,

$$E\big|_{\Sigma} = \eta\, J_{vol}\big|_{\Sigma} = \eta\, T\; I = \eta\, T\; 2\pi a\; H\big|_{\Sigma} = \zeta_S\, H\big|_{\Sigma}\,, \qquad (20)$$

where the surface impedance is defined as,

$$\zeta_S = \frac{\sqrt{2}\,\eta}{i^{5/2}\,\delta}\,\frac{J_0\left(i^{3/2}\sqrt{2}\,\frac{a}{\delta}\right)}{J_1\left(i^{3/2}\sqrt{2}\,\frac{a}{\delta}\right)} \cong \begin{cases} \eta\,\dfrac{2}{a} & \delta >> a \\ \eta\,\dfrac{(1+i)}{\delta} & \delta << a \end{cases}. \qquad (21)$$

Note that the high frequency limit of equation (21) reduces to the standard Leontovich expression.

In the range of frequency in which δ and a are comparable, instead of the exact expression of equation (21) it is often used the following heuristic *coth* law [14, 16],

$$\zeta_S = \eta\,\frac{(1+i)}{\delta}\coth\left(\frac{a}{2}\sqrt{\frac{j\,\omega\,\mu}{\eta}}\right), \qquad (22)$$

that provides the values of equation (21) in the high and low frequency limits, since,

$$\lim_{\omega\to 0}\coth\left(\frac{a}{2}\sqrt{\frac{i\,\omega\,\mu}{\eta}}\right) = \frac{2}{a}\sqrt{\frac{\eta}{i\,\omega\,\mu}} = \frac{2}{a}\,\frac{\delta}{1+i}\,, \qquad (23)$$

$$\lim_{\omega\to +\infty}\coth\left(\frac{a}{2}\sqrt{\frac{i\,\omega\,\mu}{\eta}}\right) = 1\,. \qquad (24)$$

Note that the impedance of equation (21) is spatially homogeneous.

IV. NUMERICAL RESULTS

The analyzed test-case is a typical broad-band wire interconnect, namely an unshielded twisted pair (UTP) cable, made of cylindrical copper conductors. Let us assume Cu resistivity $\eta = 1.7\cdot 10^{-8}\ \Omega\,\mathrm{m}$, twist pitch 10 mm, radius a = 0.1 mm, center-to-center distance of 0.5 mm, and a total length equal to 2 twist pitches.

The surface mesh used for the computation is plotted in Fig. 2. The mesh is made of 576 triangular elements, giving up to 876 degrees of freedom (DoFs). We have evaluated the impedance, Z_{in} computed at one end when the other one is short-circuited. This has been done both using the exact formula of equation (21), and the *coth* law of equation (22), so to compare the error introduced by using the latter approximated law.

The results are further compared to those obtained by the 3D volumetric code CARIDDI [17-19] in two different discretization conditions. The mesh for the case "CARIDDI 1" (7448 points, 6600 elements, giving rise to 12688 DoFs) is characterized by a fine discretization along the longitudinal and radial directions of the cylinders, as depicted in Fig. 3.

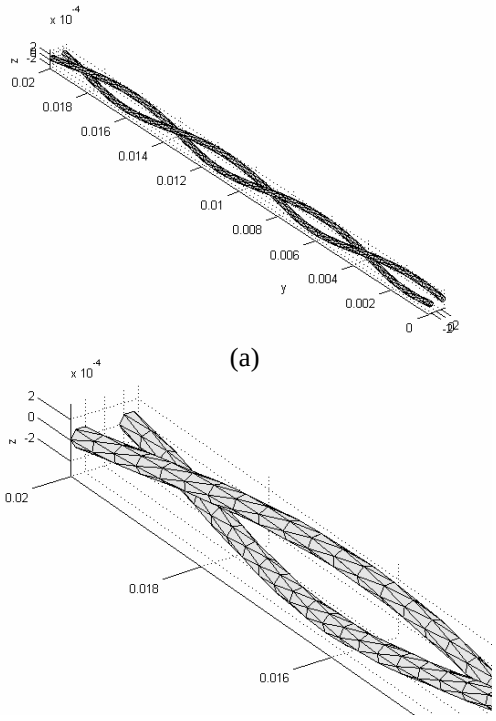

(a)

(b)

Fig. 2. Surface mesh used for the UTP (a); detail (b).

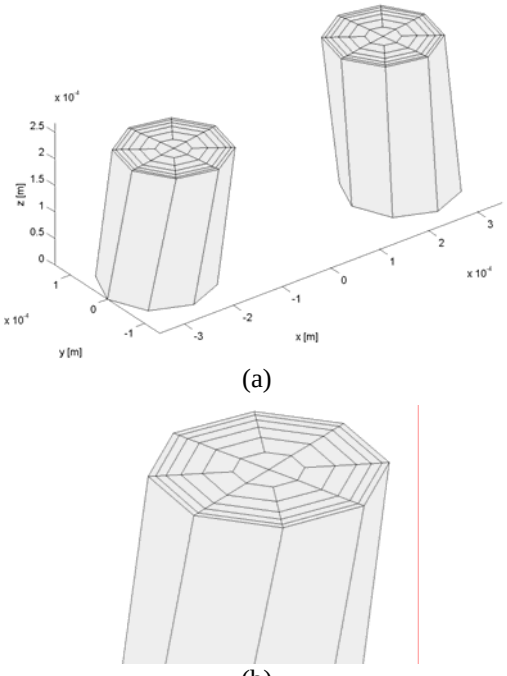

(a)

(b)

Fig. 3. Volume mesh (a), detail (b) for the case "CARIDDI 1".

Conversely, in case "CARIDDI 2" the mesh is characterized by a fine discretization in the poloidal direction of each cylinder (3796 points, 3200 elements, giving rise to 6128 DoFs).

Figure 4 shows the comparison between the surface and volume approaches in a transition region. The results agree satisfactorily, being the displacement between the related curves within 8%. For $f < 40$ kHz, we have a ratio $\delta/a > 3$, hence, the conductors can be considered as fully penetrated. As clearly shown, the low frequency behaviour of the resistance is correctly modelled. Indeed, the real part of the impedance approximates the DC resistance of the wire. For f >10MHz we have $\delta/a < 0.2$ and the solution CARIDDI 2 suffers for a lack of precision, due to the discretization along the conductor radius, too coarse to describe the skin effect. This may also explain the (even small) mismatch of the results at higher frequencies. Note that the solution obtained by using the *coth* law approximates the exact one within a 20% error.

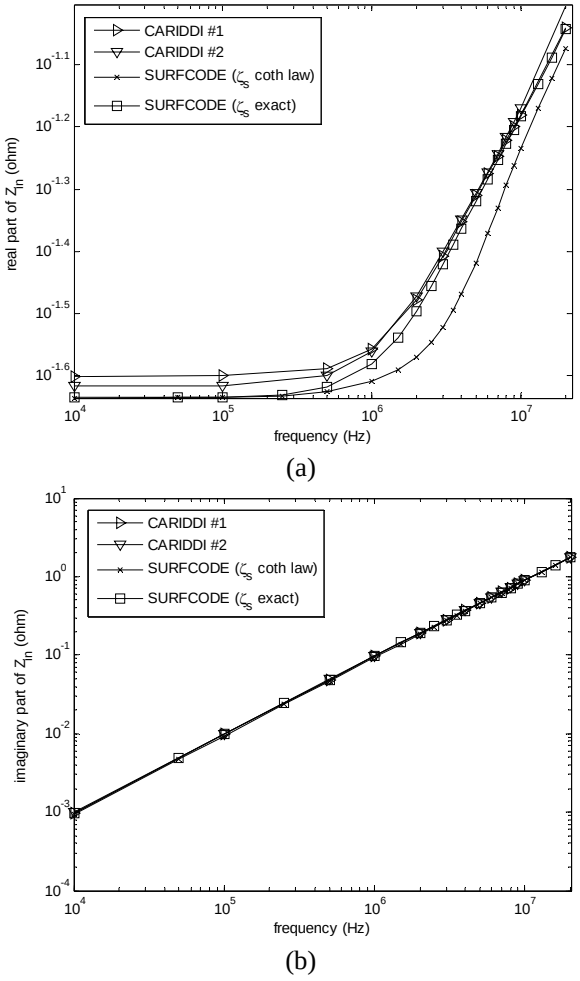

Fig. 4. Input impedance of a UTP in a transition region. Real (a) and imaginary (b) parts.

Figure 5 shows the broad-band frequency behaviour of the input impedance computed by our code. The considered range deeply enters the asymptotic regions $\delta/a >> 1$ and $\delta/a << 1$.

Finally, in Fig. 6 it is plotted the current density pattern computed at 20 MHz, highlighting a non-uniform distribution due to proximity effect.

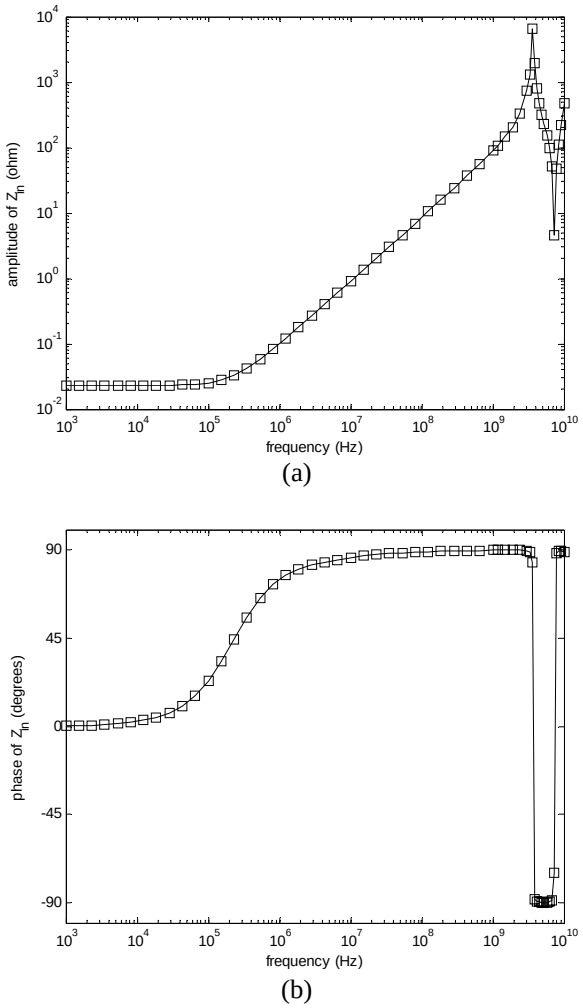

Fig. 5. Input impedance of a UTP in broad interval of frequency. Real (a) and imaginary (b) parts.

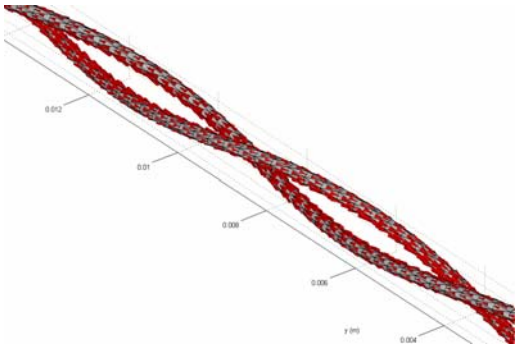

Fig. 6. Current density pattern at 20 MHz.

V. CONCLUSIONS AND PERSPECTIVES

In this paper a surface integral formulation is used to obtain a broad-band characterization of 3D wire interconnects. The use of null-pinv basis functions in the numerical model allows an automatic treatment of arbitrarily complex geometries, while retaining all the benefits of a decomposition that does not suffer from low-frequency breakdown problems. The presence of lossy conductors is correctly taken into account at any frequency by introducing suitable surface effective impedance, obtained by solving the diffusion problem.

The test case (characterization of a UTP cable) shows the consistency of the approach with volumetric techniques in the low frequency region, and the inaccuracy of the approximated *coth* law is often used to describe lossy conductors.

In principle, the definition of an effective impedance presented here could be extended to the case of more complicated geometries. This could be achieved by solving numerically the internal diffusion equation inside the region occupied by the conductors, *e.g.*, with a differential code.

VI. ACKNOWLEDGEMENTS

This work was supported in part by by Consorzio CREATE and by the Italian Ministry of Research under a Program for the development of Research of National Interest (PRIN Grant #2004093025).

REFERENCES

[1] J. S. Zhao and W. C. Chew, "Integral equation solution of Maxwell's equations from zero frequency to microwave frequency," *IEEE Trans. Antennas Propag.*, vol. 48, pp. 1635–1645, 2000.

[2] S. M. Rao, D. R. Wilton, and A. W. Glisson, "Electromagnetic scattering by surface of arbitrary shape," *IEEE Trans. Antennas Propag.*, vol. AP-30, pp. 409–418, 1982.

[3] G. Vecchi, "Loop-star decomposition of basis functions in the discretization of EFIE," *IEEE Trans. Antennas Propag.*, vol. 47, pp. 339–346, 1999.

[4] D. R. Wilton, "Topological considerations in surface patch and volume cell modeling of electromagnetic scatterers," in *Proc. URSI Int. Symp. Electromagn. Theory*, pp. 65–68, Santiago de Compostela, Spain, Aug. 1983.

[5] V. I. Okhmatovski, "An efficient algorithm for generation of loop-tree basis in 2.5D interconnect models," *Proc. of 14th EPEP Meeting*, pp. 297-300, Oct. 2005.

[6] S. Chakrabortry, D. Gope, G. Ouyang, and V. Jandhyala, "A three-stage preconditioner for geometries with multiple holes and handles in integral equation based electromagnetic simulation of integrated packages," *Proc. of 14th EPEP Meeting*, pp. 199-202, Oct. 2005.

[7] D. Belfiore, G. Miano, F. Villone, and W. Zamboni, "A surface integral formulation for Maxwell's equations," *Proc. 11th IGTE Symp. Conf.*, pp. 62–67, Graz, Austria, Sep. 2004.

[8] A. Chiariello, A. Maffucci, G. Miano, F. Villone, and W. Zamboni, "Analysis of interconnects in huge frequency ranges with a 3-D superficial integral formulation," *Proc. of 9th IEEE Workshop on Signal Propagation on Interconnects (SPI)*, pp. 89-92, Garmish, Germany, 10-13 May 2005.

[9] G. Miano and F. Villone, "A surface integral formulation of Maxwell equations for topologically complex conducting domains," *IEEE Trans. Antennas Propag.*, vol. 53, pp. 4001-4014, 2005.

[10] S. Caniggia, A. Maffucci, F. Maradei, F. Villone, and W. Zamboni "Time-domain analysis of the performances of unshielded twisted pairs in high-speed circuits," *Proc. of EMC-Europe 2006*, pp.550-555, Barcelona, Spain, 4-8 Sept. 2006.

[11] A. G. Chiariello, A. Maffucci, G. Miano, F. Villone, and W. Zamboni, "Full-wave numerical analysis of single-layered substrate planar interconnects," *Proc. of IEEE Workshop on Signal Propagation on Interconnects*, pp. 57-60, Berlin, Germany, 9-12 May 2006.

[12] Y. Wang, D. Gope, V. Jandhyala, and C. J. R. Shi, "Generalized Kirchhoff's current and voltage law formulation for coupled circuit-electromagnetic simulation with surface integral equations," *IEEE Trans. Microwave Theory Tech.*, vol. 52, pp. 1673–1682, 2004.

[13] A. Rong, A. C. Cangellaris, and L. Dong, "Comprehensive broad-band electromagnetic modeling of on-chip interconnects with a surface discretization-based generalized PEEC model," *IEEE Trans. Advanced Packaging*, vol. 28, no. 3, pp. 434 - 444, Aug. 2005.

[14] D. De Zutter and L. Knockaert, "Skin effect modeling based on a differential surface admittance operator," *IEEE Trans. Microwave Theory Tech.*, vol. 53, no. 8, pp. 2526 - 2538, 2005.

[15] F. Barozzi and F. Gasparini, "Fondamenti di elettrotecnica. Elettromagnetismo," Ed.*UTET*, Torino Italy, 1989.

[16] A. G. Chiariello, A. Maffucci, G. Miano, F. Villone, and W. Zamboni, "Broad-Band characterization of conductors with arbitrary topology using a surface integral formulation," *Proc. of 15th EPEP Meeting*, pp. 131-134, Scottsdale (USA), 23-25 Oct. 2006.

[17] R. Albanese and G. Rubinacci, "Integral formulation for 3D eddy current computation using edge-elements," *IEE Proceedings*, vol. 135, Part A, no. 5, pp. 457-462, 1988.
[18] R. Albanese and G. Rubinacci, "Finite element methods for the solution of 3D eddy current problems," *Advances in Imaging and Electron Physics*, vol. 102, pp. 1-86, Academic Press, 1998.
[19] A. Maffucci, G. Rubinacci, A. Tamburrino, S. Ventre, and F. Villone, "Fast low-frequency impedance extraction using a volumetric three-dimensional integral formulation," *Proc. of ACES 2007*, pp. 1652-1657, Verona, Italy, 19-23 March 2007.

Antonio Maffucci received in 1996 the Laurea Degree in Electronic Engineering *summa cum laude* and in 2000 the Ph.D. degree in Electrical Engineering from the University of Naples "Federico II", Italy.
In 1997 he was with the nuclear fusion laboratory JET (Culham, U.K.). From 1998 to 2002 he was with the Department of Electrical Engineering at the University of Naples. From 2002 he is with the Elettrotecnica Group at the Faculty of Engineering of the University of Cassino, Italy, where he is currently an Associate Professor, teaching courses on circuit theory and electromagnetic compatibility.
His research areas include electromagnetic modeling of distributed systems, electromagnetic compatibility, computational electromagnetism, and nanotechnology.
He is author of more than 80 technical papers on international journals, conference proceedings and essays on books. He is also co-author of the book *Transmission lines and lumped circuits* (New York, Academic Press, 2001). He is Associate Editor of the *IEEE Transactions on Advanced Packaging*.

Guglielmo Rubinacci received the Laurea degree (*summa cum laude*) in Electronic Engineering from the University of Naples "Federico II", Italy, in 1975.
Currently, he is a Full Professor of fundamentals in electrical engineering at the University of Naples "Federico II." He was the Dean of the Faculty of Engineering of the University of Cassino from 1996 to 2003. As a Fulbright-Hays Fellow he was a Visiting Scientist at MIT in 1980/81. He has been a Researcher at the University of Naples (1982/85), Associate Professor at the Universities of Calabria (1979–84), Salerno (1984/88) and Napoli (1988/90), and Full Professor at the University of Cassino (1990–2004). He is the author/coauthor of more than 100 papers in refereed scientific journals and books and coeditor of two volumes. His research interests are mainly in computational electromagnetics with applications in several fields such as plasma engineering in tokamaks and electromagnetic nondestructive evaluation

Salvatore Ventre received in 1990 the Laurea Degree in Electronic Engineering *summa cum laude* in Electrical Engineering from the University of Naples "Federico II", Italy. From 1993 is with the Elettrotecnica Group at the Faculty of Engineering of the University of Cassino, Italy, where he is currently a Research Scientist.
His research interests are mainly in computational electromagnetic with application in several fields such as electromagnetic nondestructive evaluation, electromagnetic compatibility, analysis of the time evolution of MHD equilibria, for the identification of the plasma boundary in tokamaks.
He is author/coauthor of more than 30 technical papers on international journals and conference proceedings.

Fabio Villone received the Laurea degree (summa cum laude) in Electronic Engineering in 1994 at the University of Naples Federico II, and the Ph.D. in Industrial Engineering in 1998 at the University of Cassino.
Currently, he is Full Professor at the Faculty of Engineering of the University of Cassino, where he formerly was Research Assistant (1997-2001) and Associate Professor (2001-2007). He teaches "Basic Electrical Engineering".
In 1996 he was visiting scientist at CRPP-Lausanne (Switzerland), and in the last years at JET (Joint European Torus), close to Oxford (UK).
His scientific interests are in the field of computational electromagnetics, with particular reference to fusion plasma modelling and engineering, electromagnetic compatibility and eddy current non destructive testing.
He is co-author of more than 60 papers on international journals and essays on books, and more than 50 contributions to international conferences, among which several invited papers. He was Scientific Coordinator of several experiments carried out at JET, and Principal Investigator of a national research project on fusion plasma modelling and control.

Walter Zamboni received the Laurea degree in Electrical Engineering (*summa cum laude*) in 2001 and the Ph. D. degree in Electrical Engineering in 2004 from the Faculty of Engineering, Università degli Studi di Napoli "Federico II", Italy. In 2003 he has been Stager at CERN, Geneva, Switzerland, and Visiting Scientist at EPFL-CRPP Superconductivity Group, Villigen-PSI, Switzerland. From 2005 he is with the the Faculty of Engineering, Università degli Studi di Cassino, Italy, where he works as a research assistant. From 2006 he teaches Circuits Theory at the Università degli Studi del Sannio, Italy

His scientific interests are in the field of computational electromagnetics, with particular reference to interconnects and applied superconductivity.

High-Frequency Full-Wave Analysis of Interconnects with Inhomogeneous Dielectrics through an Enhanced Transmission Line Model

A. G. Chiariello[1], A. Maffucci[2], G. Miano[1], F. Villone[2], and W. Zamboni[2]

[1] Ass. EURATOM/ENEA/CREATE, DIEL
Università degli Studi di Napoli "Federico II", I-80125 Napoli, Italy
{miano, a.chiariello}@unina.it

[2] Ass. EURATOM/ENEA/CREATE, DAEIMI
Università degli Studi di Cassino, I-03043 Cassino (FR), Italy
{maffucci, villone, zamboni}@unicas.it

Abstract – The paper deals with the inclusion of inhomogeneous dielectrics in a full-wave transmission line model for high-frequency analysis of interconnects. This "enhanced" transmission line model is derived from a full-wave integral formulation of the electromagnetic problem, and the inclusion of dielectrics is performed by an accurate semi-analytical evaluation of the Green functions for layered planar structures. The resulting model has a computational cost typical of a TL model but is able to perform a full-wave analysis in frequency ranges where the standard TL model may no longer be used. Moreover, as shown in the proposed examples, the model gives the possibility to investigate separately several phenomena affecting the high-frequency behavior of interconnects, like losses in dielectrics, unwanted radiation and excitation of parasitic modes.

Keywords**:** High-speed interconnects, transmission line model, full-wave analysis, Green functions, and parasitic modes.

I. INTRODUCTION

Electrical interconnects in high-speed circuits are usually modeled by means of the popular *transmission line model*, which assumes a propagation of quasi-TEM mode type. This model has been thoroughly studied in the past and it has been proven to be described in a simple and accurate way, the effects of interconnects on the signal (delays, mismatching, crosstalk, …) [1]. However, in many cases of practical interest due to the ever-increasing operating frequencies and to size decreasing, the quasi-TEM hypothesis of propagation no longer holds. In such cases high-frequency effects arise, such as radiation, mode conversion and dispersion, which are crucial to correctly estimate the system performance. These effects are not included in the *standard transmission line* model (*STL*) and would require, in principle, a full-wave analysis. This kind of analysis has two disadvantages: a high computational cost and a poor qualitative insight on the solution. It is indeed difficult to distinguish between the different phenomena quoted above. To solve both problems, several efforts have been made to obtain *generalized* transmission line models able to overcome the validity limits of the *STL* model while retaining the same simplicity and a low computational cost (e.g., [2-5]).

The Authors have recently proposed an *enhanced transmission line* (*ETL*) model which is able to describe in the frequency domain interconnects for which the characteristic transverse dimension is comparable to the characteristic wavelength of the carried signals. This has been done for two-conductor interconnects in [6-8] and for a multiconductor interconnect in [9-10]. The model has been successfully used to foresee effects like radiation in the transverse plane, dispersion due to the finite length of the interconnect, differential to common mode conversion in asymmetric interconnects and high-frequency crosstalk. However in all these papers the embedding dielectric has been assumed uniform. In this paper the multiconductor *ETL* model is extended to inhomogeneous dielectrics, so that the analysis of the above mentioned high-frequency effect may be performed for interconnects of practical interest such as the microstrips.

Section II is devoted to the problem formulation in presence of inhomogeneous dielectrics. The starting point is the integral formulation of the electromagnetic problem based on the vector and scalar potentials satisfying the Lorenz gauge. The formulation involves the Green functions for the considered structure: a general case is considered, where an expression of the Green functions for dielectric layers with different permittivity and a ground plane is used. These Green functions are

evaluated semi-analytically: the principal part describing the propagation of signals is extracted analytically, whereas the remainder describing parasitic modes due to the non-ideal behavior of the interconnect is represented through equivalent low-order systems identified by a vector fitting procedure [11].

In Section III the *ETL* model is derived with suitable approximations from this integral formulation. The *ETL* model has the same mathematical structure as the *STL* model, the only difference being in the relations between the per-unit-length (p.u.l.) magnetic flux and the current and between the voltage and the *p.u.l.* charge, respectively. In the *STL* model they are local, whereas in the *ETL* they involve spatial convolutions.

In Section IV first the *ETL* model predictions are successfully compared to the full-wave solutions obtained by two different 3D numerical codes. The case study highlights the inaccuracy of the *STL* model in high-frequency ranges. Then a deep investigation of the high-frequency solution is performed, by analyzing the effects of different phenomena like frequency-dependent dielectric losses and unwanted radiation in the transverse plane. A second case-study refers to a coupled microstrip, and is analyzed in order to evaluate the high-frequency crosstalk noise.

II. INTEGRAL FORMULATION AND THE INCLUSION OF INHOMOGENEOUS DIELECTRICS

Let us consider the interconnect of Fig. 1, of total length *l*, made by two signal conductors on a dielectric layer of thickness *h* and a ground plane. Let us assume the conductors to be ideal and the dielectric permittivity to be $\varepsilon_r\varepsilon_0$ in the layer and ε_0 outside it (the magnetic permeability is everywhere $\mu = \mu_0$). Let us denote with Σ_1 and Σ_2 the signal conductor surfaces.

In frequency domain we can express the fields in terms of the electrical scalar and magnetic vector potentials φ and $\mathbf{A}$ (*Lorenz* gauge),

$$\mathbf{E} = -j\omega\mathbf{A} - \nabla\varphi, \quad \mathbf{B} = \nabla\times\mathbf{A}\,. \tag{1}$$

It is convenient to express the vector and scalar potentials in terms of the current density $\mathbf{J}_s(\mathbf{r}_\perp, x)$ and charge density $\sigma(\mathbf{r}_\perp, x)$, through the integrals,

$$\varphi(\mathbf{r}) = \frac{1}{\varepsilon_0}\iint_S G_\varphi(\mathbf{r},\mathbf{r}')\sigma(\mathbf{r}')dS, \tag{2}$$

$$\mathbf{A}(\mathbf{r}) = \mu_0\iint_S G_A(\mathbf{r},\mathbf{r}')\cdot\mathbf{J}_s(\mathbf{r}')dS \tag{3}$$

which involve the Green functions for the considered multilayered structure (including the ground plane).

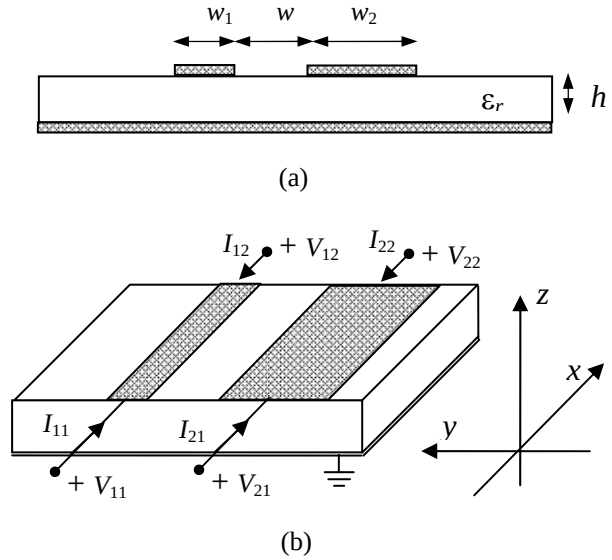

Fig. 1. The considered interconnect: (a) cross-section view; (b) adopted references for terminal voltages and currents .

The layers properties change along $\hat{z}$ (see Fig. 1), hence $G_A(r)$ has the structure [12],

$$G_A = \begin{bmatrix} G_{xx} & 0 & G_{xz} \\ 0 & G_{yy} & G_{yz} \\ G_{zx} & G_{zy} & G_{zz} \end{bmatrix}. \tag{4}$$

In many practical applications the thickness of conductors is small compared to their width *w*. If we consider zero-thickness for the signal conductors and assume the current density $\mathbf{J}_s$ directed along $\hat{x}$, we have the simple expression $G_A = G_{xx}$. We consider perfect conductors hence the sources are located on the surface $S = \Sigma_1\bigcup\Sigma_2$ of the two conductors.

As for the dielectric, we can introduce frequency-dependent losses through a simple Debye model, assuming (e.g., [13]),

$$\varepsilon_r(\omega) = \varepsilon_\infty + \frac{\varepsilon_{DC} - \varepsilon_\infty}{1 + i\omega\tau}, \tag{5}$$

where ε_∞, ε_{DC} and τ are constant values associated to the particular dielectric chosen.

For the considered structure the Green functions may be evaluated in closed form in the spectral domain: let $\tilde{G}_{xx}(k_\rho)$ and $\tilde{G}_\varphi(k_\rho)$ be their transforms in such a domain, where k_ρ is the spectral domain variable. The spatial domain functions are obtained by evaluating the Sommerfeld integrals (e.g., [14]),

$$G_{xx}(r)=\frac{1}{4\pi}\int_{-\infty}^{+\infty}\tilde{G}_{xx}(k_\rho)H_0^{(2)}(k_\rho r)k_\rho dk_\rho, \quad (6)$$

$$G_{\varphi}(r)=\frac{1}{4\pi}\int_{-\infty}^{+\infty}\tilde{G}_{\varphi}(k_\rho)H_0^{(2)}(k_\rho r)k_\rho dk_\rho, \quad (7)$$

where $H_0^{(2)}$ is the Hankel function. The cost for computing such integrals is extremely high because of the slow decay of the integrands. A way to overcome this problem is to extract analytically the terms which are dominant in the low frequency range, referred to as the *quasi-static terms* [15],

$$G_{xx}^0(r)=\frac{e^{-ik_0\sqrt{x^2+y^2}}}{4\pi\sqrt{x^2+y^2}}-\frac{e^{-ik_0\sqrt{x^2+y^2+(2h)^2}}}{4\pi\sqrt{x^2+y^2+(2h)^2}}, \quad (8)$$

$$G_{\varphi}^0(r)=(1+K)\frac{e^{-ik_0\sqrt{x^2+y^2}}}{4\pi\sqrt{x^2+y^2}}+ +(K^2-1)\sum_{n=1}^{\infty}K^{n-1}\frac{e^{-ik_0\sqrt{x^2+y^2+(2nh)^2}}}{4\pi\sqrt{x^2+y^2+(2nh)^2}}, \quad (9)$$

in which $K=(1-\varepsilon_r)/(1+\varepsilon_r)$ and $k_0=\omega\sqrt{\varepsilon_0\mu_0}$ is the vacuum space wavenumber. Once these terms have been extracted, the remainders (*dynamic terms*) may be evaluated in an efficient way by approximating the corresponding expressions in the spectral domain, for instance by using a vector fitting technique [11],

$$\tilde{G}_{Adyn}(k_\rho)=\sum_{n=1}^{N}\frac{b_n}{k_\rho^2-\alpha_n^2},\ \tilde{G}_{\varphi dyn}(k_\rho)=\sum_{n=1}^{N}\frac{d_n}{k_\rho^2-\beta_n^2}, \quad (10)$$

so that the final expressions are given by

$$G_A^{xx}(r)=G_{A0}(r)-\frac{j}{4}\sum_{n=1}^{N}b_nH_0^{(2)}(\alpha_n r), \quad (11)$$

$$G_{\varphi}(r)=G_{\varphi 0}(r)-\frac{j}{4}\sum_{n=1}^{N}d_nH_0^{(2)}(\beta_n r)\,. \quad (12)$$

The quasi-static terms are associated to the fundamental mode, are the only terms left when $f\to 0$ and dominate the local range interactions. The dynamic terms are associated to parasitic waves (surface waves, leaky waves), vanish as $f\to 0$ and dominate the long-range interactions. Figure 2 gives an example of scalar potential Green function G_φ for a single microstrip with $\varepsilon_r=4.9$ and $h=0.7mm$. The quasi-static term dominates the near-field region, whereas for increasing distances the dynamic terms become the principal ones. Unless very high frequencies are considered, in practical interconnects the quasi-static terms are dominant, hence the approximation of the remainder is usually satisfactorily pursued by a low-order model. A reliable criterion [16] states that the Green functions are accurately represented by the quasi-static terms when $k_0h\sqrt{\varepsilon_r-1}<0.1$.

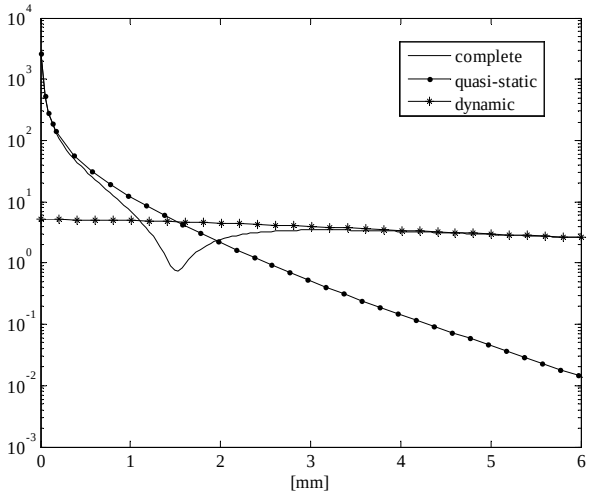

Fig. 2. Typical high-frequency behaviour of the scalar potential Green function: contributions of the quasi-static and dynamic terms.

III. THE ENHANCED TRANSMISSION LINE MODEL

In order to derive a transmission line model, let us impose the *charge conservation law*,

$$\nabla^{(s)}\cdot\mathbf{J}_s=-j\omega\sigma, \quad (13)$$

where $\nabla^{(s)}$ is the *surface divergence operator*. In addition we must impose the *PEC boundary condition*,

$$\left(-j\omega\mathbf{A}-\nabla\varphi\right)\big|_S\times\hat{\mathbf{n}}=\mathbf{0}. \quad (14)$$

Let us assume the dependence of the sources to be of separable type,

$$\sigma_1(s_1,x)=F_1(s_1)Q_1(x),\ \sigma_2(s_2,x)=-F_2(s_2)Q_2(x), \quad (15)$$

$$J_{s1}(s_1,x)=F_1(s_1)I_1(x),\ J_{s2}(s_2,x)=-F_2(s_2)I_2(x) \quad (16)$$

where $Q_{1,2}(x)$ and $I_{1,2}(x)$ are, respectively, the p.u.l. charges and the currents on the two signal conductors, $s_{1,2}$ are the curvilinear abscissas along the conductor

contours Γ_1 and Γ_2, whereas the shape functions $F_{1,2}(s)$ describe the transverse distributions of the sources. Let a_n be a "characteristic dimension" of the cross-section of the *n*-th conductor, *i.e.* a characteristic distance between two points on the conductor contour. For instance a_n would be equal to the diameter for a circular cross-section. For this case we may assume $a_1 = w_1$ and $a_2 = w_2$ (Fig. 1). Next, let us introduce a "characteristic dimension" h_c of the transverse section. For a single trace microstrip we can assume $h_c = h$, where *h* is the dielectric thickness, whereas for the general case of coupled microstrips as in Fig.1 we may assume h_c as the mean value between *h* and the distance between the two traces *w*. Now, assuming $k_0 a_n << 1$ for any *n* and $h_c k_0 < 5$ it is possible to evaluate $F_{1,2}(s)$ once for all by solving a quasi-static problem in the transverse plane and to approximate at any abscissa *x* the values of $A(s_{1,2}, x)$ and $\varphi(s_{1,2}, x)$ on the surfaces Σ_1 and Σ_2 with their average values $< A_{1,2}(x) >$ and $< \varphi_{1,2}(x) >$ [7]. In all these conditions it is easy to derive from equations (13) and (14) the following *governing equations*,

$$\frac{d\mathbf{I}(x)}{dx} = -i\omega \mathbf{Q}(x), \quad \frac{d\mathbf{V}(x)}{dx} = -i\omega \mathbf{\Phi}(x), \tag{17}$$

$\mathbf{\Phi}(x)$ being the p.u.l. magnetic flux vector. In the same conditions, from equations (2) and (3) we derive the *constitutive relations*,

$$\mathbf{\Phi}(x) = \mu_0 \int_0^l H_I(x - x')\mathbf{I}(x')dx', \tag{18}$$

$$\mathbf{V}(x) = \frac{1}{\varepsilon_0} \int_0^l H_V(x - x')\mathbf{Q}(x')dx' \tag{19}$$

where the entries of the kernel H_I are given by,

$$H_I^{ik}(\zeta) = \frac{1}{c_i} \oint_{\Gamma_i} ds_i \oint_{\Gamma_k} G_{xx}(s_i, s_k'; \zeta) F_i(s_k') ds_k', \tag{20}$$

whereas H_V has the same expression involving G_φ. The kernels *H*(*x*) are computed numerically, paying attention to the logarithmic singularity of their diagonal terms, arising from the quasi-static parts of the Green functions [8-10].

The *ETL* model is given by equations (17) to (19) and is a generalization of the *STL* model, which is obtained when relations (18) and (19) are of *local type*. This happens for interconnects *electrically small* in the transverse plane ($h_C k_0 << 1$) and of infinite length along *x*. In this case the kernels in equations (18) and (19) tend to spatial Dirac pulses,

$$H_I(x) \to [\int_0^{+l} H_I(x')dx']\delta(x) = H_{I0}\delta(x), \tag{21}$$

$$H_V(x) \to [\int_0^{+l} H_V(x')dx']\delta(x) = H_{V0}\delta(x). \tag{22}$$

Hence equations (18) and (19) reduce to

$$\mathbf{\Phi}(x) = \mu_0 H_{I0}\mathbf{I}(x) = L\mathbf{I}(x), \tag{23}$$

$$\mathbf{V}(x) = \frac{1}{\varepsilon_0} H_{V0}\mathbf{Q}(x) = C^{-1}\mathbf{Q}(x). \tag{24}$$

Note that for homogeneous dielectrics it is $H_I = \varepsilon_r H_V$, hence $H_{I0} = \varepsilon_r H_{V0}$, and equations (23) and (24) yield the classical result $LC = \varepsilon_r \varepsilon_0 \mu_0 I$. By combining equations (23), (24), and (17) we obtain the *standard transmission line mode*l,

$$\frac{d\mathbf{I}(x)}{dx} = -i\omega C\mathbf{V}(x), \quad \frac{d\mathbf{V}(x)}{dx} = -i\omega L\mathbf{I}(x) \tag{25}$$

In conclusion, the *ETL* model (17) to (19) generalizes the *STL* one (*i.e.*, equation (25)), removing the assumptions that the transverse characteristic dimension of the interconnect is electrically small and that the interconnect is infinite. The *ETL* model is valid in the following limits: (i) the characteristic dimensions of the terminal devices are small compared to the interconnect length; (ii) the characteristic transverse dimension *a* of the conductors is electrically small, $k_0 a_n << 1$; and (iii) $h_c k_0 < 5$, where h_c is a characteristic dimension in the transverse plane.

IV. NUMERICAL RESULTS

The first case considered refers to a PCB microstrip, with the geometry of Fig. 1, assuming a single signal conductor above a ground plane and a length of 36 mm. The signal conductor has zero thickness, width $w_1 = 1.8$ mm and lies on a FR-4 dielectric layer of thickness $h = 1.016$ mm, dielectric constant $\varepsilon_r = 4.9$ and magnetic permeability $\mu = \mu_0$. The conductors and dielectric are assumed ideal.

The *ETL* model solution is compared to the *STL* one and to two 3D full-wave solutions; one provided by the commercial FEM code *HFSS* [17] and the other by the tool *SURFCODE*, which is based on the *Electric Field Integral Equation* formulation [18]. Assuming for this case $h_c = h$, since $\varepsilon_{reff} \approx 3.65$ we have $k_0 h_c \approx 0.1$ at 1.4 GHz, hence we expect the *STL*, *ETL* and full-wave

solutions to agree up to frequencies around 1 GHz. This is clearly put on evidence in Fig. 3, where the input impedance of the line left open at the far end is plotted from DC to 0.8 GHz. For higher frequencies, the *STL* solution becomes inadequate, whereas the *ETL* one is still able to reproduce the full-wave solution, as shown in Fig. 4.

Since the conductors and the dielectric are assumed to be ideal, the finite amplitude of the peak is only due to the lossy effects related to the presence of unwanted parasitic modes (surface waves, leaky waves). In this condition a small but non-negligible amount of power is associated with radiation in the transverse plane. The real power absorbed by the interconnect fed at one end by a sinusoidal current of *rms* value I_0 and left open at the other end is given by,

$$P_{in}(\omega) = real\{Z_{in}(\omega)\} I_0^2 / 2. \quad (26)$$

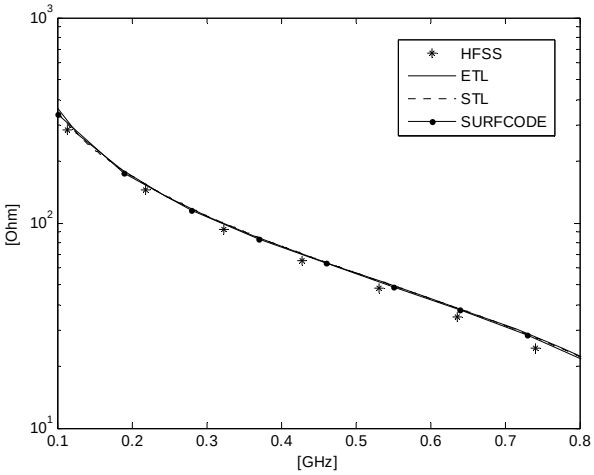

Fig. 3. Low frequency behaviour of the absolute value of the input impedance, Case 1.

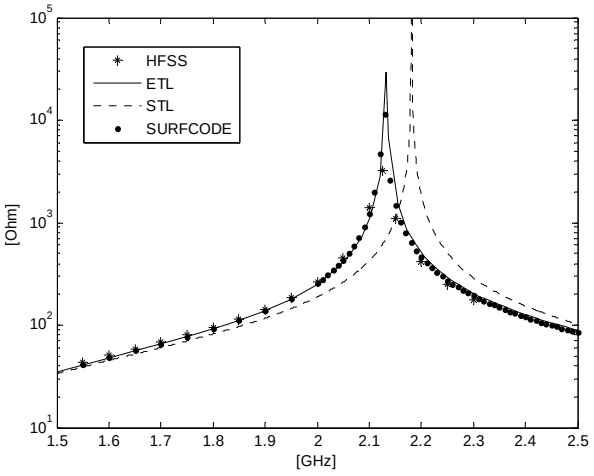

Fig. 4. High frequency behaviour of the absolute value of the input impedance, Case 1.

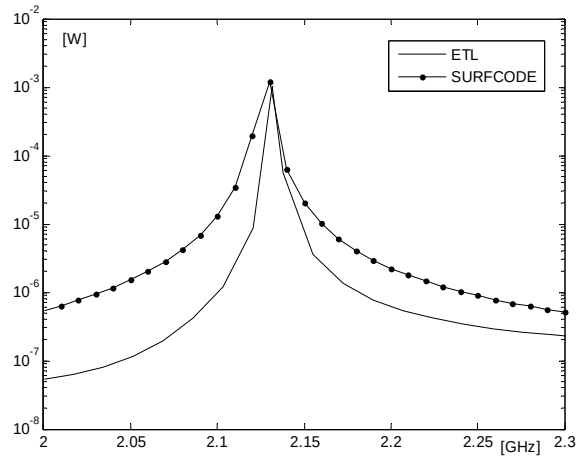

Fig. 5. Absorbed power for ideal dielectric, Case 1.

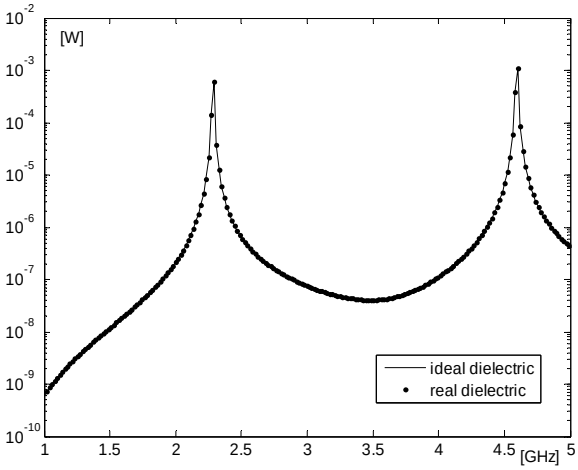

Fig. 6. ETL solution for absorbed power with ideal and real dielectric, Case 1.

In Fig. 5 it is shown the absorbed real power computed with $I_0 = 1mA$. The *ETL* solution is in good agreement with the full-wave one around the peak, whereas there is a deviation in the other ranges (however, the values of power are very low). Note that, since we are in the ideal case, the *STL* input impedance is strictly imaginary; hence the absorbed real power predicted by the *STL* model is always zero.

Let us now introduce a lossy dielectric described by the Debye model of equation (5), with $\varepsilon_\infty = 4.07, \varepsilon_{DC} = 4.178$, and $\tau = 1.15\,\text{ps}$. Figure 6 shows the dissipated power computed in the same conditions described for Fig. 5, both considering a real and an ideal dielectric with $\varepsilon_r = \varepsilon_{DC} = 4.178$. It is clear that in this case the dielectric losses are negligible with

respect to the losses associated to the other high-frequency phenomena.

The *ETL* model may be used to perform qualitative analysis on the solution. For instance, it is possible to distinguish between the high-frequency effects associated to the fundamental mode from those related to the excitation of parasitic modes. As shown in Section II, this could be easily done by switching on and off the contribution of the dynamic terms in the expression of the Green functions. Figure 7 shows, for instance, the mutual impedance of the above-considered line, computed by the *STL* model and by the *ETL* one, with or without the contribution of the dynamic terms. For this case, the quasi-static term is the only relevant, even for frequencies up to 7 GHz.

A second example is provided by a coupled microstrip made by two signal conductor and a ground plane. In this case (see Fig. 1) we have considered $w_1 = w_2 = w = 1.8\,\text{mm}$, $h = 1\,\text{mm}$, $\varepsilon_r = 4.17$ and a total length of 36 mm. The line behavior is investigated in the frequency range $(0-6)$ GHz, so extending to values of $k_0 h_c$ high enough to expect inaccurate results from the *STL* model. Here a crosstalk analysis has been performed, by assuming line 1 (see references in Fig. 1) to be fed at the near end by a unitary sinusoidal voltage source and open at the far end. The near and far ends of line 2 are both terminated on open circuits. Figure 8 shows the frequency behaviour of the near and far end crosstalk voltage defined as V_{21}/V_{11} and V_{22}/V_{11}, respectively. Note that in this case-study we have approximated the complete Green functions, considering only the contribution of the quasi-static term, which is again the dominant one.

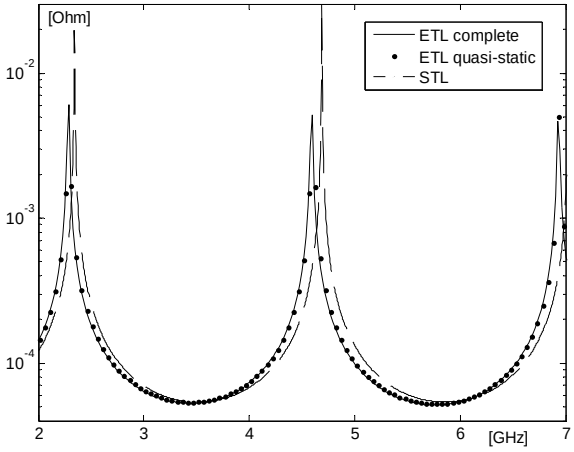

Fig. 7. Absolute value of the mutual impedance, Case 1.

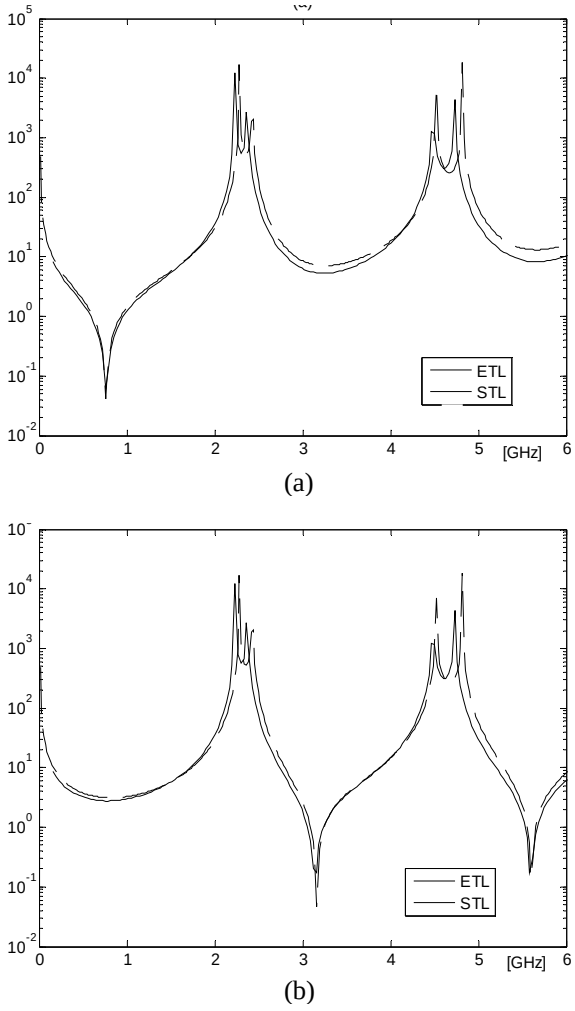

Fig. 8. Near-end (a) and far-end (b) crosstalk voltage normalized to the input voltage, Case 2.

V. CONCLUSIONS

The extension to inhomogeneous dielectrics of a full-wave transmission line model is obtained by including in the integral formulation a semi-analytical expression of the Green function for planar layered interconnects. Case-studies show the reliability of the model, as compared to 3D full-wave numerical solutions. The model is able to foresee high-frequency effects like radiation and dispersion due to excitation of unwanted parasitic modes. The way used to include inhomogeneous dielectrics into such a formulation is promising, since it is possible to split the Green function in terms describing the signal propagation (evaluated analytically) and remainders associated to the unwanted parasitic modes. This allows an accurate evaluation of the influence of such unwanted modes, exploiting the possibility to switch on and off the corresponding terms in the Green function expression.

VI. ACKNOWLEDGEMENTS

This work was supported in part by Italian Ministry of Research (PRIN Grant # 2004093025) and by Consorzio CREATE.

REFERENCES

[1] C. R. Paul, *Multiconductor transmission lines*, Wiley, New York, 1994.

[2] S. Tkatchenko, F. Rachidi, and M. Ianoz, "Electro-magnetic field coupling to a line of finite length: theory and fast iterative solutions in the frequency and time domain," *IEEE Trans. on Electr. Compatibility*, vol. 37, pp. 509-518, 1995.

[3] D. A. Larrabee, "Interaction of an electromagnetic wave with transmission lines, including radiation," *Proc. of IEEE Symp. Electrom. Compatibility*, pp. 106-111, 1998.

[4] T. J. Cui and W. C. Chew, "A Full-wave model of wire structures with arbitrary cross-sections," *IEEE Trans. on Electr. Comp.*, vol. 45, pp. 626-635, 2003.

[5] H. Haase, J. Nitsch, and T. Steinmetz, "Transmission-line super theory: a new approach to an effective calculation of electromagnetic interactions," *URSI Bulletin*, pp. 33-59, Dec. 2003.

[6] A. Maffucci, G. Miano, and F. Villone, "Full-wave transmission line theory," *IEEE Trans. on Magnetics*, vol. 39, pp. 1593–1597, 2003.

[7] A. Maffucci, G. Miano, and F. Villone, "An enhanced transmission line model for conducting wires," *IEEE Trans. on Elect. Compat.*, vol. 46, pp. 512-528, Nov. 2004.

[8] A. Maffucci, G. Miano, and F. Villone, "An enhanced transmission line model for conductors with arbitrary cross-sections," *IEEE Trans. on Adv. Packaging*, vol. 28, pp. 174–188, May 2005.

[9] A. G. Chiariello, A. Maffucci, G. Miano, F. Villone, and W. Zamboni, "Evaluation of crosstalk in high-frequency interconnects with an enhanced transmission line model," *15th Topical Meeting on Electrical Performance of Electronic Packaging EPEP 2006*, pp. 91-94, Scottsdale, Arizona, USA, 23-25 Oct. 2006.

[10] A. G. Chiariello, A. Maffucci, G. Miano, F. Villone, and W. Zamboni, "Mode conversion on high-frequency signal propagation on asymmetric interconnects," *Proc. of EMC-Europe 2006, 7th Inter. Symp. on Electromagnetic Compatibility*, pp. 365-370, Barcelona, Spain, 4-8 Sept. 2006.

[11] B. Gustavsen and A. Semlyen, "Rational approximation of frequency domain responses by vector fitting," *IEEE Transactions on Power Delivery*, vol. 14, no. 3, 1999.

[12] K. A. Michalski and D. Zheng, "Electromagnetic scattering and radiation by surfaces of arbitrary shape in layered media. I. Theory," *IEEE Trans. on Antennas and Propag.*, vol. 38, pp. 335-344, March 1990.

[13] G. Miano and A. Maffucci, *Transmission lines and lumped circuits*, Academic Press: New York 2001.

[14] V. N. Kourkoulos and A. C. Cangellaris, "Accurate approximation of Green's functions in planar stratified media in terms of a finite sum of spherical and cylindrical waves," *IEEE Trans. on Antennas and Propag.*, vol. 54, pp. 1568 – 1576, May 2006.

[15] Y. L. Chow, J. J. Yang, D. G. Fang and G. E. Howard, "A closed-form spatial Green's function for the thick microstrip substrate," *IEEE Trans. on Microwave Theory and Techniques*, vol. 39, pp. 588 – 592, March 1991.

[16] A. G. Chiariello, A. Maffucci, G. Miano, F. Villone, and W. Zamboni, "Full-wave numerical analysis of single-layered substrate planar interconnects," *IEEE Workshop on Signal Propa-gation on Interconnects SPI 2006*, pp. 57-60, Berlin, Germany, 9-12 May 2006.

[17] http://www.ansoft.com/products/hf/hfss/

[18] G. Miano and F. Villone, "A surface integral formu-lation of Maxwell equations for topologically complex conducting domains," *IEEE Trans. on Antennas and Propag.*, vol. 53, no. 12, pp. 4001-4014, Dec. 2005.

Andrea G. Chiariello received in 2004 the Laurea Degree in Electronic Engineering *summa cum laude* and from the 2004 he is a Ph.D. student in Electrical Engineering from the University of Naples "Federico II" , Italy.

In 2006 he was a visiting scholar at the electrical and computer engineering of the University of Illinois, Urbana Champain, USA. His research interests are the electromagnetic modeling of high-speed interconnects and the electromagnetic compatibility.

Antonio Maffucci received in 1996 the Laurea Degree in Electronic Engineering *summa cum laude* and in 2000 the Ph.D. degree in Electrical Engineering from the University of Naples "Federico II", Italy.

In 1997 he was with the nuclear fusion laboratory JET (Culham,

U.K.). From 1998 to 2002 he was with the Department of Electrical Engineering at the University of Naples. From 2002 he is with the Elettrotecnica Group at the Faculty of Engineering of the University of Cassino, Italy, where he is currently an Associate Professor, teaching courses on circuit theory and electromagnetic compatibility.
His research areas include electromagnetic modeling of distributed systems, electromagnetic compatibility, computational electromagnetism, and nanotechnology.
He is author of more than 80 technical papers on international journals, conference proceedings and essays on books. He is also co-author of the book *Transmission lines and lumped circuits* (New York, Academic Press, 2001). He is Associate Editor of the *IEEE Transactions on Advanced Packaging*.

Giovanni Miano received the Laurea (*summa cum laude*) and Ph.D. degrees in electrical engineering from the University of Naples Federico II in 1983 and 1989, respectively.
From 1984 to 1985, he was with the PS Division, CERN, Geneva, Switzerland, where he was engaged in research on magnetic plasma lenses. From 1989 he Full Professor at the faculty of Engineering of the University of Naples Federico II, where he served as a Researcher until 1992 and as Associate Professor from 1992 to 2000. From 2005 he is the Director of the Dipartimento di Ingegneria Elettrica.
In 1996 he was a Visiting Scientist at the GSI Laboratories, Darmstadt, Germany, and in 1999 a Visiting Professor at the Department of Electrical Engineering, University of Maryland, College Park.
His research interests include ferromagnetic materials, nonlinear dielectrics, plasmas, electrodynamics of continuum media, nanotechnology and modeling of lumped and distributed circuits.
He is the author or co-author of more than 70 papers published in international journals, 60 papers published in international conference proceedings, two items in the *Wiley Encyclopedia of Electrical and Electronic Engineering* (New York: Wiley, 1999), and the monograph *Transmission Lines and Lumped Circuits* (New York: Academic, 2001). He is a Reviewer for various journals of the IEEE and past member of the Editorial Boards of the Conference on Electromagnetic Field Computation and the Conference on the Computation of Electromagnetic Field

Fabio Villone received the Laurea degree (summa cum laude) in Electronic Engineering in 1994 at the University of Naples Federico II, and the Ph.D. in Industrial Engineering in 1998 at the University of Cassino.
Currently, he is Full Professor at the Faculty of Engineering of the University of Cassino, where he formerly was Research Assistant (1997-2001) and Associate Professor (2001-2007). He teaches "Basic Electrical Engineering" and "Numerical models for electromagnetic fields and circuits".
In 1996 he was visiting scientist at CRPP-Lausanne (Switzerland), and in the last years at JET (Joint European Torus), close to Oxford (UK).
His scientific interests are in the field of computational electromagnetics, with particular reference to fusion plasma modelling and engineering, electromagnetic compatibility and eddy current non destructive testing.
He is co-author of more than 60 papers on international journals and essays on books, and more than 50 contributions to international conferences, among which several invited papers.
He was Scientific Coordinator of several experiments carried out at JET, and Principal Investigator of a national research project on fusion plasma modelling and control.

Walter Zamboni received the Laurea degree in Electrical Engineering (*summa cum laude*) in 2001 and the Ph. D. degree in Electrical Engineering in 2004 from the Faculty of Engineering, Università degli Studi di Napoli "Federico II", Italy. In 2003 he has been Stager at CERN, Geneva, Switzerland, and Visiting Scientist at EPFL-CRPP Superconductivity Group, Villigen-PSI, Switzerland. From 2005 he is with the the Faculty of Engineering, Università degli Studi di Cassino, Italy, where he works as a research assistant. From 2006 he teaches Circuits Theory at the Università degli Studi del Sannio, Italy

His scientific interests are in the field of computational electromagnetics, with particular reference to interconnects and applied superconductivity.

Circuit Models for Interconnects Using 3D Computational Techniques

[1]B. Essakhi, [1]J. Benel, [1]M. Smail , [2]G. Akoun, and [1]L. Pichon

[1] Laboratoire de Génie Electrique de Paris
UMR 8507 CNRS, SUPELEC, Université Paris-Sud, Université Pierre et Marie Curie
Plateau de Moulon, 91192 Gif-sur-Yvette cedex, France

[2] European Aeronautic Defence and Space – Innovation Works,
12 rue Pasteur, 92150 Suresnes, France

Abstract **–** This paper presents a method to generate circuit models from 3D distributed structures. In the first step a broadband characterization of the device is obtained through a reduced order modeling technique. Then in the second step a rational approximation of the coefficients of the impedance matrix is derived using a root mean squared procedure. An equivalent circuit is then synthesized and allows a global circuit simulation of the whole structure. The proposed methodology can be used with a segmentation technique for the analysis of complex structures: a whole 3D structure can be subdivided into smaller parts. Each part is characterized by an equivalent circuit deduced from wideband analysis. The connection between the substructures makes available a global simulation of the whole system inside a circuit platform (SPICE for example). Numerical results are shown for different kinds of interconnects (tracks and cables).

Keywords: Electromagnetic compatibility, interconnecting wires, and equivalent circuits.

I. INTRODUCTION

With the increasing use of on-board electronic equipment, mastering Electromagnetic Compatibility (EMC) compliance at early design stage is becoming a crucial technical issue for the automotive industry. Computer simulation of the EMC properties of electronic devices is a promising way to make EMC design faster and cost-effective, since it can be applied to the virtual product before fabrication.

In complex equipments involving interconnecting wires and electronic components a complete understanding requires a global analysis studying both electromagnetic modelling (for distributed parts) and circuit simulation (for lumped components). For a reliable simulation at the sub-system or system level efficient techniques are needed to address a hybrid field-circuit analysis. For a time domain analysis a strong coupling between a field solver in the time domain and a circuit simulator leads to a heavy process updating at each time step both the field quantities and the circuit values [1].

An efficient solution for transient analysis is to extract lumped circuit parameters from broadband field computation. Circuit extraction is a well known procedure in case of high speed interconnects [2]. Equivalent circuits or circuit macromodels can be easily derived from a rational approximation of the frequency response of the structure [2, 3]. In case of conducting cables an adequate modelling technique is usually achieved in the frame of the transmission line theory. However such approach does not remain valid because of the increase of the frequency range involved in EMC analysis. In [4] a technique based on a full wave integral approach has been developed and applied to unshielded cables.

The main computational cost relevant to circuit extraction techniques is the broadband full wave analysis. In order to minimize this computational cost a Padé approximation procedure provides an efficient way [5]. However such an approach requires getting the solution for a set of frequencies distributed over the whole frequency band. The results may be sensitive to the choice of the sample frequencies. A much more powerful approach is reduced order modelling: instead of solving the field problem, the equations characterizing the device are first brought to the state space form of the linear system and the system is reduced by appropriate algebraic transformation.

In recent years many reduced-order modelling (ROM) techniques have been studied [6-9]. In [9] a Laguerre SVD (Singular Value Decomposition) algorithm was shown to provide an efficient ROM technique. The capabilities of the approach were demonstrated in the case of linear systems resulting from the telegrapher equations or from the PEEC (Partial Element Equivalent Circuit) method. In our work we show that such a technique can be efficiently used in connection with a 3D finite element approach. With such an approach the impedance of distributed structures can

be easily obtained over a broadband. Then circuit models are deduced using a root mean square procedure and can be directly incorporated into a circuit simulator if required.

II. REDUCED-ORDER MODELING

Consider an electromagnetic problem involving one excitation port. From a 3D edge finite element approach the metrical system governing the vector of unknowns e(t) is given by [10],

$$\begin{cases} M_m \dfrac{d^2 e}{dt^2} + M_d \dfrac{de}{dt} + M_s e = Lu(t) \\ y(t) = L^T e(t) \end{cases} \quad (1)$$

where $\mathbf{M_m}$ is the mass matrix, $\mathbf{M_d}$ is the damping matrix, $\mathbf{M_s}$ is the stiffness matrix, **L** is a selector matrix, u(t) is the excitation and y(t) is the output of interest.
In the Laplace domain with zero initial condition the transfer function H(s), Y(s) = H(s)U(s) is given by,

$$H(s) = L^T \left(M_s + sM_d + s^2 M_m \right)^{-1} L \quad (2)$$

the second-order system can be reformulated as a first-order linear system of order N,

$$\begin{aligned} C\frac{dx}{dt} + Gx(t) &= Bu(t) \\ y(t) &= B^T x(t) \end{aligned} . \quad (3)$$

Consequently from equation (3) the transfer function can be written as,

$$H(s) = B^T (G + sC)^{-1} B . \quad (4)$$

The aim of model order reduction is to replace the mathematical model (equation (4)) by a model which is much smaller but keeps the same behaviour over a given frequency band. In other words the purpose is to find a system governed by a reduced state space form,

$$\begin{aligned} C_r \frac{dx}{dt} + G_r x(t) &= B_r u(t) \\ y(t) &= B_r{}^T x(t) \end{aligned} \quad (5)$$

where the dimension q of the reduced matrices $\mathbf{C_r}$, $\mathbf{G_r}$, and $\mathbf{B_r}$ verifies $\mathbf{q} << \mathbf{N}$.
The new transfer function $\mathbf{H_r}$ is,

$$H_r(s) = B_r{}^T (G_r + sC_r)^{-1} B_r . \quad (6)$$

The ROM technique used in this work has been described in [9]. It is based on a system description in terms of orthonormal Laguerre functions. It uses the singular value decomposition and Arnoldi algorithm. To illustrate, the efficiency of this ROM technique is demonstrated in the case of the loop antenna shown in Fig. 1. The variation of the impedance computed with the reduced order method is compared to Fig. 2 with a standard 3D finite element method for two different orders **(q = 7, and q = 10)**. It is shown that for **q = 10** an excellent agreement is obtained over the entire frequency band.

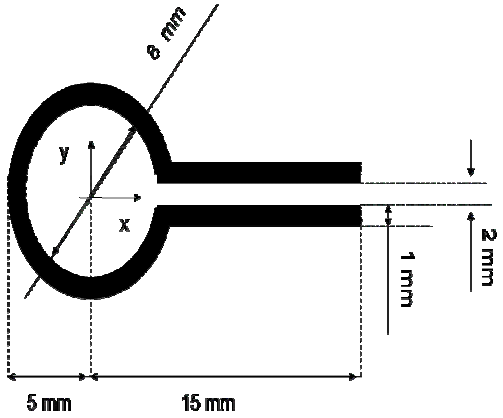

Fig. 1. Loop antenna.

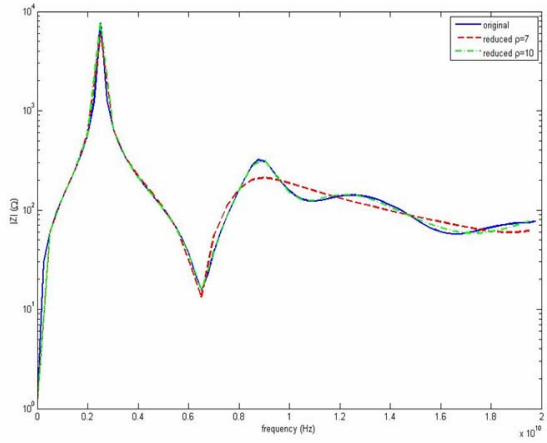

Fig. 2. Comparison between ROM technique and standard 3D finite element method.

III. CIRCUIT MODELS

Once the impedances of distributed structures are known over a given frequency band, an approximate expression based on rational functions can be determined. For a lossless transmission line of length l, the coefficients of the two port impedance matrix are known analytically [11],

$$Z_{11}(s) = Z_{22}(s) = Z_c \coth(\tau s)$$
$$Z_{12}(s) = Z_{21}(s) = Z_c \frac{1}{sh(\tau s)} \quad (7)$$

where $Z_c = \sqrt{\frac{L}{C}}$ is the characteristic impedance and $\tau = l\sqrt{LC}$.

These coefficients can be expressed as Fourier series,

$$Z_{11}(s) = \frac{Z_c}{\tau}\left(\frac{1}{s} + \sum_{n\geq 1} \frac{2s}{s^2 + n^2\omega_0^2}\right)$$
$$Z_{12}(s) = \frac{Z_c}{\tau}\left(\frac{1}{s} + \sum_{n\geq 1} \frac{(-1)^n 2s}{s^2 + n^2\omega_0^2}\right) \quad (8)$$

where $\omega_0 = \frac{\pi}{\tau}$.

Since the structures studied in this work behave like transmission lines, a rather natural rational approximation of this impedance uses second order rational functions with real coefficients. It is determined via a least mean squared procedure. The whole band is divided into $\mathbf{N_b}$ sub-intervals where $\mathbf{N_b}$ is the number of resonant frequencies. For example, the value of $\mathbf{Z_{11}}$ is searched as,

$$Z_{11}(s) \approx \sum_{k=1}^{N_b} Z_{ap}^k(s) = \sum_{k=1}^{N_b} \frac{b_o^k + b_1^k s}{a_o^k + a_1^k s + a_2^k s^2}. \quad (9)$$

Each second order rational function corresponds to an electrical circuit constituted with an inductance L with resistive loss (corresponding to a resistance R_1) in parallel with a capacitance C with a leakage conductance $G = 1/R_2$ shown in Fig. 3.

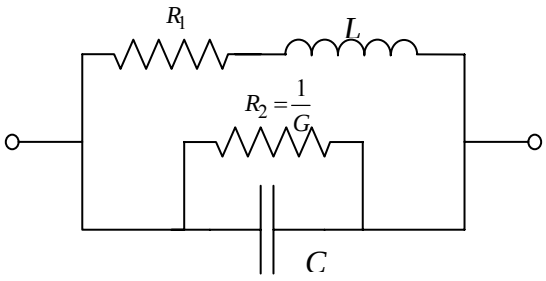

Fig. 3. Equivalent circuit for a second order rational function.

IV. CONDUCTING CABLES

Figure 4 shows a perfectly conducting cable above a ground plane. The load is 50 Ω. The ground plane is a perfect conductor. Figure 5 shows the 3D finite element computation over the whole band and the corresponding rational approximation. This approximated impedance is built using a sum of 4 second order rational functions. Each rational function corresponds to a resonance peak. The distances between the different peaks characterize the resonances of the transmission line. A reasonable agreement between the finite element based approach and the approximation is obtained.

$$Z_{11}(s) \approx \sum_{k=1}^{4} \frac{b_o^k + b_1^k s}{a_o^k + a_1^k s + a_2^k s^2} \quad (10)$$

where the coefficients are given in Table 1.

Table 1. Coefficients of the rational approximation.

	i	b_i^k	a_i^k
k = 1	0	-3.14	1
	1	-1.56e+02	-5.21e-02
	2		2.02
k = 2	0	-2.19	1
	1	4.33e+01	3.54e-02
	2		5.09e-01
k = 3	0	-3.52e-01	1
	1	-1.74e+01	-1.80e-02
	2		2.20e-01
k = 4	0	-3.75	1
	1	9.48	1.88e-02
	2		1.27e-01

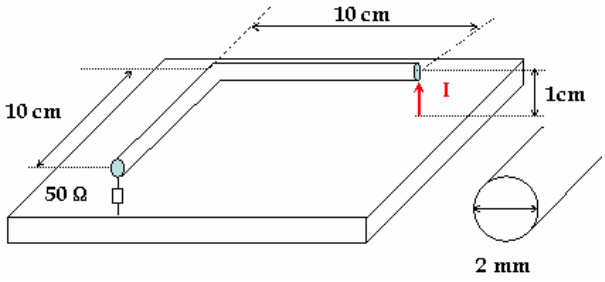

Fig. 4. Cable of diameter 1 mm above the ground plane.

Figure 6 shows a more complicated case: the cable is 50 cm long and the height is not constant. The corresponding numerical results for the full wave computation and the approximation are shown on Fig. 7. The coefficients are given in Table 2. The rational series can be directly incorporated into a circuit simulator like SPICE for example and can provide an efficient time domain simulation of the signal propagating along the transmission lines.

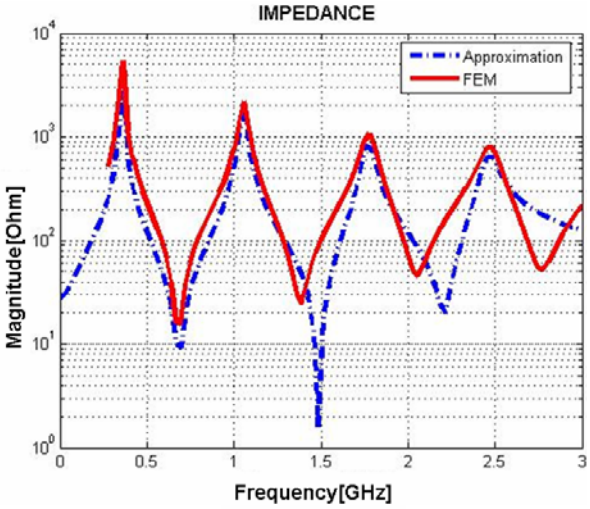

a) Magnitude of the impedance.

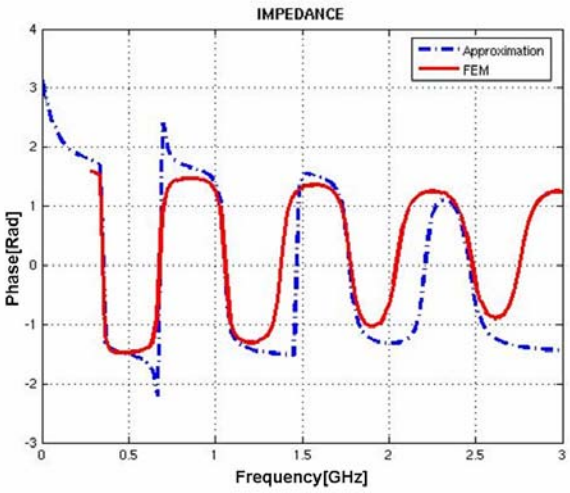

b) Phase of the impedance.

Fig. 5. Comparison between direct 3D FEM computations (solid line) and rational approximation (dashed line).

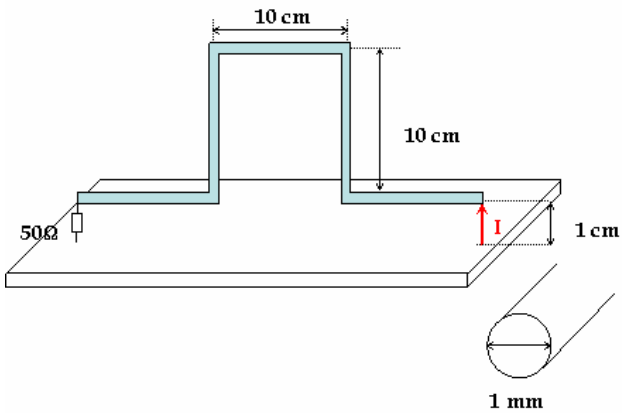

Fig. 6. Cable of diameter 1 mm above the ground plane.

Table 2. Coefficients of the rational approximation.

	i	b_i^k	a_i^k
k = 1	0	-1.89e+01	1
	1	4.31e+02	5.52e-03
	2		1.84e+01
k = 2	0	-5.00	1
	1	4.58e+01	2.32e-01
	2		3.75
k = 3	0	-5.38	1
	1	2.20e+01	4.62e-02
	2		1.41
k = 4	0	2.62	1
	1	1.79e+01	2.11e-02
	2		7.94e-01

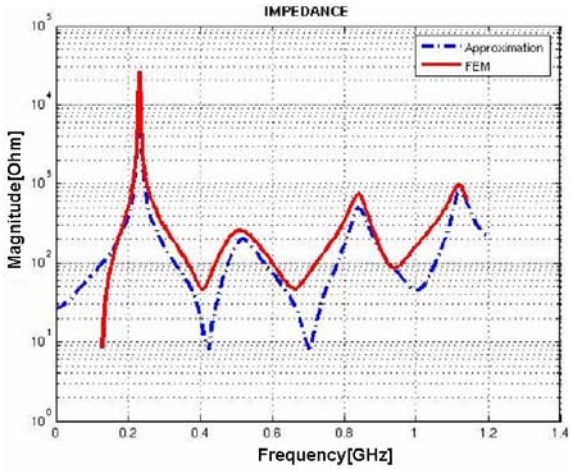

a) Magnitude of the impedance.

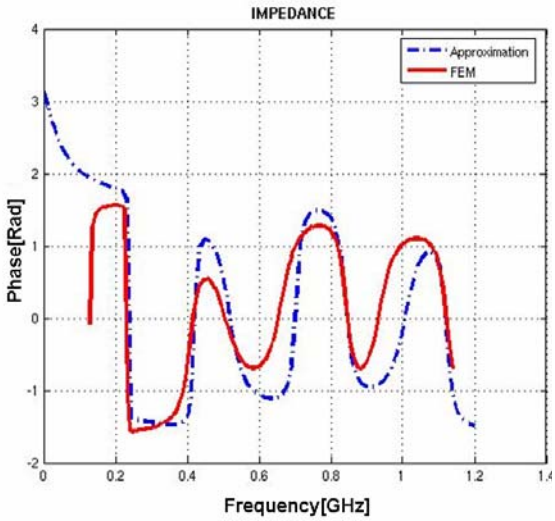

b) Phase of the impedance.

Fig. 7. Comparison between direct 3D FEM computation (solid line) and rational approximation (dashed line).

V. TRACKS ETCHED ON PRINTED CIRCUIT BOARDS

The loop antenna studied in Section I is associated with a section of a multi-conductor transmission line etched on the same substrate (Fig. 8). The characteristic impedance of the transmission line can be evaluated through a 2D cross-section analysis. So a global impedance of the whole structure (loop antenna + transmission line) can be determined at the input of the transmission line according to the rules of the transmission line theory. An approximate analytical expansion of including only two rational functions is also evaluated. A good agreement is obtained between the SPICE rational result and the two kinds of analytical solutions (Fig. 9). These solutions are compared to the whole 3D computation: it is worth noting that the SPICE result is closed to the global impedance deduced from the full wave 3D code ASERIS-BE (from EADS). This can be explained by the fact that the electromagnetic coupling between the loop antenna and the transmission line is weak in this case: the global behaviour of the structure roughly follows the theory of the transmission lines. This electromagnetic coupling is significant in the low frequency range: the global structure does not behave like a transmission line and a macromodelling SPICE simulation is no longer available in this range.

This methodology could provide an efficient way to simulate how conducted emissions can be induced along systems of transmissions lines by a perturbating electromagnetic field. The whole 3D transmission line system can be divided into sub-structures. Each part can be separately handled and the corresponding equivalent SPICE circuit can be deduced. As shown in the example above, in the high frequency case, all the parts can be connected together making available a global circuit model. So, provided that the spectrum of the illuminating exciting source is in a high frequency range, a SPICE simulation will allow giving how a conducted interference will be carried by the system of transmission lines.

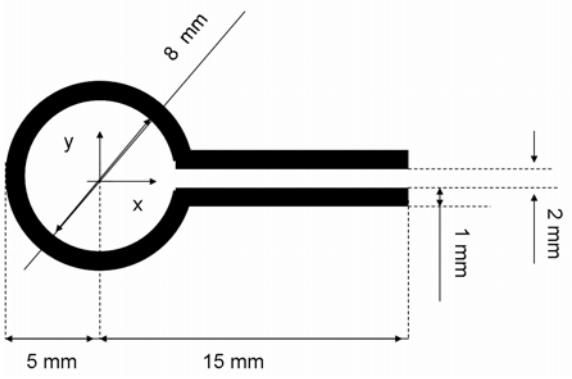

a) Loop antenna.

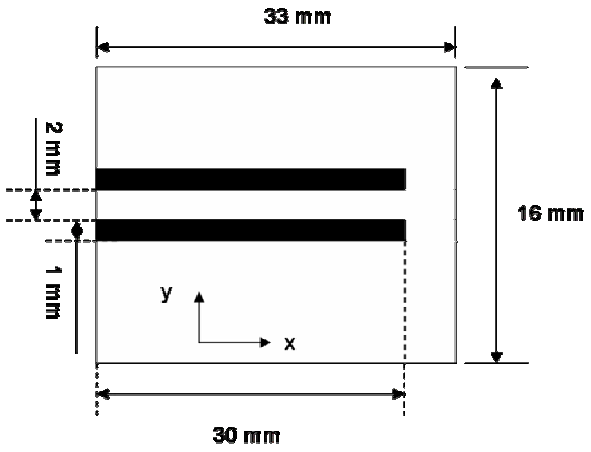

b) Transmission line.

Fig. 8. Global 3D structure.

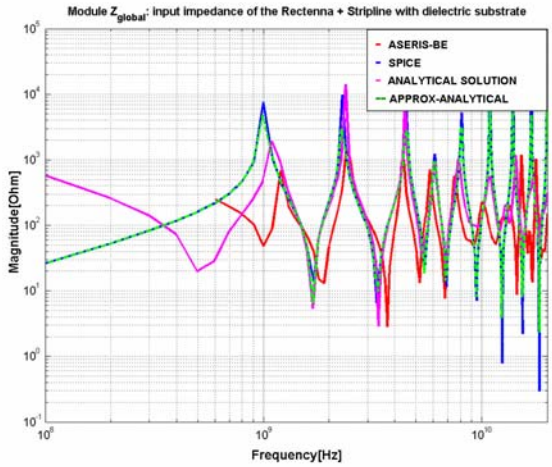

Fig. 9. Global impedance obtained with full wave computation, SPICE, and analytical expressions.

VI. CONCLUSION

A macromodelling approach was presented for EMC analysis of interconnected systems in the field of electromagnetic compatibility. In the methodology a broad-band characterization of distributed structures is performed with a finite element based approach. Then circuit models are deduced using a root mean square procedure. These circuit macromodels, SPICE compatible for example, provide a straightforward technique to simulate the propagation of parasitic signals along tracks and/or transmission lines. The procedure can be efficiently used in the simulation of time domain reflectometry for cable diagnosis.

REFERENCES

[1] K. Guillouard, M.-F. Wong, V. Fouad Hanna, and J. Citerne, "A new global time domain electromagnetic simulator of microwave circuits including lumped elements based on finite element method," *IEEE Trans. on Microwave Theory and Techniques*, vol. 47, no. 10, pp. 2045-2048, 1997.

[2] M. Elzinga, K. Virga, L. Zhao, and J. L. Prince, "Pole-residue formulation for transient simulation of high frequency interconnects using householder LS curve fitting," *IEEE Trans. on Adv. Pack.*, vol. 25, pp. 142-147, 2000.

[3] G. Antonini, "SPICE equivalent-circuits from frequency domain responses," *IEEE Transactions on Electromagnetic Compatibility*, vol. 45, no. 3, pp. 502-511, 2003.

[4] S. Caniggia, A. Maffucci, F. Maradei, F. Villone, and W. Zamboni, "3D numerical modeling and circuit extraction techniques for the analysis of unshielded twisted pairs," *IEEE Trans. on Magnetics*, vol. 43, no. 4, pp. 1357-1360, 2007.

[5] B. Essakhi and L. Pichon, "An efficient broadband analysis of an antenna via 3D FEM and Padé approximation," *ACES (Applied Computational Electromagnetic Society) Journal*, vol. 21, no. 2, pp. 143-148, 2006.

[6] A. C. Cangellaris and L. Zhao, "Model order techniques for electromagnetic macromodelling based on finite methods," *International Journal of Numerical Modeling*, no. 13, pp. 181-197, 2000.

[7] J. Rubio, M. A. Gonzalez, and J. Zapata, "Analysis of cavity-backed microstrip antennas by a 3D finite element / segmentation method and a matrix Lanczos-Padé algorith (SFELP)," *Antennas and Wireless Propagation Letters*, vol. 1, no. 1, pp. 193-195, 2002.

[8] Y. Zhu and A. C. Cangellaris, "A new finite element model for reduced order electromagnetic modelling," *IEEE Microwave and Wireless Components Letters*, vol. 11, no. 5, pp. 211-213, 2001.

[9] L. Knockaert and D. De Zutter, "Laguerre-SVD reduced-order modelling," *IEEE Trans. on Microwave Theory and Techniques*, vol. 48, no. 9, pp. 1469-1475, 2000.

[10] W. P. Carpes Jr, L. Pichon, and A. Razek, "A finite element method for the numerical modelling of bounded and unbounded electromagnetic problems in the time domain," *International Journal of Numerical Modelling (Electronic networks, Devices and Fields)*, vol. 13, pp. 527-540, 2000.

[11] R. B. Schulz, V. C. Plantz, and D. R. Brush, "Shielding theory and practice," *IEEE Trans. on Electromagnetic Compatibility*, vol. 30, no. 3, pp. 187-201, 1988.

Brahim Essakhi was born in Rabat, in 1974. He obtained a Master's in Applied Mathematics from Ecole Normale Supérieure (ENS) in Cachan (France) in 2001. In 2002 he joined the Laboratoire de Génie Electrique de Paris (LGEP) associated to CNRS, SUPELEC, University of Paris-Sud and University of Pierre et Marie Curie where he earned a PhD in 2005. His main scientific interests are numerical methods, wave propagation modeling, and electromagnetic compatibility.

Jérémie Benel was born in Clamart, France, in 1980. He is graduated from the Ecole Normale Supérieure de Cachan. He received the M.S. degree in electrical engineering from Univ Paris-Sud in 2006. He is currently pursuing a Ph.D. degree at the Laboratoire de Génie Electrique de Paris (LGEP). His main scientific interests are electromagnetic compatibility and computational electromagnetics.

Mostafa Kamel Smail was born in Guelma, Algeria, in 1981. He received the master degree in components and antennas for telecommunications from University of Paris-Sud, France in 2007 and is currently working toward the Ph.D. degree at the Laboratoire de Génie Génie électrique de Paris (LGEP), Paris, France. His current research interests are wave propagation modelling, reliability, and electromagnetic compatibility.

Lionel Pichon was born in Romorantin, France, in 1961. He obtained the Dip. Eng. from Ecole Supérieure d'Ingénieurs en Electronique et Electrotechnique (ESIEE) in 1984. In 1985 he joined the Laboratoire de Génie Electrique de Paris LGEP associated to CNRS, SUPELEC, University of Paris-Sud, University of Pierre et Marie Curie where he earned a PhD in 1989. He is now Chargé de Recherche at the CNRS. His research interests include computational electromagnetics in microwaves, and electromagnetic compatibility.

Gilles Akoun was born in Bordeaux, France, in 1959. He obtained the Dip. Eng. from Ecole Nationale Supérieure des Ingénieurs Electriciens de Grenoble (ENSIEG) in 1982. In 1983, he joined the Laboratoire d'Electrotechnique de Grenoble associated to CNRS where he eraned a PhD in 1986. Actually, he is an Electrical Research Engineer at Innovation Works - EADS. His research interests ElectroMagnetic Compatability (EMC) and also computational electromagnetics developments.

Eddy Current Imaging of Surface Breaking Defects by Using Monotonicity Based Methods

[1]G. Rubinacci, [2]A. Tamburrino and [2]S. Ventre

[1] Dipartimento di Ingegneria Elettrica, Università di Napoli "Federico II"
Via Claudio 21, Napoli, I-80125, Italy
rubinacci@unina.it

[2] DAEIMI, Università di Cassino
Via G. Di Biasio 43, Cassino (FR), I-03043
tamburrino@unicas.it, ventre@unicas.it

Abstract – This paper is in the framework of the non-destructive evaluation of conductive materials by means of eddy current testing. In particular, we consider the imaging of surface breaking volumetric defects. In this case, it is possible to use relatively "high-frequencies" and, in the limit of skin-depth negligible with respect to the relevant geometrical sizes and negligible displacement current, the problem can be modeled as a magnetostatic one. The elliptic nature of magnetostatic allows proving a monotonicity property of the operator mapping the defects geometry into the measured quantity. This makes possible to use a recently proposed fast (non-iterative) imaging algorithm.

***Keywords*:** Non-destructive testing, eddy current testing, inverse problem, and fast imaging algorithms.

I. INTRODUCTION

The solution of the inverse problem in a non destructive evaluation test based on eddy currents is usually formalized as the minimization of an error functional with respect to a given set of unknowns describing the features of the anomaly affecting the specimen under test. The evaluation of the error functional, relating the measurements to the computed data, requires the solution of the forward problem (compute the measurements for given anomalies) that should be repeated many times in the minimization procedure. Moreover the presence of local minima is a critical issue penalizing many local minimization algorithms. Recently a non-iterative method solving the inverse problem has been proposed for estimating a resistivity distribution approximated by a number of voxels [1-4]. The data consists of measurements of the impedance matrix at several frequencies acquired using a coil array. The method is based on a monotonicity property of the operator mapping the defects geometry into the measurements. However, in the approach adopted so far, the monotonicity has been achieved for the real part of the impedance matrix in the low frequency limit when the skin depth is larger than the relevant sizes of the problem. The evaluation of the impedance in this limit is a very difficult issue since the signal at low frequency is relatively weak and presence of noise can "destroy" the monotonicity property.

In this paper we prove the monotonicity property of the operator mapping the defects geometry into the measured quantity, in the high frequency limit. In this case the forward problem can be conveniently approximated by a magnetostatic equivalent model, thanks to the skin effect that imposes a vanishing field inside the specimen (and a vanishing normal component of the magnetic flux density on its surface). In this limit we can solve the inverse problem leading to the imaging of surface defects on a conductive specimen, in a non iterative way.

The paper is organized as follows: in Section 2 the mathematical model is described, in Section 3 the monotonicity is proved and in Section 4 numerical examples, aimed to verify the monotonicity and to show the performance of the inversion algorithm, are presented.

II. MATHEMATICAL MODEL

Let us consider a measurement system consisting of an array of several coils eventually mounted on a magnetic support that we assume to be linear (Fig. 1). The measured quantity is the impedance matrix (self and mutual impedances between coils) at the angular frequency ω. Under the assumption of negligible displacement current, the mathematical model is that of eddy current, eventually in the presence of magnetic materials. The mathematical model is, therefore,

$$\begin{cases} \nabla \times \mathbf{H} = \mathbf{J}_s \text{ in } \mathrm{IR}^3 \setminus V_c \\ \nabla \cdot (\mu \mathbf{H}) = 0 \text{ in } \mathrm{IR}^3 \setminus V_c \\ \nabla \times \mathbf{E} = -j\omega\mu \mathbf{H} \text{ in } V_c \\ \nabla \times \mathbf{H} = \sigma \mathbf{E} \text{ in } V_c \\ \nabla \cdot (\mu \mathbf{H}) = 0 \text{ in } V_c \end{cases} \quad (1)$$

together with proper continuity conditions on material interfaces and regularity conditions at infinity. In equation (1) V_c is the conducting domain, **E** and **H** are the electric and magnetic fields, respectively, σ is the electrical conductivity (**J**(**r**) = σ(**r**) **E**(**r**) in V_c, **J** is the induced current density), μ is the magnetic permeability (**B**(**r**) = μ(**r**) **H**(**r**) in IR^3, where **B** the magnetic flux density) and $\mathbf{J}_s$ is the prescribed source current density, that is the current density due to the currents circulating in the excitation coils. In addition, we assume the conductor to be non-magnetic.

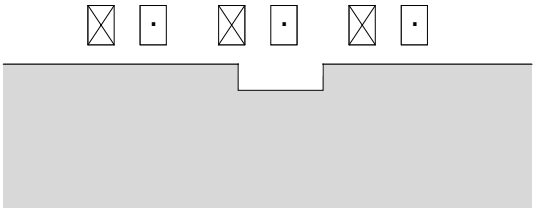

Fig. 1. A conductor is probed by an array of three coils. A surface breaking volumetric defect is present. The measured quantity is the impedance matrix (in this case a 3×3 symmetric matrix).

If the frequency is high enough so that the skin-depth is negligible with respect to the typical dimensions of the conductor, the fields vanish inside the conducting domain V_c. As long as the displacement current is negligible, the magnetic field outside the conductor satisfies a magnetostatic problem in the free space with the boundary condition $\mathbf{B} \cdot \hat{\mathbf{n}} = 0$ on ∂V_c,

$$\begin{cases} \nabla \times \mathbf{H} = \mathbf{J}_s \text{ in } \mathrm{IR}^3 \setminus V_c \\ \nabla \cdot \mathbf{B} = 0 \text{ in } \mathrm{IR}^3 \setminus V_c \\ \mathbf{B} \cdot \hat{\mathbf{n}} = 0 \text{ on } \partial V_c \\ \mathbf{B}(\mathbf{r}) = \mu(\mathbf{r}) \mathbf{H}(\mathbf{r}) \text{ in } \mathrm{IR}^3 \setminus V_c \end{cases} \quad (2)$$

Moreover, in this regime (negligible skin-depth and displacement current) the linked flux with the excitation coils approaches the linked flux for the magnetostatic problem of equation (2). Therefore, the impedance matrix approaches $j\omega \underline{\underline{L}}_{V_c}$, being $\underline{\underline{L}}_{V_c}$ the magnetostatic inductance matrix relating currents and linked fluxes in the excitation coils, $\underline{\varphi} = \underline{\underline{L}}_{V_c} \underline{i}$ where $\underline{\varphi}$ is the column vector of the linked fluxes and $\underline{i}$ is the column vector of the currents circulating in the coils. The mapping $V_c \subset \mathrm{IR}^3 \rightarrow \underline{\underline{L}}_{V_c}$ defines an operator hereafter termed Π.

III. MONOTONICITY

In this section we prove the following (monotonicity) property of the operator Π,

$$\Omega \subseteq \Xi \subset \mathrm{IR}^3 \Rightarrow \underline{\underline{L}}_{\Xi} \leq \underline{\underline{L}}_{\Omega} \quad (3)$$

where $\underline{\underline{L}}_{\Omega}$ ($\underline{\underline{L}}_{\Xi}$) is the (magnetostatic) inductance matrix following from equation (2) for V_c=Ω (V_c=Ξ) and $\underline{\underline{L}}_{\Xi} \leq \underline{\underline{L}}_{\Omega}$ means that the matrix $\underline{\underline{L}}_{\Xi} - \underline{\underline{L}}_{\Omega}$ is negative semi-definite. To prove equation (3), we first notice that the solution of equation (2) can be conveniently expressed in variational form (see [5] for instance) as,

$$\min_{\mathbf{a} \in A(V_c)} \Psi(\mathbf{a}') \quad (4)$$

where

$$\Psi(\mathbf{a}') = \frac{1}{2} \int_{\mathrm{IR}^3} \mu^{-1} |\nabla \times \mathbf{a}'|^2 \, \mathrm{d}V - \int_{\mathrm{IR}^3} \mathbf{J}_s \cdot \mathbf{a}' \, \mathrm{d}V \ , \quad (5)$$

$$A(V_c) = \left\{ \mathbf{a}' \in \mathrm{IL}^2_{\mathrm{rot}}(\mathrm{IR}^3) : \int_{V_c} |\nabla \times \mathbf{a}'|^2 \, \mathrm{d}V = 0 \right\}. \quad (6)$$

It is worth noting that if **a** is solution of equation (4), then

$$\Psi(\mathbf{a}) = -\frac{1}{2} \int_{\mathrm{IR}^3} \mu^{-1} |\nabla \times \mathbf{a}|^2 \, \mathrm{d}V \ , \quad (7)$$

and the inductance matrix $\underline{\underline{L}}_{V_c}$ can also be defined through the magnetostatic energy,

$$\frac{1}{2} \underline{i}^T \underline{\underline{L}}_{V_c} \underline{i} = \frac{1}{2} \int_{\mathrm{IR}^3} \mu^{-1} |\nabla \times \mathbf{a}|^2 \, \mathrm{d}V = -\Psi(\mathbf{a}). \quad (8)$$

The proof of equation (3) easily follows from the variational principle equation (4) and from $\Omega \subseteq \Xi \Rightarrow A(\Xi) \subseteq A(\Omega)$.

Let us assume that $\Omega \subseteq \Xi$, then $A(\Xi) \subseteq A(\Omega)$ and, therefore, from equation (4) it follows that $\Psi(\mathbf{a}_\Omega) \leq \Psi(\mathbf{a}_\Xi)$ where $\mathbf{a}_\Omega$ and $\mathbf{a}_\Xi$ are the solutions of equation (4) for V_c=Ω and V_c=Ξ, respectively. From equation (8) it follows,

$$-\frac{1}{2}\underline{i}^{T}\,\underline{\underline{L}}_{\Omega}\,\underline{i}=\Psi(\mathbf{a}_{\Omega})\le\Psi(\mathbf{a}_{\Xi})=-\frac{1}{2}\underline{i}^{T}\,\underline{\underline{L}}_{\Xi}\,\underline{i}\,, \qquad (9)$$

that, from the arbitrariness of the coils current vector $\underline{i}$, is equivalent to equation (3).

Monotonicity of equation (3) allows identifying volumetric anomalies by the fast and efficient imaging algorithm described in [1-4]. Here we sketch the main idea underlying the imaging algorithm. Let V be an unknown anomaly present in V_c and let V_k a test anomaly placed in a known position. If $V_k \subseteq V$ then $V_c \backslash V \subseteq V_c \backslash V_k$ and $\underline{\underline{L}}_{V_c\backslash V_k} \le \underline{\underline{L}}_{V_c\backslash V}$. Therefore, if $\underline{\underline{L}}_{V_c\backslash V_k} \le \underline{\underline{L}}_{V_c\backslash V}$ is false, then V_k is not contained in V. The test can be repeated for V_k taken in many different positions covering the "tentative region" where the anomaly is supposed to be present. In practice, $\underline{\underline{L}}_{V_c\backslash V}$ is a measured quantity whereas $\underline{\underline{L}}_{V_c\backslash V_k}$ is computed numerically.

IV. NUMERICAL EXAMPLES

IV.I Monotonicity: Numerical Validation

In this section we validate numerically monotonicity of equation (3) by means of simple canonical numerical examples. The test geometry consists of a conductive half-space (conductivity $5.88\cdot10^8$ S/m, copper) where several type of volumetric defects are considered. The numerical model consists of an edge-element based integral formulation where the unknown is the induced current density represented as the curl of the electric vector potential [6]. The height of the anomalies is 0.5mm, whereas their cross section is union of 0.33mm×0.33mm elements. The skin-depth can be retained negligible if significantly smaller than 0.5mm. For copper (conductivity $5.88\cdot10^8$ S/m) this is the case for frequencies greater than 172kHz (the skin-depth in copper at 172kHz is 0.05mm). It is worth noting that, in typical eddy current testing configurations, the displacement current is negligible up to few MHz, depending on the particular setting. From the numerical perspective, in these conditions, the unknown current density flows in a thin superficial layer mainly beneath the array of coils. Therefore, the finite element discretization has been limited to this superficial layer only (Fig. 2).

Figure 3 shows the different surface breaking test "anomalies" used to validate equation (3). Let V_c be the region (the half-space) occupied by the defect-free conductor and let V_1, V_2, V_3 and V_4 be the volumes occupied by the four different anomalies. To validate the monotonicity, we have carried out two different tests. In the first case we selected ordered pairs of anomalies (V_i, V_j) where the first anomaly V_i contains the second anomaly V_j (for instance, (V_1, V_2), (V_1, V_3) and (V_1, V_4)). Thus, from equation (3) we expect all eigenvalues of the difference $\underline{\underline{L}}_{V_c\backslash V_i} - \underline{\underline{L}}_{V_c\backslash V_j}$ to be positive. This is clearly the case as shown in Table 1 where is reported the sign index of $\underline{\underline{L}}_{V_c\backslash V_i} - \underline{\underline{L}}_{V_c\backslash V_j}$, defined as,

$$s\left(\underline{\underline{L}}_{V_c\backslash V_i} - \underline{\underline{L}}_{V_c\backslash V_j}\right)=\frac{\sum_k \lambda_k}{\sum_k |\lambda_k|} \qquad (10)$$

λ_k being the k-th eigenvalues of the matrix $\underline{\underline{L}}_{V_c\backslash V_i} - \underline{\underline{L}}_{V_c\backslash V_j}$, for different test cases. It is worth noting that the sign index is equal to +1 (−1) if $\underline{\underline{L}}_{V_c\backslash V_i} - \underline{\underline{L}}_{V_c\backslash V_j}$ is positive (negative) semi-definite and it assumes values in the open interval (−1, +1) when $\underline{\underline{L}}_{V_c\backslash V_i} - \underline{\underline{L}}_{V_c\backslash V_j}$ has eigenvalues with different sign.

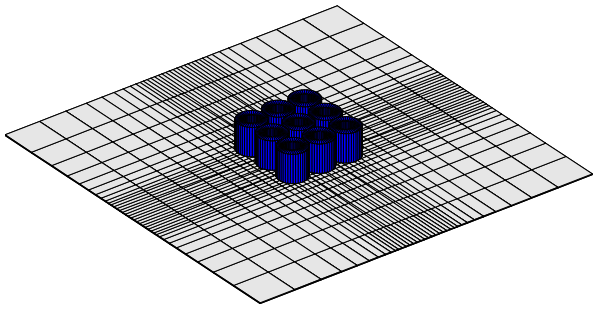

(a)

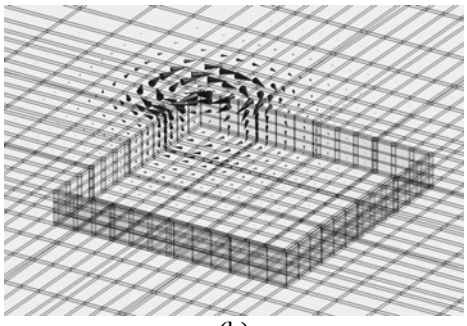

(b)

Fig. 2. (a) The finite element discretization together with the array made by 3×3 coils. The discretization is limited to a 0.05mm superficial layer. (b) The real (dominant) part of the induced eddy current density at 172kHz (skin-depth equal to 0.05mm) in the presence of a surface breaking volumetric anomaly. Only one coil is energized.

In the second test we have selected ordered pairs of anomalies (V_i, V_j) where V_i is not contained in V_j and vice versa (for instance (V_2, V_3), (V_2, V_4) and (V_3, V_4)). In this case (see Table 1) we are no longer guaranteed that

$\underline{\underline{L}}_{V_c \setminus V_i} - \underline{\underline{L}}_{V_c \setminus V_j}$ must be either a positive or negative semi-definite matrix.

Table 1. Sign index for different configurations. The element *ij* is the sign index for matrix $\underline{\underline{L}}_{V_c \setminus V_i} - \underline{\underline{L}}_{V_c \setminus V_j}$

	V_1	V_2	V_3	V_4
V_1	-	1	1	1
V_2	-1	-	0.861	0.879
V_3	-1	-0.861	-	0.426
V_4	-1	-0.879	-0.426	-

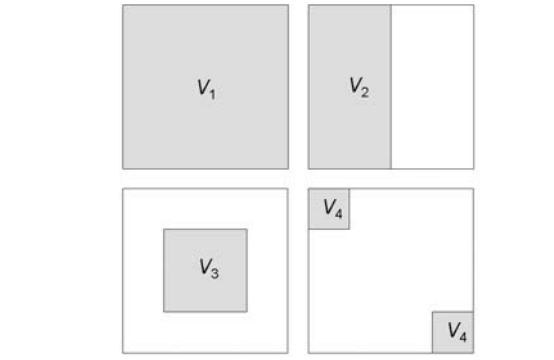

(a)

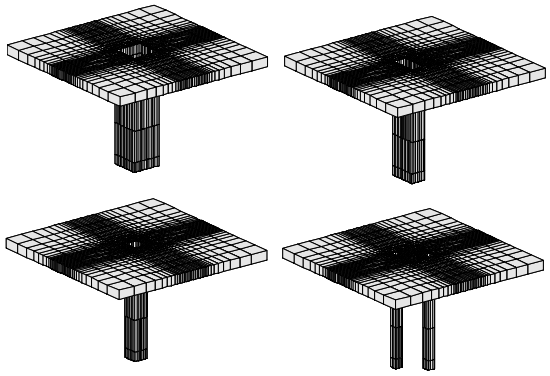

(b)

Fig. 3. (a) 2D (top) view of four different test anomalies having the same depth. (b) The corresponding 3D view (not in scale) consisting of only a thin superficial layer at the air-conductor interface (thickness 0.05mm right beneath the array of coils).

IV.II Monotonicity: Imaging Method

Here we apply the monotonicity to solve the inverse problem. The test configuration is similar to the one described in section 4.1. The region of interest is 36mm×36mm and it is subdivided into a 72×72 regular grid of test anomalies. From the computational viewpoint, each test anomaly is discretized using 2×2 elements in the transverse direction (see Fig. 4).

The probe is an array made by 23 coils arranged in the closest packed array configuration (see Fig. 4). Each coil has the inner radius of 0.3 mm, the outer radius of 0.6mm and the height of 6mm. The lift-off between the specimen and the probe is 2mm. In this test example we assume that each coil is made by one turn. The results can be easily scaled in case of coils made by an arbitrary number of turns.

To evaluate the visible region, i.e. the area "illuminated" by the probe, we computed the spatial distribution of the norm of $\underline{\underline{L}}_{V_c \setminus V_j} - \underline{\underline{L}}_{V_c}$ where the subscript *j* refers to the j^{th} test anomaly. Higher values of this norm are related to the visible region. From Fig. 4, it results that the visible region is made by 12×12 test anomalies, corresponding to a 6mm×6mm area. It is worth noting that the spatial map of the norm of $\underline{\underline{L}}_{V_c \setminus V_j} - \underline{\underline{L}}_{V_c}$ can be related to the order of magnitude of the maximum amount of measurement noise that does not "destroy" the reconstruction.

Since the scanned area (36mm×36mm) is larger than the visible region, the probe is placed at different locations. Specifically, the probe is moved onto a regular 8×8 grid corresponding to the intersections of the orthogonal lines in Fig. 5. The orthogonal lines subdivide the scanned area in 9×9 blocks; each block consists of 8×8 pixels (test anomalies). For a given pixel *j* (test anomaly *j*) in a block *B*, we compute the sign index,

$$s\left(\underline{\underline{L}}^{k}_{Meas} - \underline{\underline{L}}^{k}_{V_c \setminus V_j}\right) \tag{11}$$

related to the measurements when the probe is placed at the four corner of the block (k=1,..,4). In equation (11) $\underline{\underline{L}}^{k}_{Meas}$ and $\underline{\underline{L}}^{k}_{V_c \setminus V_j}$ are the (noisy) measured inductance matrix and the numerically computed inductance matrix related to pixel *j*, respectively (in both cases the probe is located in the k^{th} corner of the block *B*). Then, we associate to pixel *j* the quantity s_j that is the maximum of the four sign indices arising from the corners of block *B*.

In the absence of noise, when V_j is contained in the unknown anomaly *V*, we have s_j =1, as discussed in Sections 3 and 4.1 (lower values are obtained in the presence of noise). Finally, we compute the map $\hat{s}_j = 1/\left(1 - s_j\right)$. This last map provides a qualitative image of the defects (see Fig. 5) [1]. To obtain a quantitative reconstruction, we apply a threshold to the spatial map $\hat{s}_j$ (see Fig. 6). We found numerically that proper threshold values are those related to large gaps or local minima of the histogram of the values assumed by $\hat{s}_j$.

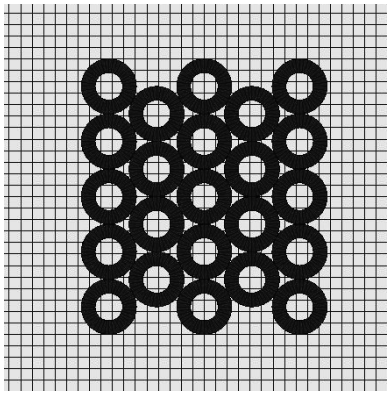

(a)

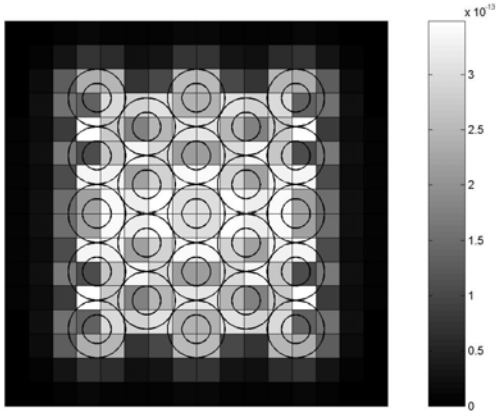

(b)

Fig. 4. (a) The array (view from the top) with a portion of the finite element mesh used during the computations. Each element has a transverse dimension of 0.25mm and each test anomaly consists of 2×2 elements in the transverse direction. (b) The array together with the spatial distribution of the norm of $\underline{\underline{L}}_{V_c \setminus V_j} - \underline{\underline{L}}_{V_c}$. The visible region is made by 12×12 pixels.

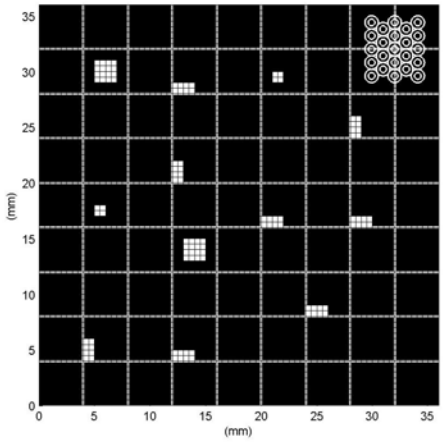

(a)

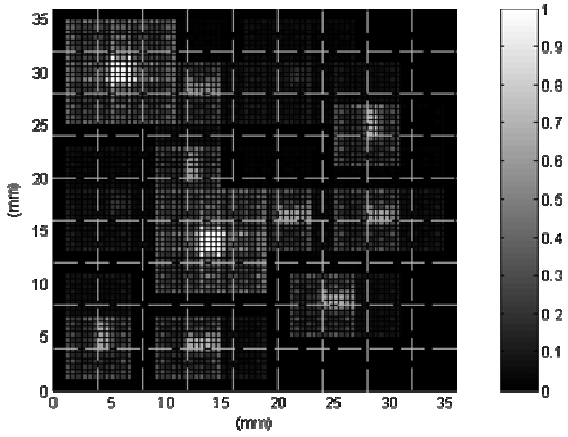

(b)

Fig. 5. (a) The distribution of the anomalies (white) together with the array and the grid use to place the array in different positions. (b) The (normalized) spatial maps of the $\hat{s}_j$'s.

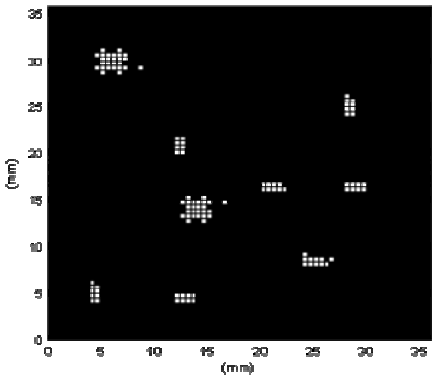

(a)

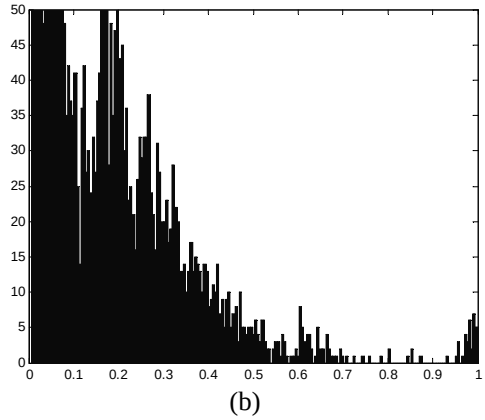

(b)

Fig. 6. (a) : the reconstructed map of anomalies obtained by applying a threshold of 0.54 to the spatial distribution of the $\hat{s}_j$'s. (b) : the histogram of the spatial distribution of the $\hat{s}_j$'s.

Finally, we mention that the measurements (matrices $\underline{\underline{L}}^k_{Meas}$) have been numerically computed and corrupted with an additive noise uniformly distributed in the range $(-\varepsilon,\varepsilon)$ where ε is 11% of the minimum norm of $\underline{\underline{L}}_{V_c \setminus V_j} - \underline{\underline{L}}_{V_c}$ in the visible region.

IV.III Noise and Resolution

Although this is beyond the scope of this work, in this subsection we present some considerations about noise and resolution in the framework of the proposed imaging method. The starting point is given by the following decomposition (see [3] for low frequency ECT) of $\underline{\underline{L}}^k_{Meas} - \underline{\underline{L}}^k_{V_c \setminus V_j}$,

$$\underline{\underline{L}}^k_{Meas} - \underline{\underline{L}}^k_{V_c \setminus V_j} = \left(\underline{\underline{L}}^k_{V_c \setminus \Omega} - \underline{\underline{L}}^k_{V_c}\right) + \left(\underline{\underline{L}}^k_{V_c} - \underline{\underline{L}}^k_{V_c \setminus V_j}\right) + \underline{\underline{N}}^k \quad (12)$$

where we have exploited that $\underline{\underline{L}}^k_{Meas} = \underline{\underline{L}}^k_{V_c \setminus \Omega} + \underline{\underline{N}}^k$, where Ω is the unknown anomaly, $\underline{\underline{L}}^k_{V_c \setminus \Omega}$ is the noise-free data and $\underline{\underline{N}}^k$ is the noise term. The amount of noise limits from below the minimum size of the V_j's, i.e. the resolution. Indeed, from equation (12) it follows that $\left\| \underline{\underline{L}}^k_{V_c} - \underline{\underline{L}}^k_{V_c \setminus V_j} \right\| \geq \alpha \left\| \underline{\underline{N}}^k \right\|$, where α is of the order of unity, is a necessary condition otherwise the noise term destroies the information content depending on V_j. Since the norm of $\underline{\underline{L}}^k_{V_c} - \underline{\underline{L}}^k_{V_c \setminus V_j}$ decreases as the size of V_j decreases, it is clear that the noise sets a limit to the achievable resolution or, vice versa, for a given resolution the maxim amount of noise compatible with the method is limited. Another limit to the resolution is set by the sensitivity of the instruments, specifically, $\left\| \underline{\underline{L}}^k_{V_c} - \underline{\underline{L}}^k_{V_c \setminus V_j} \right\| \geq \beta \left\| \underline{\underline{L}}^k_{V_c} \right\|$ where β is a dimensionless constant, significantly smaller than the unity, and representing the sensitivity of the measurement apparatus.

Figure 7 shows the behavior of $f = \max_k \left\| \underline{\underline{L}}^k_{V_c} - \underline{\underline{L}}^k_{V_c \setminus V_j} \right\|$ and $g = \max_k \left\| \underline{\underline{L}}^k_{V_c} - \underline{\underline{L}}^k_{V_c \setminus V_j} \right\| \Big/ \left\| \underline{\underline{L}}^k_{V_c} \right\|$ as a function of the of the ratio γ between the external radius of a coil and the diagonal of the voxel V_j. For the sake of simplicity the array is made by three coils (fig. 7(a)) and each coil consists of one single turn. The array is moved onto a regular 5×5 Cartesian grid with step-size of 0.5mm; the maximum in f and g is taken over these 25 different positions. It is interesting to see that increasing γ the function f decreases, i.e. the sensitivity with respect to the background measurement decreases. In other words, it increases the difficulty in appreciating the variations of the inductance matrix due to the test anomaly. We also notice that g presents a maximum for a proper value of γ. This means that for a given coil size, there is a proper value for the size of the voxel V_j that maximizes the immunity to the noise.

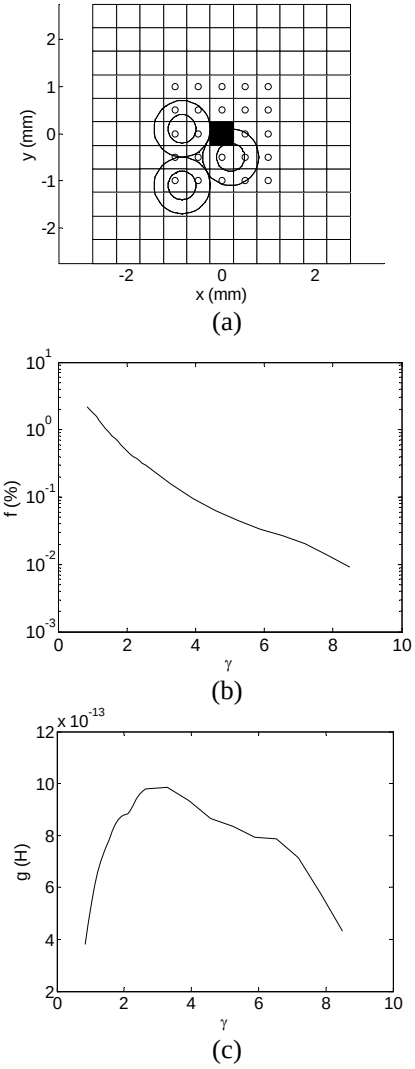

Fig. 7. (a) The voxel V_j (black pixel) together with the three coils probe of a given size, and the positions (o) where the probe is moved. (b) Plot of $f(\gamma)$. (c) Plot of $g(\gamma)$ assuming that the each coil has one single turn. γ is the ratio between the external radius of a coil and the diagonal of the voxel V_j.

V. CONCLUSIONS

The main contribution of this paper is the development of a fast imaging method based on the monotonicity property of the operator Π mapping the defects geometry into the inductance matrix measured at high enough frequencies. In this regime (negligible skin-depth and displacement current) the problem can be modeled as a magnetostatic one and this, thanks to the elliptic nature of magnetostatic, allows proving the monotonicity. Numerical examples confirm this property and, moreover, prove the effectiveness of the related fast imaging algorithm.

ACKNOWLEDGEMENTS

This work is supported in part by the Italian Ministry of University (MIUR) under a Program for the Development of Research of National Interest (PRIN grant # 2004095237) and by the CREATE Consortium.

REFERENCES

[1] A. Tamburrino and G. Rubinacci, "Fast methods for quantitative Eddy-current tomography of conductive materials," *IEEE Transactions on Magnetics*, MAG-42, no. 8, pp. 2017–2028, 2006.

[2] A. Tamburrino and G. Rubinacci, "A new non-iterative inversion method for electrical resistance tomography," *J. of Inverse and Ill-posed Problems*, vol. 18, pp. 1809-1829, December 2002.

[3] G. Rubinacci, A. Tamburrino, and S. Ventre, "Numerical optimization and regularization of a fast eddy current imaging method," *IEEE Transactions on Magnetics*, vol. 42, no. 4, pp. 1179-1182, 2006.

[4] A. Tamburrino, "Monotonicity based imaging methods for elliptic and parabolic inverse problems," *J. of Inverse and Ill-posed Problems*, vol. 14, no. 6, pp. 633-642, September 2006.

[5] A. Bossavit, *Computational Electromagnetism, Variational Formulations, Edge Elements, Complementarity*, Boston, MA: Academic Press, 1998.

[6] R. Albanese and G. Rubinacci, *Finite Element Methods for the Solution of 3D Eddy Current Problems, Advances in Imaging and Electron Physics*, edited by Peter W. Hawkes, vol. 102, pp. 1-86, Academic Press, 1998.

Guglielmo Rubinacci received the Laurea degree (*summa cum laude*) in Electronic Engineering from the University of Naples "Federico II," Naples, Italy, in 1975. Currently, he is a Full Professor of fundamentals in electrical engineering at the University of Naples "Federico II." He was the Dean of the Faculty of Engineering of the University of Cassino from 1996 to 2003. As a Fulbright-Hays Fellow he was a Visiting Scientist at MIT in 1980/81. He also engaged in research, in particular, at the Max Planck Institut fur Plasmaphysik, Garching and the Istituto Gas Ionizzati, CNR, Padova. He has been a Researcher at the Università di Napoli (1982/85), Professor in Charge and Associate Professor of electrical engineering at the Universities of Calabria (1979–84), Salerno (1984/88) and Napoli (1988/90), and Full Professor at the University of Cassino (1990–2004). He is the author/coauthor of more than 100 papers in refereed scientific journals and books and coeditor of two volumes. His research interests are mainly in computational electromagnetics with applications in several fields such as plasma engineering in tokamaks and electromagnetic nondestructive evaluation.

Antonello Tamburrino (M'97) received the Laurea degree (*summa cum laude*) in electronic engineering from the University of Naples "Federico II", Naples, Italy, in 1992, and the Ph.D. degree in electronic engineering from the Polytechnic of Turin, Turin, Italy, in 1996. Since December 2006, he is full professor of Electrotechnics at the College of Engineering, University of Cassino, Italy, where he is also the Head of the Laboratory of Computational Electromagnetism and Electromagnetic Nondestructive Evaluation. He has been Research Scientist (1994-2001) and Associate Professor (2001-2006) at the same university. From 2000 to 2002, he was a Visiting Scientist at Iowa State University, Ames. In 2002, he joined Michigan State University, East Lansing, where, since 2003, he has been an Adjunct Professor in the Department of Electrical and Computer Engineering. His research interests are mainly in the field of computational electromagnetics, with particular reference to electromagnetic non-destructive evaluation, inverse problems and integral methods. He is the coauthor of about 70 papers published in refereed scientific journals and books, among which several were invited papers. Dr. Tamburrino is member of the International Standing Committee of the Electromagnetic Nondestructive Evaluation Workshop, member of the Editorial Board of several international conferences and Reviewer for several journals.

Salvatore Ventre received in 1990 the Laurea Degree (*summa cum laude*) in Electrical Engineering from the University of Naples "Federico II", Italy. From 1993 he is at the Faculty of Engineering of the University of Cassino, Italy, where he is currently a Research Scientist. His research interests are mainly in computational electromagnetic with application in several fields such as electromagnetic nondestructive evaluation, electromagnetic compatibility, analysis of the time evolution of MHD equilibria, for the identification of the plasma boundary in tokamaks. He is author/coauthor of more than 30 technical papers on international journals and conference proceedings.

Design and Analysis of Partitioned Square Loop Antennas

[1]R. Hasse, [2]V. Demir, [1]W. Hunsicker, [1]D. Kajfez, and [1]A. Elsherbeni

[1] Department of Electrical Engineering
The University of Mississippi, University, MS 38677, USA
rhasse@olemiss.edu, wfhunsic@olemiss.edu, eedarko@olemiss.edu, atef@olemiss.edu

[2] Department of Electrical Engineering
Northern Illinois University, DeKalb, IL 60115, USA
demir@ceet.niu.edu

Abstract **–** A novel antenna design is presented for operation at 5.8 GHz with omni-directional pattern characteristics. The antenna employs square loop geometry of one wavelength perimeter. The loop is partitioned with capacitive elements in order to minimize phase variations in the current flow and thereby enhance the radiation efficiency. Five capacitive elements are used to achieve optimal loop current flow, resulting in phase variations smaller than ± 6°. The performance of the antenna is first analyzed with a thin-wire antenna using method of moments (MoM) solver and later validated using a custom finite difference time domain (FDTD) package. The calculated radiation pattern in the plane of the loop is close to omni-directional with directive gain of 1.5 dBi. A printed circuit antenna is manufactured with alternating top- and bottom-layer conductors, with the overlapped regions acting as physical capacitors. The measured radiation patterns of the printed antenna confirm the predicted omni-directional behavior in the equatorial plane, while the input impedance demonstrates a close match to 50 Ω. The mean value of the gain is 2.15 dB at 5.869 GHz. A second printed antenna, having top-layer conductors only and gap capacitors, is simulated using finite element (FEM) software, and the performance is nearly omni-directional with a directive gain of 1.66 dBi. Both designs are very sensitive to the dimensions of the physical capacitors and require a highly accurate method of fabrication.

Keywords: Loop antenna, partitioned, and omni-directional.

I. INTRODUCTION

The loop antenna has proven to be one of the most practical and adaptable types of antennas [1], with circular and rectangular geometries representing the most popular configurations. This popularity stems primarily from their inherent low cost, simplicity of fabrication, and ease of implementation as front-end elements in RF and communication systems. However, their performance in comparison with other antenna designs is limited with respect to gain, bandwidth, and directionality of radiation. For example, when the perimeter of the loop antenna is small with respect to wavelength, its radiation impedance is extremely small and thus inconvenient for matching to a 50 Ω transmission line. Conversely, when the loop perimeter is of the order of one wavelength or larger, the current flowing in the loop exhibits large phase variations that ultimately degrade the radiation efficiency [2]. This results in a poor radiator and a shift of the radiation pattern maximum from in the plane of the loop to a plane normal to the loop, which may not be desirable for the intended application.

It is possible to minimize the phase variation of the loop current by partitioning the loop into several sections that are small in comparison to wavelength, and then inserting lumped capacitive elements in a series configuration [3, 4]. The resulting antenna structure is simple and can be investigated using a thin-wire model radiating into free space. The physical dimensions are then converted to an equivalent printed model with overlapping conductors on a low-loss dielectric substrate. A second printed loop antenna is designed using top-layer conductors only with gap capacitors. The procedure used to design both the wire and printed antennas is discussed, while simulation results using custom finite difference time domain (FDTD) software and a commercial finite element (FEM) package are presented which validate the final printed designs. Measurements of the return loss and radiation patterns for the overlapped design are also presented to compare the performance of this partitioned loop antenna with the simulation results.

II. WIRE ANTENNA MODEL

A thin-wire square loop antenna of radius a = 0.5 mm and side $s = \lambda/4$ was designed and simulated using the commercial software package entitled Analysis of Wire Antennas and Scatterers (AWAS) [5]. The loop

antenna was centered in the *xy* plane at $z = 0$ and modeled with copper wire segments ($\sigma = 5.81\times10^7$ S/m). A total of 6 wire segments comprise the antenna geometry, as shown in Fig. 1. Since the aspect ratio $s/a \cong 26$ (relatively thick antenna), three polynomial coefficients per λ were used to model the current and charge distributions along segments 1, 3, 4, and 6, respectively, while five coefficients were used for segments 2 and 5 in the numerical solution of the two-potential equation [6].

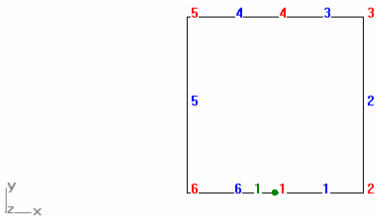

Fig. 1. Thin-wire model for partitioned loop antenna with source, nodes and wire segments indicated.

An ideal voltage generator of 1.0 V was fixed between segments 1 and 6 (node 1) with a port impedance of 50 Ω. Concentrated capacitive loadings were positioned at the four corners and between segments 3 and 4 (node 4) directly opposite to the source. Five capacitive elements ranging in value from 0.046-0.069 pF were used to minimize the current phase variations.
The antenna was simulated in transmission mode in free space from 1 GHz to 10 GHz using a total of 450 points, and optimization of the capacitor values yielded an input impedance of $50.64 - j\ 1.96$ Ω, a corresponding input admittance of $19.72 + j\ 0.0076$ mS, and a return loss of -34 dB at 5.8 GHz, as shown in Fig. 2. The simulated current magnitude and phase variations on each wire

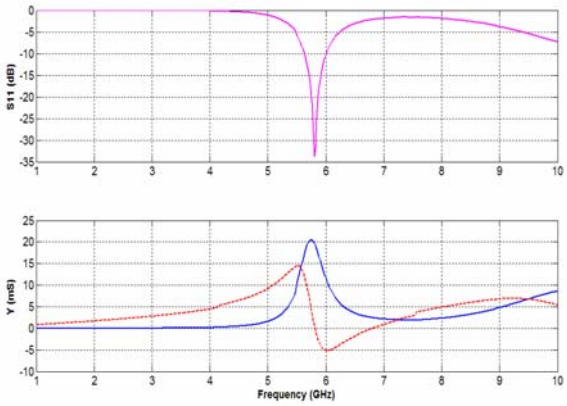

Fig. 2. Return loss and input admittance for wire partitioned loop antenna at 5.8 GHz.

segment of the antenna with lumped capacitors are plotted in Fig. 3, with phase variations on the order of ± 6°, indicating good stability of the current phase over the entire loop length. For comparison, the current magnitude and phase on each wire segment of the loop antenna without lumped capacitors is shown in Fig. 4, where the current phase varies approximately 180°.

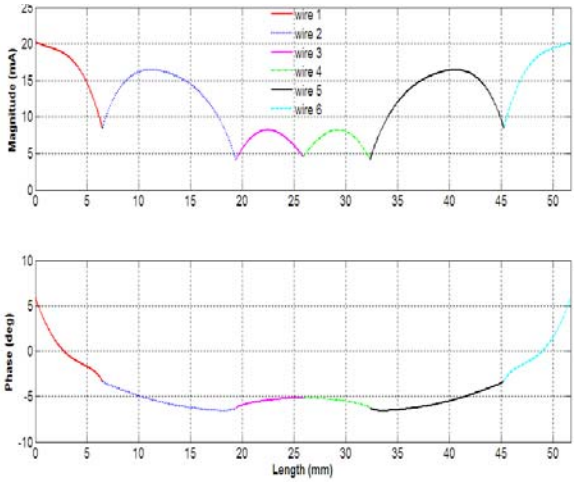

Fig. 3. Current magnitude and phase for thin-wire loop antenna with lumped capacitors at 5.8 GHz.

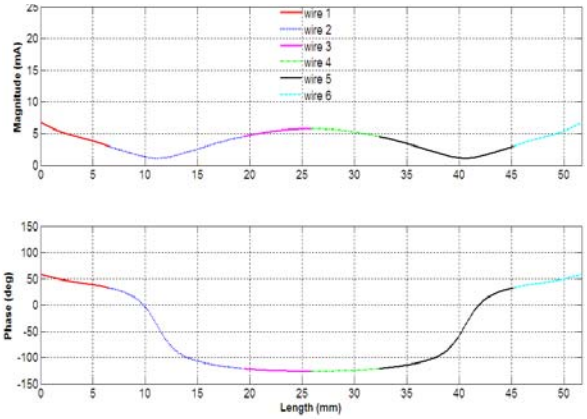

Fig. 4. Current magnitude and phase for thin-wire loop antenna without lumped capacitors at 5.8 GHz.

The simulated E_ϕ component of the far-field, in three principle planes, is shown in Fig. 5. The radiation pattern is omni-directional to within 0.5 dB in the loop antenna plane. The cross-polarization components are negligible due to the symmetry of the loop and therefore are not visible on the patterns in Fig. 5. The far-field directive gain is equivalent to 1.5 dBi.

III. OVERLAPPED PRINTED LOOP ANTENNA MODEL

A printed square loop antenna, as illustrated in Fig. 6, was designed by converting the loop wire conductors using a cylinder-to-ribbon current equivalence approximation $w \cong 2d$ [7], to a strip width of 2.0 mm. The antenna is realized on a substrate with alternating top and bottom layer conductors using Rogers RT/Duroid 5880

with $\varepsilon_r = 2.2$, substrate height h = 0.787 mm (31 mil), tan $\delta = 0.0004$, and conductor thickness t = 0.035 mm. The capacitances are realized by overlapping the end sections of strips on opposite sides of the substrate. The areas of overlap for the five physical capacitors were computed as,

$$A = \frac{h\,C}{\varepsilon_0\ \varepsilon_r} \qquad (1)$$

where A is the required overlapped area, h is the substrate height, and C is the required capacitance. The corresponding areas are 1.84 μm^2 (0.046 pF), 2.63 μm^2 (0.065 pF), and 2.80 μm^2 (0.069 pF), respectively.

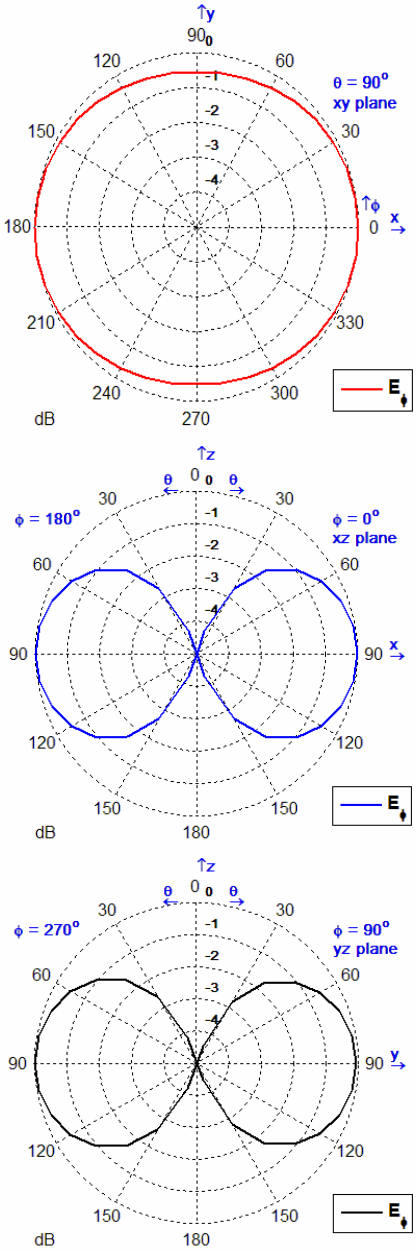

Fig. 5. Simulated far-field radiation patterns for thin-wire partitioned loop antenna at 5.8 GHz.

Figure 7 (a) shows the dimensions of a partitioned loop antenna with a feeding line in which the overlapping areas of strips are approximated to these calculated values. Simulation of this antenna using a custom 3-D FDTD solver verified that it operates at 5.8 GHz. The antenna has been fabricated using a LPKF ProtoMat C100/HF milling machine, and the return loss was measured using an Agilent Technologies model E8363B PNA network analyzer with 801 frequency points. The measurement shows that the antenna operates at a center frequency of 6.02 GHz with –19.6 dB return loss.

This result demonstrates that the center frequency has shifted from the desired value of 5.8 GHz. During fabrication the milling tool removed part of the substrate while rubbing out the extraneous copper, resulting in a substrate thickness of 0.55 mm (except for regions covered by copper), which is less than the nominal 0.787 mm. Such a change in substrate thickness likely altered the physical capacitors and their associated fringing fields. Additional FDTD simulations including the actual substrate thickness after fabrication demonstrated that this thinning effect increases the frequency. Thus the exact values of the individual capacitances proved to be very critical in achieving the desired center frequency, and the printed loop antenna dimensions had to be modified slightly in order to lower the center frequency of operation.

The modified dimensions are illustrated in Fig. 7 (b) and include increasing the area of overlap for the physical capacitor opposite to the source, as well as for the capacitors in the upper left- and right-hand corners of the loop layout. A new antenna was then fabricated using these modified dimensions. Figure 8 shows the back and front views of this antenna. The return loss measurement is compared to the FDTD simulated results as shown in Fig. 9. The fabricated antenna resonates at 5.869 GHz with a bandwidth of 6%, while the simulated curve shows a peak return loss at 5.78 GHz. The substrate of this new antenna is measured to be 0.5 mm and is thinner than the simulated thickness, and this produces the discrepancy between the simulated and measured results, but the measurement still shows good performance at 5.8 GHz (-18 dB).

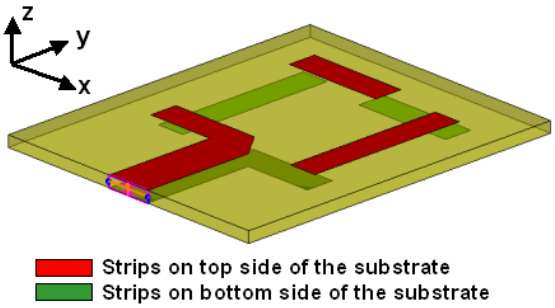

Fig. 6. Schematic of the overlap printed partitioned loop antenna on a substrate material.

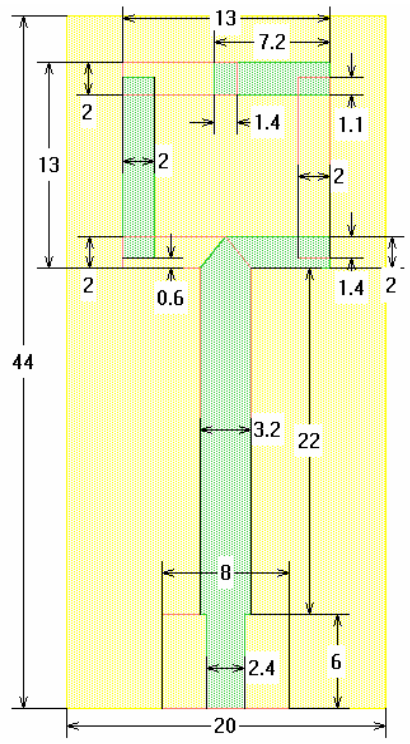

(a)

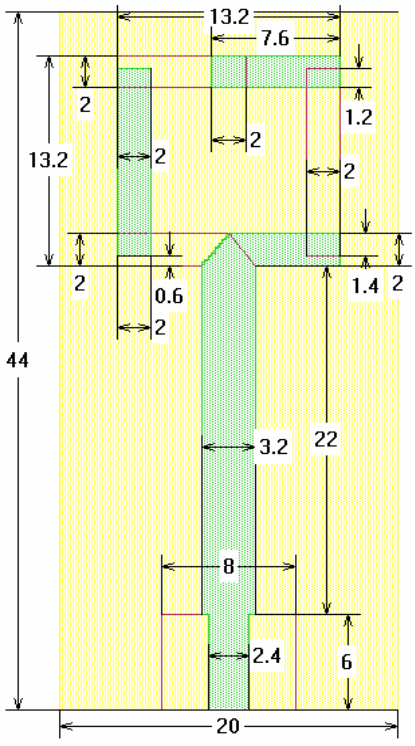

(b)

Fig. 7. (a) Initial design dimensions of the overlap partitioned loop antenna in mm. (b) Modified design dimensions of the overlap partitioned loop antenna in mm.

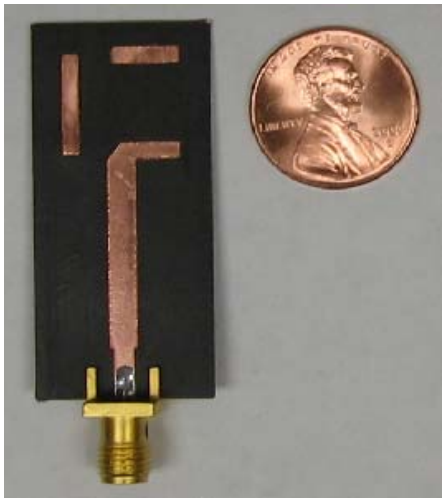

(a)

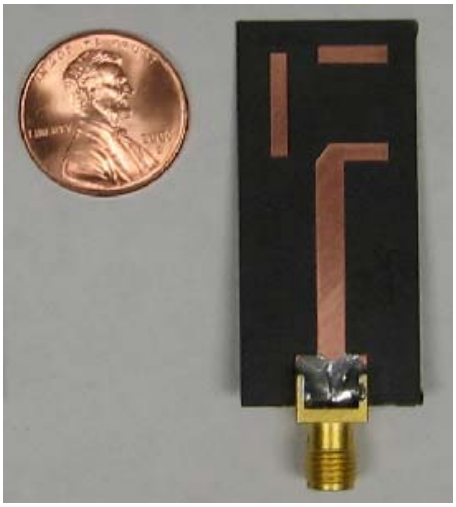

(b)

Fig. 8. Overlap partitioned loop antenna: a) front view and b) back view.

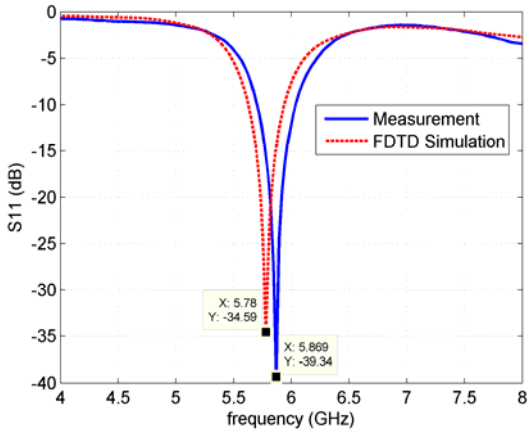

Fig. 9. Measured and simulated return losses for overlap partitioned loop antenna.

Radiation patterns of the fabricated antenna were measured inside a rectangular anechoic chamber using a ETS-Lindgren model 3117 double-ridged waveguide horn (1-18 GHz) as the excitation source, with a source-to-receiver distance of 3.65 m. An automated measurement system, comprised of an HP 8350B sweep oscillator, HP8514B S-parameter test set, HP8530A microwave receiver, and motorized rotator, was calibrated at 5.869 GHz using a Narda model 642 (5.4-8.20 GHz) standard gain horn (SGH) [8].

Simulated directivity patterns calculated by FDTD in three principal planes at 5.8 GHz are shown in Fig. 10, while Fig. 11 shows the corresponding radiation patterns measured at 5.869 GHz for comparison. Good agreement is observed between the simulated and measured patterns. Radiation is omni-directional in the *xy* plane with ϕ-polarization. The slightly higher cross-polarization levels (E_ϕ) seen in each plane in Fig. 11, as compared to the simulation results, are likely caused by the presence of surface currents on the receiver cable in the anechoic chamber due to the absence of a balun transformer in the antenna feed path during measurement.

The gain comparison method was used to measure the absolute gain of the printed loop antenna using the relation [2],

$$(G_T)_{dB} = (G_S)_{dB} + 10\log_{10}\left(\frac{P_T}{P_S}\right) \qquad (2)$$

where G_S = 15.42 dB at 5.869 GHz for the SGH. As seen in Fig. 11, the gain of the loop antenna in the *xy* plane is not uniform, with a maximum of 4.64 dB (135°), a minimum of -1.27 dB (45°), and a mean value of 2.15 dB, which is in good agreement with the directivity simulation. By improving the accuracy of fabrication using high resolution techniques, such as chemical etching or laser milling, it is possible that a more uniform radiation pattern in the plane of the loop antenna would result. More importantly, the overlap design represents a natural implementation of physical capacitors in the partitioned antenna structure without the need for incorporating SMT chip capacitors, which will add additional costs into the manufacturing process.

IV. TOP LAYER PRINTED LOOP ANTENNA MODEL

A second printed square loop antenna was designed with top layer conductors only in order to minimize engineering design and fabrication costs, and this partitioned structure is realized by using straight-edge gap capacitances at the same strategic locations as for the overlap printed loop antenna, as shown in Fig. 12. A fully parameterized model was developed using the High Frequency Structure Simulator (HFSS) [9] software package in order to independently vary the gap widths for the capacitors, conductor widths, and loop size. A feed port with nominal impedance of 50 Ω excited the antenna across a source feed gap of 3.0 mm using an interpolating frequency sweep from 4 GHz to 8 GHz with 12 adaptive passes and a delta S convergence level of 0.005 to ensure accurate meshing of the minute gap capacitances.

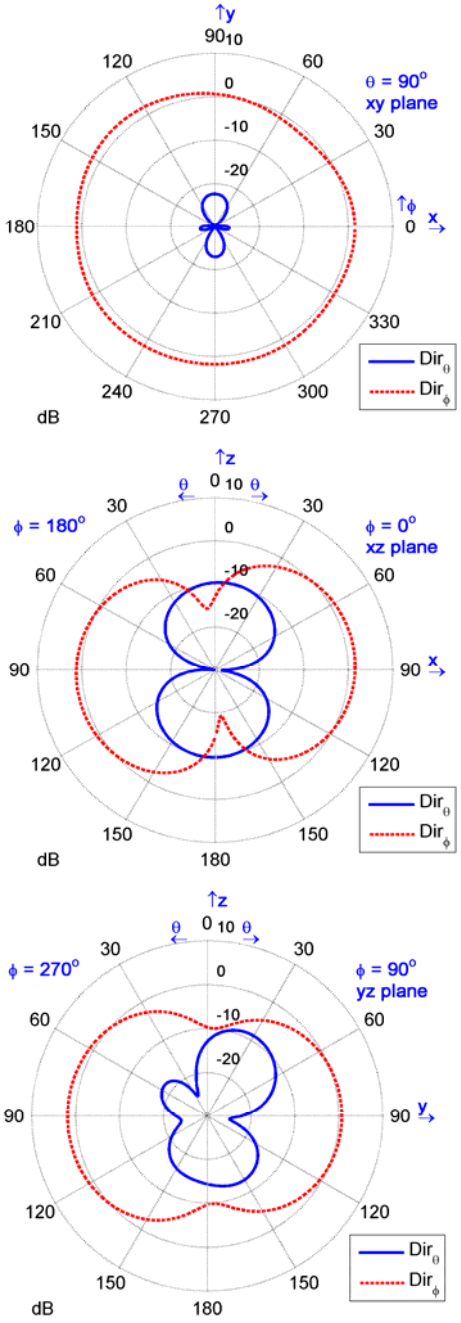

Fig. 10. Simulated directivity patterns for overlap printed loop antenna at 5.8 GHz (FDTD).

A perfectly matched layer acting as the absorbing boundary was applied to the outer faces of the solution space in order to create an open model. The simulated

gap widths for the capacitors were optimized to the values of 0.10 mm (top corners), 0.13 mm (bottom corners), and 0.11 mm (opposite the source). The simulated electric surface current distribution at 5.8 GHz is shown in Fig. 13, where the highest currents are found near the lumped source and along the inner edges of the conductors. It was necessary to increase the side length *s* to 15 mm for this design in order to achieve good radiation resistance, with a return loss of -21.5 dB at the meshed solution frequency of 5.8 GHz (see Fig. 14).

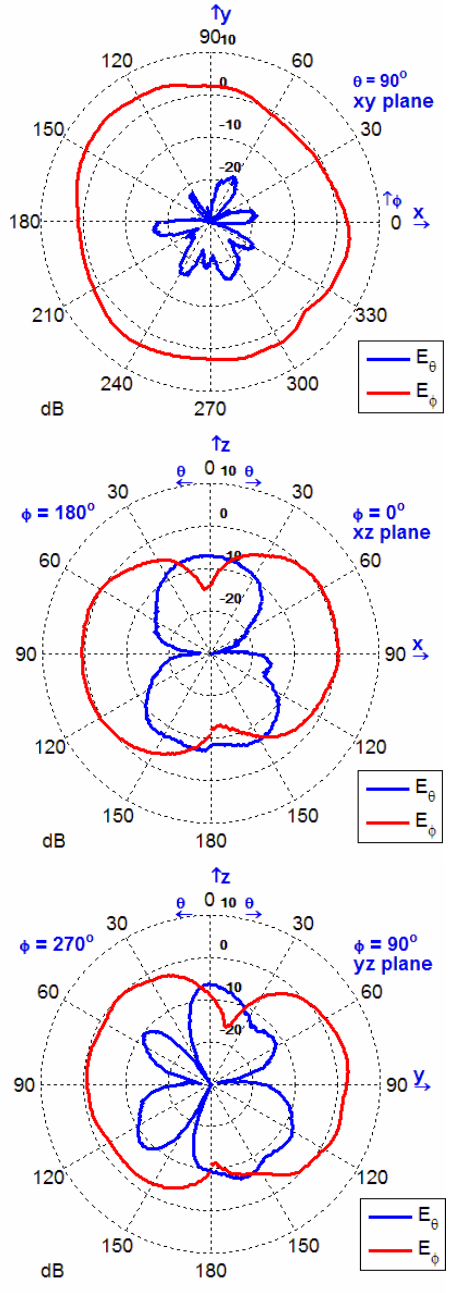

Fig. 11. Measured radiation patterns for overlap printed loop antenna at 5.869 GHz.

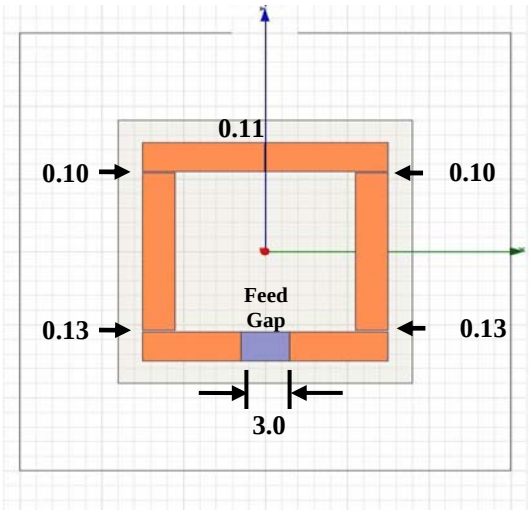

Fig. 12. Schematic of top layer printed loop antenna with gap capacitor dimensions in mm.

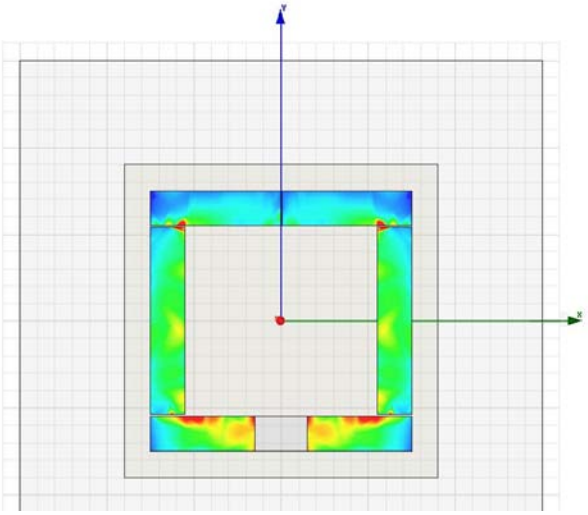

Fig. 13. Simulated electric surface currents for top layer printed loop antenna at 5.8 GHz (HFSS).

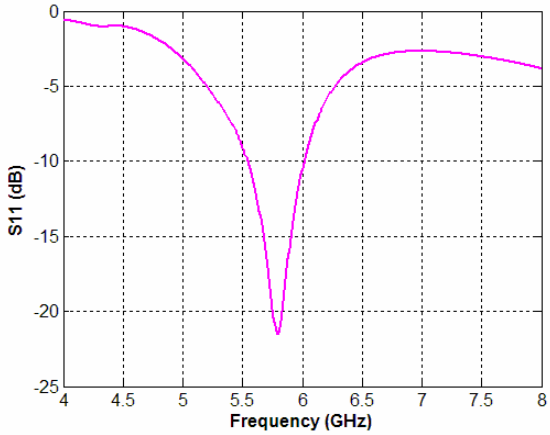

Fig. 14. Simulated return loss for top layer printed loop antenna using HFSS.

The calculated directive gain is 1.66 dBi with a radiation efficiency of 0.989 and corresponding bandwidth of 8 %. The calculated co-polarized and cross-polarized far-field radiation patterns in three principal planes are shown in Fig. 15, with nearly omni-directional radiation in the loop antenna plane as desired. For this design the electric field lines in the capacitive regions extend primarily into the air dielectric, as there is little confinement of the electric field in the substrate dielectric without the presence of conductors on the bottom layer, and the sensitivity of the gap capacitors to environmental factors is thereby increased.

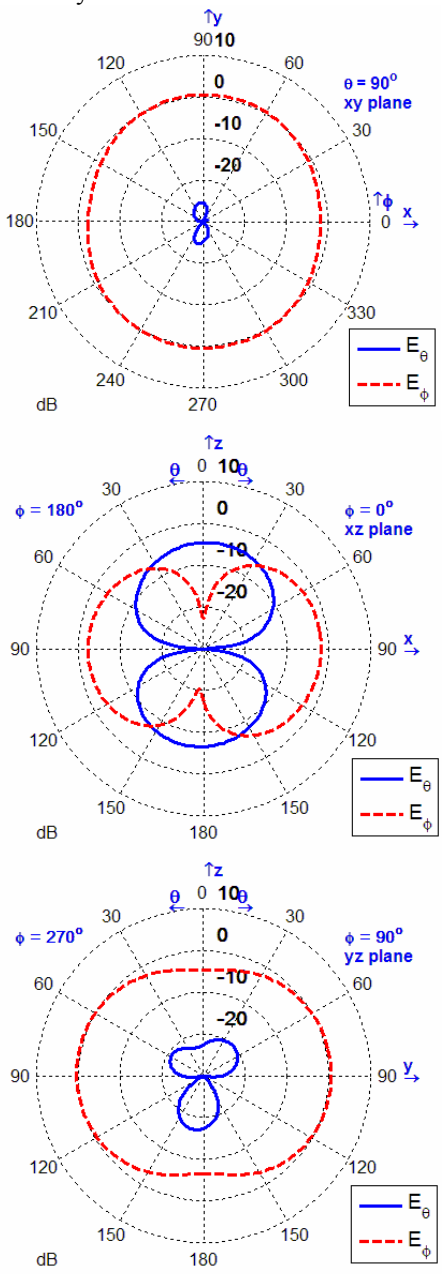

Fig. 15. Simulated far-field radiation patterns for top layer printed loop antenna at 5.8 GHz (HFSS).

Several attempts were made at fabricating the top-layer design using the LPKF milling machine with a 0.1 mm universal cutting tool, but visual inspection of the cuts using an optical eye piece revealed that the accuracy of the milled gap dimensions was poor and non-reproducible. Alternative fabrication processes (e.g. chemical etching) are currently being explored in order to minimize the design sensitivity to fabrication tolerances. Note that the source gap dimension of 3.0 mm is intended to excite the antenna with a balun transformer. A sample of a commercial balun transformer at 5.8 GHz was obtained from a preferred manufacturer, however, the device dimensions are sub-miniature and not practical for use with this antenna, therefore, a custom split tube balun transformer of diameter 3.5 mm and length $\lambda_g = 35$ mm is currently being fabricated with symmetrical slot lengths of $\lambda_g/4 = 8.75$ mm, in order to balance any surface currents and achieve a good match to the input impedance of the antenna.

V. CONCLUSIONS

A novel loop antenna design is presented which utilizes capacitive elements at strategic locations in order to minimize phase variations in the current flow and thereby enhance the radiation efficiency. Initial design parameters are obtained using AWAS, a thin-wire antenna MoM solver, and then an overlap partitioned loop antenna is designed on a planar substrate and optimized using a custom FDTD solver. The design is fabricated and return loss and radiation pattern measurements are performed. The radiation pattern measurements reveal that the antenna provides the desired omni-directional radiation characteristics, with an input impedance close to 50 Ω and a mean value for the gain of 2.15 dB at 5.869 GHz. A second printed loop antenna is also designed with top layer conductors and straight-edge gap capacitors and optimized for performance at 5.8 GHz using HFSS. The simulated radiation pattern is nearly omni-directional in the antenna plane. The return loss simulation yields a result of -21.5 dB at a center frequency of 5.8 GHz. Attempts at fabricating this antenna demonstrated that it is extremely sensitive to fabrication imperfections, and alternative fabrication processes such as chemical etching or laser milling are currently being explored in order to minimize the sensitivity of both printed designs to fabrication tolerances.

REFERENCES

[1] G. S. Smith, “Loop antennas,” in *Antenna Engineering Handbook*, Third Edition, Chapter 5, McGraw-Hill, Inc., New York, 1993.

[2] C. A. Balanis, *Antenna Theory: Analysis and Design*, Second Edition, Chapter 5, John Wiley & Sons, Inc., New York, 1982.
[3] V. Demir, R. Hasse, D. Kajfez, and A. Z. Elsherbeni, "Partitioned square loop antenna," *The 23rd Annual Review of Progress in Applied Computational Electromagnetics Society, ACES'07*, Verona, Italy, March 2007.
[4] D. M. Dobkin, S. M. Weigand, and N. Iyer, "Segmented magnetic antennas for near-field UHF RFID," *Microwave Journal*, pp. 96-102, June 2007.
[5] A. R. Djordjević, M. B. Dragović, V. V. Petrović, D. I. Olćan, T. K. Sarkar, and R. F. Harrington, *Analysis of Wire Antennas and Scatterers (ver. 2.0), Software and User's Manual, Chapter 8*, Artech House, Norwood, MA, 2002.
[6] B. D. Popović, M. B. Dragović, and A. R. Djordjević, *Analysis and Synthesis of Wire Antennas*, John Wiley & Sons, Inc., 1982.
[7] R. F. Harrington, *Time-Harmonic Electromagnetic Fields*, Chapter 5, McGraw-Hill, Inc., New York, 1961.
[8] Narda Company, 435 Moreland Road, Hauppauge, NY, 11787, www.nardamicrowave.com, 2006.
[9] High Frequency Structure Simulator (HFSS), Ver.10, Ansoft Corporation, Pittsburgh, PA, 2006.

Roger Hasse received a Bachelor of Science degree in physics from Oakland University, Rochester, Michigan, in 1991. He was awarded a U.S Department of Energy SERS fellowship from January 1994 to December 1994 at the Pacific Northwest National Laboratory, Richland, Washington, where he applied pulse echo and swept frequency acoustic techniques in the nondestructive testing of materials. From April 1995 to November 1997, he was awarded a Graduate Research Assistant fellowship at the Los Alamos National Laboratory, Los Alamos, New Mexico, where he conducted acoustic interferometry experiments in support of chemical weapons verification technology. He later joined the staff at Cornell University from November 1997 to January 2001 as a Research Support Specialist, where he provided hardware development and software maintenance support for visiting scientists, technical staff, and graduate students at the Cornell High Energy Synchrotron Source (CHESS). He joined the National Center for Physical Acoustics (NCPA), Oxford, Mississippi, as a Research and Development Engineer from February 2001 to January 2005. He conducted acoustic experiments and developed hardware and software in support of USDA-sponsored research in New Orleans, Louisiana. He also conducted research in nonlinear acoustics at the NCPA using the Schlieren imaging technique. He is currently pursuing his Master of Science degree in Electrical Engineering, with a concentration in electromagnetics, in the Department of Electrical Engineering at the University of Mississippi. In addition, he is presently a Systems Engineer with the Raytheon Company, working on low-power and high-power near field measurements and data analysis in support of the F/A-18 Active Electronically Steered Array (AESA) APG-79 radar antenna, both on-site in Forest, Mississippi, and off-site in El Segundo, California. Mr. Hasse is a member of The Applied Computational Electromagnetic Society (ACES), and a member of the Acoustical Society of America (ASA).

Veysel Demir was born in Batman, Turkey, in 1974. He received his Bachelor of Science degree in electrical engineering from the Middle East Technical University, Ankara, Turkey, in 1997. He received a scholarship award from the Renaissance Scholarship Program for graduate study in the United States (2000-2004). He studied at Syracuse University, Syracuse, New York, where he received both the Master of Science and Doctor of Philosophy degrees in Electrical Engineering in 2002 and 2004, respectively. During his graduate studies, he worked as a Research Assistant for Sonnet Software, Inc., Liverpool, New York. He worked as a Visiting Research Scholar in the Department of Electrical Engineering at the University of Mississippi from 2004 to 2007. He joined the Department of Electrical Engineering at Northern Illinois University as an Assistant Professor in August 2007. His research interests include numerical analysis techniques (FDTD, FDFD, and MoM), as well as microwave and RF circuit analysis and design. Dr. Demir is a member of the IEEE and ACES, and he has coauthored more than 20 technical journal and conference papers. He has been serving as a reviewer for both the Applied Computational Electromagnetics (ACES) Journal and the Transactions on Microwave Theory and Techniques (MTT) Journal.

Walker Hunsicker was born in Tupelo, Mississippi, in 1978. He received his Bachelor of Science degree in electrical engineering from the University of Mississippi, Oxford, Mississippi, in 2000. In 2002 he worked as a Research Engineer at the Naval Air Warfare Center, Aircraft Division, at Naval Air Station, Patuxent River, Maryland, where he performed analysis on spatial power combiners using the Method of Moments (MoM) technique. He is presently working as an Antenna Design Engineer with Radiance Technologies, Inc., Oxford, Mississippi, since 2004, and will complete his Master of Science degree in electrical engineering, with a concentration in electromagnetics, in December 2007. He plans on pursuing graduate studies towards a PhD degree in electrical engineering in 2008. His research interests include wideband antennas, array synthesis techniques, and computational electromagnetics.

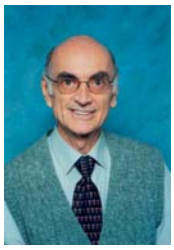

Darko Kajfez is Emeritus Professor of Electrical Engineering at the University of Mississippi. He obtained the electrical engineer's degree (Dipl. Ing.) from the University of Ljubljana, Slovenia, in 1953, and the PhD degree from the University of California Berkeley, in 1967. He co-edited the book entitled *Dielectric Resonators*, and authored the books *Notes on Microwave Circuits* and *Q Factor*. His research interests include RF and microwave measurement techniques and analysis. He can be contacted by email at eedarko@olemiss.edu.

Atef Elsherbeni received an honor B.Sc. degree in Electronics and Communications, an honor B.Sc. degree in Applied Physics, and a M.Eng. degree in Electrical Engineering, all from Cairo University, Cairo, Egypt, in 1976, 1979, and 1982, respectively, and a Ph.D. degree in Electrical Engineering from Manitoba University, Winnipeg, Manitoba, Canada, in 1987. He was a part time Software and System Design Engineer from March 1980 to December 1982 at the Automated Data System Center, Cairo, Egypt. From January to August 1987, he was a Post Doctoral Fellow at Manitoba University. Dr. Elsherbeni joined the faculty at the University of Mississippi in August 1987 as an Assistant Professor of Electrical Engineering. He advanced to the rank of Associate Professor on July 1991, and to the rank of Professor on July 1997. On August 2002 he became the director of The School of Engineering CAD Lab, and the associate director of The Center for Applied Electromagnetic Systems Research (CAESR) at The University of Mississippi. He was appointed as Adjunct Professor, at The Department of Electrical Engineering and Computer Science of the L.C. Smith College of Engineering and Computer Science at Syracuse University on January 2004. He spent a sabbatical term in 1996 at the Electrical Engineering Department, University of California at Los Angeles (UCLA) and was a visiting Professor at Magdeburg University during the summer of 2005. Dr. Elsherbeni received the 2006 School of Engineering Senior Faculty Research Award for Outstanding Performance in research, the 2005 School of Engineering Faculty Service Award for Outstanding Performance in Service, The 2004 Valued Service Award from the Applied Computational Electromagnetics Society (ACES) for Outstanding Service as 2003 ACES Symposium Chair, the Mississippi Academy of Science 2003 Outstanding Contribution to Science Award, the 2002 IEEE Region 3 Outstanding Engineering Educator Award, the 2002 School of Engineering Outstanding Engineering Faculty Member of the Year Award, the 2001 ACES Exemplary Service Award for leadership and contributions as Electronic Publishing Managing Editor 1999-2001, the 2001 Researcher/Scholar of the year award in the Department of Electrical Engineering, The University of Mississippi, and the 1996 Outstanding Engineering Educator of the IEEE Memphis Section. Dr. Elsherbeni has conducted research dealing with scattering and diffraction by dielectric and metal objects, finite difference time domain analysis of passive and active microwave devices including planar transmission lines, field visualization and software development for EM education, interactions of electromagnetic waves with human body, sensors development for monitoring soil moisture, airports noise levels, air quality including haze and humidity, reflector and printed antennas and antenna arrays for radars, UAV, and personal communication systems, antennas for wideband applications, and antenna and material properties measurements. He has co-authored 94 technical journal articles, 24 book chapters, and contributed to 266 professional presentations, offered 17 short courses and 18 invited seminars. He is the coauthor of the book entitled "*Antenna Design and Visualization Using Matlab*", Scitech, 2006, the book entitled "*MATLAB Simulations for Radar Systems Design*", CRC Press, 2003, the book entitled *"Electromagnetic Scattering Using the Iterative Multiregion Technique"*, Morgan & Claypool, 2007, the book entitled *"Electromagnetics and Antenna Optimization using Taguchi's Method"*, Morgan & Claypool, 2007, and the main author of the chapters "*Handheld Antennas"* and "*The Finite Difference Time Domain Technique for Microstrip Antennas"* in Handbook of Antennas in Wireless Communications, CRC Press, 2001. He was the main advisor for 31 MS and 8 PhD students. Dr. Elsherbeni is a Fellow member of the Institute of Electrical and Electronics Engineers (IEEE) and a fellow member of The Applied Computational Electromagnetic Society (ACES). He is the Editor-in-Chief for ACES Journal, and an Associate Editor to the Radio Science Journal. He serves on the editorial board of the Book Series on Progress in Electromagnetic Research, the Electromagnetic Waves and Applications Journal, and the Computer Applications in Engineering Education Journal. He was the Chair of the Engineering and Physics Division of the Mississippi Academy of Science and was the Chair of the Educational Activity Committee for the IEEE Region 3 Section. Dr. Elsherbeni's home page can be found at http://www.ee.olemiss.edu/atef and his email address is Elsherbeni@ieee.org.

Interval-Based Robust Design of a Microwave Power Transistor

P. Lamberti and V. Tucci

Department of Electrical and Information Engineering
University of Salerno, I-84084 Fisciano (SA), ITALY
plamberti@unisa.it, vtucci@unisa.it

Abstract – An interval-based approach aimed at the robust design of a specific performance of a Double Hetero-junction Bipolar Transistor (DHBT) for microwaves applications is presented. The robust design is obtained by looking at the range of the performance function by means of an overestimation, given in analytical form, of its amplitude. The proposed approach is described by referring to two theoretical performance functions to show the reliability for both the univariate and multivariate cases. The worst case approach is considered in order to study the minimum variation of the max oscillation frequency of the DHBT, obtained by a regression model from numerical results, in presence of given parameters variations. The physical and geometrical parameters affecting the performance are regarded as implicitly uncorrelated and uniformly distributed in an assigned range and therefore all their combinations are kept into account. The implemented approach permits to achieve a greater robustness of the solution without assuming approach-specific settings and additional computations dependent on designer's ability and can be used to maximize the production yield.

Keywords: Robust design, uncertain parameters, and optimization.

I. INTRODUCTION

The real behavior of a component is inevitably different from that considered in the design process owing to the uncertainties in the values of physical and geometrical parameters, to the effective operating conditions and to the drift and aging effects. Such an inconvenience may be faced up during the prototyping process of the component by a costly and time consuming dynamic adjustment of the parameters values whose convergence is based on the designer ability. However, it is possible to obtain a component realization, satisfying the imposed constraints even in presence of parameters changes, if in the early design phase such variations are properly taken into account. It is therefore possible to achieve a robust design that is the chosen combination of the design parameters ensures that component performance presents the minimal variations with respect to the parameters changes. The possibility to accomplish a robust design is particularly relevant in those fields, as in the dimensioning of an electronic device, in which the realization of prototypes is expensive and lengthy [1].

As shown in [2], an innovative approach, based on the use of Interval Analysis, leads to a robust design of a component able to satisfy the desired constraints even when the geometric dimensions, the physical properties or the operating conditions assume any possible value in an assigned range. For a given Performance Function (PF) described by a polynomial form, it furnishes the Most Robust Stationary Solution (MRSS), i.e. the set of nominal parameters such that its first derivative is zero, and an over-bounding of the PF. This systematic approach leads to the quick identification of the most suitable combination of the parameters values thus allowing to increase the production yield, reduce the optimization time and consequently the overall time-to-market process.

In this paper the main properties of the interval-based robust design approach are discussed by considering two theoretical performance functions in order to show the reliability for both the univariate and the multivariate cases. The method is then applied to the design of a PF represented by the max oscillation frequency of a Double Hetero-junction Bipolar Transistor (DHBT) for microwave applications. In particular, the dependency of the PF with respect to the influencing factors, given by a polynomial form obtained by interpolating the numerical results of a physical simulator [1], is analyzed. It is shown that the application of the interval-based method allows achieving more general and approach-independent information on the robustness of a particular solution with a slight investment in terms of computations.

The proposed approach can also be extended to other regression models describing further relevant performances controlling the electrical and thermal behaviour of the DHBT, such as common emitter breakdown voltage, max collector current density, etc. However, we explicitly remark that the main purpose of the present work is to show the effectiveness of the interval-based approach, rather than to perform a systematic and exhaustive design of the electronic device and hence only the variability of the max oscillation frequency with respect to physical and geometrical characteristics is discussed.

The paper is organised as follows. After a brief presentation of the Interval-based design approach in sect. II, two theoretical applications will be illustrated in sect. III. In sect. IV the model based design of the max oscillation frequency of a DHBT is discussed and in Sect V the main conclusions are drawn.

II. INTERVAL-BASED ROBUST DESIGN

The Performance Function (PF) describes the device performance as a function of ν design parameters, $\underline{x} = (x_1, x_2, \cdots, x_\nu)$. Let us suppose that the objective is to find a solution, i.e. a set of nominal parameters values, which satisfies assigned design constraints. A *robust solution* is one which guarantees that the constraints are fulfilled also in presence of assigned parameters variations $\underline{\Delta} = (\Delta_1, \Delta_2, \cdots, \Delta_\nu)$ [3]. Around such solution the range of the PF is generally narrow, tending to a point if the PF is locally flat. Not all the robust solutions have the same characteristics. A robust solution which implies that the PF variations are localised at the boundary of the Region of Acceptability (ROA) may become a non robust one if one of the parameters exhibits a variation greater that the expected one. It is possible to discriminate the level of solution robustness by looking at the range of the PF. In fact, a robustness index can be simply obtained by considering the amplitude of the range function with respect to a given parameter variation. The lower is the amplitude of the range, the greater is the robustness. For example, if the PF is a function of one parameter *x*, as shown in Fig. 1, the robustness index with respect to a variation of ±Δ around the nominal solution x_0 is given by the value $w(f_X)$ correspondent to,

$$w(f_{\underline{X}}) = \max_{\underline{x} \in \underline{X}_0} f(\underline{x}) - \min_{\underline{x} \in \underline{X}_0} f(\underline{x}) \qquad (1)$$

$w(f_X)$ is the range width of $f(x)$ when $x \in [x_0 - \Delta, x_0 + \Delta] = X$ and f_X represents the range of the PF for such variation.

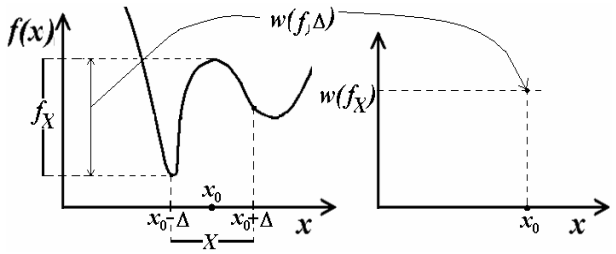

Fig. 1. A monodimensional PF $f(x)$ and the space of the range amplitude for a given parameter variation Δ.

In the design process it would be useful to have an algorithm that furnishes $w(f_X)$ to obtain a biunique correspondence as shown in Fig. 1. Indeed, it is not easy to obtain $w(f_X)$ and an approximation of it is generally adopted, typically in discrete way, by computing the equation (1) for each point. Moreover, the algorithms available in the literature lead to an overestimation of the actual robustness of the PF, due to an intrinsic characteristic of equation (1). In fact, the research of the range of $f(x)$ is conditioned by the presence of local minima/maxima and the quality of the result is somehow discretionary, since it depends on the choice of the parameters of the searching algorithm [4]. As a consequence, it may happen to select a robust one as a nominal solution that actually is not robust. Therefore, an underestimation of the robustness index must be adopted in order to guarantee its reliability and it can be obtained by means of an overestimation of equation (1). In fact, since the lower is the amplitude of the range, the greater is the robustness, an overestimation of equation (1) leads to an underestimation of the robustness of the nominal solution.

The Interval Analysis (IA) is an arithmetic that furnishes a reliable inclusion of the true range of a function for a given interval of values of the variables. Therefore the overestimation of the range amplitude can be achieved by exploiting the peculiarities of the IA and, in particular, the "over-bounding" of the function [5-6]. The function bounding and a generic over-bounding in presence of a given uncertainty of the variable are depicted in Fig. 2.

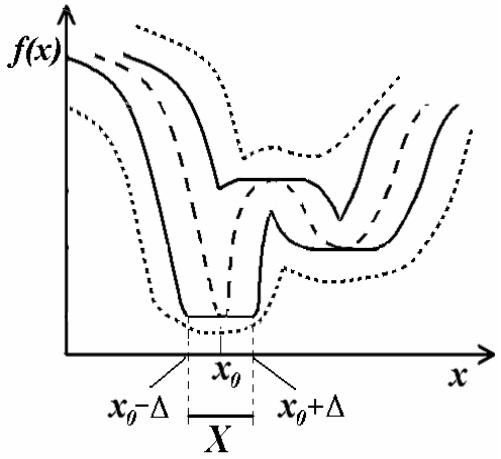

Fig. 2. Bounding (continuous lines) and over-bounding (dotted lines) of $f(x)$ for a parameter variation ±Δ.

The bounding is given by the two solid curves: the upper-bound, that is the locus of the maxima of the function $f(x)$ when the parameter *x* spans the "moving" interval $[x_0 - \Delta, x_0 + \Delta] \equiv X$, and the lower-bound that is the locus of the minima for the same moving interval. Instead, an over-bounding is given by the two dotted curves: they include the function bounding, i.e. represent

an overestimation of the upper-bound and an underestimation of the lower-bound.

A possible over-bounding can be easily obtained by applying the Interval Arithmetic to *f(x)* when the variable *x* is substituted by the interval *X* [5]. In fact IA is arithmetic defined on sets of intervals rather then sets of real numbers. An interval *X* is an ordered pair of real numbers $X=[a,b]$ such that, $X=[a,b]=\{x|a<x<b,\ with\ a,x,b\in\Re\}$, and all the values in *X* are equally probable. The sets of intervals on $\Re$ is denoted as $I\Re$. The interval width is defined as $w(X)=b-a$. In the following we will refer to a symmetric interval $X=[x-\Delta,x+\Delta]$, centred around the nominal point *x*, whose width is 2Δ. In presence of multivariate function, the IA treats the variables as uncorrelated. In presence of parameters variations, IA permits a straight determination of an interval that certainly includes the true range of a function; thanks to the "inclusion property" [5] and it can be suitably adopted in a worst-case design [7].

If the IA is applied to the Taylor series expansion of the PF around a nominal solution we obtain an interval, and if the nominal solution varies we obtain an interval function named Interval Taylor Extension (ITE) [2]. As an example, for a PF of a single parameter and for a generic point x_0 representing a particular nominal solution, we have the following ITE,

$$F_{ITE}(X)=\sum_{k=0}^{\infty}\frac{f(x_0)^{(k)}}{k!}(X-x_0)^k= \\ =\sum_{k=0}^{n}\alpha_k Y^k+\frac{f(X)^{(n+1)}}{(n+1)!}\Delta^{n+1}Y^{n+1}\in I\Re \tag{2}$$

where $Y=[-1,1]\in I\Re$ is a constant interval and $\alpha_k=\Delta^k\frac{f^{(k)}(x_0)}{k!}$.

It results that $\forall x\in X=[x_0-\Delta,x_0+\Delta]\subset\Re$ $f(x)\in F_{ITE}(X)$, where *X* is the compact given by a tolerance Δ on the nominal parameter. Therefore, ITE is an inclusion of the range of *f(x)*. The Width of ITE (WITE) for polynomial PF is characterised by the following properties [2]:

a) It is a continuous, non differentiable function which can be expressed in symbolic form;
b) It presents local minima positioned in the stationary points of the corresponding PF;
c) A maximum variation of the parameters can be found such that WITE reaches its absolute minimum in correspondence of the most robust stationary point;
d) Representing a valuable robustness index, it furnishes an accurate means for classifying the relative robustness of the stationary points.

Therefore, thanks to the property (a), the robustness of the nominal solution can be evaluated by considering a continuous, non differentiable function, $w(F_{ITE}(X))$ or WITE. In particular, if $f(\underline{x})=f(x_1,x_2,\cdots,x_\nu)$ is a ν-variate polynomial function of *n-th* order, then $w(F_{ITE}(\underline{X}))$ is,

$$w(F_{ITE}(\underline{X}))=\sum_{1\le i_1+\ldots+i_\nu\le n}\beta_{i_1\ldots i_\nu}|\alpha_{i_1\ldots i_\nu}|\ge 0 \tag{3}$$

with $\beta_{i_1\ldots i_\nu}=\begin{cases}2 & if\ i_k\ odd,\ k=1,2,\ldots,\nu\\ 1 & otherwise\end{cases}$ and

$$\alpha_{i_1\ldots i_\nu}=\frac{\Delta_1^{i_1}\cdots\Delta_\nu^{i_\nu}}{i_1!\cdots i_\nu!}\frac{\partial^{i_1}}{\partial x_1^{i_1}}\left(\ldots\left(\frac{\partial^{i_\nu}f(\underline{x}_0)}{\partial x_\nu^{i_\nu}}\right)\right).$$

Besides, thanks to the properties (b) and (c), it is possible to obtain robust solution by solving the following minimization problem [2],

$$\min_{\underline{x}_0\in\Re^n}\left(w(F_{ITE}(\underline{X}))\right) \tag{4}$$

rather than equation (1). In this way the problem of local maxima/minima point presents in equation (1) is avoided and the discretionary choice of the parameter of the searching algorithm is limited to the external minimum. It is useful to remark that equation (3) is an overestimation of $w(f_{\underline{X}})$ and the robustness index represented by WITE gives an underestimation of the effective robustness, as a result of "monotonic inclusion" [5]. Therefore equation (4) is not equivalent to equation (1), but the same overestimation guarantees that the true variation of the PF is certainly lower than that indicated by the WITE index, i.e. the particular solution is more robust than that pointed out. As a result, the reliability of the solution increases. Moreover, the robustness index represented by WITE has an analytic expression that can be treated in a symbolic way for any PF. Finally, this methodology can be extended also to generic functions which not necessarily are expressed in a polynomial form.

III. THEORETICAL EXAMPLES

A. A 9-th order univariate polynomial function

In order to show the properties of the proposed approach for the monodimensional-case, let us consider the following 9-th order PF,

$$f(x)=7.9\times10^{-8}x^9-9.8\times10^{-6}x^8+5.1\times10^{-4}x^7-0.014x^6+ \\ +0.24x^5-2.4x^4+13x^3-33.8x^2+25.7x+21.3 \tag{5}$$

In the interval $x\in[1, 24]$ it shows 3 minima and 4 maxima, two of which are located at the extremes of the compact as evidenced in Fig. 3.

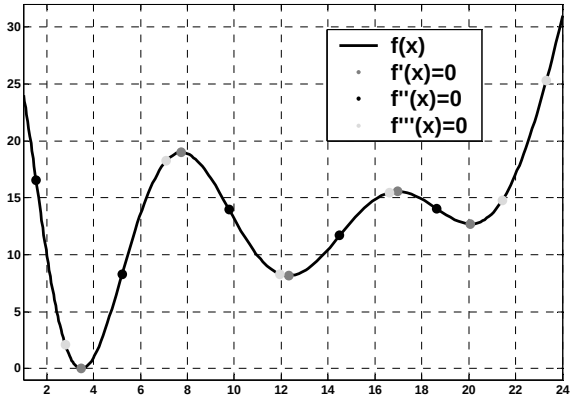

Fig. 3. 9-th order univariate polynomial function.

The Taylor series expansion of such a function around the nominal solution x_0 can be expressed as,

$$f(x)=\sum_{k=0}^{9}\frac{f^{(k)}(x_0)}{k!}(x-x_0)^k \tag{6}$$

Let us choose the interval $X\in I\Re$ characterised by a radius Δ coincident with the variation of the design parameter and centred in its nominal value. By substituting x with X in equation (6) and proceeding with the IA we obtain the $F_{ITE}(X)$ corresponding to equation (5). It results $\forall x\in X=[x_0-\Delta,x_0+\Delta]\in I\Re$

$$f(x)\in F_{ITE}(X)=\sum_{k=0}^{9}\frac{f^{(k)}(x_0)}{k!}(X-x_0)^k\ , \tag{7}$$

or $f_X\subseteq F_{ITE}(X)$. Moreover, we get $w(f_X)\le w(F_{ITE}(X))$ (overbounding IA property). By simple algebra the $F_{ITE}(X)$ can be rewritten as,

$$F_{ITE}(X)=\sum_{k=0}^{9}\Delta^k\frac{f^{(k)}(x_0)}{k!}([-1,1])^k=\sum_{k=0}^{n}\alpha_k Y^k \tag{8}$$

with the same significance of α_k and Y as in the previous section. In this case the WITE is given by,

$$\begin{aligned} &w(F_{ITE}(X))=\sum_{j=1}^{9}\beta_j|\alpha_j|= \\ &=(|\alpha_1|+|\alpha_3|+|\alpha_5|+|\alpha_7|+|\alpha_9|)+ \\ &+2(|\alpha_2|+|\alpha_4|+|\alpha_6|+|\alpha_8|)\ge 0\ . \end{aligned} \tag{9}$$

In the examined range $w(F_{ITE}(X))$ has 31 non derivable points, 5 of which corresponding to the roots of $f'(x)$ in the range [1,24], i.e. $x_k\in\{20.08,16.97,12.32,7.74,3.48\}\subset[1,24]$. These are points of minimum of $w(F_{ITE}(X))$ for each considered Δ (Fig. 4).

The absolute minimum is one of these points and $w(F_{ITE}(X))$ gives a precise information concerning the relative robustness of the stationary points, as evidenced by the light grey curves in Fig. 4. In particular, the relative magnitude of the robustness coincides with the values of the curves (light grey squares) in such points.

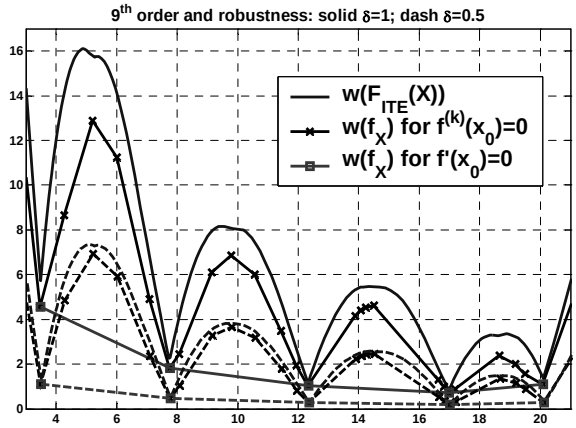

Fig. 4. WITE and $w(f_X)$ for the 9-th polynomial function.

The MRSS is found in x_0=16.97 for $\Delta\in\{0.5,1\}$. It is also evident that the amplitude of the PF range, i.e. the solution of (1), can be obtained by means of a discrete analysis for each nominal point: it corresponds to finding the difference between the max and min in the considered interval. The resulting curve, obtained by linear interpolation between two contiguous points, is discontinuous. Its level of accuracy can be improved by considering a greater number of points. The $w(F_{ITE}(X))$ instead, is a continuous function (curves without marker in Fig. 4) described by a symbolic expression which is valid for each nominal solution. Besides, in addition to the sorting in terms of robustness of the stationary points, an over-bounding is achievable without additional computational efforts (Fig. 5).

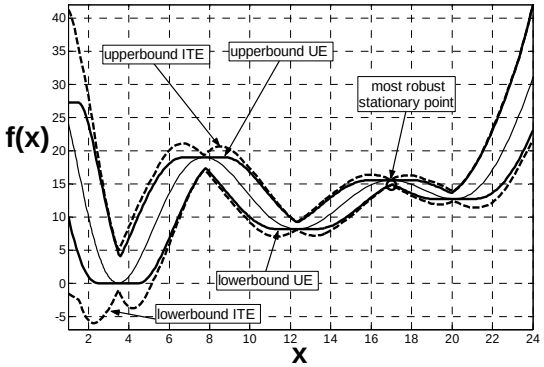

Fig. 5. ITE function bounding for δ=1.

B. A 3-rd order bivariate polynomial function

The properties and the reliability of the ITE are kept also in presence of multidimensional PFs. In order to show the simplicity of the proposed approach also for

multivariate problems, we take into consideration the case of 2-variate function $f(\underline{x})$ that is the case of dependency on 2 design parameters. Now we suppose that $f(\underline{x})$ is the following 3rd order polynomial PF (Fig. 6),

$$f(x_1,x_2)=\sum_{\substack{i_1,i_2=0\\ i_1+i_2\le n}}^{n} a_{i_1 i_2 \ldots i_\nu} x_1^{\,i_1} x_2^{\,i_2} = 3+2x_1^2x_2+ \\ -5x_1^2+x_1x_2-4x_2^2+2x_1x_2^2-2x_1^3 \tag{10}$$

The PF (equation 10) has a local maximum in [0, 0] for $(x_1,x_2)\in[-5,5]\times[-5,5]\subset\Re^2$ where it shows also a very smooth region.

It can be expressed in the $\Re$ domain by means of its complete Taylor series around a nominal solution $\underline{x}_0=(x_{10},x_{20})\in\Re^2$,

$$f(\underline{x})=\sum_{k=0}^{3}\frac{\left[((\underline{x}-\underline{x}_0)\cdot\nabla)^k f\right](\underline{x}_0)}{k!}= \\ =\sum_{k=0}^{3}\frac{\left[\left((x_1-x_{10})\frac{\partial}{\partial x_1}+(x_2-x_{20})\frac{\partial}{\partial x_2}\right)^k f\right](\underline{x}_0)}{k!} \tag{11}$$

then, by substituting the vector $\underline{x}\in\Re^2$ with the interval vector $\underline{X}=([x_{10}-\Delta_1,x_{10}+\Delta_1],[x_{20}-\Delta_2,x_{20}+\Delta_2])\in I\Re^2$ we obtain the ITE of equation (10) [8],

$$F_{ITE}(\underline{X})=\sum_{k=0}^{3}\frac{\left[((\underline{X}-\underline{x}_0)\cdot\nabla)^k f\right](\underline{x}_0)}{k!}= \\ =\sum_{k=0}^{3}\frac{\left[\left([-\Delta_1,\Delta_1]\frac{\partial}{\partial x_1}+[-\Delta_2,\Delta_2]\frac{\partial}{\partial x_2}\right)^k f\right](x_{10},x_{20})}{k!}= \\ =\sum_{k=0}^{3}\frac{\left[(\Delta\underline{Y}\cdot\nabla)^k f\right](\underline{x}_0)}{k!} \tag{12}$$

with $\Delta\underline{Y}=(\Delta_1Y_1,\Delta_2Y_2)$ and $Y_i=[-1,1]\in I\Re\ \forall i=1,2$.

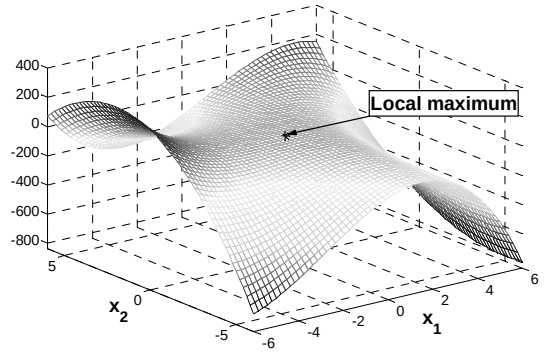

Fig. 6. A bi-variate PF.

Due to the IA properties, the previous computed $F_{ITE}(\underline{X})$ contains the PF in equation (10) $\forall\underline{x}\in\underline{X}=([x_{10}-\Delta_1,x_{10}+\Delta_1],[x_{20}-\Delta_2,x_{20}+\Delta_2])$, $f(\underline{x})\in F_{ITE}(\underline{X})$, i.e. it is an overbounding of equation (10) in presence of a Δ_i variation around the nominal parameter solution x_{0i}, $\forall i=1,2$.

By using the binomial coefficients to express the power of a sum, the equation (12) leads to the following expression,

$$F_{ITE}(\underline{X})= \\ =\sum_{k=0}^{3}\frac{\sum_{h=0}^{k}\binom{k}{h}\Delta_1^{\,k-h}\Delta_2^{\,h}\frac{\partial^{k-h}}{\partial x_1^{\,k-h}}\left(\frac{\partial^h f(x_{10},x_{20})}{\partial x_2^{\,h}}\right)Y_1^{\,k-h}Y_2^{\,h}}{k!}= \\ =\sum_{k=0}^{3}\sum_{h=0}^{k}\alpha_{k,h}Y_1^{\,k-h}Y_2^{\,h} \tag{13}$$

where $\alpha_{k,h}=\frac{\Delta_1^{\,k-h}\Delta_2^{\,h}}{h!(k-h)!}\frac{\partial^{k-h}}{\partial x_1^{\,k-h}}\left(\frac{\partial^h f(x_{10},x_{20})}{\partial x_2^{\,h}}\right)$ is a real number and $Y_1=Y_2=[-1,1]$ are constant intervals.

The equation (13) can be useful to understand the resulting analytic expression of its width, given by equation (3). In fact, for n=3 the width of $F_{ITE}(X)$ can be expressed as follows,

$$w(F_T(X_1,X_2))=2|\alpha_{10}|+2|\alpha_{11}|+|\alpha_{20}|+2|\alpha_{21}|+ \\ +|\alpha_{22}|+2|\alpha_{30}|+2|\alpha_{31}|+2|\alpha_{32}|+2|\alpha_{33}| \tag{14}$$

The equation (14) is a positive non-differentiable function with potential minima in $\alpha_{k,h}=0$. In particular, by considering k=1 and h=0,1, the following system must be solved,

$$\begin{cases}\alpha_{10}=0\\ \alpha_{11}=0\end{cases}. \tag{15}$$

The system in equation (15) corresponds to cancelling the gradient of f($\underline{x}$),

$$\begin{cases}\delta_1\frac{\partial f(x_1,x_2)}{\partial x_1}=0\\ \delta_2\frac{\partial f(x_1,x_2)}{\partial x_2}=0\end{cases}\Rightarrow\begin{cases}\frac{\partial f(x_1,x_2)}{\partial x_1}=0\\ \frac{\partial f(x_1,x_2)}{\partial x_2}=0\end{cases} \tag{16}$$

and to find a stationary point of $f(\underline{x})$, if the Hessian matrix eigenvalues have equal sign [9], such occur in the local maximum in Fig. 6. In fact, if we look at the Fig. 7. where the WITE obtained for $\Delta_1=\Delta_2=1$ is depicted, it is possible to verify that the width of $F_{ITE}(X)$ is minimum just in [0,0] and it corresponds to the MRSS.

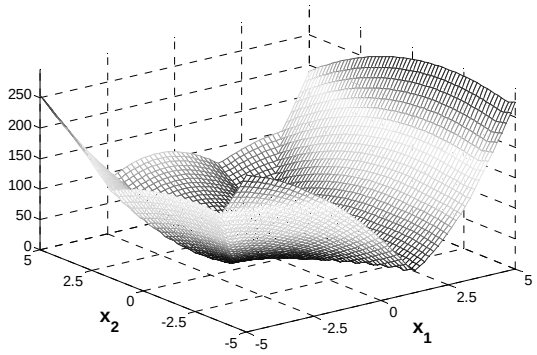

Fig. 7. WITE for the PF of the application II.

Furthermore, if the contour plot of WITE is kept in to account (Fig. 8), we can obtain additional information about the behaviour of the PF without computational efforts.

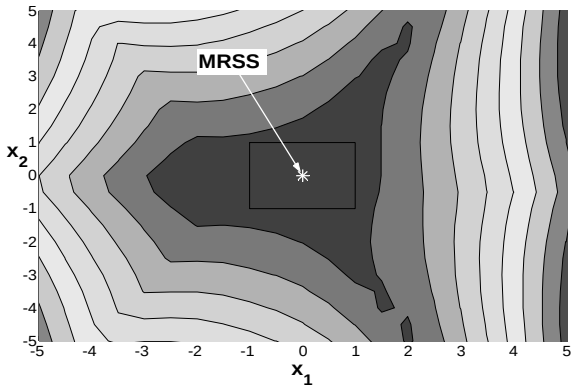

Fig. 8. WITE contour plot for the PF of the application II and the MRSS (*) in the variability box (rectangle).

In fact it is possible to highlight the flat region around the stationary point of $f(\underline{x})$ by considering the wide equipotent area around the MRSS. Such an information can be give to the designer a degree of freedom for his choice, that can adopt, for example, a wider tolerances on the nominal parameter to perform a lower cost design or that can pick up a nominal solution between the commercial value that are in the equipotent area of robustness.

IV. ROBUST DESIGN OF THE MAX OSCILLATION FREQUENCY OF A DHBT

In order to apply the proposed method to a real design problem we consider the max oscillation frequency of a Double-Heterojunction Bipolar Transistors (DHBT). Such devices have been proposed for microwave power applications (up to 20GHz), e.g., in airborne radars or mobile phones, because of their high output power, and superior power efficiency with respect to Single Heterojunction Bipolar Transistors (SHBT) [1] and [10].

The second Heterojunction between base and collector, which is added in DHBT in order to increase the common-emitter breakdown voltage, however, perturbs the electron flow across this junction, a problem that can be tackled by means of a GaAs spacer between the base and collector (Fig. 9). In order to examine the critical dependence of the DHBT performances on the physical and geometrical parameters of the spacer and collector, without recurring to lengthy and costly experimental realizations, simple behavioural mathematical models are considered [1]. In particular, polynomial forms interpolating the numerical values obtained from suitable simulation experiments (for specified operating points of the device) are employed to study the variability of relevant performance characteristics as a function of some major factors describing the structure and the processing of the component through a Design of Experiment (DoE) approach [11].

In our study we follow the same approach and focus our attention to the PF represented by the max oscillation frequency f_{max} of the DHBT. Indeed, the procedure can also be extended to other relevant performances, such as common emitter breakdown voltage, max collector current density and static current gain, controlling the electrical and thermal behaviour of the DHBT. However, since the main goal of the present work is to highlight the effectiveness of the interval-based approach, rather than to perform an in-depth design of the DHBT, only the variability of the f_{max} with respect to physical and geometrical characteristics is discussed.

In particular, we use the same interpolating polynomial adopted in [1] and compare our results with those reported there. With reference to Fig. 9, the following expression describes the influence on f_{max} of the impurity concentration (x_1) and the thickness of the base–collector spacer (x_2), the impurity concentration (x_3) and thickness of the collector (x_4),

$$f_{\max} = 66.42 + 0.3823x_2 + 6.334x_3 - 10.95x_4 + \\ -1.181x_1^{\,2} - 1.515x_2^{\,2} + 6.487x_3x_4 \qquad (17)$$

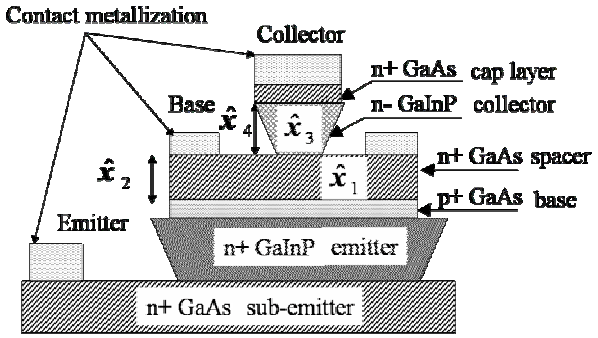

Fig. 9. Schematic setup of a collector-up DHBT [1].

where the variables have been normalized. In Table the adopted intervals of variation of the four actual parameters values $\hat{x}_i$ are reported. As usual in experiment design in presence of non-isodimensional and inhomogeneous factors [12], they are normalized in [-1, 1] by using the coded values x_i, $\forall i$=1,…,4.

Table 1. Interval of variation of the four considered factors.

	values	
	min	**max**
$\hat{x}_1$ [log[cm^{-3}]]	log(5×10^{15})	log(1×10^{18})
$\hat{x}_2$ [nm]	15	60
$\hat{x}_3$ [log[cm^{-3}]]	log(5×10^{15})	log(8×10^{16})
$\hat{x}_4$ [μm]	0.2	1.2
x_i ,$\forall$ i=1,2,3,4	-1	1

By imposing the minimization of the f_{max} variations in presence of an assigned uncertainty on the four design parameters $\underline{\delta} = (\log 2{,}30\%, \log 1.5{,}15\%)$, the objective function to be analysed is given by,

$$\min\left[\max_{\underline{x}\in D} f_{\max}(\underline{x}) - \min_{\underline{x}\in D} f_{\max}(\underline{x})\right] = \min\left(\Delta f(\underline{x}_0, \underline{\delta})\right). \qquad (18)$$

It is an optimization problem on a discrete parameter space defined by the set of pairs of the min/max values achieved by the performance function in the hyper-cube whose side length is given by the variations vector $\underline{\delta}$ moving in the hyper-space $D\subseteq\Re^4$ around a nominal solution $\underline{x}_0$. By adopting the ITE approach, the problem can be more easily formulated as an unconstrained optimization problem corresponding to the search of the minimal amplitude of the ITE, $w(F_{ITE}(\underline{X}))$. In particular, the ITE can be expressed as,

$$\begin{aligned} F_{ITE}(\underline{X}) &= \sum_{k=0}^{2} \frac{\left[((\underline{X}-\underline{x}_0)\cdot\nabla)^k f\right](\underline{x}_0)}{k!} = f(\underline{x}_0) + \\ &+ \left[((\underline{X}-\underline{x}_0)\cdot\nabla) f\right](\underline{x}_0) + \frac{1}{2}\left[((\underline{X}-\underline{x}_0)\cdot\nabla)^2 f\right](\underline{x}_0) \end{aligned} \qquad (19)$$

where $\underline{X}-\underline{x}_0 = [-\delta_1,\delta_1],[-x_{20}\delta_2, x_{20}\delta_2],[-\delta_3,\delta_3],[-x_{40}\delta_4, x_{40}\delta_4]$ due to the presence of absolute, x_1 and x_3, and relative, x_2 and x_4, tolerances.

By employing the dependences of the four variables the ITE becomes,

$$\begin{aligned} F_{ITE}(\underline{X}) &= f(\underline{x}_0) + \delta_1[-1,1] f_{x_1}(\underline{x}_0) + \\ &+ \delta_2 |x_{20}| [-1,1] f_{x_2}(\underline{x}_0) + \delta_3 [-1,1] f_{x_3}(\underline{x}_0) + \\ &+ \delta_4 |x_{40}| [-1,1] f_{x_4}(\underline{x}_0) + 2\delta_1^2 [0,1] f_{x_1x_1}(\underline{x}_0) + \\ &+ 2\delta_2^2 x_{20}^2 [0,1] f_{x_2x_2}(\underline{x}_0) + 2\delta_3\delta_4 |x_{40}| [-1,1] f_{x_2x_4}(\underline{x}_0) \end{aligned} \qquad (20)$$

whereas the remaining terms of the expression are null.

The equation (20) gives an over-bounding of the performance function: given the particular nominal solution, $\underline{x}_0$ and by assigning, through the vector $\underline{\delta}$, the variation that each parameter can assume, the performance function will be certainly included in the range of values defined by the particular interval $F_{ITE}(\underline{X}_0)$. By using just the over-bounding of the function we have an overestimation of the maximum value of the equation (17) and an over-estimation of its minimum value: their difference can be used to evaluate the robustness of each solution. In such a way we can use the problem of equation (4) to obtain a robust solution. In particular, if we adopt an easy uniform grid of 11 points for each coded parameter in the range [-1, 1] and we evaluate the minimum of the 11^4 ITE amplitudes, we obtain that it is in the nominal solution reported in Table at the ITE column. In such nominal point the max oscillation frequency is f_{max}=74.455 GHz and the equation (20) gives the inclusion of the range of possible values that the performance of equation (17) can assume in presence of the considered $\underline{\delta}$ variation. It is reported in the last row of Table 1. Moreover, by looking at Table 2, we can observe that in this particular solution point the amplitude of the range of the performance function is almost 3.251 GHz. Instead, the Optimal Robust Solution (ORS), reported in the same Table at the column ORS, is achieved by the authors in [1] through an adaptive random search. Indeed, this approach is not easy in the same way and depends on the choice of suitable setting parameters. A nominal value of f_{max}=74.786 GHz is obtained for the PF and an inclusion of the range of its possible values as the interval $F_{ITE}(\underline{X})$=[72.777,76.223] GHz is also achieved. This last interval is easily obtained by evaluating once the equation (20). Therefore, the range of the PF is 3.446 GHz, bigger than that obtained by the ITE solution. Hence, if we adopt the ORS approach the robustness decreases of about 6% with respect to that achieved by the ITE.

Table 2. Actual nominal values and interval of inclusion of the PF for ITE and ORS.

	ITE	**ORS**
$\hat{x}_{10}$ [cm^{-3}]	7.07×10^{16}	5.7×10^{16}
$\hat{x}_{20}$ [nm]	37.5	40
$\hat{x}_{30}$ [cm^{-3}]	4.59×10^{16}	2.5×10^{16}
$\hat{x}_{40}$ [μm]	0.4	0.33
$F_{ITE}(\underline{X}_0)$ **[GHz]**	[72.593,74.844]	[72.777,76.223]

The ORS solution is more favourable than that based on the ITE approach if the maximum value of the oscillation frequency is the first designer's objective. In fact, in such solution the PF range is larger but it is also shifted toward higher frequency values. The designer

must decide which aspect is prevalent for his scope. Actually, the ITE approach furnishes, without particular settings and additional computations dependent on designer's ability, a look-up table indicating the range of the PF and its amplitude in presence of a given parameter variation $\underline{\delta}$ for each considered nominal solution. By using such table the designer can choose a solution rather than another by exploiting at the same time the information concerning the maximization of the PF and the minimization of its variation.

V. CONCLUSIONS AND REMARKS

An interval-based approach to the robust design with applications to a specific performance of a Double Hetero-junction Bipolar Transistor (DHBT) for microwaves applications has been proposed. The considered performance function is the max oscillation frequency of the DHBT, obtained by a regression model from numerical results. The use of the Interval Analysis allows to efficiently implement the worst case approach for determining the minimum variation of the performance in presence of uncertain parameters. The physical and geometrical parameters affecting the performance are considered implicitly uncorrelated and uniformly distributed in an assigned range and therefore all their combinations are kept into account. The robust design is obtained by means of an overestimation of the amplitude of the performance function range. The procedure allows to achieve a greater robustness of the solution without assuming approach-specific settings and performing additional computations dependent on designer's ability. The implemented approach can also be extended to other single relevant performances controlling the electrical and thermal behaviour of the device or employed in a multi-objective optimization problem. This last aspect is now under study and will be dealt with in forthcoming communications.

ACKNOLEDGEMENTS

This research is carried out with the financial support of ex MURST 60% funds of the University of Salerno.

REFERENCES

[1] S. Hadjihassan, A. Henkel, E. Walter, S. Delage, L. Pronzato and I. Vuchkov, "Model-based approach to robust design, with application to microwave power transistors," *IEEE Trans. on Circuits and Systems - I: fundamental theory and applications*, vol. 49, no. 1, pp. 76-80, 2002.

[2] P. Lamberti and V. Tucci, "Interval approach to robust design," *International Journal COMPEL*, vol. 26, no. 2, pp. 285-297, 2007.

[3] Y. Wu and A. Wu, *Taguchi Methods for Robust Design*, ASME Press, 2000.

[4] K. H. Lee, G. J. Park and W. S. Joo, "A global robust optimization using the Kriging based approximation model," *6th World Congresses of Structural and Multidisciplinary Optimization*, ISMMO, Rio de Janeiro, Brazil, 2005.

[5] R. E. Moore, *Interval Analysis*, Prentice Hall, Englewood Cliffs, NJ, 1966.

[6] L. Jaulin, *Applied Interval Analysis*, Springer Verlag, 2001.

[7] G. Spagnuolo, "An interval arithmetic-based yield evaluation in circuit tolerance design," *IEEE ISCAS 2002*, vol. 1, pp. 753-756, 2002.

[8] M. Berz and G. Hoffstatter, "Computation and application of taylor polynomials with interval remainder bounds," *Reliable Computing*, no. 4, pp. 83-97, 1998.

[9] E. Giusti, *Analisi matematica 1* (in italian) , ed. B. Boringhieri, 1993.

[10] P. F. Chen, Y. T. Hsin, R. J. Welty, P. M. Asbeck, R. L. Pierson, P. J. Zampardi, W. J. Ho, M. C. V. Ho and M. F. Chang, "Application of GaInP/GaAs DHBT's to power amplifiers for wireless communications," *IEEE Trans. on Microwave Theory and Techniques*, vol. 47, no. 8, pp. 1433-1438, 1999.

[11] J. M. Lucas, "Optimum composite designs," *Technometrics*, vol. 16, no. 4, pp. 561–567, 1974.

[12] R. H. Myers, D. C. Montgomery, *Response Surface Methodology – Process and Product Optimization Using Designed Experiments*, 2nd ed., John Wiley & Sons, 2002.

Patrizia Lamberti (1974) received the laurea degree in Electronic Engineering and the Ph.D in Information Engineering from the University of Salerno (Italy) in 2001 and 2006 respectively. She is currently Assistant Professor with the Department of Information and Electrical Engineering, University of Salerno, Italy. Her researches concern numerical methods for electromagnetic fields, tolerance analysis and design in power electronics circuits and magnetic components.

Vincenzo Tucci (1956) received the laurea degree in electronic engineering with honors from the University of Naples (Italy) in 1981. Since Nov. 2000 he is Full Professor at the University of Salerno (Italy). He is also engaged in the Ph.D. course program in Information Engineering at the same University. His main research fields are: electromagnetic characterization of innovative materials, analytical and numerical methods for the design of electrical components, analysis and simulation of discharge phenomema and power electronic circuits. He is member of IEEE/AEI, the WG 36B of CEI responsible of setting the standards for High Voltage Insulators.

7 Tesla MRI with RF Power and Field Homogeneity Comparable to 4 Tesla using Computational Electromagnetics

L. Tang[2] and T. S. Ibrahim[1, 2]

[1.] Departments of Radiology and Bioengineering
University of Pittsburgh, Pittsburgh, Pennsylvania, USA
tsi2@pitt.edu (Correspondence)

[2]School of Electrical and Computer Engineering and Bioengineering Center
University of Oklahoma, Norman, Oklahoma, USA

Abstract – In ultrahigh (≥ 7 Tesla) field magnetic resonance imaging (MRI), the electromagnetic interactions between the coil, its excitation sources, and the biological load become more significant compared to low MRI applications. Computational electromagnetic (CEM) techniques are currently playing a major role in the evaluation of MRI radiofrequency (RF) coils (commonly now, within ultrahigh field context, referred to as transmit arrays).
This work compares the RF power requirements in 4 and 7 Tesla human MRI using CEM. Furthermore, we demonstrate that at ultrahigh MRI, high-quality/homogenous RF excitation fields could be obtained simultaneously with total RF power deposition lower than that achieved at lower field strengths. These results dispel what has been widely accepted from quasistatic approximations, namely that pushing the envelope of MRI field strength results in more RF power requirements and therefore, more RF power absorption in human tissue. This study is presented using the finite difference time domain (FDTD) method and a gradient-based optimization method.

Keywords: MRI, RF coil, transmit array, FDTD, optimization, RF power, B_1 field, coupling, and high filed.

I. INTRODUCTION

Since Magnetic Resonance Imaging (MRI) was first demonstrated in early 70s, MRI has become the primary technique in the routine diagnosis of many disease processes throughout the body. Although it faces some difficulties, operation at higher magnetic field strength and therefore higher frequency has been a constant goal for the advancement of MRI research. High field MRI brings the promise of high quality MR images as it is associated with increased signal-to-noise ratio [1], contrast-to-noise ratio, and high resolution. On the opposite end of the spectrum however, ultrahigh field (≥ 7 Tesla) imaging [2-4] is associated with significant technical complexities, the most notable of which is designing and building radiofrequency (RF) coils and/or transmit arrays. At such field strength, the complex interactions between the electromagnetic waves and the human head degrade the homogeneity of the MRI excitation field [5-6] (commonly referred to a B_1^+ field) and potentially increase the RF power absorption in the human head [7-8]. In order to analyze the electromagnetics of high frequency MRI, circuit/quasistatic approximations are no longer appropriate as the human head/body could be on the order of multiple wavelengths. As a result, full-wave CEM methods have been widely utilized for designing and predicting the performance of the RF coils/transmit arrays [6, 9, 10].

The interest in experimentally/theoretically investigating ultrahigh field technical and physical difficulties has been more academic than practical, since the technology to build ultrahigh field human systems did not exist. As field strength of human MRI magnets is growing at a staggering pace (currently performed at field strengths reaching 7 [3, 11], 8 [2, 12], and 9.4 [13] Tesla), accurately predicting and managing the RF power absorption and B_1^+ field homogeneity, associated with such operation has become essential to classify their future research potential as well as clinical practicality. A major hurdle that limits the clinical potential of ultrahigh field systems is finding means to improve the homogeneity of B_1^+ field distribution while maintaining acceptable RF power requirements to achieve it.

Unless combined with Transmit SENSE [14], for the purpose of improving the B_1^+ field homogeneity, it has been widely believed that the use of a phased array [15-16] (variable phase and variable amplitude) excitation with transmit arrays results in a significant increase in the total RF power deposition. In this paper, the FDTD method combined with a coupled-element coil model functioning as a transmitting phased array device were used to demonstrate that 7 Tesla human MRI can be

potentially achieved with 1) B_1^+ field distribution homogeneity, simultaneously with 2) total RF power deposition that are better than what is obtained at 4 Tesla using the same coupled-element coil operating under the standard quadrature excitation [17].

II. METHODS

A. The Coil Model

A 16-element transverse electromagnetic (TEM) resonator [12, 18] loaded with an anatomically detailed, 18-tissue, human head mesh [19] was utilized in this simulation study. The coil structure is composed of 16 elements, which are contained in an open cavity with the dimension of 34.6 cm in diameter and 21.2 cm in length. Each of the elements consists of coaxial line with a circular cross section. Two conductor rings are attached at the top and bottom of the cavity. The human head mesh is placed in the center of the coil such that the chin was aligned with the bottom ring. In our FDTD modeling approach, both the RF coil (including the coaxial rods, the shield, top and bottom rings, and excitation source(s)) and the human head mesh were modeled as a single system and therefore accounting for all of the coupling effects between the TEM resonator and the human head. The FDTD grid of the coil and human head mesh is shown in Fig. 1 (a). The in-house FDTD domain is divided into approximately 8 million cells with a resolution of 2 mm × 2 mm × 2mm. Perfectly matched layers (PML) [20] were used as the boundaries of the domain where 16 PML layers were placed on the 6 boundaries in the x, y, and z planes.

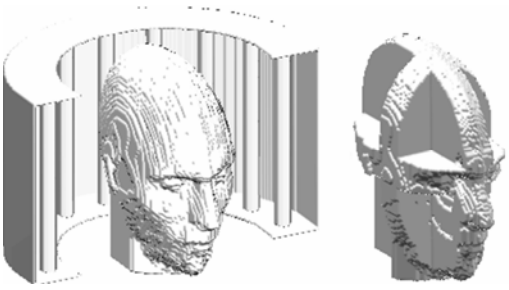

(a) (b)

Fig. 1. 3D FDTD model of the anatomically detailed human head mesh loaded within a 16-element TEM resonator (a) and the selected three 28mm slabs (b) oriented in axial, coronal and sagittal directions, respectively. In the simulations, the TEM resonator is completely surrounding the head model.

A stair-step approximation was used to model the coil shield and the top and bottom rings of the coil and a modified FDTD algorithm was used where the coaxial elements were modified into octagon shapes [19] to minimize the errors caused by stair stepping and to maintain an 8-fold symmetry.

B. Excitation and Tuning

The TEM resonator tuning was realized by adjusting the gap between each of the inner coaxial of elements with the load present in the coil. According to multi-conductor transmission line theory [21], there exist 9 modes exist in the 16-element TEM coil. The second mode (mode 1) on the spectrum is selected since at low frequencies/small electrical sizes, this mode produces a linearly polarized field in the center of the load. The resonating frequencies were set to 170 MHz (4 Tesla for ^{1}H imaging) and 295MHz (approximately 7 Tesla for ^{1}H imaging). The frequency spectra of the coil response are shown in Fig. 2.

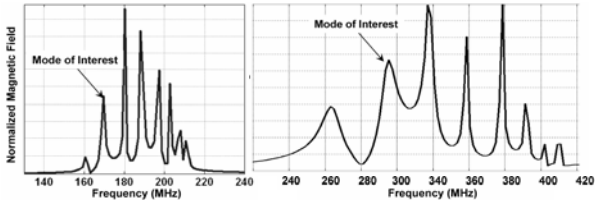

(a) (b)

Fig. 2. Frequency spectra for the 16-element TEM resonator loaded with the head model system at 4 Tesla (a) and 7 Tesla (b) by the FDTD method.

C. Experimental Validation

The aforementioned FDTD modeling technique has demonstrated excellent agreement with experimental measurements for this particular coil. Specifically this was achieved for predicting the 1) transmit and 2) receive magnetic fields and therefore 3) images as was shown in [6, 22], and 4) electric fields as was shown in [23] and therefore specific absorption rate and power deposition. To demonstrate the validity of multi-port excitation (the method utilized in this study), a similar highly-coupled TEM coil (8 elements) was modeled, built, and tested on a 7 Tesla human MRI system using 2-port excitation/reception. Arbitrarily chosen phase shifts (difference of 30 degrees between the coil excitation/reception ports) were implemented on the coil ports using costume made coaxial cables that are cut to these specifications. Figure 3 shows an excellent agreement between the FDTD calculations and the experimental images.

D. B_1^+ and Power Calculations

In MRI applications, the excitation magnetic field (typically referred to as B_1^+ field) is a circularly polarized component (in this study was chosen to possess clockwise rotational sense) of the total transverse, B_1, field as shown below,

$$B_1^+ = \left| \frac{B_{1x} + j * B_{1y}}{\sqrt{2}} \right|; \quad (1)$$

where B_{1x} and B_{1y} are the x and y components of the B_1 field, respectively. A homogenous B_1^+ field in a biological region of reset is needed in order to achieve useful MRI clinical information. In this study, a coefficient of variation (COV) is used to evaluate the homogeneity of B_1^+ field distribution. The total real input power entering the coil can be evaluated as,

$$P_{in} = P_{abs} + P_{rad} = \frac{\sigma}{2} \iiint_V \left| \vec{E} \right|^2 dv + \frac{1}{2} \iint_s (\vec{E} \times \vec{H}^*) \bullet d\vec{s} \quad (2)$$

where P_{abs} and P_{rad} are the absorbed and radiated power, respectively while $\iiint_v$ is the volume integral of the object to be imaged and $\iint_s$ is the integral of a closed surface that encloses the coil structure and the imaged object. The volume integration is done over the human head model. The surface integration is done by choosing a surface that encloses the coil and the sample and then performing the numerical integration over that surface.

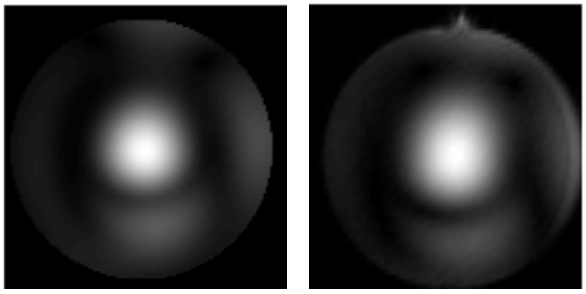

FDTD Simulations **7 tesla Experiment**

(a) (b)

Fig. 3. FDTD calculations (a) and experimental sagittal image (b) obtained using a 7 Tesla whole body system. The excitation/reception is performed in two ports using a TEM resonator loaded with 17-cm in diameter spherical phantom that posses dielectric constant = approx. 79 and conductivity = 0.46 S/m.

Because the percentage of the coil's radiated power (and therefore efficiencies) varies at different frequencies, the comparison of power requirements at different field strengths is unclear even for the same (geometry and dimensions) RF coil. More importantly, the absorbed power is associated with tissue dissipation and heating concerns. As a result, the absorbed power rather than the total power entering the coil was used in determining the power requirements in this study. In the FDTD domain, power absorbed was calculated from equation (3).

$$Power = \sum_i \sum_j \sum_k [\frac{1}{2} \sigma_{(i,j,k)} \times (E^2_{x_{(i,j,k)}} + E^2_{y_{(i,j,k)}} + E^2_{z_{(i,j,k)}})] \quad (3)$$

where $\sigma_{(i,j,k)}$ (S/m) is the conductivity of the FDTD cell at the (i,j,k) location; Ex, Ey and Ez (V/m) are the magnitudes of the electric field components in the x, y, and z directions, respectively; the summation is performed over the whole volume of the human head mesh.

E. Comparison Studies for the B_1^+ Distribution and Total Power Deposition

Using the FDTD mode, comparisons between 4 Tesla and 7 Tesla imaging were focused on homogeneity of the B_1^+ field and the power requirements to achieve the same excitation. By exciting all the elements of the coil in a phased-array fashion at 7 Tesla, variable phase/variable amplitude phased-array excitation was applied to achieve: 1) a coefficient of variation (COV) of the B_1^+ field in the region of interest with 2) total (in the whole human head mesh) RF power deposition lower than that obtained with 4-port fixed phases/amplitude (quadrature) excitation at 4 Tesla.

In the 4-port quadrature condition, all the 4 excitation sources were set with the same amplitude and $\pi/2$ phase shift between every two adjacent sources. 16-port optimized condition was carried-out by applying variable amplitude and phase for each excitation signal to achieve a better B_1^+ field distribution homogeneity within the region of interest and lower total power absorption. The optimization routine uses gradient algorithms were 32 unknown inputs (amplitude and phase variables) are varied to lower 1) the COV of B_1^+ field over slices and slabs with various orientations as well as 2) total power absorption by the human head mesh. In our calculation, B_1^+ field was normalized to 1.174μT, which is the field strength needed to produce a flip angle of $\pi/2$ with a 5-msec rectangular RF pulse; the power requirement is the scale to obtain the same B_1^+ field intensity.

III. RESULTS AND DISCUSSION

Optimization of the B_1^+ field was done on the slices (2mm thickness) and slabs (28mm thickness) oriented in the axial, coronal, and sagittal directions (as shown in Fig. 1 (b)) at 7 tesla in order to obtain more homogeneous B_1^+ field distribution (target is the 4Tesla/4port quadrature excitation COV) and lower total RF power absorption by the whole head mesh (target is the 4Tesla/4port quadrature excitation total power absorption for a fixed average B_1^+ field intensity in the region of interest). Similar to fluid-dynamics Mach number [24], the optimization target combines these two parameters into a non-linear relationship and was constantly changing throughout the iterations.

A. B_1^+ Field Distributions and Total RF Power Absorption

Figure 4 and Table 1 show the results including the B_1^+ field distributions and the associated RF power

deposition using 4-port quadrature excitation at 4 and 7 Tesla and 16-port variable phases/amplitude excitation for 2mm/28mm axial, coronal and sagittal slabs.

Table 1. The coefficient of variations and the total RF power absorption for the B_1^+ field distributions shown in Fig. 4.

Excite Condition	1-- 4T/4P Qua		2-- 7T/4P Qua		3-- 7T/16Pt Opt	
Parameter	COV	Power (w)	COV	Power (w)	COV	Power (w)
A (Axial Slice)	0.18	0.89	0.30	2.22	0.18	0.80
C (Coronal Slice)	0.25	1.17	0.30	2.44	0.24	0.99
S (Sagittal Slice)	0.24	1.09	0.25	2.16	0.23	1.04
A_Slab (Axial_slab)	0.18	0.92	0.31	2.44	0.18	0.77
C_Slab (Coronal_slab)	0.24	1.18	0.30	2.62	0.24	0.91
S_Slab (Sagittial_slab)	0.24	1.10	0.25	2.22	0.24	1.01

The results from a 4-port quadrature excitation at 4 and 7 Tesla demonstrate that the increased electromagnetic wave interactions in high field strength (7 Tesla) cause a decrease of B_1^+ field uniformity under the same excitation conditions. Additionally, the power required to obtain the same average B_1^+ field intensity (over a slice/slab of interest) increases at 7 Tesla compared to 4 Tesla. When a 16-port variable phases/amplitude excitation is applied however, the B_1^+ field uniformity can be greatly improved while significantly reducing the total absorbed power. From the data shown in Table 1, under 7 Tesla/16 port optimized conditions, 1) the B_1^+ field homogeneity over 2D slices and 3D slabs were improved to the same level of the ones under 4Tesla/4port quadrature conditions, with 2) the associated total RF power absorptions at 7 Tesla lower than that at 4 Tesla.

B. Distributions of the RF Power Absorbed in Tissue

To compare the effects of homogenizing the B_1^+ field homogeneity on RF power absorption, the distributions of the power deposition inside the head model were calculated and are displayed under different excitation conditions in Fig. 5. Coefficient of variations (COV) of the RF power distributions (corresponding to each subfigure in Fig. 5) are given in Table 2. This set of results show that, with similar total absorbed power, the power deposition (and therefore potential temperature rises) inside the head mesh varies under quadrature and optimized excitation conditions. Compared to quadrature excitation, the power absorption by tissue is more uniformly distributed with optimized excitation. Spreading the energy deposition through the whole head reduces the probability of local spots.

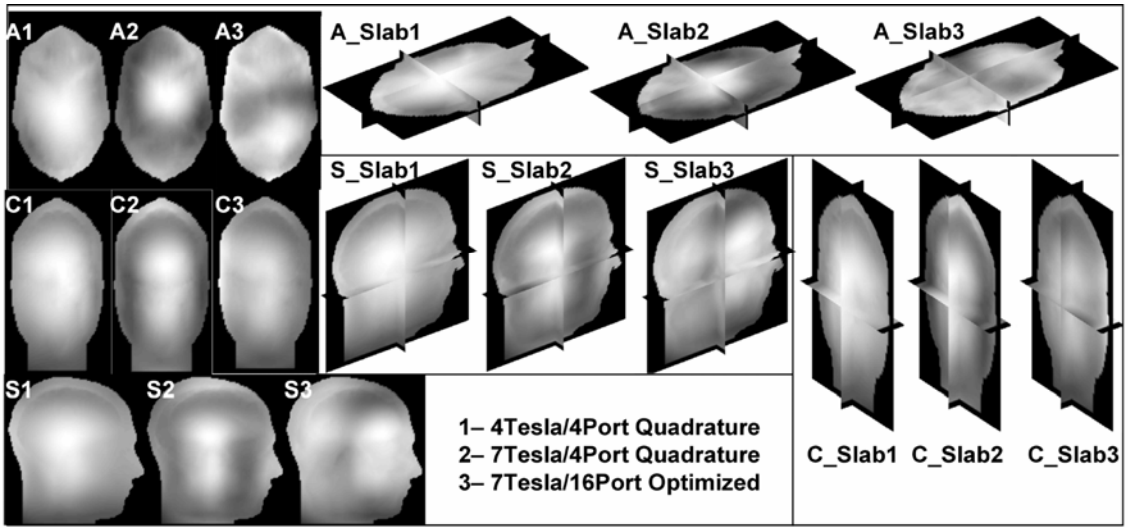

Fig. 4. The B_1^+ field distributions over axial (A1-A3), coronal (C1-C3) and sagittal (S1-S3) slices as well as axial (A_Slab1-3), coronal (C_Slab1-3) and sagittal (S_Slab1-3) slabs at 4 Tesla and 7 Tesla under different excitation conditions. 1, 2, and 3 represent the different excitation types as annotated in the figure.

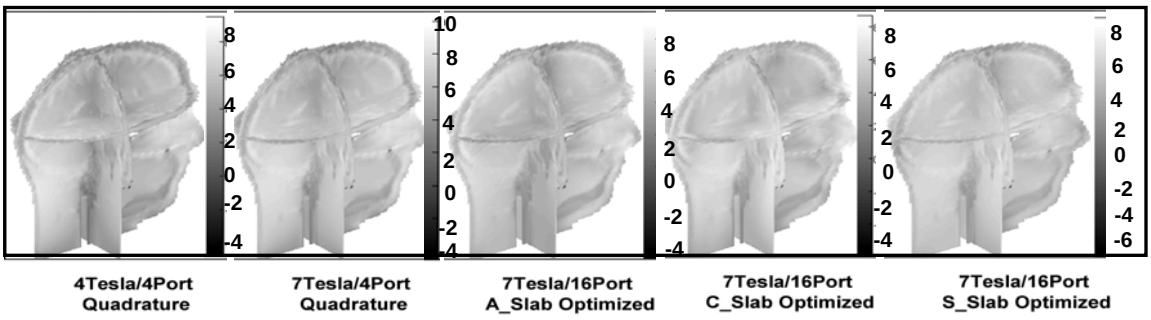

Fig. 5. Power distributions (dB) over the whole head mesh under different excitation conditions.

Table 2. The coefficient of variations for the RF power distributions (over the whole head mesh) shown in Fig. 5.

Excit-ation Types	4T/4P Qua.	7T/4P Qua.	7T/16P A_Slab Opt.	7T/16P C_Slab Opt.	7T/16P S_Slab Opt.
COV	0.56	0.50	0.45	0.41	0.40

As such with the optimization scheme presented in this work, compared to 4 Tesla 4-port quadrature excitation, more homogeneous B_1^+ field (as denoted by lower COV) simultaneously with lower total RF power absorption could be obtained at 7 Tesla. The presented results dispel what has been widely accepted from quasistatic approximations namely that pushing the envelope of MRI field strength results in more RF power requirements and therefore more RF power absorption in human tissue. The numerical simulations presented in this work indicate that the severe inhomogeneity associated with quadrature excitation at 7 Tesla is resultant from the lack of a B_1^+ field but not necessarily from the lack of electromagnetic energy. The rearrangement of B_1^+ field distribution or increase of B_1^+ field intensity affects only a component of the total RF magnetic field and does not necessarily cause increases in total RF power absorption.

IV. CONCLUSION

In high and ultra high field human MRI applications, computational electromagnetic techniques are playing a significant role in the design of the needed RF coils/transmit arrays and excitation approaches to obtain high quality images and manage the RF power deposition. Utilizing FDTD method, this work demonstrates that homogenous excitation can be achieved at 7 Tesla MRI for human head applications with a lower than the amount of RF power required for 4 Tesla MRI.

ACKNOWLEDGEMENT

The authors would like to acknowledge YiK-Kiong Hue for his assistance in creating the numerical result in Fig. 3.

REFERENCES

[1] D. I. Hoult and R. E. Richards, "The signal-to-noise ratio of the nuclear magnetic resonance experiment," *Journal of Magn. Reson. (1969)*, vol. 24, pp. 71-85, 1976.

[2] P. M. L. Robitaille, A. M. Abduljalil, A. Kangarlu, X. Zhang, Y. Yu, R. Burgess, S. Bair, P. Noa, L. Yang, H. Zhu, B. Palmer, Z. Jiang, D. M. Chakeres, and D. Spigos, "Human magnetic resonance imaging at 8 T," *Nmr in Biomedicine*, vol. 11, pp. 263-265, 1998.

[3] J. T. Vaughan, M. Garwood, C. M. Collins, W. Liu, L. DelaBarre, G. Adriany, P. Andersen, H. Merkle, R. Goebel, M. B. Smith, and K. Ugurbil, "7T vs. 4T: RF power, homogeneity, and signal-to-noise comparison in head images," *Magn. Reson. Med.*, vol. 46, pp. 24-30, 2001.

[4] B. Beck, D. H. Plant, S. C. Grant, P. E. Thelwall, X. Silver, T. H. Mareci, H. Benveniste, M. Smith, C. Collins, S. Crozier, and S. J. Blackband, "Progress in high field MRI at the University of Florida," *Magma*, vol. 13, pp. 152-7, 2002.

[5] T. S. Ibrahim, R. Lee, A. M. Abduljalil, B. A. Baertlein, and P. M. Robitaille, "Dielectric resonances and B(1) field inhomogeneity in UHFMRI: computational analysis and experimental findings," *Magn. Reson. Imaging*, vol. 19, pp. 219-26, 2001.

[6] T. S. Ibrahim, C. Mitchell, P. Schmalbrock, R. Lee, and D. W. Chakeres, "Electromagnetic perspective on the operation of RF coils at 1.5-11.7 Tesla," *Magn. Reson. Med.*, vol. 54, pp. 683-90, 2005.

[7] C. M. Collins and M. B. Smith, "Signal-to-noise ratio and absorbed power as functions of main magnetic field strength, and definition of "90 degrees" RF pulse for the head in the birdcage coil," *Magn. Reson. Med.*, vol. 45, pp. 684-91, 2001.

[8] D. I. Hoult, C. N. Chen, and V. J. Sank, "The field dependence of NMR imaging. II. Arguments concerning an optimal field strength," *Magn. Reson. Med.*, vol. 3, pp. 730-46, 1986.

[9] O. P. Gandhi and X. Bin Chen, "Specific absorption rates and induced current densities for an anatomy-based model of the human for exposure to time-varying magnetic fields of MRI," *Magn. Reson. Med.*, vol. 41, pp. 816-823, 1999.
[10] J. Chen, Z. M. Feng, and J. M. Jin, "Numerical simulation of SAR and B-1-field inhomogeneity of shielded RF coils loaded with the human head," *IEEE Transactions on Biomedical Engineering*, vol. 45, pp. 650-659, 1998.
[11] L. L. Wald, G. C. Wiggins, A. Potthast, C. J. Wiggins, and C. Triantafyllou, "Design considerations and coil comparisons for 7 T brain imaging," *Applied Magn. Reson.*, vol. 29, pp. 19-37, 2005.
[12] T. S. Ibrahim, A. Kangarlu, and D. W. Chakeress, "Design and performance issues of RF coils utilized in ultra high field MRI: experimental and numerical evaluations," *IEEE Transactions on Biomedical Engineering*, vol. 52, pp. 1278-84, 2005.
[13] J. T. Vaughan, "How to do RF at high fields," in *The International Society of Magn. Reson. Med. Annual Meeting: MORNING CATEGORICAL COURSE: Human MRI and MRS at High Static Magnetic Fields*. Miami, Florida: ISMRM, 2005.
[14] U. Katscher, J. Rohrs, and P. Bornert, "Basic considerations on the impact of the coil array on the performance of Transmit SENSE," *Magn. Reson. Materials in Physics Biology and Med.*, vol. 18, pp. 81-88, 2005.
[15] T. S. Ibrahim, R. Lee, B. A. Baertlein, A. Kangarlu, and P. L. Robitaille, "Application of finite difference time domain method for the design of birdcage RF head coils using multi-port excitations," *Magn. Reson. Imaging*, vol. 18, pp. 733-42, 2000.
[16] F. Liu, B. L. Beck, J. R. Fitzsimmons, S. J. Blackband, and S. Crozier, "A theoretical comparison of two optimization methods for radiofrequency drive schemes in high frequency MRI resonators," *Physics in Med. and Biology*, vol. 50, pp. 5281-5291, 2005.
[17] G. H. Glover, C. E. Hayes, N. J. Pelc, W. A. Edelstein, O. M. Mueller, H. R. Hart, C. J. Hardy, M. O'Donnell, and W. D. Barber, "Comparison of linear and circular polarization for magnetic resonance imaging," *Journal of Magn. Reson. (1969)*, vol. 64, pp. 255-270, 1985.
[18] J. T. Vaughan, H. P. Hetherington, J. O. Otu, J. W. Pan, and G. M. Pohost, "High-frequency volume coils for clinical NMR imaging and spectroscopy," *Magn. Reson. Med.*, vol. 32, pp. 206-218, 1994.
[19] T. S. Ibrahim, "Ultrahigh-field MRI whole-slice and localized RF field excitations using the same RF transmit array," *IEEE Transactions on Medical Imaging*, vol. 25, pp. 1341-7, 2006.
[20] J. P. Berenger, "A perfectly matched layer for the absorption of electromagnetic-waves," *Journal of Computational Physics*, vol. 114, pp. 185-200, 1994.
[21] B. A. Baertlein, O. Ozbay, T. Ibrahim, R. Lee, Y. Yu, A. Kangarlu, and P. M. Robitaille, "Theoretical model for an MRI radio frequency resonator," *IEEE Transactions on Biomedical Engineering*, vol. 47, pp. 535-46, 2000.
[22] T. S. Ibrahim, C. Mitchell, R. Abraham, and P. Schmalbrock, "In-depth study of the electromagnetics of ultrahigh-field MRI," *NMR Biomed*, vol. 20, pp. 58-68, 2007.
[23] T. S. Ibrahim and R. Lee, "Evaluation of MRI RF probes utilizing infrared sensors," *IEEE Transactions on Biomedical Engineering*, vol. 53, pp. 963-967, 2006.
[24] J. H. Zhao, J. O. Burns, M. L. Norman, and M. E. Sulkanen, "Instabilities in astrophysical jets .2. numerical simulations of slab jets," *Astrophysical Journal*, vol. 387, pp. 83, 1992.

Lin Tang received her B.S. degree in physics from Sichuan University, China, in 1999 and M.S. degree in physics from University of Oklahoma, US, in 2005. She is currently a Ph.D. candidate of electric and computer engineering at University of Oklahoma. Her research interests include performance of high field magnetic resonance imaging (MRI) and computational electromagnetics.

Tamer S. Ibrahim received his B.S. with distinction and honors in electrical engineering and with option in computer science, M.S.E.E, and Ph.D. degrees from Ohio State University in 6/96, 12/98, and 3/03, respectively. Since 01/03, he has been an assistant professor in The School of Electrical and Computer Engineering and a Faculty Member in The Bioengineering Center at University of Oklahoma; since 02/06 he has been an assistant professor in the Departments of Radiology and Bioengineering at the University of Pittsburgh. Dr. Ibrahim is the technical director for human ultra high field magnetic resonance imaging (MRI) at the University of Pittsburgh where he leads the radio-frequency research and development for human and animal MRI. His research also focuses on the development of wireless micro-neural interfaces, radome characterization technology, and wireless sensor networks for intelligent high-way systems. Dr. Ibrahim has authored/co-authored more than 115 scientific journal articles/book chapters/international conference proceedings; since 01/06, his average ISI, non-self, citations has ranged between 4-5 times per month. He has given numerous plenary/educational seminars in International meetings and research centers. He was the recipient of the ElectroScience Laboratory's Outstanding Journal Paper and Master Thesis Awards and of conference paper awards at IEEE Antenna and Propagation Society and International Society of Magnetic Resonance in Medicine Meetings. His biography is listed in *Who is Who* of *Emerging Leaders*, *American Education*, *Science and Engineering*, and *America*. Dr. Ibrahim has served as a reviewer for numerous journals and for funding agencies such as NIH, NSF, and DOD. Currently, he serves as an Associate Editor of the International Journal on Antennas and Propagation and as a member of the NIH Small Business Medical Imaging Technology Study Section.

On-Wafer Measurement and Modeling of Silicon Carbide MESFET's

L. Jordan, D. Elsherbeni, E. Hutchcraft, R. K. Gordon, and D. Kajfez

Department of Electrical Engineering
University of Mississippi, University, MS 38677-1848, USA
ltjordan@olemiss.edu, daelsher@olemiss.edu, eeweh@olemiss.edu, eegordon@olemiss.edu, eedarko@olemiss.edu

Abstract **–** The goal of this work was to characterize Silicon Carbide (SiC) transistor devices, with measurements and modeling using an advanced software package. To characterize and model the SiC Metal-Semiconductor Field-Effect Transistors (MESFETs), on-wafer measurements of the transistors were performed and their behavior was characterized. The transistors were measured using a vector network analyzer in conjunction with a probing station to make contact with the individual devices on the wafers. Once measurements were complete and typical performance characteristics found, equivalent circuit models were designed and the components optimized to create equivalent circuits with matching characteristics.

Keywords: Silicon carbide, MESFET, on-wafer measurements, and optimization.

I. ON-WAFER MEASUREMENT OF SIC TRANSISTORS

A study of a Silicon Carbide transistor behavior was performed using a variety of different transistors on a fabricated wafer. Silicon Carbide transistors, because of their high temperature capability, are expected to be used for high power devices in the future. The Silicon Carbide MESFET's were made using a proprietary process, and one goal of this research was to supply performance characteristics of these transistors so that further refinement and enhancement of the fabrication process could be achieved. The transistors were measured using the Agilent 8510C vector network analyzer (VNA), the Cascade Microtech Summit 9000 probing station, and several Agilent DC power supplies and multimeters. The small-signal measurements were made, with the operating point for each device typically chosen in the saturation (active) region of the devices. From these measured results, an analytical characterization using curve fitting and a numerical characterization using optimization of the microwave transistor were obtained. In addition, for the curve fitting procedure, a measurement was made with the device in the "cold" or pinched off region. The measurements were performed in the frequency range from 0.1 to 8 GHz with 201 frequency points; with the calibration of the network analyzer completed using the SOLT (short-open-load-through) method. The calibration substrate used for successful calibrations was included with the Cascade Microtech probe station and designed for the appropriate size probe pitch, 100 μm pitch for these measured transistors. A sample wafer from the fabrication company is shown in Fig. 1, below.

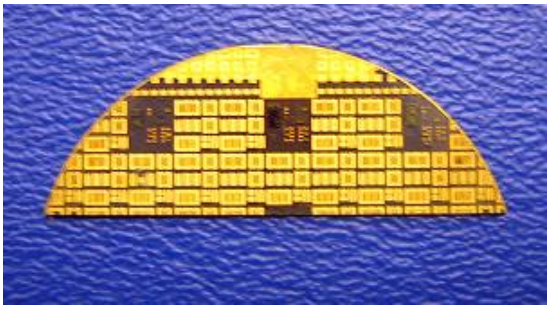

Fig. 1. Typical silicon carbide wafer measured and modeled.

The wafer was composed of several different sizes of transistors as seen on the left in Fig. 2, each with its individual DC curves for choosing an appropriate operating point. Several types of transistors with different sizes are shown in Fig. 2, with the gate, drain, and source labeled as compared to a typical transistor symbol [1].

The wafer was composed of several different sizes and types of transistors, each with its individual DC curves for choosing an appropriate operating point. An example of these curves is shown below in Fig. 3. The transistors measured were n-channel depletion mode devices, and therefore the gate voltage must be kept negative with respect to the drain voltage for operation in the active region [2]. In the DC characteristics, the different colored curves represent values of V_{GS}, the voltage from the gate to the source. For the shown curves, V_{GS} varies from -7 Volts to 1 Volt. The V_{GS} curves are plotted as functions of V_{DS}, the voltage from the drain to the source, versus I_D, the current through the drain.

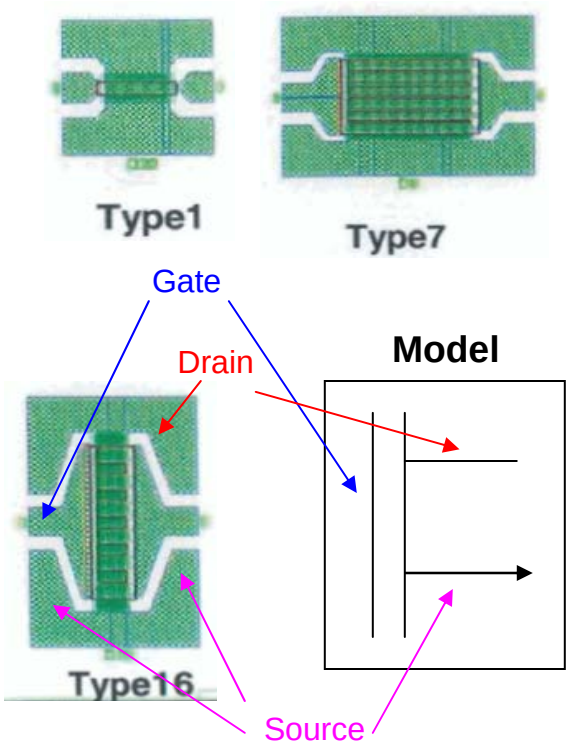

Fig. 2. Different transistor types compared along with typical MESFET symbol.

II. DATA DISPLAY

Once measurements were completed using the VNA, useful RF characteristics for each device were computed and provided to the manufacturer. Typical performance characteristics such as the gain and stability of the transistor are displayed in Fig. 4.

These characteristics are obtained from the measured S-parameters; the measured S-parameter data is processed through simulation in Agilent's Advanced Design System (ADS) to provide the useful characteristics [3]. The stability is shown in terms of the μ-factors, both required to be above unity for unconditional stability, and in terms of the K-factor, also required to be above one for stability [4]. The maximum gain in decibels is also given, with these results shown at 1 GHz and 2.4 GHz. These frequencies were chosen for display because they are in the GPS, wireless local-area network, WLAN, and WiMAX frequency bands. They are also typical operating frequencies for which Silicon Carbide transistors expect to be utilized. The S-parameters are displayed in the Smith Chart format for the input and output reflection coefficients, S_{11} and S_{22}, and are shown in decibels as functions of frequency for the amplitude of the forward transmission S_{21} and the reverse transmission S_{12}.

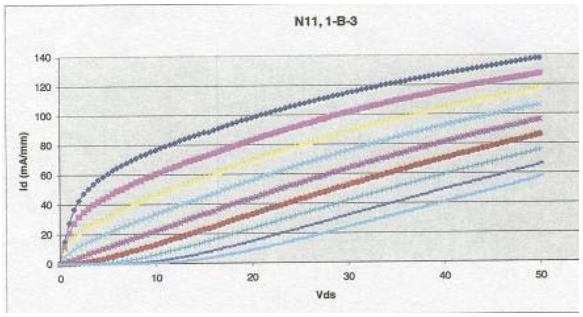

Fig. 3. DC characteristic curves.

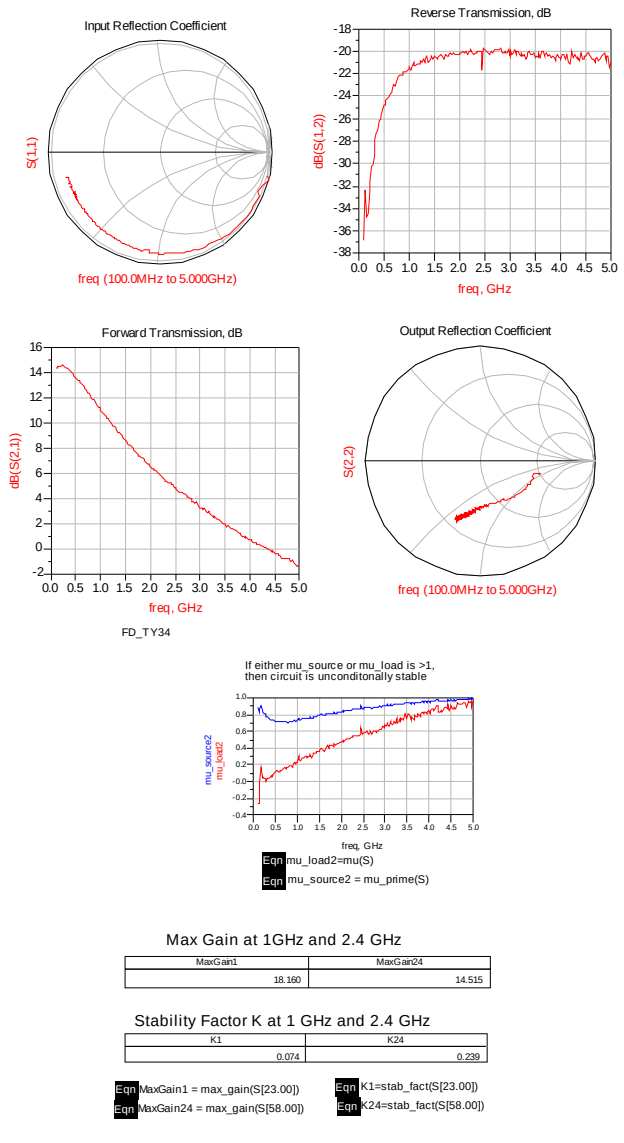

Fig. 4. Typical performance characteristics of a SiC device.

III. EQUIVALENT CIRCUIT MODELING

With the measurements completed, a conventional small signal equivalent circuit was used to find the values of the individual elements in the circuit. An advantage of finding a matching equivalent circuit for each transistor is the insight it provides into the correlation between each element to its physical dimension on the actual device. Therefore the equivalent circuit model can be used to possibly make improvements in the design of the transistor. The equivalent circuit can also provide helpful information for the device performance analysis, such as gain and noise [5]. It also can provide an estimate of results in a greater frequency range, if the measurement equipment is not capable of measuring the entire range needed [6].

The individual elements in the equivalent circuit were first found using two techniques: an analytical procedure which utilized curve fitting and required two measurements, one with the device "off" and another with the device "on", and an optimization procedure which only required one measurement. The equivalent circuit layout used, a common source configuration, is shown in Fig. 5 [7], with the gate, drain and source labeled as G, D, and S, respectively. This is a typical model for any FET. Other models could be used, but the capacitors and resistors in this model correlate well with the physical characteristics of the transistor.

Initially only the internal elements, shown in the red box, were used to find the equivalent circuit for both procedures. For several of the smaller transistors, this was all that was needed to create matching S-parameters of the model with the measured results. For the larger transistors, the external elements, which are the extrinsic parasitic elements, were added for a more accurate model. These external elements, independent of biasing [8], represent the finite length of the metallic strip between the probe tips and the semiconductor device and account for the parasitic capacitance and series inductance and resistance associated with the metal to metal contact. The leads of packaged devices can also attribute to the parasitic elements and can be represented in the external elements. In the layout in Fig. 5, each internal element is as follows: C_{GD}: gate-to-drain capacitance, C_{GS}: gate-to-source capacitance, C_{DS}: drain to source capacitance, R_{GS}: small gate-to-source channel resistance (charging resistance of C_{GD}), R_{DS}: drain to source resistance and Gm: transconductance. Tau is not shown in the layout but is an element of the equivalent circuit included in the voltage controlled current source, and it is the electron transit time through the channel. The capacitances $C_{GD,}$ C_{GS}, and C_{DS} are created from the small gaps between the gate, drain and source on the physical transistor itself. The gain of the device is produced by the dependent current generator, which depends on the voltage across $C_{GS,}$ leading to $|S_{21}| > 1$. The reverse signal path, S_{12}, is controlled solely by C_{GD} and is typically very small [9].

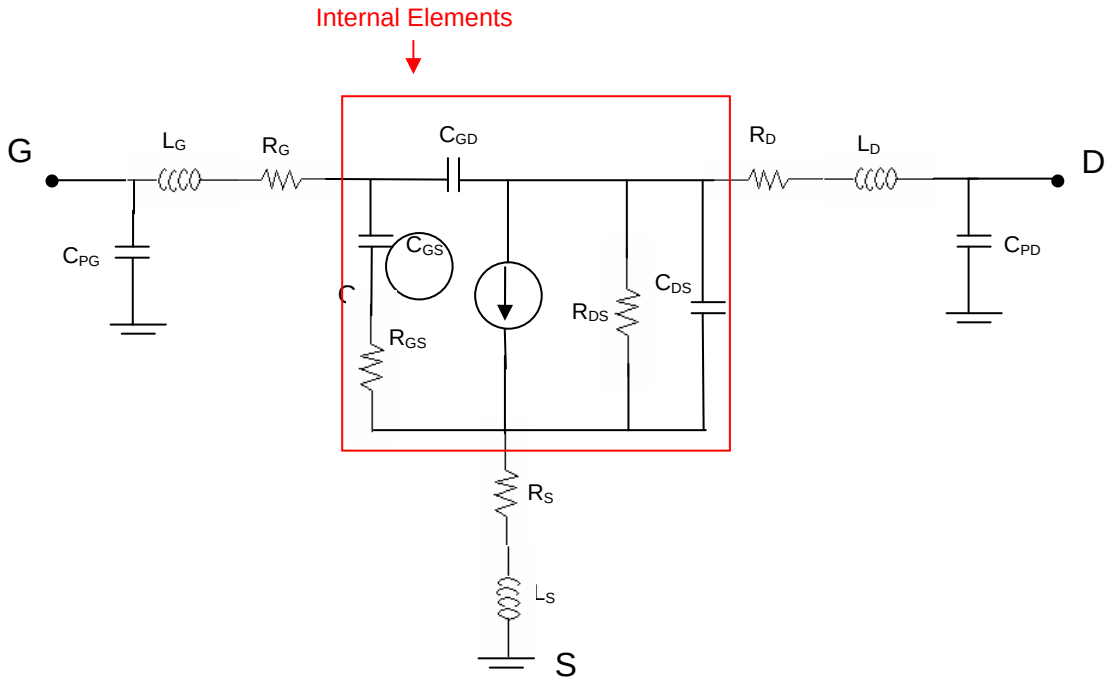

Fig. 5. Transistor equivalent circuit.

This layout was created in the schematic shown in Fig. 6 using ADS, and the elements were optimized to create matching S-parameters to the measured results. Originally, the values obtained from the curve fitting procedure were entered as a starting value, and the optimization proceeded to better fit the curves. The optimization was also run starting with random numbers (but still within a reasonable range), and it reached the same goal, confirming the accuracy of the optimization procedure. A conjugate gradient optimization was used to find the local optimum point, and then a random optimization was utilized to make sure that the minimum was not just a local minimum. One important thing to note about the optimization procedure is that it takes into account the effects of the interaction between the different elements. It simulates the circuit as a whole, whereas the curve fitting technique only analyzes the individual elements or a couple of them at a time. Therefore the efficiency and accuracy of the optimization eliminates the need for the more time-consuming linear curve fitting technique for each transistor. An initial estimate based on experience can be accurate enough for the optimization procedure to reach its optimal values [10]. The goal of optimization was to minimize the difference between the measured and simulated curves of all four S-parameters, each with equal weights. The analytic values were also used in a separate schematic and held constant for comparison. The results show the optimized results being the closer match, but all three, measured, analytic, and optimized, were similar.

Shown in Fig. 6 is the full equivalent circuit schematic used for the larger transistors. Parasitic series inductances and resistances and shunt capacitances were added to the gate and drain, and at the source, a series combination of inductance and resistance.

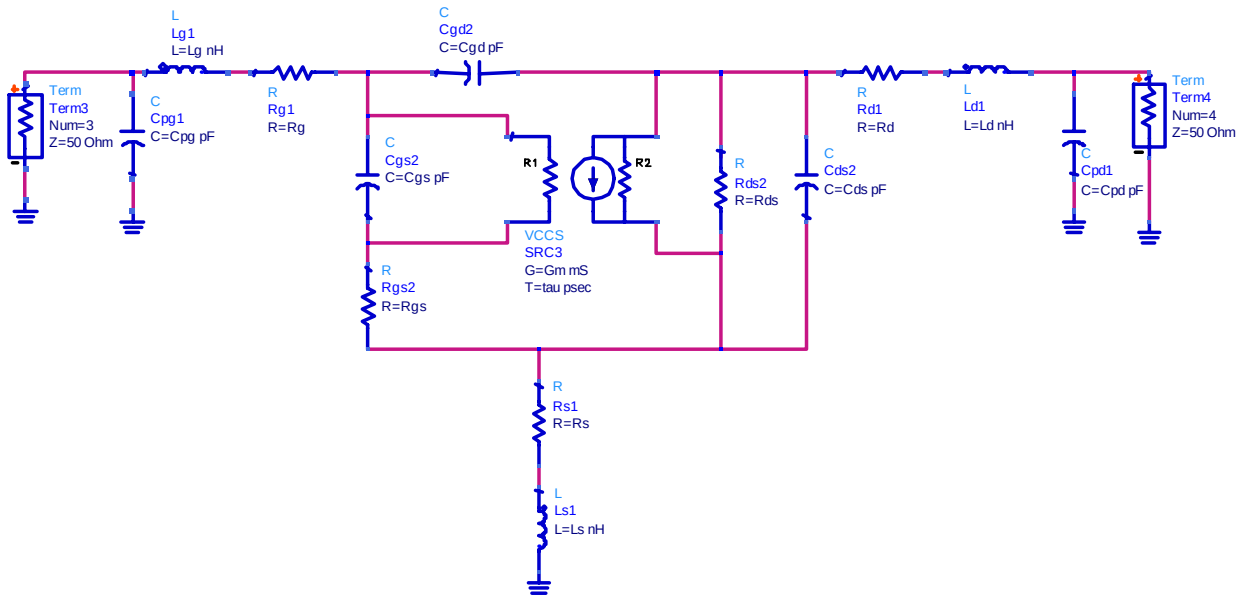

Fig. 6. Layout of equivalent circuit with external elements.

IV. RESULTS

The results for two different transistors, a small one and a large one, are included in tables listing the different element values and also in the form of the S-parameters plotted on Smith Charts. In Table 1, the elements from the small transistor are listed with the analytic values and the optimized values, with the percentage difference included in the last column. The difference is typically around 3%, indicating good agreement of the analytic procedure with the optimization. The reason for the larger percentage difference for C_{DS} is unknown; however, the optimized results do show better accuracy and this capacitance, which is nearly five times smaller than C_{GS}, does not have the deleterious effect that C_{GS} has on the performance of a common source amplifier.

Table 1. Element values for small transistor.

Small Transistor	Analytic	Optimized	Percent Difference
C_{GS} (pF)	0.5424	0.530	2.29
R_{GS} (Ω)	11.4	11.82	3.68
C_{GD} (pF)	0.1936	0.1981	2.32
Gm (mS)	16.94	16.55	2.3
R_{DS} (Ω)	277.3	285.6	2.99
C_{DS} (pF)	0.1424	0.1068	25
tau (ps)	7.1576	6.6662	6.92

From the small transistor listed in Table 1, Fig. 7 contains the results from simulations with only the internal elements, and Fig. 8 is with the external elements added to the previous model, both with the measured results in green, the analytic in blue, and the optimized results in magenta. On both Smith Charts, the better fitting curve is the one simulated with the optimized element values.

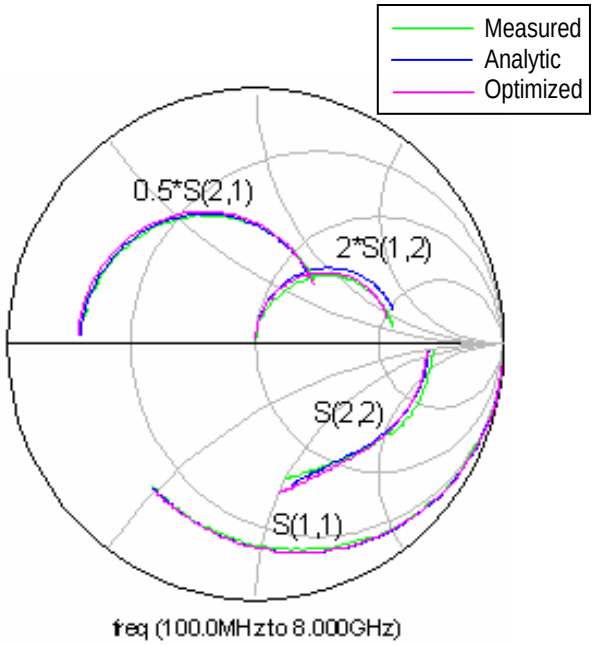

Fig. 7. Results with only internal elements.

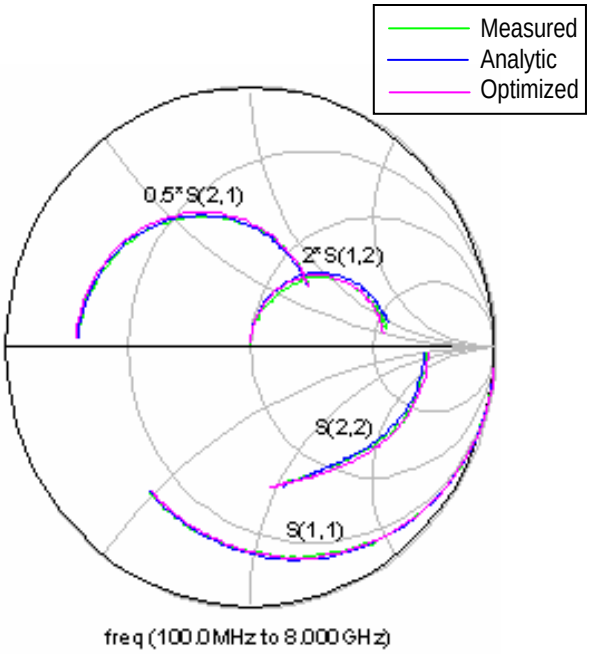

Fig. 8. Results with external elements.

In this case, the external elements create only a slightly closer match with the measured results, but the difference is not significant. As seen from these results from the small transistor, the network including only the internal elements is an accurate model for it. Therefore for simplicity, the equivalent circuit with fewer elements can be used for the small transistors.

In Fig. 9, a different, larger transistor is shown, labeled as Type 14. The top right picture is its physical layout, the larger blue picture is a layout of the die, with the red circles showing where this particular type of transistors are located, and the curves shown are the DC characteristic curves. All four of these Type 14 transistors contained on the individual die were measured with the probing station.

Table 2 below contains the optimized element values from the equivalent circuit for the Type14 transistor. The numbers, #1, #2, and #3, refer to three of the transistors measured at three different physical locations on the die, as shown in Fig. 9. The fourth transistor did not function properly and results are not shown from it. Each of the individual transistors was measured at several different bias voltages, and the bias voltages for each measurement are included in Table 3.

As seen in Table 2, the element values for each transistor vary at different bias points as the internal elements are bias-dependent [10], and they also vary between the three different transistors. These variations show the effect that DC biasing has on the intrinsic elements; different bias points produce different results. Also seen from the table is that no two transistors will produce identical results. They are similar but still not exact, as the measurement #1 (c) and the measurement #2 (a) were measured at the same exact bias voltages, but producing different results with different drain currents. Thus, to obtain a model that works perfectly for every transistor is a challenging task.

The S-parameters shown in Fig. 10 on the Smith Chart compare the measured results from one Type 14 transistor with the equivalent circuit with only the internal elements included and also with the results from the full equivalent circuit including the external parasitic elements. It can be seen that the circuit including the external elements is a better fit for this transistor, as this is one of the larger types measured and the external parasitics are more prevalent. The green curves are the measured data, the magenta is the optimized data with no external elements, and the blue curves are the optimized data with external elements. These results were typical for the larger transistors, showing that the full equivalent circuit creates a closer match for these devices and should therefore be used when modeling them. In particular, the results from the model including the external elements provide a much better match for S_{12} and S_{22} to the measured results, as the circuit with only internal elements could not produce an accurate agreement. The

optimized results for each transistor create a close match to the measured but are never exact. One possibility for inexact matching of the S-parameters is poor contact with the probe and the transistor. The wafer under test was particularly small and the vacuum system of the probe station was not efficient at holding the wafer in place, and instability of the probe tips may have occurred. This appears as "wiggles" at the upper frequency range. Overall, however, successful results were achieved, with accurate measurements and modeling.

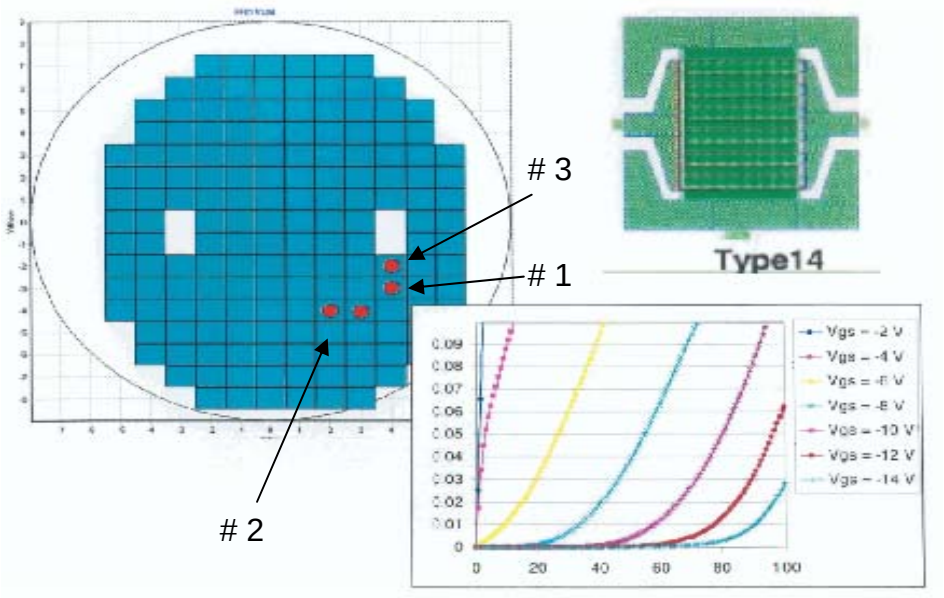

Fig. 9. Die layout, DC characteristic curves, and transistor layout.

Table 2. Element values for large transistor.

TYPE 14	C_{GS}(pF)	R_{GS}(Ω)	C_{GD}(pF)	Gm(mS)	R_{DS}(Ω)	C_{DS}(pF)	Tau(ps)
# 1 (a)	2.47389	1.26921	0.08195	66.2317	149.255	0.574277	14.5083
# 1 (b)	2.32202	1.60175	0.279425	64.9661	145.266	0.555315	14.4285
# 1 (c)	2.48972	1.21685	0.267132	76.6272	130.792	0.56288	14.3795
# 2 (a)	2.19978	0.693172	0.290189	59.5484	131.87	0.550824	13.8515
# 2 (b)	2.48747	0.528603	0.261274	79.0292	116.633	0.566017	13.898
# 3 (a)	3.1535	2.67609	0.265302	72.3178	132.464	0.657601	21.2513
# 3 (b)	3.1288	2.58207	0.222869	81.7162	124.204	0.645889	20.5984
# 3 (c)	3.57608	2.6709	0.20941	99.8517	102.227	0.676571	21.0207

Table 3. Bias voltages.

TYPE 14	V_{GS} (V)	V_{DS} (V)	I_D (mA)
# 1 (a)	-7	30	36
# 1 (b)	-7.5	48	45
# 1 (c)	-7	48	71
# 2 (a)	-7	48	54.5
# 2 (b)	-6	48	91.2
# 3 (a)	-6	20	39
# 3 (b)	-6	30	55.8
# 3 (c)	-5	25	109.1

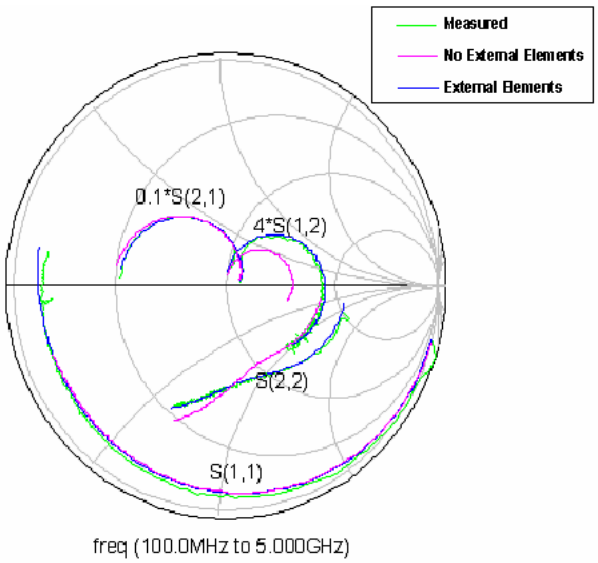

Fig. 10. Comparison of internal and external elements.

V. CONCLUSION

As seen from the above results, the optimization process yields a rather accurate model with little error for the transistor. A possible reason for this small error in inexact matching of the S-parameters is poor contact with the probe and the device under test. Some of the devices were so small that the vacuum system of the probe station was not efficient in holding the wafer in place, and instability may have occurred. In addition, it was shown that the external parasitic elements could be added to the circuit optimization with better expected results, albeit while taking more computational time.

ACKNOWLEDGMENTS

The authors would like to thank the U.S. Army Space and Missile Defense Command for sponsoring this research as part of the Radar Power Technology program.

REFERENCES

[1] R. R. Spencer and M. S. Ghausi, *Introduction to Electronic Circuit Design,* Upper Saddle River, NJ: Pearson Education, Chapter 7, pp. 301 – 370, 2003.

[2] R. J. Trew, "Wide bandgap semiconductor transistors for microwave power amplifiers," *IEEE Microwave Magazine,* vol. 1, no. 1, pp. 46-54, March 2000.

[3] Agilent Technologies' Advanced Design System (ADS) (2004A, Oct.). *Available: http://www.agilent.com* [Online]

[4] R. Gilmore and L. Besser, *Practical RF Circuit Design for Modern Wireless Systems, Volume II, Active Circuits and Systems*, Norwood, MA: Artech House, Chapters 1 – 3. pp. 1 – 192, 2003.

[5] G. Dambrine, A. Cappy, F. Heliodore, and E. Playez, "A new method for determining the FET small-signal equivalent circuit," *IEEE Transactions on Microwave Theory and Techniques,* vol. 36, no. 7, pp. 1151-1159, July 1988.

[6] G. Crupi, D. Xiao, D. M. M.-P. Schreurs, E. Limiti, A. Caddemi, W. De Raedt, and M. Germain, "Accurate multibias equivalent-circuit extraction for GaN HEMTs," *IEEE Transactions on Microwave Theory and Techniques*, vol. 54, no. 11, pp. 3616-3622, November 2006.

[7] M. C. Lau, "Small signal equivalent circuit extraction from a Gallium Arsenide MESFET device," *Master's Thesis*, Virginia Polytechnic Institute and State University, July 1997.

[8] M. J. McCullagh, *RF Amplifier Design*, printed and published by The IEE, Savoy Place, London WC2ROBL, UK, 2000.

[9] D. M. Pozar, *Microwave Engineering*, 3rd ed., New York: John Wiley & Sons, Chapter 5, 10, and 11, pp. 222 – 265, 486 – 576, 2005.

[10] A. Sayed and G. Boeck, "Two-stage ultrawide-band 5-W power amplifier using SiC MESFET," *IEEE Transactions on Microwave Theory and Techniques,* vol. 53, no. 7, pp. 2441-2449, July 2005.

Lisa Jordan graduated from the University of Mississippi in May of 2004 with a Bachelor of Science in Electrical Engineering. She continued her education at Ole Miss and pursued a master's degree in electrical engineering with an emphasis in electromagnetics. She received her Master of Science in December, 2006. While studying for her master's degree, she first worked as a research assistant for Dr. Elliott Hutchcraft and then began working for Radiance Technologies in Oxford, MS. She currently lives in Bangkok, Thailand, teaching English and Java programming at Mahidol Wittayanusorn School, a Thai math and science high school.

Dalia Elsherbeni received an undergraduate degree in electrical engineering from The University of Mississippi in 2004. In December 2006 she received a Master's degree in electromagnetics at the University of Mississippi. Her thesis entitled, "Measurement of Non-Coaxial RF Components Using the TRL Calibration Technique" was written under her advisor Dr. Elliott Hutchcraft. Ms. Elsherbeni is a member of IEEE.

She was the recipient of the Mississippi Academy of Sciences (MAS) Third Place Oral Presentation Award in Vicksburg, MS in 2006. Since 2004 she has been employed full time by Radiance Technologies working in the technology and development department.

W. Elliott Hutchcraft was born in Lexington, Kentucky on April 29, 1973. He earned his B.S. in electrical engineering at the University of Mississippi, Oxford, MS in 1996, his M.S. in electrical engineering at the University of Mississippi, Oxford, MS in 1998 and his Ph. D. in electrical engineering at the University of Mississippi, Oxford, MS in 2003. He is an Assistant Professor in the Department of Electrical Engineering at the University of Mississippi in Oxford, Mississippi. Dr. Hutchcraft is a member of Eta Kappa Nu, Sigma Xi, IEEE, Tau Beta Pi, Phi Kappa Phi, and ARFTG.

Richard K. Gordon was born in Birmingham, Alabama on November 26, 1959. He earned his B.S. in physics at Birmigham Southern College, Birmingham, AL in 1983, his M.S. in mathematics at the University of Illinois, Urbana, IL in 1986 and his Ph. D. in electrical engineering at the University of Illinois, Urbana, IL in 1990. He is an Associate Professor in the Department of Electrical Engineering at the University of Mississippi in Oxford, Mississippi. Dr. Gordon is a member of Eta Kappa Nu, Phi Beta Kappa, and Tau Beta Pi.

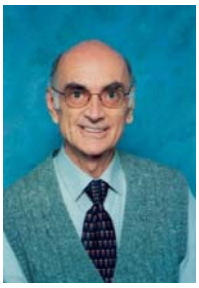

Darko Kajfez is Emeritus Professor of Electrical Engineering at the University of Mississippi. He obtained the electrical engineer's degree (Dipl. Ing.) from University of Ljubljana, Slovenia, in 1953, and the PhD degree from U.C. Berkeley in 1967. He co-edited the book *Dielectric Resonators*, and authored the books *Notes On Microwave Circuits*, and *Q Factor*. His research interests include rf and microwave measurement and analysis. He can be reached at eedarko@olemiss.edu.

Extracting the Electrical Properties of Polymeric Composite Materials through Circuit Simulation and Optimization

[1]L. Bennett, [1]W. E. Hutchcraft, [1]R. K. Gordon, [2]E. Lackey, [2]J. G. Vaughan, and [2]R. Averill

[1] Department of Electrical Engineering,
University of Mississippi, University, MS 38677-1848, USA
lpbennet@olemiss.edu, eeweh@olemiss.edu, eegordon@olemiss.edu

[2] Department of Mechanical Engineering
University of Mississippi, University, MS 38677-1848, USA
melackey@olemiss.edu, mejgv@olemiss.edu, raverill@hotmail.com

Abstract **–** The electrical properties of polymeric composite materials were extracted from measured data using optimization techniques in Advanced Design System (ADS), a circuit simulation tool. A vector network analyzer was used to measure the S-parameters of the composite materials. The materials were inserted in an X-band waveguide and measured from 8 GHz to 13 GHz. The measured data was used to reconstruct the relative permittivity and loss tangent against a modeled setup in ADS. Two techniques were implemented in the reconstruction of the permittivity, one with the permittivity and loss tangent assumed to be constant and the other with them considered to be a function of frequency. The results show that for both techniques the modeled data does converge to the measured data yielding an optimized permittivity and loss tangent.

Keywords**:** Permittivity, loss tangent, optimization, and composite materials.

I. INTRODUCTION

Polymeric composite materials have gained a growing interest in the electromagnetic community. These materials can be tailored to provide desired effects, such as being transparent or conductive in the microwave frequency range. In order to make these composites with the desired effects, one must know the electrical properties of such materials. Thus, it is important to find new ways to take more accurate and efficient measurements from these materials in the microwave frequency range.

Material measurements are a broad and growing field in the microwave community. There are many methods for measuring electrical properties of materials such as resonant cavity methods or reflection methods [1].

In the experimental setup for this study, a reflection/transmission waveguide method was used to measure the S-parameters of the composite material. The Nicholson Ross Weir (NRW) algorithm and other variation of this method have been traditionally used to reconstruct the permittivity and/or permeability from the measured data [2-7]. Instead of using one of those approaches, ADS was used to extract the permittivity and loss tangent of these materials through optimization.

The measurement setup and ADS layouts will be shown and discussed in detail in the experimental setup section. A comparison between the optimizing permittivity and loss tangent as a constant and as a function of frequency will be made in the results and discussion section. Then, conclusions will be drawn from the results about the extraction of the permittivity for these low loss composite materials.

II. EXPERIMENTAL SETUP

The S-parameters of the composite materials were measured with an HP 8510C vector network analyzer. Composite materials were placed in a brass waveguide. The waveguide itself was X-band, with a length of 15.88 cm. A relatively low loss composite that was made with E-glass fiber and polyester resin was used as the material under test (MUT) for this investigation. This composite filled the entire 15.88 cm of the test fixture. Having a MUT of this length is known to cause difficulties with the NRW algorithm, but there is not a problem using the optimization technique. A Thru-Reflect-Line (TRL) two port calibration was done on the network analyzer. Once the composite was measured, the data was imported into ADS to find the permittivity and loss tangent.

The goal of the design was to determine values for permittivity and loss tangent so that the measured S-parameters matched the S-parameters from a circuit simulation model. The modeled setup consisted of a dielectric filled waveguide that has the same dimension as the actual waveguide that was used to take the

measurements. For the electrical properties, it was assumed that the composite material was homogenous and isotropic, only the reflection and transmission are needed to satisfy the experimental goals.

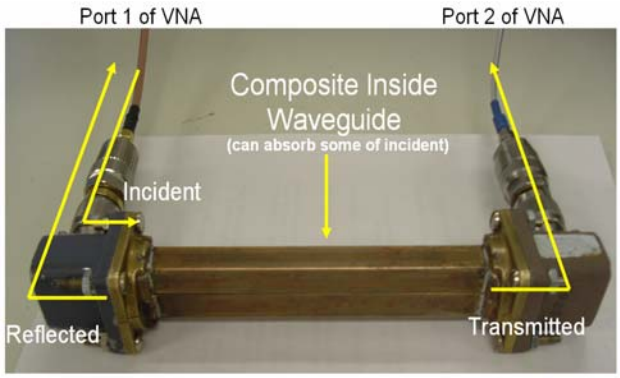

Fig. 1. Photograph of the waveguide used to measure the reflection/transmission behavior of the composite samples [8].

Two different types of setups were made in ADS to reconstruct the permittivity of the materials. In these two setups, it was also assumed that these composite materials were not magnetic. The first setup considered the complex permittivity to be constant along the span of the tested frequency range. The second setup allowed the permittivity and loss tangent to vary linearly or quadratically as a function of frequency. Equations (1) and (2) are the permittivity and loss tangent for the linear setup, respectively. Equations (3) and (4) are the permittivity and loss tangent for the quadratic setup. This allowed the permittivity and loss tangent to be unique in the given frequency range. Note that constants A, B, C, D, E, and F were considered as variables that ADS was solving for in the optimization process. The variables were optimized to meet the goal requirements at each frequency. These goals, which are seen in Fig. 2, were to minimize the difference between the measured and modeled reflection (S11) and transmission (S21) coefficients. The weights of each goal could be varied, and this could be of importance for a lossy composite, but for this investigation, the weights were equal.

$$Er = 1 + \left| A + B * (freq / 10^9) \right|, \quad (1)$$

$$TanD = \left| C + D * (freq / 10^9) \right|, \quad (2)$$

$$Er = 1 + \left| A + B * (\tfrac{freq}{10^9}) + C * (\tfrac{freq}{10^9})^2 \right|, \quad (3)$$

$$TanD = \left| D + E * (\tfrac{freq}{10^9}) + F * (\tfrac{freq}{10^9})^2 \right|. \quad (4)$$

ADS has several built-in optimization types available such as the random, gradient, or genetic algorithm methods. Random optimization was applied first to help narrow the optimization range. It also was important to use this optimization technique because it is not susceptible to convergence to a local maximum or minimum solution. Once the optimization range was reduced, the gradient technique was applied to further satisfy the goals. The gradient technique was also chosen because of its speed in converging to the minimum.

III. RESULTS AND DISCUSSION

A comparison between the measured and modeled S-parameters will be made in the following figures. The permittivity and loss tangent will also be shown for each method to finalize the results.

Figures 3 and 4 show the optimized real permittivity and loss tangent of an air filled waveguide using a linear model for the frequency dependence.

This data was generated to insure that the program was working properly by investigating air as a known standard. As it can be seen in Fig. 3, the program optimized the real permittivity to one. The loss tangent was optimized from 0.00034 to 0.00056, which is relatively close to zero. This test provided expected results and insured that our measurements and modeling were working properly.

Figures 5 and 6 show the reflection and transmission when both the permittivity and loss tangent of the material is considered to be constant, thus assuming the material under measurement is perfectly homogenous and not frequency dependent. In both these figures, the reflection and transmission from the modeled data does converge to the measured data. Looking at the figures, it shows the transmission does not match up quite as well as the reflection. There seems to be a few discrepancies between the modeled and measured data at the peaks for both goals. In both graphs there seems to be no more than a 0.5 dB in error which is almost negligible.

Figures 7 and 8 show the results where the permittivity and the loss tangent were allowed to vary linearly over the frequency range. For both the transmission and reflection, the modeled results compare better to the measured data than the previous method. This can be seen more clearly in Fig. 11 which compares the measured data against both the constant and frequency dependent real permittivities. This would indicate that the material itself is not ideally frequency independent.

Figures 9 and 10 illustrate the case when the permittivity and loss tangent vary in a quadratic fashion. From the figures one can see that the goals matched up just as well as the linear case, if not better. The profile of the modeled data is almost mirrored to the measured data for both goals. Seen in Fig. 11 one can see that both the linear and quadratic goal for the transmission is in close proximity to the measured data. It should also be noted

that both the quadratic/linear method satisfied the goals better than the constant method thus considering the frequency dependent methods to be the correct approach on optimizing the electromagnetic properties for this type of composite material.

The resulting permittivity and loss tangent for both methods can be seen in Figs. 12 and 13. The constant setup yielded a real permittivity of 4.26 and loss tangent of 0.0106. While for both the frequency dependent cases yielded a real permittivity in the range of 3.4 to 3.7 and loss tangent of 0.0123 to 0.01257. It should also be pointed out that the ranges for the permittivity and loss tangent are considerably small for the frequency dependent methods. If one would enlarge the ranges the permittivity and loss tangent would appear to be constant.

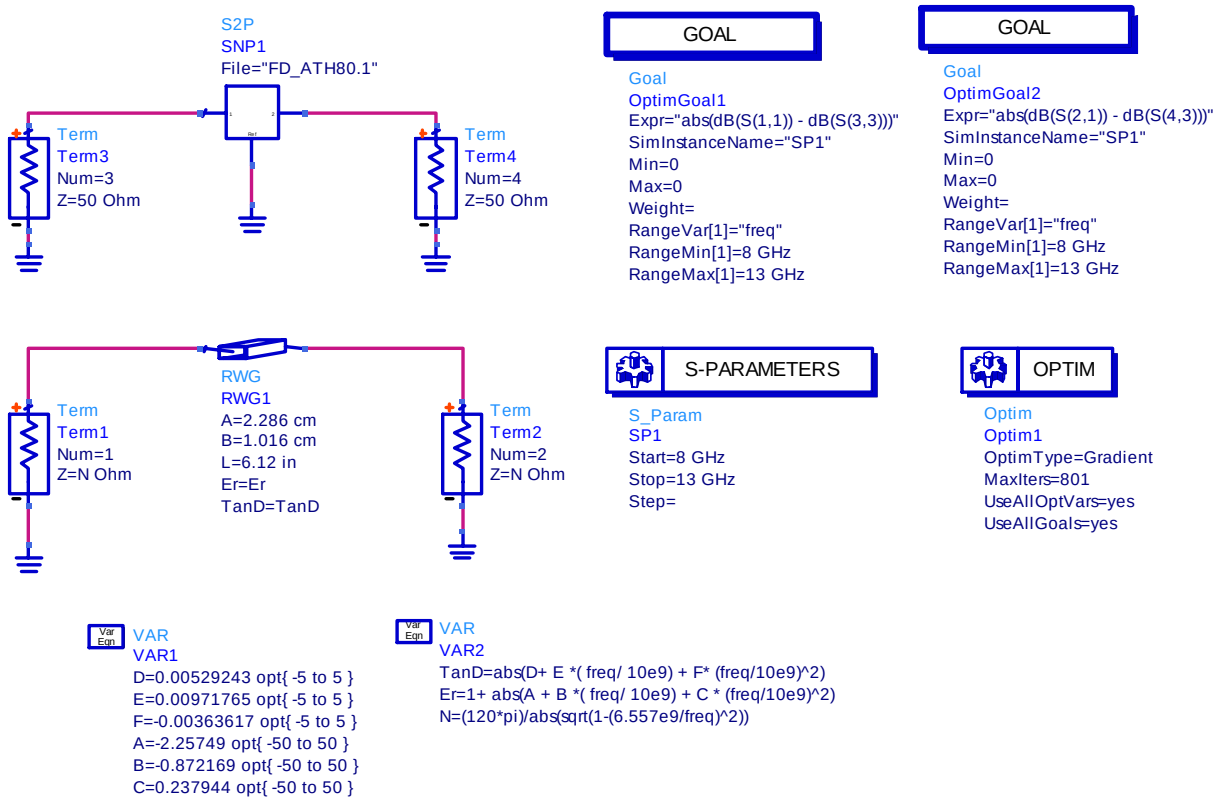

Fig. 2. ADS schematic layout for optimizing permittivity and loss tangent.

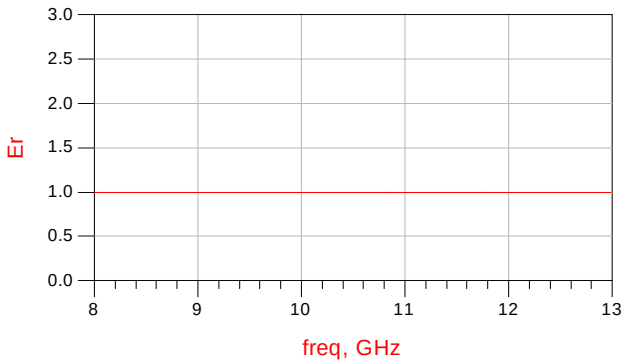

Fig. 3. Real permittivity for air filled waveguide using the linear model.

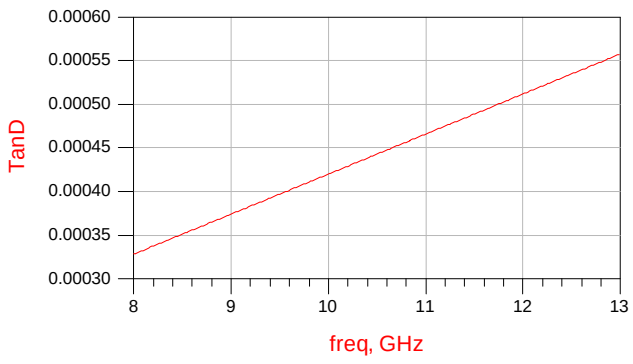

Fig. 4. Loss tangent for air filled waveguide using the linear model.

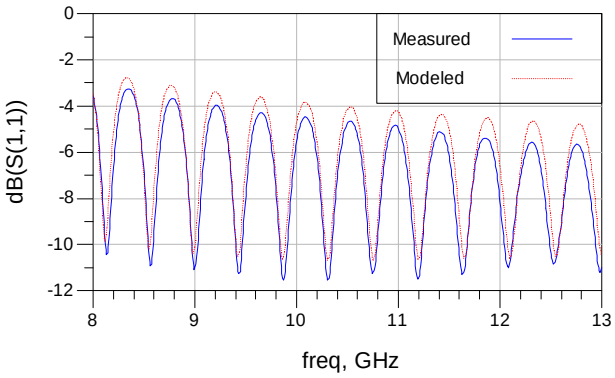

Fig. 5. Return loss for the constant permittivity setup.

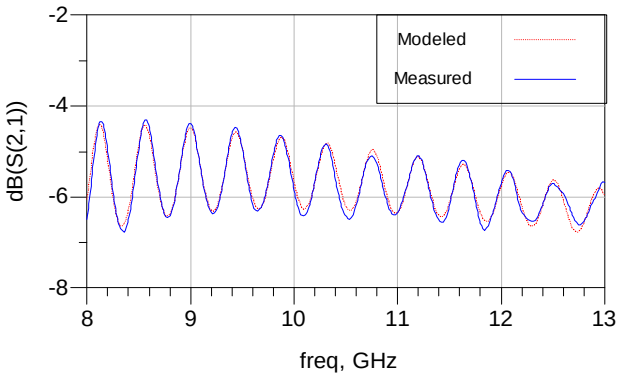

Fig. 8. Insertion loss for the linear permittivity setup.

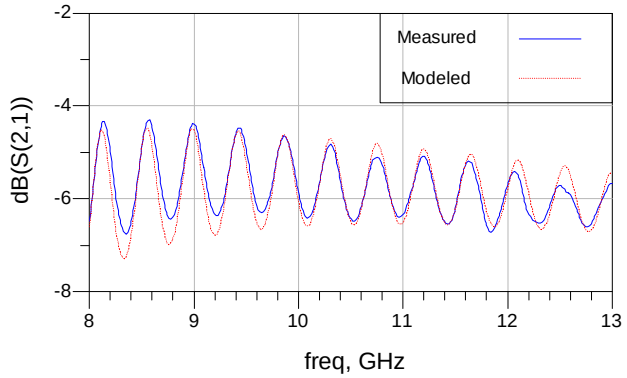

Fig. 6. Insertion loss for the constant permittivity setup.

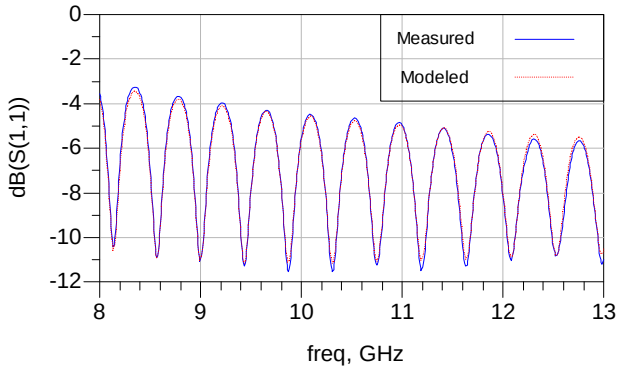

Fig. 9. Return loss for the quadratic permittivity setup.

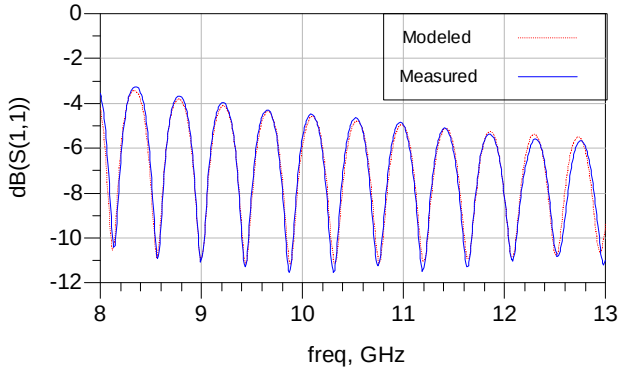

Fig. 7. Return loss for the linear permittivity setup.

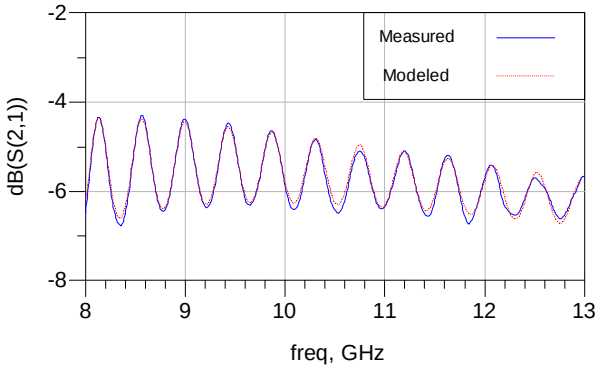

Fig. 10. Insertion loss for the quadratic permittivity setup.

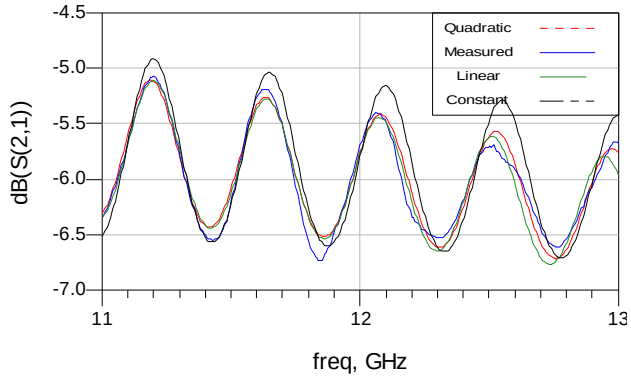

Fig. 11. Insertion loss for the constant and frequency dependent permittivity setups in a narrow frequency range.

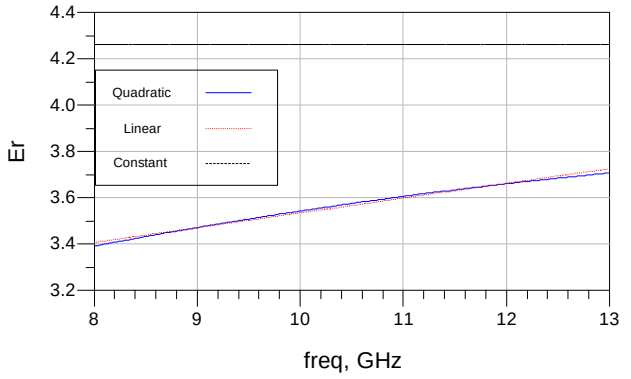

Fig. 12. The real permittivity of the constant and frequency dependent setups.

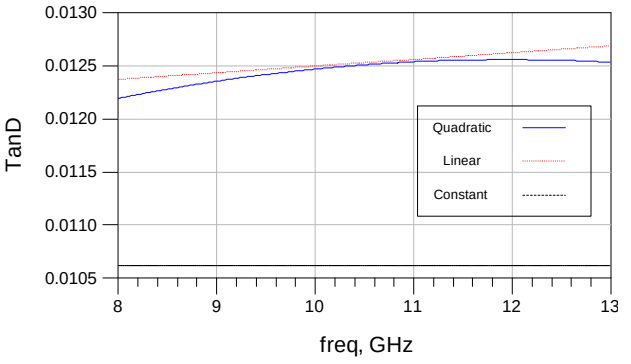

Fig. 13. The loss tangent of the constant and frequency dependent setups.

IV. CONCLUSION

The permittivity and loss tangent were found for both setups. A comparison was made for each method. Other methods consider the MUT to be frequency independent, and this technique does not require that. Allowing the frequency dependency doesn't change the outcome greatly, but it does indeed match the measured data better. In future research, this method can be improved for various other types of composite materials, such as highly conductive materials or composites made with veils. Since these materials could be very frequency dependant, a more elaborate model might be necessary.

REFERENCES

[1] L. F. Chen, C. K. Ong, C. P. Neo, V. V. Varadan, and V. K. Varadan, *Microwave Electronics: Measurement and Materials Characterization*, pp 37-38, John Wiley and Sons, Inc., New York, 2004.

[2] A. M. Nicolson and G. F. Ross, "Measurement of the intrinsic properties of materials by time domain techniques," *IEEE Trans. Instrum. Meas.*, vol. IM-17, pp. 395-402, Dec. 1968.

[3] W. W. Weir, "Automatic measurement of complex dielectric constant and permeability at microwave frequencies," *Proc. IEEE*, vol. 62, pp. 33-36, Jan. 1974.

[4] J. B.-Jarvis, E. J. Vanzura, and W. A. Kissick, "Improved technique for determining complex permittivity with the transmission / reflection method," *IEEE Trans. Micro. Th. Tech.*, vol. 38, no. 8, Aug. 1990.

[5] G. A. Deschamps, "Determination of reflection coefficients and insertion loss of a waveguide junction," *IA. P. Pl. Phys.*, vol. 24, no. 8, pp. 1046-1051, Aug. 1953.

[6] M. S. Freeman, R. N. Nottenburg, and J. B. DuBow, "An automated frequency domain technique for dielectric spectroscopy of materials," *J. Phys. E: Sri. Instrum.*, vol. 12, pp. 899-903, 1977.

[7] S. S. Stuchly and M. Matuszewski, "A combined total reflection transmission method in application to dielectric spectroscopy," *IEEE Trans. Instrum. Meas.*, vol. IM-27, pp. 285-288, Sept. 1978.

[8] J. G. Vaughn, E. Lackey, E. Hutchcraft, and R. Gordon, "Some effects on mineral fillers on electrical characteristics on Pultruded composites," *Composites 2006*. 2006.

[9] D. M. Pozar, *Microwave Engineering*, Third Edition, John Wiley and Sons, Inc., New York, 2005.

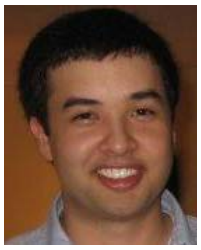

Lorenzo P. Bennett Jr. graduated from the University of Mississippi with a bachelor's degree in electrical engineering in 2005. Since then, he is currently pursuing his master's degree in electrical engineering with an electromagnetic emphasis at the University of Mississippi. In his study, he has been learning how to characterize EM properties of composite materials through various methods. During the summer of 2004, he interned at SPAWAR, in San Diego, California, with the telecommunications branch. While he was there he learned about mobile ad-hoc networks and radio systems. He is a member of Tau Beta Pi and Eta Kappa Nu, both academic engineering societies. He is also a member of Phi Kappa Phi. Lorenzo is an IEEE member and served as treasurer of IEEE's Ole Miss section for one year. While not in school, he enjoys working out at the gym and playing sports.

W. Elliott Hutchcraft was born in Lexington, Kentucky on April 29, 1973. He earned his B.S. in electrical engineering at the University of Mississippi, Oxford, MS in 1996, his M.S. in electrical engineering at the University of Mississippi, Oxford, MS in 1998 and his Ph. D. in electrical engineering at the University of Mississippi, Oxford, MS in 2003. He is an Assistant Professor in the Department of Electrical Engineering at the University of Mississippi in Oxford, Mississippi. Dr. Hutchcraft is a member of Eta Kappa Nu, Sigma Xi, IEEE, Tau Beta Pi, Phi Kappa Phi, and ARFTG.

Richard K. Gordon was born in Birmingham, Alabama on November 26, 1959. He earned his B.S. in physics at Birmigham Southern College, Birmingham, AL in 1983, his M.S. in mathematics at the University of Illinois, Urbana, IL in 1986 and his Ph. D. in electrical engineering at the University of Illinois, Urbana, IL in 1990. He is an Associate Professor in the Department of Electrical Engineering at the University of Mississippi in Oxford, Mississippi. Dr. Gordon is a member of Eta Kappa Nu, Phi Beta Kappa, and Tau Beta Pi.

Ellen Lackey is an associate professor of mechanical engineering at the University of Mississippi (UM). She also holds a certified composites technician instructor (CCT-I) certification from the American Composites Manufacturers Association. She has been involved with composite materials research for the past sixteen years. During this time, she has conducted projects related to mechanical and physical property characterization of polymeric composites, microscopy, and development of composite manufacturing techniques.

Dr. James Vaughan is a F. A. P. Barnard Distinguished Professor of Mechanical Engineering and Associate Dean of the School of Engineering at The University of Mississippi. Professor Vaughan also serves as the director of the Composite Materials Research Group (CMRG) which he founded at the University. Since its inception in 1987, the CMRG has been actively involved in composite materials research and has developed an internationally recognized program in pultrusion research serving both suppliers and manufacturers.

Reid Averill is currently the Technical Sales Manager for Inspec Foams, ROHACELL, North America. Reid is in the final stages of completing his thesis in studying the behavior of low cost composite materials which absorb and reflect electromagnetic radiation. Reid has 4 years experience in the composite industry.

A Review of Statistical Methods for Comparing Two Data Sets

[1]A. Duffy and [2]A. Orlandi

[1] School of Engineering and Technology
De Montfort University, The Gateway, Leicester LE1 9BH
apd@dmu.ac.uk

[2] UAq EMC Laboratory
University of L'Aquila, L'Aquila, Italy I-67040
Orlandi@ing.univaq.it

Abstract – Statistical approaches to compare data for validation of computational electromagnetics have been used for several years. They provide an accepted means of obtaining a numerical value to quantify the data under consideration. However, the use and meaning of these 'numbers' depends, by necessity, on the application. This paper provides an overview of some of the most widely applicable techniques, relating the output of these to visual assessment. It further includes comparison with the FSV (Feature Selective Validation) method allowing a triangulation between statistical approaches, visual approaches and heuristic approaches to validation. It is important that the decision to use or reject a particular technique for validation is based on a rational and objective selection approach. This paper suggests a framework to support this selection approach.

Keywords: Validation, statistical analysis, and feature selective validation.

I. INTRODUCTION

The complexity of electromagnetic systems being analyzed and modeled can produce results which are, themselves, excessively complicated. This is particularly true when models tend 'in the limit' to replicate reality. Statistical electromagnetics is a topic that has become part of the general approach to study the results from these simulation activities. A standard starting point for statistical electromagnetics is [1]. A more recent contribution to the need for a better understanding and application of statistics in electromagnetics is [2] where the *a priori* assumption that there are unknown contributors to the model is acknowledged and these can be treated statistically. In both cases, these publications demonstrate the benefits to be gained by considering a statistical analysis under appropriate circumstances. However, correct application relies on appropriate selection and while there are obvious circumstances where one, or other, technique can be applied; there are many other circumstances where non-statistical approaches are more appropriate. This paper presents a short overview of statistical and non-statistical approaches for validation with the aim of helping those involved in validation make more appropriate selection of techniques to quantify the comparison of numerical data with experimental data or with other numerical models.

Validation of numerical models involves determining whether the agreement of a simulation with experiments, other simulations or analytically resolvable systems is adequate. Identifying what 'adequate' means may, in practice, involve the following:

- Expectations of agreement based on previous experience.
- Accounting for known assumptions embedded in both or either the model or (e.g.) the experiments.
- The end application to which the model is being used.

Clearly, accounting for these does suggest that there will only rarely be an absolute pass/fail decision to be made and more frequently whether there is a high / low probability that the model is good enough. The concept of defining adequacy as part of a model validation framework is likely to become a more relevant and pertinent issue in the near future as concepts such as satisfactions [3-4] and error budgets in models become part of the language of modelers.

The use of statistics in the validation of computational electromagnetics is not clearly defined. Hence, reviewing some of the statistical validation options does appear to be a relevant contribution to the debate on how best to perform quantitative validation. An example of the current state of the debate can be seen in the topic of modeling reverberation chambers, particularly in comparing models against experiments, where, one hand, [5] suggests that the nature of the reverberation chamber is such that the probability distribution of the fields is an appropriate way of comparing the models with measurements. On the other hand, [6] suggests that it is relatively straightforward to get statistical agreement even if there is total disagreement between the actual modeled and measured results.

This paper provides a general overview of some of the more widely used statistical techniques and compares them against a sub-set of visual assessments. Visual assessment, the "eye-balling" of graphs, is probably the most common, widespread and accepted approach to validation. It is important that any approach to quantify results for validation purposes is empathetic to this and not in opposition. Hence, the use of a set of comparisons for which a bank of visual assessments is available is seen as a reasonable starting point to analyze the potential contribution for a bank of possible statistical techniques. An increasingly popular heuristic approach, FSV (Feature Selective Validation) is reviewed and a simple approach to quantifying visual comparisons is also reviewed.

II. TEST DATA

In order to be able to discuss the various techniques later in this paper, some test data is required to illustrate the quality of the comparisons. The first column of Fig. 1 shows three comparison graphs. Approximately 50 engineers were asked their assessment of these comparisons using a six point rating scale which are presented in histogram form in column 2 of Fig. 1 (these results are a subset of those presented in [7], where further methodological details are also presented). The use of the terms for the histograms is based on common natural language descriptors. The visual rating scale used is presented in Fig. 2.

A mean value was determined for these three comparisons by averaging the numerical scores from the survey. According to the visual assessment 'Graph 4' (average score 5.95) is the worst, 'Graph 5' is the best (average score 4.56) and 'Graph 8' is approximately mid-way between the other two (5.36). This provides a benchmark to test candidate statistical approaches. In particular, agreement in rank-ordering the results would be expected from any technique used because, often, the absolute score is not as important as knowing whether one comparison is much better or worse than another comparison.

III. STATISTICAL TECHNIQUES[1] [9 - 12]

III.1. Correlation and visually based approaches

The most common approach to correlate two sets of data is the Pearson r correlation, which provides a numerical measure of how closely related two variables are.

The Pearson Correlation Coefficient is calculated using equation (1),

$$r = \frac{\sum xy - (\sum x \sum y)/n}{\sqrt{(\sum x^2 - (\sum x)^2/n)(\sum y^2 - (\sum y)^2/n)}} \quad (1)$$

X = data set 1,
Y = data set 2,
n = Total number of points in both data sets.

An alternative correlation technique is the Spearman Rank Correlation. Which measures the association of the ranks of the two variables. The point at which the largest value of the data-set occurs would be given a rank of 1; the next largest point would be given a rank of 2 and so on. The Spearman Rank Correlation is then based on the difference between the ranks for the two data sets. No results are presented for this here, it is simply mentioned to demonstrate that even for something as apparently straightforward as correlation, there are a number of options open to the modeler.

Correlation values have the range [-1,+1] with +1 indicating a perfect positive correlation and -1 a perfect negative correlation (i.e. a change in one variable produces an opposite change in the other variable).

A scatter-plot can be used to provide a visual indication of the correlation of the two sets of data. Here, the numerical values of the data sets are put into two columns; the notional independent axis information presented in the original data sets is ignored. These columns then form the x and y coordinates of the plotted graph. The closeness of the resulting data to a straight line indicates the level of association between the two data sets.

Boxplots provide a summary of the data distribution for the individual data sets by determining the distribution of the data displaying a box representing the upper and lower quartiles of the distribution, with the median value given as a straight line within this box. Fences give the extremes and outliers are specifically highlighted. From here, outlier values can be removed. However, the removal of outliers may not be appropriate in electromagnetics as an outlier could represent a correct, but extreme; result such as a high Q resonance.

The Pearson correlation coefficients for the three sets of data in Fig. 1 are given in Table 1.

Table 1. Correlation coefficients (Pearson r) for the three comparisons above.

	"Graph 4"	"Graph 5"	"Graph 8"
Correlation Coefficient	0.022	0.383	0.040

The scatterplots and boxplots are given in Fig. 3. "Data A" and "Data B" refer to the two data sets presented on each graph.

[1] All data has been generated using the SPSS statistical Software package

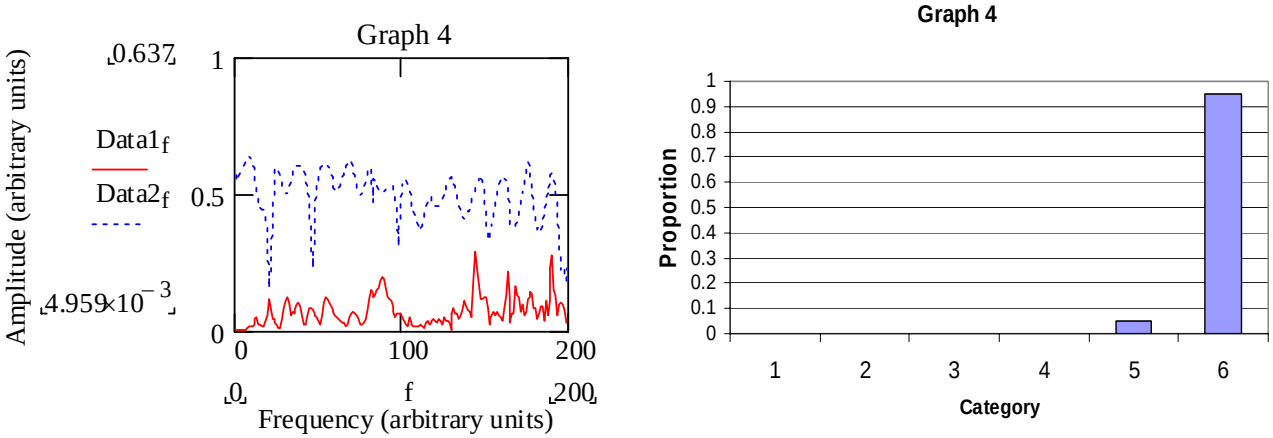

(a) Data and visual assessment of 'Graph 4' from [7].

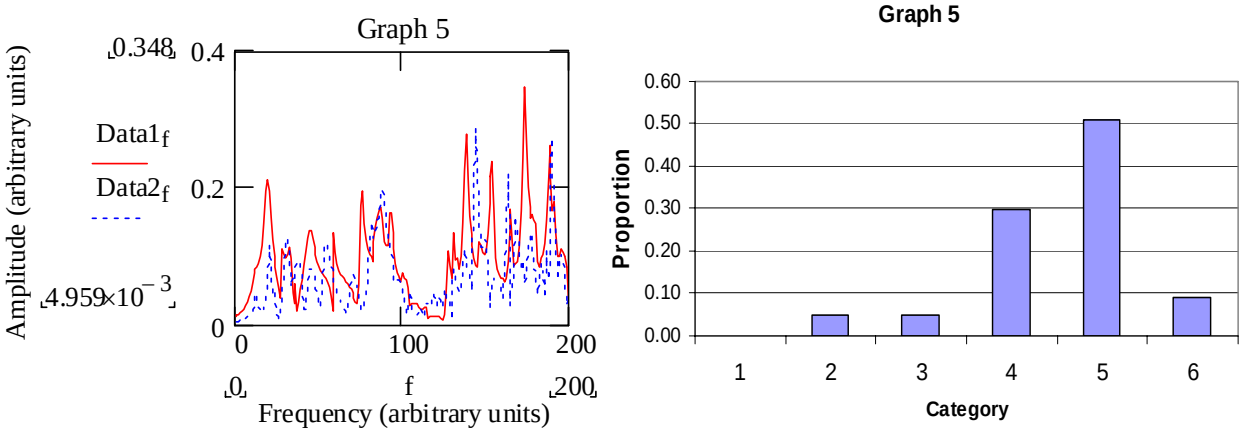

(b) Data and visual assessment of 'Graph 5' from [7].

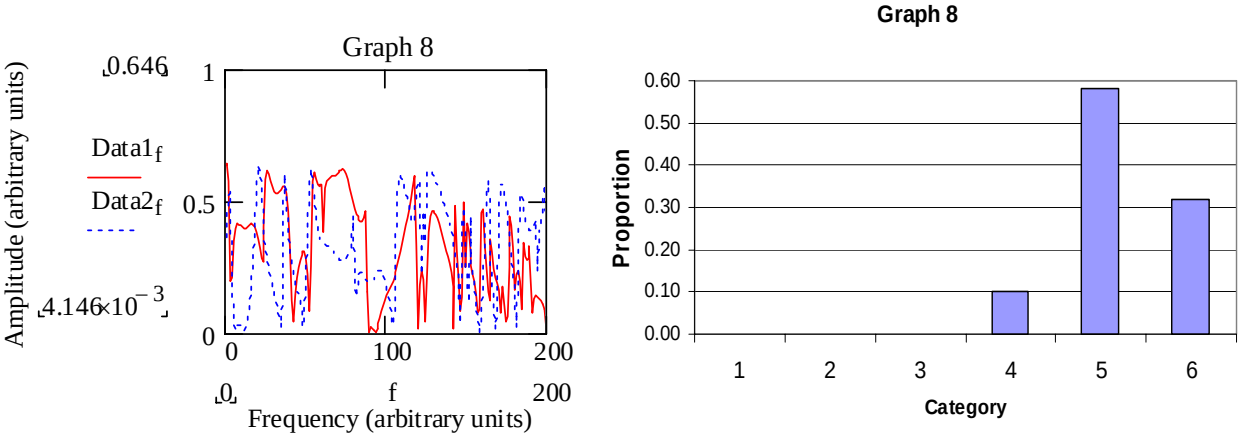

(c) Data and visual assessment of 'Graph 8' from [7].

Fig. 1. Original data for comparison and visual assessment based on approximately fifty responses. The Graph number refers to that used in [7]. The categories (x axis) in column 2 are 1- excellent, 2 - very good, 3 - good, 4 - fair, 5 - poor, and 6 - very poor.

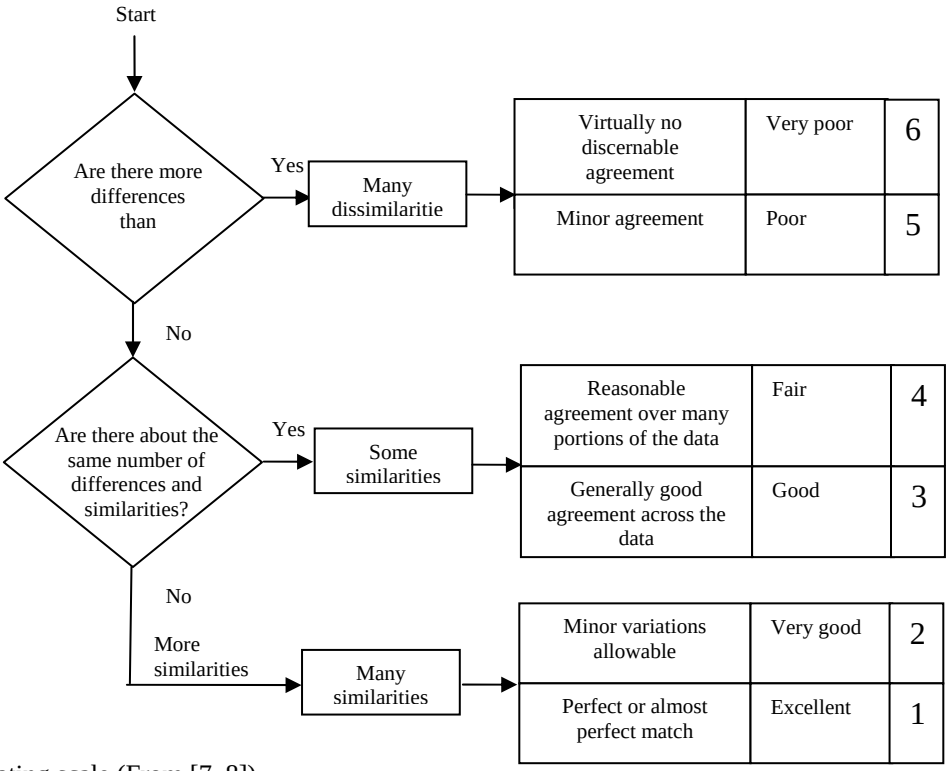

Fig. 2. Visual rating scale (From [7, 8]).

These statistics show some interesting properties. The rank ordering of the correlation coefficients is the same as the visual rank-ordering. However, the magnitude of the differences does not reflect the visual assessment. The generally low level of correlation could be seen to reflect the visual assessment. The scatterplots suggest that “Graph 8” is random, “Graph 4” has a slightly better association (the points are less randomly distributed across the graph) and “Graph 5” almost shows a hint of a positive gradient straight line. Interpretations of the scatterplots also support the visual assessment. The boxplots simply relate the data distributions with “Graph 8” clearly showing the greatest agreement.

III.2. Parametric tests

It is inappropriate to make the assumption that the data has a normal probability distribution, an implicit requirement of parametric tests, i.e. tests which consider the comparison of data parameters, such as means. However, for large sample sizes, the Central Limit Theorem does allow parametric tests to be used. The most common of these, the Student’s t-test evaluates the difference in means for two groups. The resulting p-level gives a probability of error associated with rejecting the null hypothesis, i.e. the hypothesis that there is no difference in the two groups, when, in fact the hypothesis is correct. The results are summarized in Table 2.

Table 2. t-test results for the three original data sets.

	“Graph 4”	“Graph 5”	“Graph 8”
t-parameter	-56	4.7	0.7
P value	0.000	0.000	0.473

These values show that only the data in “Graph 8” are similar. It shows that “Graph 4” is the worst comparison. Of course, as the purpose of the t-test is to compare means of groups, the results will confirm what has been demonstrated in the Boxplots of Fig. 3

III.3. Non-parametric tests

Non-parametric tests make no assumptions about the normality or otherwise of the data. They take into account the shape of the distributions. Two popular tests in electromagnetics are the χ^2 test and the Kolmogorov-Smirnov (KS) test. The χ^2 test measures the level of association between the two results. The KS test makes an assessment of whether there is sufficient evidence to reject the null hypothesis. It should, however, be noted that outliers can have a serious effect on the results.

The χ^2 test is based on a measure of the difference between two samples. The problem with this test is that it relies on dividing the square of the differences by the value of one of the data points and this results in the potential for different results depending on which data set is taken as a reference. The χ^2 parameter for the three graphs is given in Table 3.

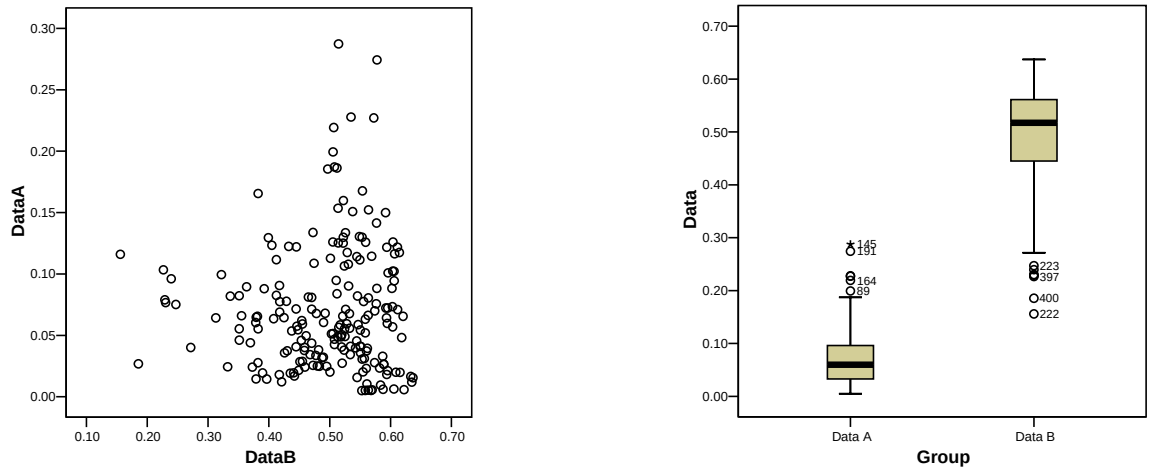

(a) Scatterplot and Boxplot for “Graph 4” from [7].

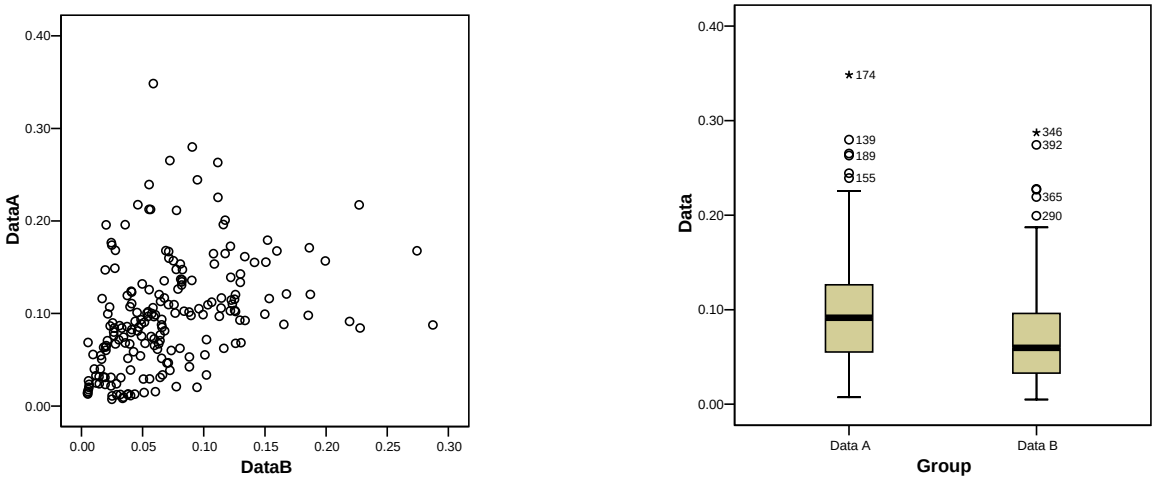

(b) Scatterplot and Boxplot for “Graph 5” from [7].

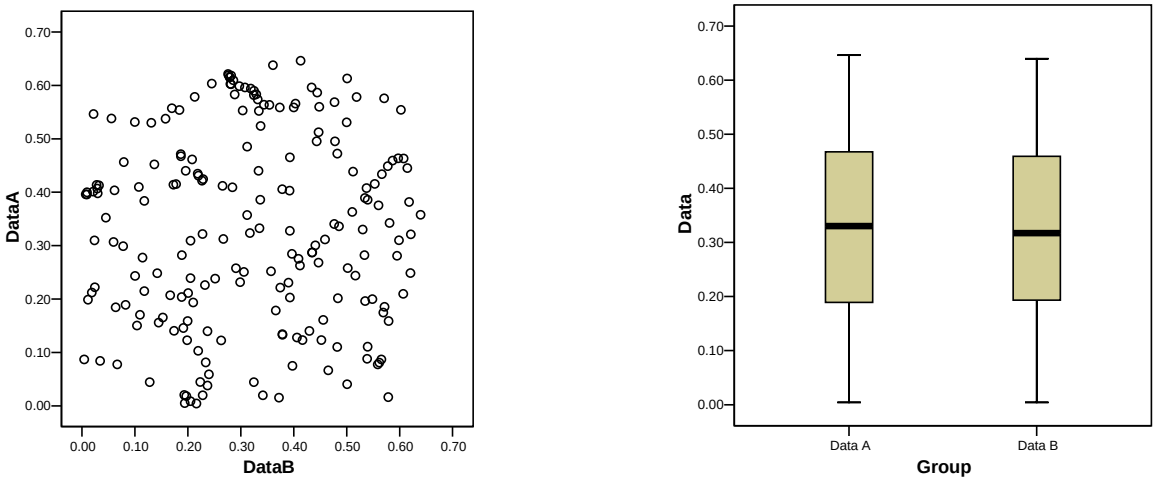

(c) Scatterplot and Boxplot for “Graph 8” from [7].

Fig. 3. Scatter plots and Boxplots for “Graph 4”, “Graph 5” and “Graph 8”, respectively.

Table 3. χ^2 parameter.

	"Graph 4"	"Graph 5"	"Graph 8"
χ^2	75	20	149

This surprisingly suggests that "Graph 8" is much worse than "Graph 4".

The KS test converts the data sets into distributions and compares those distributions, looking for the maximum difference. Commonly, it is used to compare a data set with a known distribution but has here been used to compare two independent data sets. The results are given in Table 4. "Graph 8" comes out as a clear best comparison.

Table 4. KS-test results for the three original data sets.

	"Graph 4"	"Graph 5"	"Graph 8"
KS Z parameter	9.8	2.8	0.7
P value	0.000	0.000	0.714

IV. FEATURE SELECTIVE VALIDATION (FSV)

FSV is not a canonical statistical technique. It is, however, an increasingly accepted heuristic technique that finds favor particularly in the EMC community for validation of computation electromagnetics and has been discussed in detail in [7-13]. It is presented here because, like statistical techniques, its aim is to quantify confidence in the comparison of the data sets fed into it. Correlation techniques do this through the value of the correlation coefficient, other techniques do this based on the p-values, FSV does this using a variety of inbuilt metrics, the most general of which being the Global Difference Measure. The FSV tool with which the following results has been computed can be download from the official FSV web page [14] or directly from [15].

In overview, FSV works by taking the two original data sets and low and high pass filtering each of these. The low pass data is differenced, as detailed in [14], to give the Amplitude Difference Measure (ADM) which measures the level of (dis)agreement of the data envelope. First and second derivatives of the low and high pass data are differenced (as in [14]) to give the Feature Difference Measure (FDM), which measures the level of disagreement of the finer detail and features in the original data. The ADM and FDM are then combined to give the GDM as in equation (2)

$$GDM = \sqrt{ADM^2 + FDM^2} \qquad (2)$$

As well as the single figure of merit given by the GDM, one particular useful feature of FSV is the confidence histogram, where the proportion of the GDM curve (on a point-by-point basis) is binned into the categories as noted in the visual rating scale of Fig. 2. The resulting probability density function has been shown to provide close analogue of the visual assessment of a group visual assessment.

The GDM values are given in Table 5; the confidence histograms for the data of Fig. 1 is given in Fig. 4.

Table 5. FSV (Global Difference Measure) results for original comparisons.

	"Graph 4"	"Graph 5"	"Graph 8"
GDM	5.26	4.41	4.67

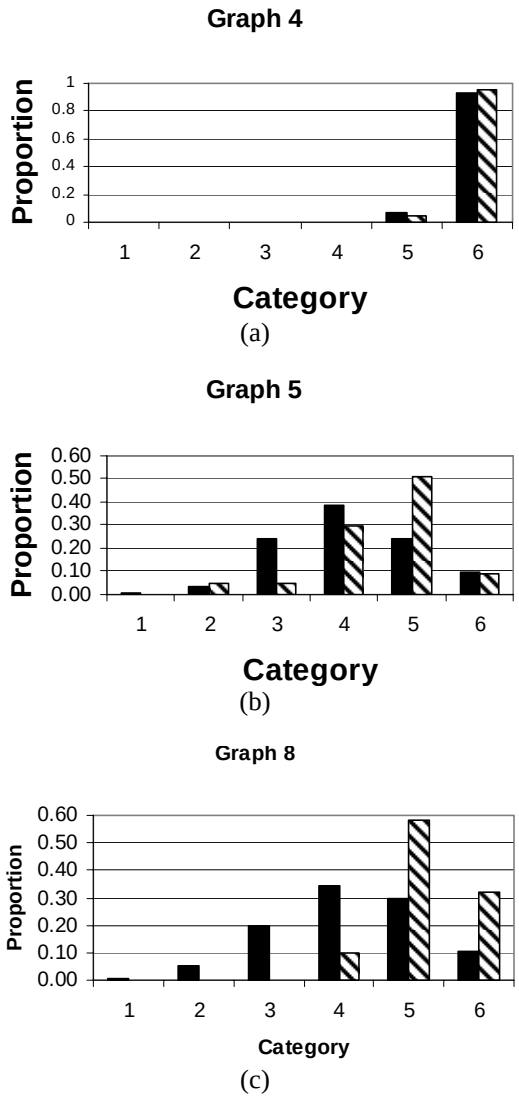

Fig. 4. FSV (dashed bars) compared to visual evaluation (solid bars) for the data in Fig. 1 from [7]. (a) "Graph 4", (b) "Graph 5", and (c) "Graph 8".

V. DISCUSSION

This paper has presented a non-mathematical summary of some of the most widely used statistical techniques as applied to computational electromagnetic validation. In particular, the emphasis has been to take a set of results already visually assessed by engineers familiar with performing this task and applying the techniques to see whether agreement could be obtained between the statistical techniques and the visual assessment. It should be noted that a paper such as this cannot prove the applicability or otherwise of individual statistical techniques, it can highlight the range of techniques available and suggest which are possibly more suitable than others.

All the comparisons used in this paper have shown a marked difference between the two components. In order to show how the tests compare when there is very little difference, by way of a 'lower bound', the data of Fig. 5(a) was compared using the techniques discussed above. Fig. 5(b) shows the visual assessment and FSV assessment, Fig. 5(c) shows the scatter plot and Fig. 5(d) shows the box plots. The Pearson r correlation is 0.999, the χ^2 value is 0.05 (irrespective of the order of variables) and the t-test value is 0.004. Clearly, there is little doubt as to the generally very high level of agreement between the two graphs irrespective of which method is used in the comparison.

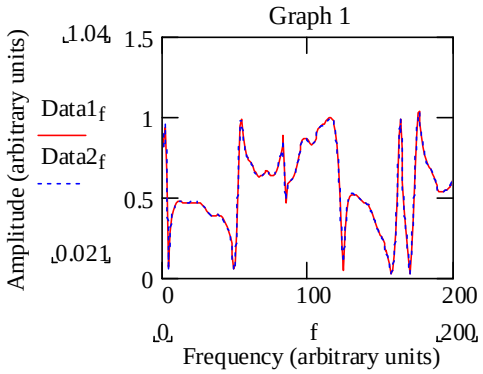

(a) From [7].

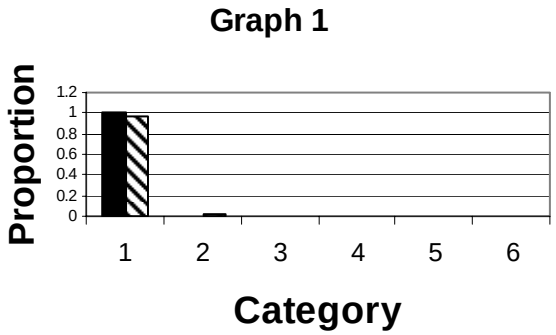

(b) From [7] - solid bar is visual assessment, dashed bar is FSV.

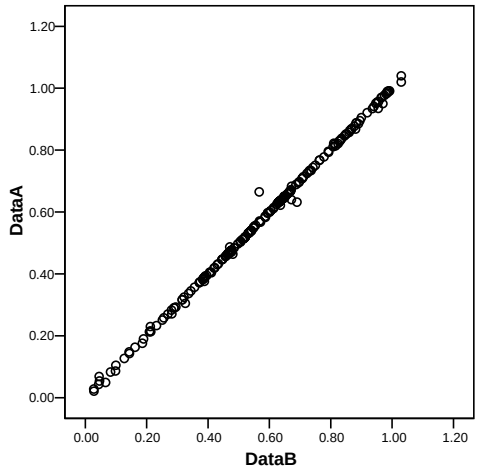

(c)

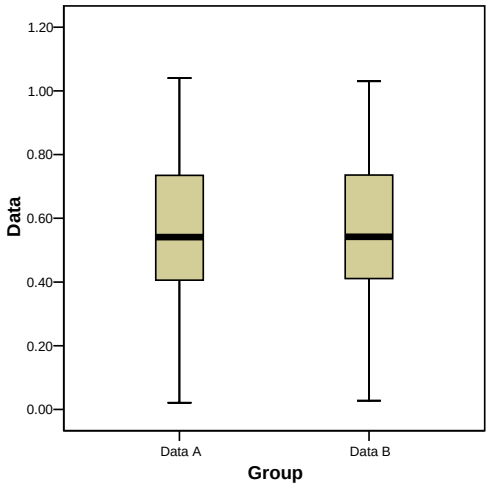

(d)

Fig. 5. Comparison of two data sets with very little difference. (a) Original data, (b) visual comparison compared to FSV comparison, (c) scatterplot, and (d) boxplots.

Scatterplots and correlation demonstrated the same rank-ordering of the data as the visual assessment. The boxplots and t-test results were in agreement but did not agree with visual assessment. The χ^2 test correctly identifies the best comparison whereas the KS test agrees with the t-test. In practice, the non-parametric tests are probably not well suited to large data sets [9] with parametric tests being more reliable due to the Central Limit Theorem. However, where there is a need to compare a data set with a known distribution, such as optimizing a reverberation chamber to produce a Rayleigh channel, then a χ^2 or KS approach would be well suited. A difficulty with applying χ^2 to two sets of data is that it relies on one 'reference' set. If using it to

compare models against measurements or models against models, the reference set must be unambiguous (for example, by changing the 'reference' set in the previous table, the χ^2 parameter for "Graph 4" = 1386!) and the user must be aware of points that are very close to zero in the reference set as this can produce an unnecessarily dominating effect on the final value (for example, by changing the 'reference' set in the previous table, the χ^2 parameter for "Graph 4" = 1386!).

In all cases, a real benefit derived from the application of a statistical approach to validation of computational electromagnetics is that it provides an objective starting point to discuss the comparisons and agree a conclusion.

REFERENCES

[1] R. Holland and R. St John, *Statistical Electromagnetics*, Francis, Philadelphia, PA, 1999.

[2] D. Carpenter, "Statistical electromagnetics: an end-game to computational electromagnetics," *IEEE Int. Symp. on EMC*, pp.736 – 741, 2006.

[3] H. Sasse and A. P. Duffy, "Satisficing in computational electromagnetics," *Applied Computational Electromagnetics Society Newsletter*, vol. 21, no. 2, 2006.

[4] A. Coates, H. Sasse, D. E. Coleby, A. P. Duffy, and A. Orlandi, "Validation of a three dimensional transmission line matrix (TLM) model implementation of a mode stirred reverberation chamber," *IEEE Trans. on EMC*, in press.

[5] P. Corona, J. Ladbury and G. Latmiral, "Reverberation chamber research – then and now: a review of early work and comparison with current understanding," *IEEE Trans. on EMC*, vol. 44, no. 1, pp. 87 – 94, Feb. 2002.

[6] C. Bruns and R. Vahldieck, "A closer look at reverberation chambers – 3D simulations and experimental verification," *IEEE Trans. on EMC*, vol 47, no. 3, pp. 612 – 626, Aug. 2005.

[7] A. Orlandi, A. P. Duffy, B. Archambeault, G. Antonini, D. E. Coleby, and S. Connor, "Feature selective validation (FSV) for validation of computational electromagnetics (CEM). Part II – assessment of FSV performance," *IEEE Trans. On EMC*, vol. 48, no. 3, pp. 460 – 467, 2006.

[8] D. E. Coleby and A. P. Duffy, "A visual interpretation rating scale for the validation of numerical models," *COMPEL: The Int. Journal for Computation and Mathematics in Electrical and Electronic Engineering*, vol. 24, no. 4, pp. 1078 – 92, 2005.

[9] StatSoft Inc., *Electronic Statistics Textbook*, Tulsa, OK, Statsoft, USA, 2006.
WEB: http://statsoft.com/textbook/stathome.html

[10] D. G. Rees, "Essential Statistics, 4/e, 2000, Chapman and Hall / CRC, Boca Raton

[11] J. Devore and R. Peck, *Statistics – the exploration and analysis of data*, 2/e, Duxbury Press, Belmont, California, 1993.

[12] T. T. Soong, *Fundamentals of probability and statistics for engineers*, Wiley, Chichester, UK, 1993.

[13] A. P. Duffy, A. J. M. Martin, A. Orlandi, G. Antonini, T. M. Benson, and M. S. Woolfson, "Feature selective validation (FSV) for validation of computational electromagnetics (CEM). Part I – the FSV method," *IEEE Trans. on EMC*, vol. 48, no. 3, pp. 449 – 59, 2006.

[14] FSV official webpage:
http://www.eng.dmu.ac.uk/~apd/FSV/FSV%20web/

[15] FSV downloads at:
http://ing.univaq.it/uaqemc/FSV_3_2_2/

Using MATLAB to Control Commercial Computational Electromagnetics Software

R. L. Haupt

Applied Research Laboratory, State College, PA 16801, haupt@ieee.org

***Abstract* –** This paper provides details on how to use MATLAB to control some commercial electromagnetics software packages. FEKO is an example that can be directly called from MATLAB. Other commercial software, such as CST Microwave Studio and Ansoft HFSS, require a scripting language interface. An example of a design of an inset rectangular patch antenna is presented using a direct call to FEKO and a Visual Basic for Applications interface to CST Microwave Studio are presented.

***Keywords*:** MATLAB, optimization, microstrip antenna, and genetic algorithm.

I. INTRODUCTION

MATLAB [1] has become a ubiquitous math, data manipulation, signal processing, and graphics software package. Engineers use its powerful functions for analysis and design in many areas including antenna design. MATLAB is general-purpose software, so many arcane applications, like antenna design, are done using special purpose commercial software. Although these packages can model very complex electromagnetics systems, they lack some of the powerful analysis tools in MATLAB. Using MATLAB to control these commercial electromagnetics solvers creates a powerful tool for design, analysis, and control.

There are a number of applications where a MATLAB-commercial electromagnetics solver interface is critical. Numerical optimization is one example. Although most commercial electromagnetics codes now come with some numerical optimization, they lack the versatility of optimization routines in MATLAB. Another example is in the use of signal processing software in conjunction with beamforming in an antenna array. For instance, the commercial computational electromagnetics software models the antenna elements while MATLAB takes the signals from the elements and performs the signal processing. Other applications include modeling wireless systems, radar cross section reduction, and electromagnetic band gap material design.

This paper provides systematic instructions to interface MATLAB with FEKO [2] or via a scripting language, such as Visual Basic for Applications (VBA), to a commercial software package like CST Microwave Studio [3] or Ansoft HFSS [4]. These software combinations are used to design an inset rectangular microstrip patch antenna that is resonant at 2.0 GHz. Both combinations result in successful patch antenna designs.

II. MICROSTRIP PATCH OBJECTIVE FUNCTION

The example used in this paper is the design of an inset rectangular patch that is resonant at 2.0 GHz. Fig. 1 shows a diagram of the patch with the design variables labeled. The substrate is 1.6 mm thick and has a relative dielectric constant of 2.2. An 8 mm border (E) surrounds the metallic patch. The ground plane has the same area as the substrate. There is a 1 mm gap (G) between the feed line and the patch. The microstrip feed line is F=25 mm long and has a voltage feed 3 mm from its left end. The values of L, M, B, and W are found using numerical optimization.

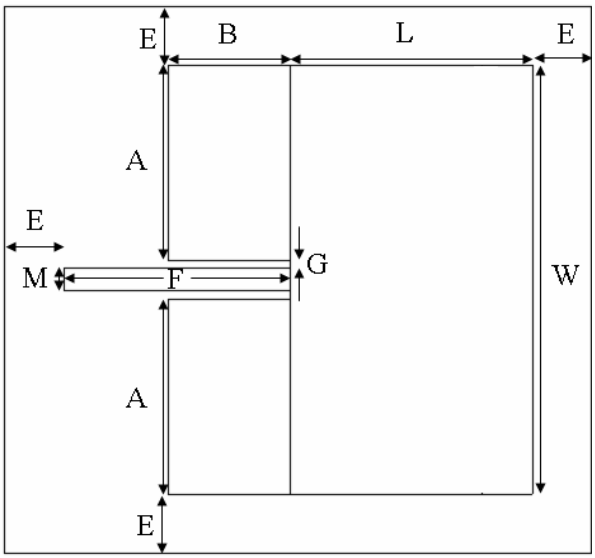

Fig. 1. Diagram of the inset patch antenna design.

This is a narrow band antenna, so minimizing the reflection coefficient at 2.0 GHz results in a very sharp decrease in s_{11} at 2.0 GHz. Finding this sharp decrease is difficult for optimization algorithms. Small changes in the patch dimensions can significantly move the resonant frequency. Local search algorithms work well with four

variables when the starting point is very close to the best solution. If a good guess is not available, then a genetic algorithm written in MATLAB is used to first find a good initial first guest for a MATLAB Nelder Mead downhill simplex algorithm (fminsearch.m). The genetic algorithm used here is described in detail in [5]. The genetic algorithm was stopped once it found a solution that had an s_{11} < -10 dB. This stopping point was chosen, because an antenna is considered matched to a transmission line when the reflection coefficient is less than -10 dB. These optimizations routines call MATLAB functions that interface with the commercial software package or scripting language. A diagram of the optimization process is shown in Fig. 2. The next two sections demonstrate the optimum design of an inset patch using a combination of MATLAB and FEKO or Microwave Studio.

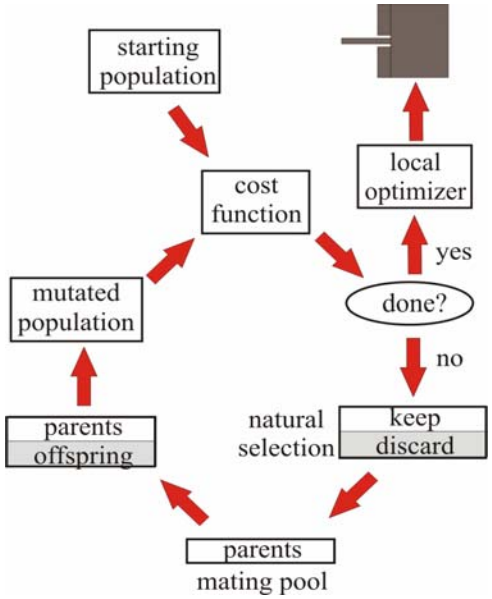

Fig. 2. Flowchart of the optimization algorithm.

Before trying the numerical algorithms, the patch is first designed using standard analytical approaches [6]-7] The patch and microstrip line are designed for 50 ohms. These values can be used to seed the numerical optimization algorithm to find dimensions that are more accurate, as shown in Table 1.

Table 1. Patch dimensions from the analytical design.

Dimension	L	B	W	M
Size in mm	32.32	17.48	59.29	4.61

III. CONTROLLING FEKO WITH MATLAB

The relevant ASCII files that are used by MATLAB and FEKO are shown in Table 2. There are a few other files generated by MATLAB and FEKO but are not important to the user. All the files have the same name but a different extension, so they are easy to associate with the same project. The MATLAB commands are in mpatch.m. Data written from MATLAB to be used by FEKO is stored in the mpatch.txt file. FEKO commands are in the mpatch.pre file. Data written by FEKO for use by MATLAB is written in the mpatch.ffe and mpatch.out files. Figure 1 is a flowchart of the MATLAB-FEKO software configuration. MATLAB can directly call FEKO to calculate s_{11} at 2.0 GHz.

Table 2. Relevant MATLAB-FEKO computer files.

File name	contents
mpatch.m	MATLAB m file
mpatch.txt	ASCII file with variable values
mpatch.pre	PREFEKO file
mpatch.out	FEKO output file
mpatch.ffe	FEKO file with angles, electric field, gain

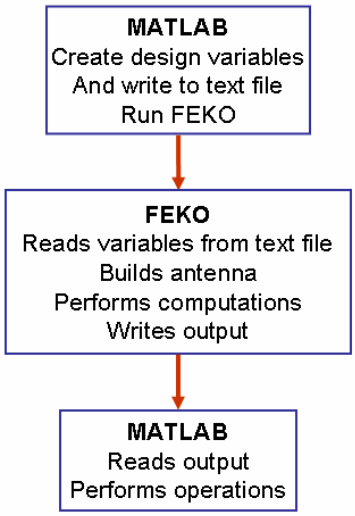

Fig. 3. MATLAB-FEKO flowchart.

The microstrip patch is represented as a lossless metal polygon in FEKO. All the polygon corners are generated by MATLAB. MATLAB plots the patch and substrate shape and labels the points. An example of a plot of half of the patch (the other half is a mirror image) is shown in Fig. 4. If the coordinates of the numbered points in Fig. 4 are (x,y), then the MATLAB code to draw the outline of the patch is given by

```
figure(1);plot(x,y,'-o');
axis equal
for ii=1:length(x)
text(x(ii),y(ii)+z(ii),num2str(ii))
end
```

This plot is useful in troubleshooting and watching the convergence of the optimization algorithm.

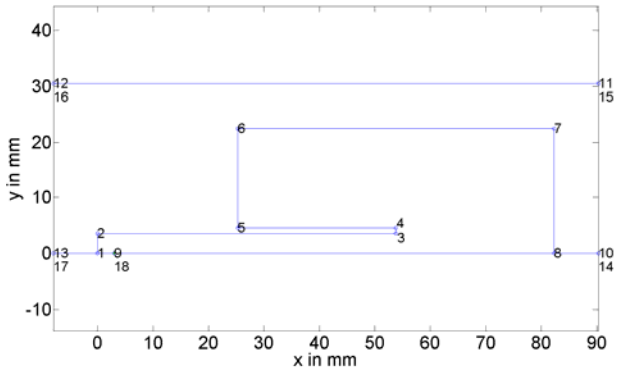

Fig. 4. Figure drawn by MATLAB before passing point to FEKO.

The numbered points in Fig. 4 are calculated from the values of the variables shown in Fig. 1. Some of these values are set while others can vary between predetermined limits. Once MATLAB has created an antenna design, all the (x,y,z) coordinates are written to the text file, `mpatch.txt` using,

```
fid=fopen('mpatch.txt','w');
N=length(x);
fprintf(fid,'%6.2f\n',N);
for q=1:N
fprintf(fid,'3%6.2f\n',x(q),y(q),z(q));
end
fclose(fid);
```

The file, mpatch.txt, has N+1 line. The first line contains the number of points. The following N lines contain the coordinates of the points.

Next, the following commands run PREFEKO and FEKO from MATLAB,

```
!prefeko mpatch > output.txt
!runfeko mpatch > output.txt
```

the "`> output.txt`" part of the commands places output generated in the running of PREFEKO and FEKO into a file rather than displaying them on the computer screen. If this part of the command is skipped, then the computer screen is filled with a lot of run data that is usually of little interest.

The lines in mpatch.pre that read from the text file and create the points defining the outline of the antenna are given by,

```
#N= fileread("mpatch.txt",1,1)
!!for #i = 1 to #N
#ax[#i]= fileread("mpatch.txt",1+#i,1)
#ay[#i]= fileread("mpatch.txt",1+#i,2)
#az[#i]= fileread("mpatch.txt",1+#i,3)
DP : p#i : #ax[#i] : #ay[#i] : #az[#i]
!!next
```

The defining points on the antenna are created by the define point (DP) command and are labeled `p1` to `pN`. After these points are formed in FEKO, then the structure is built out of triangles, polygons, wires, etc. FEKO performs the calculations and writes the output to `mpatch.out` and possibly to other files, such as `mpatch.ffe`. MATLAB can easily read the ASCII file where the far field information is written using the textread command,

```
[t,p,rEt,iEt,rEp,iEp,gt,gp,g]
=textread('mpatch.ffe','2%f (%f,%f)
(%f,%f) 3%f');
```

Reading from mpatch.out is more difficult but possible using m-files downloaded from the MATLAB website [1] (e.g. findstring.m).

Running the MATLAB-FEKO algorithm to minimize s_{11} at 2.0 GHz resulted in an s_{11} of -31 dB. The plot of s_{11} over a 4% frequency range is shown in Fig. 5. This narrow band resonance was achieved from the dimensions shown in Table 3. The values found for L and B are close to those in Table 1, while the values for W and M are considerably smaller.

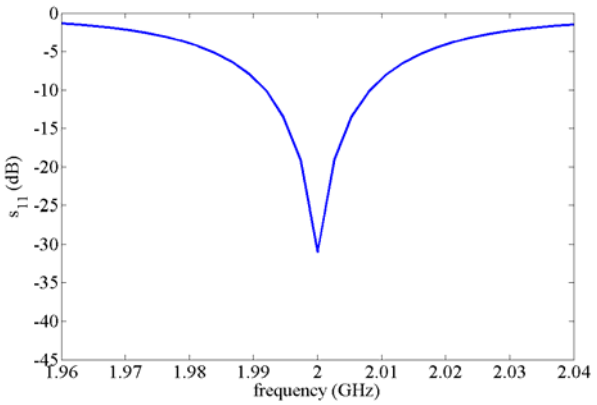

Fig. 5. Plot of s_{11} for patch antenna optimized by FEKO.

Table 3. Patch dimensions from the MATLAB-FEKO design.

Dimension	L	B	W	M
Size in mm	32.61	18.55	34.24	2.91

IV. CONTROLLING COMMERCIAL SOFTWARE PROGRAMS WITH MATLAB VIA A SCRIPT

MATLAB can control some commercial software via a scripting language. A script is a text file containing instructions written in a scripting language. The commands in the script are executed when the scripting language opens the file. VBA is widely used and Microwave Studio and Ansoft HFSS have VBA editors built in. It is a good idea to get familiar with the VBA

editor in the software package before attempting to interface with MATLAB. Commands that call various functions in the commercial software are placed in the *.bas file using the VBA editor. Types of commands include building geometry, passing variables, and engaging the main software engine.

The example described in this section uses MATLAB to control Microwave Studio via a VBA script. Microwave Studio generates a huge number of files (74) with each run. The relevant ASCII files are shown in Table 4. Again, all the files have the same name but a different extension. The s_{11} data written by Microwave Studio for use by MATLAB is written in the mspatch^d1(1)1(1).sig file. Fig. 6 shows the flow chart.

Table 4. Relevant MATLAB-Microwave Studio computer files.

File name	contents
mpatch.m	MATLAB m file
mpatch.txt	ASCII file with variable values
mpatch.bas	VBA program
mpatch.mod	Microwave Studio model file
mpatch^d1(1)1(1).sig	File containing s_{11} data

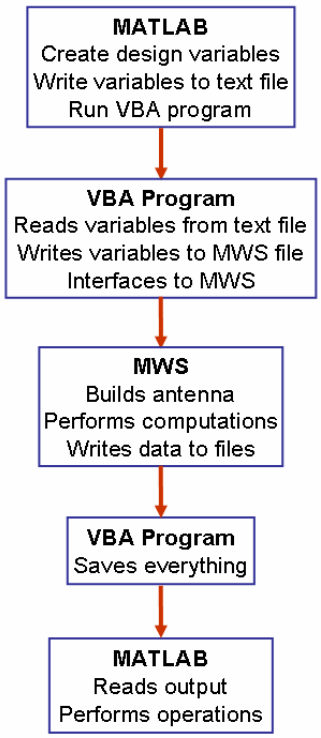

Fig. 6. MATLAB-CST Microwave Studio flowchart.

In this case, it is easier to have MATLAB write the four unknown patch dimensions to a file. The commands in mpatch.m that do this are,

```
fid=fopen('mspatch.txt','w');
fprintf(fid,'%f\r',xmin);
fprintf(fid,'%f\r',xt);
fprintf(fid,'%f\r',py);
fprintf(fid,'%f\r',cp);
fclose(fid);
```

Next, MATLAB calls the VBA program via (all on one line),

```
!"c:\program files (x86)\cst studio
suite 2006\cst design environment.exe" -
m mspatch.bas > output.txt
```

The VBA program has two parts. The first part reads the data from the mpatch.txt data file generated by MATLAB. This file contains the values for L, B, W, and M. The code that reads this data is given by,

```
Open "d:<dir>\mpatch.txt" For Input As
#1
Input#1,v(1)
Input#1,v(2)
Input#1,v(3)
Input#1,v(4)
Close #1
```

Once the data is read, then the Microwave Studio model file is opened using the command,

```
openfile("d:<dir>\mpatch.mod")
```

The model with the previously stored dimension values appears on the computer screen. In order to change the dimension values, they must be stored in the model file using the following commands,

```
storeparameter("xmin",v(1))
storeparameter("xt",v(2))
storeparameter("py",v(3))
storeparameter("cp",v(4))
```

Next, the data is saved and the model rebuild using,

```
save
Rebuild
```

The picture of the model on the screen is redrawn to reflect the new dimension values. Finally, the solver (in this case, the transient solver) is started and the results saved through the commands,

```
Solver.start
save
```

When the solver finishes and the data is stored, control returns to MATLAB and the Microwave Studio window closes. The Microwave Studio window will reopen every

time the program is called from MATLAB. MATLAB reads the s_{11} data using the line,

```
[f,s11]=textread('mspatch^d1(1)1(1).sig'
,'','headerlines',4);
```

Running the MATLAB-Microwave Studio algorithm resulted in an s_{11} of -70.8 dB at 2.0 GHz. The plot of s_{11} over a 4% frequency range is shown in Fig. 7. The final dimensions for the patch are shown in Table 5. The values of L, B, and W are very close to those predicted by Table 1.

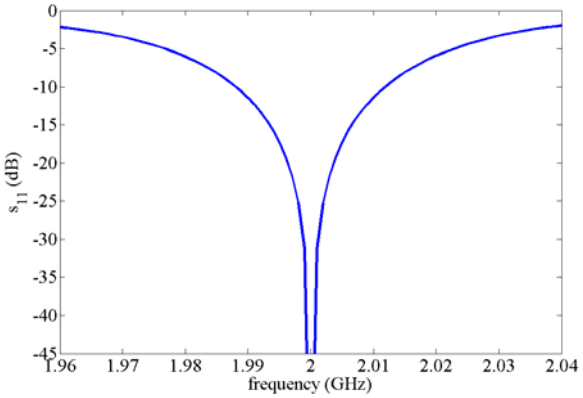

Fig. 7. Plot of s_{11} for patch antenna optimized by Microwave Studio.

Table 5. Patch dimensions from the MATLAB-Microwave Studio design.

Dimension	L	B	W	M
Size in mm	32.68	16.40	59.18	3.06

V. CONCLUSIONS

Using MATLAB to control commercial electromagnetics software creates a powerful design and systems analysis environment. This paper describes how to create the interface between MATLAB and commercial software via direct calls and via a scripting language. The different approaches to the design of an inset fed microstrip patch produced similar results. Fig. 8 shows s_{11} calculated using FEKO and the dimensions found in Tables 1, 3, and 5. The results are very close to each other (within 2.5%). Fig. 9 shows s_{11} calculated using Microwave Studio and the dimensions found in Tables 1, 3, and 5. The results are not as close together. Refining the models would likely produce better results.

There are some lessons learned here. First, the VBA interface requires learning VBA (if you did not know it already – like me). Second, the variable can be passed in a number of ways. With FEKO, it seemed easier to pass the points outlining the patch, while with Microwave Studio, it seemed easier to pass the dimensions. Third, optimizing large structures would be very time-consuming. Fourth, a number of different variables can be passed other than dimensions. For instance, material properties, type of source, source voltage, etc.

Although there are several papers that have interfaced MATLAB to particular software packages, none provide the details on how to create that interface. The purpose of this paper is to give readers enough information to create useful interactions between MATLAB and commercial electromagnetics software.

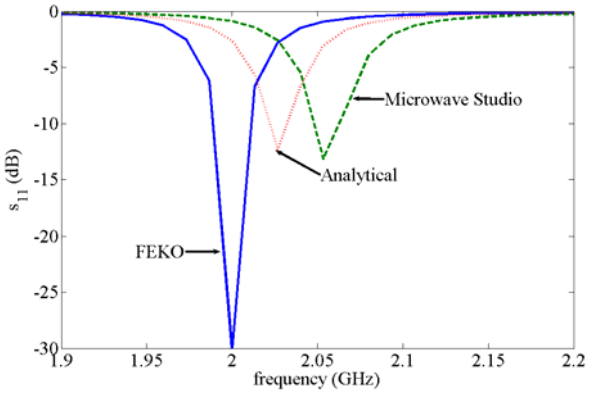

Fig. 8. The dimensions in Tables 1, 3, and 5 are used to build a patch antenna in FEKO and calculate these values of s_{11}.

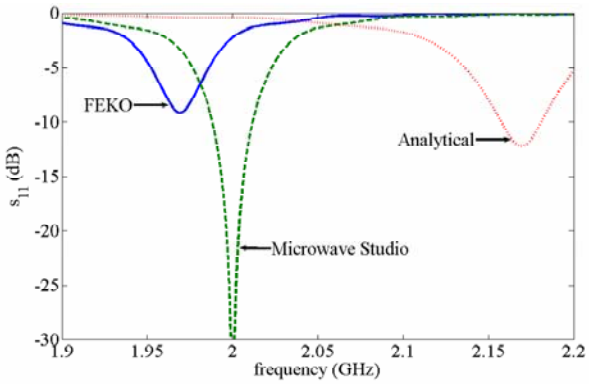

Fig. 9. The dimensions in Tables 1, 3, and 5 are used to build a patch antenna in Microwave Studio and calculate these values of s_{11}.

REFERENCES

[1] MATLAB Version 7.3.0.267, The (www.mathworks.com), Aug 3, 2006.

[2] FEKO Suite 5.1, EM Software and Systems (www.feko.info), 2005.

[3] CST Microwave Studio, Version 2006.05, April 19, 2006.

[4] High Frequency Structure Simulation (HFSS), ANSOFT Co., Pittsburgh, PA, USA.

[5] R. L. Haupt, "A mixed integer genetic algorithm for electromagnetics applications," *IEEE AP-S Trans.*, vol. 55, no. 3, pp. 577-582, Mar. 2007.

[6] http://www1.sphere.ne.jp/i-lab/ilab/tool/ms_line_e.htm
[7] C.A. Balanis, *Antenna Theory Analysis and Design*, New York: John Wiley & Sons, 1997.

Randy L. Haupt is an IEEE Fellow and Department Head of Computational Electromagnetics and Senior Scientist at the Penn State Applied Research Laboratory. He has a Ph.D. in Electrical Engineering from the University of Michigan, MS in Electrical Engineering from Northeastern University, MS in Engineering Management from Western New England College, and BS in Electrical Engineering from the USAF Academy. He was Professor and Department Head of Electrical and Computer Engineering at Utah State University from 1999-2003. He was a Professor of Electrical Engineering at the USAF Academy and Professor and Chair of Electrical Engineering at the University of Nevada Reno. In 1997, he retired as a Lt. Col. in the USAF. Dr. Haupt was a project engineer for the OTH-B radar and a research antenna engineer for Rome Air Development Center. He was the Federal Engineer of the Year in 1993 and is a member of Tau Beta Pi, Eta Kappa Nu, URSI Commission B, and Electromagnetics Academy. He served on the board of directors for the Applied Computational Electromagnetics Society and is on the IEEE Antenna and Propagation Society Administrative Committee. He has published journal articles, conference publications, and book chapters on antennas, radar cross section and numerical methods and is co-author of the book Practical Genetic Algorithms, 2 ed., John Wiley & Sons, 2004 and Genetic Algorithms in Electromagnetics, John Wiley & Sons, 2007. He has eight patents in antenna technology.

Quantifying EMC Measurement Accuracy Using Feature Selective Validation

[1]A. Denton, [1]A. Martin, and [2]A. Duffy

[1]MIRA Ltd,
Watling Street, Nuneaton, Warwickshire CV10 0TU, UK
alan.denton@mira.co.uk , anthony.martin@mira.co.uk

[2]De Montfort University,
Leicester, UK
apd@dmu.ac.uk

Abstract – It is commonplace in the field of Computational Electromagnetics (CEM) for engineers to validate models against experimental results. In some cases, this is performed with little understanding about the accuracy of the experimental data used to validate the underlying calculations from which Electromagnetic models are formed. This paper therefore explores the accuracy and more importantly the areas of inaccuracy and variability that may be associated with experimental data. The Feature Selective Validation (FSV) method is used to assess each area of variability, and thus quantify the quality of test configurations and test samples. In examining experimental repeatability rather than comparison to electromagnetic analysis results, this paper concludes that, while substantial variation between experimental results can exist, the use of FSV provides considerable assistance in quantifying repeatability and therefore assigning confidence to measurements against which CEM results can be compared. While this paper is based on experience in the automotive sector, it is anticipated that these findings are more widely applicable.

Keywords: Computational Electromagnetics (CEM), Feature Selective Validation (FSV).

I. INTRODUCTION

Between the numbers of options open to a modeller to validate a numerical model, one of the most accepted is a direct comparison with experimental measurements. A natural tendency to explain differences between the modelled and measured results is to attribute the bulk of the error to the model. After all, there are known and accepted simplifications in any model through approximating physical structures, applying spatial, time and / or frequency discretization to the problem. However, this is not always or entirely correct. All experiments are subject to some inherent inaccuracy or loading and detailed knowledge of experimental repeatability can assist in determining levels of acceptable experimental error. Within the automotive sector, statistical coverage of component level testing is low, with most vehicle manufactures calling for two samples of the same component to be tested. At vehicle level only a single vehicle sample need be tested. Electromagnetic Compatibility (EMC) test facilities include uncertainty thresholds; however, it is difficult to interpret the actual quantitative/qualitative impact of these thresholds upon test results.

The nature of the variability between test results is important to be able to perform comparisons with a high level of confidence. This can be through:

- Validation of the results taken from different test samples,
- The results gained from marginally different test configurations,
- Repeated results from the same test sample.

This type of analysis allows the assessment of questions such as:

- Are the tests repeatable?
- Are different test samples of the same product similar?
- Do minor differences in test configurations (that fall within the parameters of the test specification) produce different results?

The quality of experimental data is influenced by the method of producing and recording the data, and the degree of perfection in the experimental procedure. In addition to these variables, the repeatability of test results for multiple samples of the same product will be affected by the build quality of the product and tolerance of the individual components used to manufacture the product.

Quantitative comparisons of experimental results are therefore required to remove as much subjectivity as possible from the assessment of results. This study presents results from a number of repeated experiments performed with two different test products using two

slightly different test configurations and identifies their level of difference employing the Feature Selective Validation method [1-2]. From these investigations the origins of variability in the tests may be assessed and quantified.

The FSV method comprises two components; the Amplitude Difference Measure (ADM), and Feature Difference Measure (FDM). These measures are combined to form an overall assessment of the comparison in question or Global Difference Measure (GDM). It is these three measures that will be used in the subsequent study to assess the differences between the presented results. The ADM is obtained by, essentially, taking the normalised difference in the 'trend' ('envelope') information from two data sets to be compared, which is obtained by low-pass filtering the original data. The FDM is obtained from a composite of the differences in the derivatives of the low-pass filtered response and the high-pass filtered response to accentuate the 'high Q' feature differences between the data sets. One common way of using this information is to take the mean value of the ADM and FDM obtained across the domain of the original data as figures of merit. An overall figure of merit, the GDM, is obtained from

$$GDM = \sqrt{ADM^2 + FDM^2}\ . \qquad (1)$$

The FSV method benefits from its apparent ability to mirror human perception [3], while producing information that directly relates human variability and the confidence associated with it. The FSV method also builds on the common language of engineers and scientists alike, employing categories which relate to human interpretations of comparisons, namely: 'Excellent', 'Very Good', 'Good', 'Fair', 'Poor' and 'Very Poor'. The basic premise is that a value of zero for any of the difference measures represents perfect correlation. The interpretation for finite values is indicated in Table 1 below.

Table 1. Qualitative interpretation of FSV difference measures.

FSV Difference Measure "*x*"	**"Quality" of comparison**
$x<0.1$	Excellent
$0.1\le x<0.2$	Very good
$0.2\le x<0.4$	Good
$0.4\le x<0.8$	Fair
$0.8\le x<1.6$	Poor
$1.6\le x$	Very Poor

The qualitative interpretation of the difference measures has been developed from a statistical analysis [3] of the results of a series of selected visual assessments carried out by a group of experienced scientists and engineers. It is natural that different applications will have different expectations of what 'good' etc. actually is, but this is likely to be a shared understanding by the personnel involved.

II. TEST PROCEDURES

It was decided that within the field of Automotive EMC measurement, acceptable repeatability may be set at a GDM value not greater than 0.4 (i.e. 'Good'). This value was distilled from cumulative group experience and was agreed throughout the project team. The choice of this value in other test and measurements fields is dependent on the inherent sensitivity of the measurements and the level of precision that can be associated with the configuration of the test equipment. In an attempt to assess the influence of a products complexity on the repeatability of measurements, a complex electrical unit (DC to DC Converter) and a simple electrical unit (windscreen washer pump motor) were chosen as the devices under test for the subsequent study. For the purpose of providing a 'golden measurement' to compare models against, a GDM of 'Very Good' or even 'Excellent' may be required.

Three DC to DC converters with identical part numbers were obtained from a worldwide electronic component manufacturer. These are referred to as samples A, B, and C throughout this study. It should be noted that while the three DC to DC converters shared the same part numbers, inquiries into the manufacturing background of samples A, B, and C led to the discovery that sample C had been manufactured significantly later than either samples A and B and that the manufacturing plant producing these parts had moved geographically within that time interval. The three windscreen washer pump motors used in this study were from the same manufacturing batch and are referred to in this study as samples D, E, and F.

A comprehensive test regime was constructed to allow assessments to be made on the variability:

a) of repeated tests performed using identical test configurations and samples;
b) when the test configuration is altered slightly but within the scope of the test specification;
c) between three samples of the same product.

To assess these three areas of variability, an emissions measurement was performed, and upon completion of the initial test sweep a second test sweep was carried out with no interference to the test configuration. The sample was then incremented and the process repeated. This gave rise to repeated test results (a and b) for each sample (A to F). The test configuration was then altered slightly and the complete suite of tests was repeated as detailed in the test matrix of Table 2.

Table 2. Test matrix.

	DC to DC Converter					
	Sample A		Sample B		Sample C	
Configuration 1	01a	01b	02a	02b	03a	03b
Configuration 2	04a	04b	05a	05b	06a	06b
	Windscreen Washer Pump Motor					
	Sample D		Sample E		Sample F	
Configuration 1	07a	07b	08a	08b	09a	09b
Configuration 2	10a	10b	11a	11b	12a	12c

The standard test method [4] requires a 1.5 m section of test harness to be exposed to the measurement receive antenna. This 1.5 m section is clearly illustrated in Fig. 1 as the foremost straight section running 100 mm behind, but parallel with, the front edge of the ground plane. The Directive also calls for the product under test to be located 200 mm behind the front edge of the ground plane.

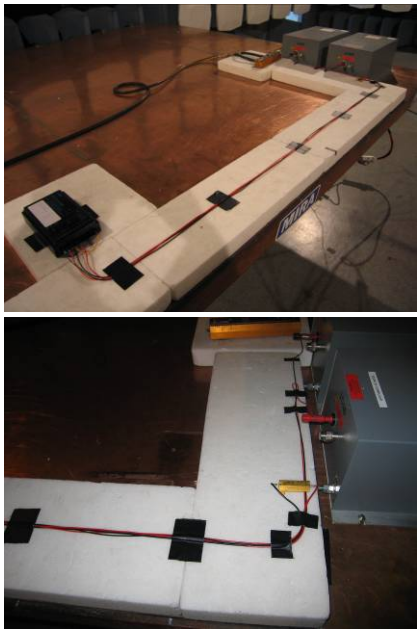

Fig. 1. Generic 2004/104/EC (Annex VII) test configuration.

Test configurations 1 and 2 were both set up within the defined test method of [4]. Small variations were introduced between them to provide a test of the sensitivity of the configurations to small changes. Configuration 1 used identical power and ground cable lengths, and the surplus of power cable due to the location of the test Line Impedance Stabilisation Networks (LISNs) was coiled slightly, see Fig. 1. Configuration 2 used the same length ground cable as configuration 1 but the overall length of the power cable was reduced by approximately 300 mm to avoid having to coil surplus cable when connecting to the test LISN.

III. TEST RESULTS

Results from the tests detailed in Table 2 are illustrated in Fig. 2 to 7.

In order of severity, it is observed from a visual evaluation that; there are significant differences between test configurations 1 and 2; the emissions profile of test sample C is significantly lower in magnitude compared to those of samples A and B; and all repeated test results are very similar for each sample tested when the same test configuration is used.

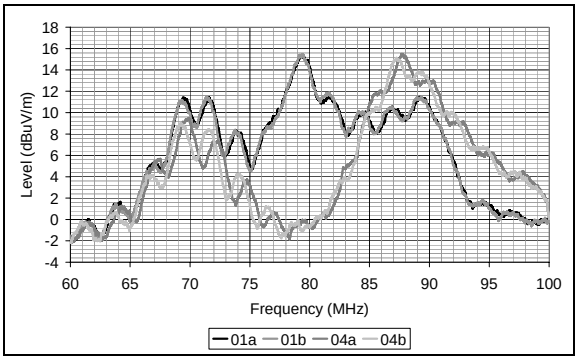

Fig. 2. Results sample A.

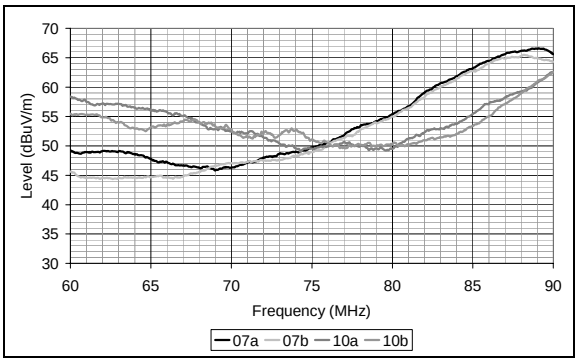

Fig. 3. Results sample D.

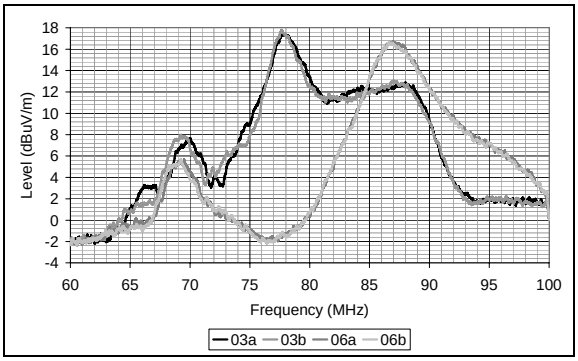

Fig. 4. Results sample B.

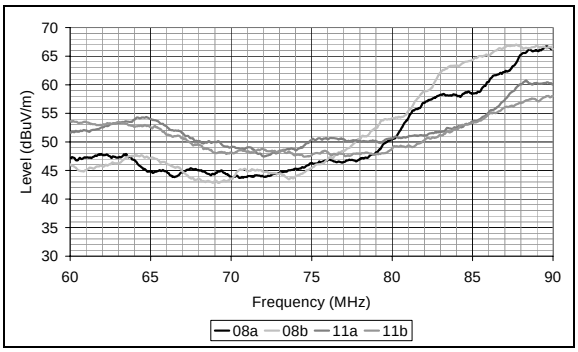

Fig. 5. Results sample E.

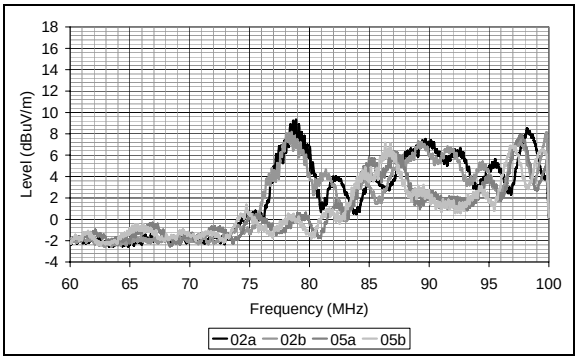

Fig. 6. Results sample C.

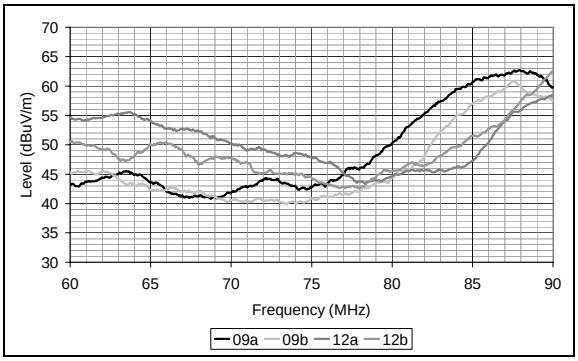

Fig. 7. Results sample F.

IV. VALIDATION RESULTS

The test results were cross-validated in sets to give rise to the following assessments:

Comparisons of repeated tests performed using identical test configurations

SET A1. Configuration 1 Samples A through C.
SET A2. Configuration 1 Samples D through F.
SET A3. Configuration 2 Samples A through C.
SET A4. Configuration 2 Samples D through F.

Comparisons of tests performed using 2 different configurations

SET B1. Configuration 1 vs. Configuration 2 - Samples A through C.
SET B2. Configuration 1 vs. Configuration 2 - Samples D through F.

Comparisons between three samples of the same product

SET C1. Test Samples A through C – cross-validation.
SET C2. Test Samples D through F – cross-validation.

The quantitative and qualitative FSV validation results (GDM, ADM and FDM) for each validation sub-set detailed above are given in Table 3, 4, and 5. The final three columns indicate the average quantitative and qualitative FSV results for each validation sub-set. It is these average results that are used in the subsequent discussions.

In Table 3, the average GDM results of sub-sets A1 and A2 indicate that test configuration 1 has a 'Very Good' level of repeatability. The results of sub-sets A3 and A4 indicate that test configuration 2 only has a 'Good' level of repeatability and therefore incurs considerably more variability in repeated test results even though no changes were made to the test configuration between each repeated test.

Results presented in Table 4 from sub-sets B1 and B2 illustrate only a 'Fair' level of similarity between test configurations for the same test sample. This indicates that if the test samples were unknown to an engineer making visual evaluations of the results presented in this study, it would be difficult to conclude that it was the same product tested in configurations 1 and 2.

Cross-validation of the results for the DC to DC converter samples (A, B and C) presented in Table 5 indicates a 'Fair' level of similarity which illustrates that the samples were significantly different. The cross-validation of samples A and B indicate that the sample variability of the DC to DC converter product is 'Good' when the samples are taken from the same batch.

Conversely, the validation results for sub-set C2 indicates that there is a 'Very Good' level of similarity between the three windscreen washer pump samples (D, E and F).

V. DISCUSSION AND CONCLUSIONS

Recognising that a preferred approach to the validation of computational electromagnetics is to compare the results of the models against an experimentally obtained reference, this paper has been concerned with investigating an approach to determining the repeatability of measurements, with a view to using this quantification to establish a level of confidence in any comparison with numerical models. It assessed three areas of experimental variability, namely:

- Test repeatability,

- Test configuration,
- Test sample variability.

Using the predefined tolerance for accurate results set earlier in this paper at a GDM value no greater than 0.4 or 'Good'; the results indicate that repeated test using the same test configuration (without modification) and for the same product are adequate as expected. It is also confirmed that test samples from the same batch tested using the same test configuration offer results with a high level of confidence.

It has also been illustrated that only a small modification (within the scope of the overall test specification) to a test configuration can have a significant impact upon the confidence that can be associated with the test results.

This paper illustrates that variability between test samples, particularly those from different batches, and differences in test configurations, have the potential to modify experimental test results to such a degree that it would be difficult to conclude that the same product was tested.

Table 3. FSV validation results – test repeatability.

		Quantitative			Qualitative			Average (Quantitative/Qualitative)		
SET	**Comparison**	**GDM**	**ADM**	**FDM**	**GDM**	**ADM**	**FDM**	**GDM**	**ADM**	**FDM**
A1	01a Vs 01b	0.05	0.00	0.05	EXCELLENT	EXCELLENT	EXCELLENT	0.15	0.01	0.15
	02a Vs 02b	0.21	0.02	0.20	GOOD	EXCELLENT	GOOD			
	03a Vs 03b	0.20	0.01	0.20	GOOD	EXCELLENT	GOOD	V GOOD	EXCELLENT	V GOOD
A2	07a Vs 07b	0.09	0.04	0.06	EXCELLENT	EXCELLENT	EXCELLENT	0.15	0.07	0.10
	08a Vs 08b	0.19	0.09	0.11	V GOOD	EXCELLENT	V GOOD			
	09a Vs 09b	0.18	0.08	0.12	V GOOD	EXCELLENT	V GOOD	V GOOD	EXCELLENT	V GOOD
A3	04a Vs 04b	0.24	0.02	0.23	GOOD	EXCELLENT	GOOD	0.24	0.04	0.22
	05a Vs 05b	0.36	0.10	0.32	GOOD	V GOOD	GOOD			
	06a Vs 06b	0.11	0.00	0.11	V GOOD	EXCELLENT	V GOOD	GOOD	EXCELLENT	GOOD
A4	10a Vs 10b	0.26	0.16	0.18	GOOD	V GOOD	V GOOD	0.27	0.17	0.17
	11a Vs 11b	0.22	0.11	0.13	GOOD	V GOOD	V GOOD			
	12a Vs 12b	0.34	0.24	0.20	GOOD	GOOD	GOOD	GOOD	V GOOD	V GOOD

Table 4. FSV validation results – test configuration variability.

		Quantitative			Qualitative			Average (Quantitative/Qualitative)		
SET	**Comparison**	**GDM**	**ADM**	**FDM**	**GDM**	**ADM**	**FDM**	**GDM**	**ADM**	**FDM**
B1	01a Vs 04a	0.46	0.31	0.26	FAIR	GOOD	GOOD	0.45	0.29	0.29
	02a Vs 05a	0.42	0.23	0.27	FAIR	GOOD	GOOD			
	03a Vs 06a	0.48	0.32	0.33	FAIR	GOOD	GOOD	FAIR	GOOD	GOOD
B2	07a Vs 10a	0.51	0.43	0.17	FAIR	FAIR	V GOOD	0.49	0.40	0.17
	08a Vs 11a	0.39	0.31	0.15	GOOD	GOOD	V GOOD			
	09a Vs 12a	0.56	0.46	0.20	FAIR	FAIR	GOOD	FAIR	FAIR	V GOOD

Table 5. FSV validation results – sample variability.

		Quantitative			Qualitative			Average (Quantitative/Qualitative)		
SET	**Comparison**	**GDM**	**ADM**	**FDM**	**GDM**	**ADM**	**FDM**	**GDM**	**ADM**	**FDM**
C1	01a Vs 02a	0.33	0.13	0.28	GOOD	V GOOD	GOOD	0.45	0.27	0.29
	01a Vs 03a	0.52	0.29	0.29	FAIR	GOOD	GOOD			
	02a Vs 03a	0.51	0.39	0.31	FAIR	GOOD	GOOD	FAIR	GOOD	GOOD
C2	07a Vs 08a	0.13	0.05	0.10	V GOOD	EXCELLENT	V GOOD	0.12	0.05	0.10
	08a Vs 09a	0.10	0.04	0.07	V GOOD	EXCELLENT	EXCELLENT			
	08a Vs 09a	0.14	0.07	0.12	V GOOD	EXCELLENT	V GOOD	V GOOD	EXCELLENT	V GOOD

The results also conclude that the windscreen washer pump samples (D, E and F) exhibit a higher level of similarity in comparison to the DC to DC converter samples (A, B and C). Over and above the reason presented earlier for this result (batch difference) it is also noted that the DC to DC converter is a significantly more complex system in comparison to the windscreen washer pump. As a result more variability is expected between results from samples of more complex products over those of lesser complexity. However, the level of sample variability should still be within the tolerance ('Good') set previously in this paper.

It is concluded that when validating CEM models against experimental results, a great deal of care should be taken. Batch differences between test samples may infer a number of areas of variability including; the tolerance of components used to manufacture the product and their origins; the manufacturing plant used for production and the build level/quality of the product. These are just a few areas of concern. Therefore, information about the variability of a product or structure should be assessed thoroughly and test configurations must be planned and accurately followed.

The use of the approach discussed in this paper will also allow a sensitivity analysis to be undertaken on the configurations used for validation. This will enable to modeller to substantiate any claims that certain differences between the results are acceptable while others are not.

Further work will look at building on this groundwork to formulate a more readily applicable methodology for quantifying confidence in the reference measurements being used to validate numerical models. Additional work is anticipated on the application of the FSV method to the area of EMC problem solving as a tool for quantifying EMC countermeasures.

REFERENCES

[1] A. J. M. Martin, "Quantitative data validation (automated visual evaluations)," *PhD thesis*, De Montfort University, Leicester, 1999.

[2] A. P. Duffy, A. J. M. Martin, A. Orlandi, G. Antonini, T. M. Benson, and M. S. Woolfson, "Feature selective validation (FSV) for validation of computational electromagnetics (CEM). Part I – The FSV method," *IEEE Trans. on EMC*, vol. 48, no. 3, pp. 449 - 459, Aug. 2006.

[3] A. Orlandi, A. P. Duffy, B. Archambeault, G. Antonini, D. E. Coleby, and S. Connor, "Feature selective validation (FSV) for validation of computational electromagnetics (CEM). Part II – assessment of FSV performance," *IEEE Trans. on EMC*, vol. 48, no. 3, pp. 460 - 7, Aug. 2006.

[4] Automotive EMC Directive, European Directive 2004/104/EC

Alan Denton studied Electrical and Electronic Engineering at the University of Nottingham, completing a PhD in Electromagnetic Compatibility in 2001. Since 2001 he has worked at MIRA Limited as an EMC Technical Specialist where he works closely with component suppliers and vehicle manufacturers resolving EMC issues and designing compliant components, systems and vehicles. His current research interests are the design of bespoke RF filters for specialist applications, data validation techniques for EMC testing, the RF susceptibility characteristics of vehicle airbag systems and advanced EMC test method development. He is a member of the Institution of Engineering and Technology and a Chartered Engineer.

Anthony Martin studied Electrical and Electronic Engineering at De Montfort University, completing a PhD in Quantitative Data Validation in 1999. His role within MIRA Limited is that of Senior EMC. Technical Specialist where he works closely with component, suppliers, and vehicle manufacturers resolving EMC issues and designing compliant components, systems and vehicles. His specialist field is the management of large Military and Special Operations EMC programmes, with emphasis on the resolution of emissions and susceptibility issues to the stringent requirements enforced within the fields of Military and Special Operations. His research activities currently include data validation techniques, the RF susceptibility characteristics of vehicle airbag systems, advanced EMC test method development and EMC control and knowledge base software systems. He is a member of the Institution of Engineering Technology and a Chartered Engineer.

Alistair Duffy was born in Ripon, UK, in 1966. He obtained a First Class BEng(Hons) degree from University College, Cardiff, in 1988 in Electrical and Electronic Engineering, and the MEng degree the following year. He joined Nottingham University in 1990 receiving a PhD in 1993 for his work on experimental validation of numerical modeling. He also holds an MBA. He is currently Reader in Electromagnetics and Head of the Engineering Division at De Montfort University Leicester, UK and has particular research interests in CEM Validation, communications cabling and technology management. He has published over 100 papers in journals and international symposia. Dr Duffy is a Fellow of the Institution of Engineering and Technology (IET) and a member of the Chartered Management Institute (CMI). He is active in the IEEE standards activity on the validation of CEM. He is a member of the International Compumag society and the Applied Computational Electromagnetics Society.

2008 INSTITUTIONAL MEMBERS

AUSTRALIAN DEFENCE LIBRARY
Northcott Drive
Canberra, A.C.T. 2600 Australia

DARTMOUTH COLL-FELDBERG LIB
6193 Murdough Center
Hanover, NH 03755-3560

DSTO-DSTORL EDINBURGH
Jets AU/33851-99, PO Box 562
Milsons Point, NSW
Australia 1565

DTIC-OCP/LIBRARY
8725 John J. Kingman Rd. Ste 0944
Ft. Belvoir, VA 22060-6218

ELSEVIER
Bibliographic Databases
PO Box 2227
Amsterdam, Netherlands 1000 CE

ENGINEERING INFORMATION, INC
PO Box 543
Amsterdam, Netherlands 1000 Am

ETSE TELECOMUNICACION
Biblioteca, Campus Lagoas
Vigo, 36200 Spain

FGAN-FHR
Neuenahrerstrasse 20
Wachtberg, Germany 53343

FLORIDA INTERNATIONAL UNIV
10555 W. Flagler Street
Miami, FL 33174

GEORGIA TECH LIBRARY
225 North Avenue, NW
Atlanta, GA 30332-0001

HANYANG UNIVERSITY
Paiknam Academic Info. Ctr Library
17 Haengdang-Dong
Seongdong-Ku
Seoul, South Korea 133-791

HRL LABS, RESEARCH LIBRARY
3011 Malibu Canyon
Malibu, CA 90265

IEE INSPEC/Acquisitions Section
Michael Faraday House
6 Hills Way
Stevenage, Herts UK SG1 2AY

INSTITUTE FOR SCIENTIFIC INFO.
Publication Processing Dept.
3501 Market St.
Philadelphia, PA 19104-3302

IPS RADIO & SPACE SERVICES
PO Box 1386
Haymarket NSW Australia 1240

LIBRARY – DRDC OTTAWA
3701 Carling Avenue
Ottawa, Ontario, Canada K1A OZ4

LIBRARY of CONGRESS
Reg. Of Copyrights
Attn: 40T Deposits
Washington DC, 20559

LINDA HALL LIBRARY
5109 Cherry Street
Kansas City, MO 64110-2498

MISSISSIPPI STATE UNIV LIBRARY
PO Box 9570Mississippi State, MS
39762

MIT LINCOLN LABORATORY
Periodicals Library
244 Wood Street
Lexington, MA 02420

NAVAL POSTGRADUATE SCHOOL
Attn:J. Rozdal/411 Dyer Rd./ Rm 111
Monterey, CA 93943-5101

NDL KAGAKU
C/0 KWE-ACCESS
PO Box 300613 (JFK A/P)
Jamaica, NY 11430-0613

OHIO STATE UNIVERSITY
1320 Kinnear Road
Columbus, OH 43212

OVIEDO LIBRARY
PO BOX 830679
Birmingham, AL 35283

PENN STATE UNIVERSITY
126 Paterno Library
University Park, PA 16802-1808

CHRIS A. PENWELL
3500 LONG DRIVE
MINDER, NV 89423

PHILIPS RESEARCH LABORATORY
Cross Oak Lane, Stella Cox
Salfords, Redhill
UK RH1 5HA

DAVID J. PINION
1122 E PIKE STREET #1217
SEATTLE, WA 98122

SOUTHWEST RESEARCH
INSTITUTE
6220 Culebra Road
San Antonio, TX 78238

SWETS INFORMATION SERVICES
160 Ninth Avenue, Suite A
Runnemede, NJ 08078

TECHNISCHE UNIV. DELFT
Mekelweg 4, Delft, Holland, 2628 CD
Netherlands

TELSTRA
TRL/M2/770 Blackburn Road
Clayton, Victoria, Australia 3168

TIB & UNIV. BIB. HANNOVER
DE/5100/G1/0001
Welfengarten 1B
Hannover, Germany 30167

TU DARMSTADT
Schlossgartenstrasse 8
Darmstadt, Hessen
Germany D-64289

UNIV OF CENTRAL FLORIDA LIB.
4000 Central Florida Boulevard
Orlando, FL 32816-8005

UNIV OF COLORADO LIBRARY
Campus Box 184
Boulder, CO 80309-0184

UNIV OF MISSOURI-ROLLA LIB.
1870 Miner Circle
Rolla, MO 65409-0001

USAE ENG. RES. & DEV. CENTER
Attn: Library/Journals
72 Lyme Road
Hanover, NH 03755-1290

ACES COPYRIGHT FORM

This form is intended for original, previously unpublished manuscripts submitted to ACES periodicals and conference publications. The signed form, appropriately completed, MUST ACCOMPANY any paper in order to be published by ACES. PLEASE READ REVERSE SIDE OF THIS FORM FOR FURTHER DETAILS.

TITLE OF PAPER:

AUTHORS(S)

PUBLICATION TITLE/DATE:

RETURN FORM TO:

Dr. Atef Z. Elsherbeni
University of Mississippi
Dept. of Electrical Engineering
Anderson Hall Box 13
University, MS 38677 USA

PART A - COPYRIGHT TRANSFER FORM

(NOTE: Company or other forms may not be substituted for this form. U.S. Government employees whose work is not subject to copyright may so certify by signing Part B below. Authors whose work is subject to Crown Copyright may sign Part C overleaf).

The undersigned, desiring to publish the above paper in a publication of ACES, hereby transfer their copyrights in the above paper to The Applied Computational Electromagnetics Society (ACES). The undersigned hereby represents and warrants that the paper is original and that he/she is the author of the paper or otherwise has the power and authority to make and execute this assignment.

Returned Rights: In return for these rights, ACES hereby grants to the above authors, and the employers for whom the work was performed, royalty-free permission to:

1. Retain all proprietary rights other than copyright, such as patent rights.
2. Reuse all or portions of the above paper in other works.
3. Reproduce, or have reproduced, the above paper for the author's personal use or for internal company use provided that (a) the source and ACES copyright are indicated, (b) the copies are not used in a way that implies ACES endorsement of a product or service of an employer, and (c) the copies per se are not offered for sale.
4. Make limited distribution of all or portions of the above paper prior to publication.
5. In the case of work performed under U.S. Government contract, ACES grants the U.S. Government royalty-free permission to reproduce all or portions of the above paper, and to authorize others to do so, for U.S. Government purposes only.

ACES Obligations: In exercising its rights under copyright, ACES will make all reasonable efforts to act in the interests of the authors and employers as well as in its own interest. In particular, ACES REQUIRES that:

1. The consent of the first-named author be sought as a condition in granting re-publication permission to others.
2. The consent of the undersigned employer be obtained as a condition in granting permission to others to reuse all or portions of the paper for promotion or marketing purposes.

In the event the above paper is not accepted and published by ACES or is withdrawn by the author(s) before acceptance by ACES, this agreement becomes null and void.

AUTHORIZED SIGNATURE — TITLE (IF NOT AUTHOR)

EMPLOYER FOR WHOM WORK WAS PERFORMED — DATE FORM SIGNED

Part B - U.S. GOVERNMENT EMPLOYEE CERTIFICATION

(NOTE: if your work was performed under Government contract but you are not a Government employee, sign transfer form above and see item 5 under Returned Rights).

This certifies that all authors of the above paper are employees of the U.S. Government and performed this work as part of their employment and that the paper is therefor not subject to U.S. copyright protection.

AUTHORIZED SIGNATURE — TITLE (IF NOT AUTHOR)

NAME OF GOVERNMENT ORGANIZATION — DATE FORM SIGNED

PART C - CROWN COPYRIGHT

(NOTE: ACES recognizes and will honor Crown Copyright as it does U.S. Copyright. It is understood that, in asserting Crown Copyright, ACES in no way diminishes its rights as publisher. Sign only if *ALL* authors are subject to Crown Copyright).

This certifies that all authors of the above Paper are subject to Crown Copyright. (Appropriate documentation and instructions regarding form of Crown Copyright notice may be attached).

AUTHORIZED SIGNATURE TITLE OF SIGNEE

NAME OF GOVERNMENT BRANCH DATE FORM SIGNED

Information to Authors

ACES POLICY

ACES distributes its technical publications throughout the world, and it may be necessary to translate and abstract its publications, and articles contained therein, for inclusion in various compendiums and similar publications, etc. When an article is submitted for publication by ACES, acceptance of the article implies that ACES has the rights to do all of the things it normally does with such an article.

In connection with its publishing activities, it is the policy of ACES to own the copyrights in its technical publications, and to the contributions contained therein, in order to protect the interests of ACES, its authors and their employers, and at the same time to facilitate the appropriate re-use of this material by others.

The new United States copyright law requires that the transfer of copyrights in each contribution from the author to ACES be confirmed in writing. It is therefore necessary that you execute either Part A-Copyright Transfer Form or Part B-U.S. Government Employee Certification or Part C-Crown Copyright on this sheet and return it to the Managing Editor (or person who supplied this sheet) as promptly as possible.

CLEARANCE OF PAPERS

ACES must of necessity assume that materials presented at its meetings or submitted to its publications is properly available for general dissemination to the audiences these activities are organized to serve. It is the responsibility of the authors, not ACES, to determine whether disclosure of their material requires the prior consent of other parties and if so, to obtain it. Furthermore, ACES must assume that, if an author uses within his/her article previously published and/or copyrighted material that permission has been obtained for such use and that any required credit lines, copyright notices, etc. are duly noted.

AUTHOR/COMPANY RIGHTS

If you are employed and you prepared your paper as a part of your job, the rights to your paper initially rest with your employer. In that case, when you sign the copyright form, we assume you are authorized to do so by your employer and that your employer has consented to all of the terms and conditions of this form. If not, it should be signed by someone so authorized.

NOTE RE RETURNED RIGHTS: Just as ACES now requires a signed copyright transfer form in order to do "business as usual", it is the intent of this form to return rights to the author and employer so that they too may do "business as usual". If further clarification is required, please contact: The Managing Editor, R. W. Adler, Naval Postgraduate School, Code EC/AB, Monterey, CA, 93943, USA (408)656-2352.

Please note that, although authors are permitted to re-use all or portions of their ACES copyrighted material in other works, this does not include granting third party requests for reprinting, republishing, or other types of re-use.

JOINT AUTHORSHIP

For jointly authored papers, only one signature is required, but we assume all authors have been advised and have consented to the terms of this form.

U.S. GOVERNMENT EMPLOYEES

Authors who are U.S. Government employees are not required to sign the Copyright Transfer Form (Part A), but any co-authors outside the Government are.

Part B of the form is to be used instead of Part A only if all authors are U.S. Government employees and prepared the paper as part of their job.

NOTE RE GOVERNMENT CONTRACT WORK: Authors whose work was performed under a U.S. Government contract but who are not Government employees are required so sign Part A-Copyright Transfer Form. However, item 5 of the form returns reproduction rights to the U. S. Government when required, even though ACES copyright policy is in effect with respect to the reuse of material by the general public.

APPLIED COMPUTATIONAL ELECTROMAGNETICS SOCIETY JOURNAL
http://aces.ee.olemiss.edu

INFORMATION FOR AUTHORS

PUBLICATION CRITERIA

Each paper is required to manifest some relation to applied computational electromagnetics. **Papers may address general issues in applied computational electromagnetics, or they may focus on specific applications, techniques, codes, or computational issues.** While the following list is not exhaustive, each paper will generally relate to at least one of these areas:

1. **Code validation.** This is done using internal checks or experimental, analytical or other computational data. Measured data of potential utility to code validation efforts will also be considered for publication.

2. **Code performance analysis.** This usually involves identification of numerical accuracy or other limitations, solution convergence, numerical and physical modeling error, and parameter tradeoffs. However, it is also permissible to address issues such as ease-of-use, set-up time, run time, special outputs, or other special features.

3. **Computational studies of basic physics.** This involves using a code, algorithm, or computational technique to simulate reality in such a way that better, or new physical insight or understanding, is achieved.

4. **New computational techniques** or new applications for existing computational techniques or codes.

5. **"Tricks of the trade"** in selecting and applying codes and techniques.

6. **New codes, algorithms, code enhancement, and code fixes.** This category is self-explanatory, but includes significant changes to existing codes, such as applicability extensions, algorithm optimization, problem correction, limitation removal, or other performance improvement. **Note: Code (or algorithm) capability descriptions are not acceptable, unless they contain sufficient technical material to justify consideration.**

7. **Code input/output issues.** This normally involves innovations in input (such as input geometry standardization, automatic mesh generation, or computer-aided design) or in output (whether it be tabular, graphical, statistical, Fourier-transformed, or otherwise signal-processed). Material dealing with input/output database management, output interpretation, or other input/output issues will also be considered for publication.

8. **Computer hardware issues.** This is the category for analysis of hardware capabilities and limitations of various types of electromagnetics computational requirements. Vector and parallel computational techniques and implementation are of particular interest.

Applications of interest include, but are not limited to, antennas (and their electromagnetic environments), networks, static fields, radar cross section, inverse scattering, shielding, radiation hazards, biological effects, biomedical applications, electromagnetic pulse (EMP), electromagnetic interference (EMI), electromagnetic compatibility (EMC), power transmission, charge transport, dielectric, magnetic and nonlinear materials, microwave components, MEMS, RFID, and MMIC technologies, remote sensing and geometrical and physical optics, radar and communications systems, sensors, fiber optics, plasmas, particle accelerators, generators and motors, electromagnetic wave propagation, non-destructive evaluation, eddy currents, and inverse scattering.

Techniques of interest include but not limited to frequency-domain and time-domain techniques, integral equation and differential equation techniques, diffraction theories, physical and geometrical optics, method of moments, finite differences and finite element techniques, transmission line method, modal expansions, perturbation methods, and hybrid methods.

Where possible and appropriate, authors are required to provide statements of quantitative accuracy for measured and/or computed data. This issue is discussed in "Accuracy & Publication: Requiring, quantitative accuracy statements to accompany data," by E. K. Miller, *ACES Newsletter,* Vol. 9, No. 3, pp. 23-29, 1994, ISBN 1056-9170.

SUBMITTAL PROCEDURE

All submissions should be uploaded to ACES server through ACES web site (http://aces.ee.olemiss.edu) by using the upload button, journal section. Only pdf files are accepted for submission. The file size should not be larger than 5MB, otherwise permission from the Editor-in-Chief should be obtained first. Automated acknowledgment of the electronic submission, after the upload process is successfully completed, will be sent to the corresponding author only. It is the responsibility of the corresponding author to keep the remaining authors, if applicable, informed. Email submission is not accepted and will not be processed.

PAPER FORMAT (INITIAL SUBMISSION)

The preferred format for initial submission manuscripts is 12 point Times Roman font, single line spacing and single column format, with 1 inch for top, bottom, left, and right margins. Manuscripts should be prepared for standard 8.5x11 inch paper.

EDITORIAL REVIEW

In order to ensure an appropriate level of quality control, papers are peer reviewed. They are reviewed both for

technical correctness and for adherence to the listed guidelines regarding information content and format.

PAPER FORMAT (FINAL SUBMISSION)

Only camera-ready electronic files are accepted for publication. The term **"camera-ready" means that the material is neat, legible, reproducible, and in accordance with the final version format listed below.**

The following requirements are in effect for the final version of an ACES Journal paper:

1. The paper title should not be placed on a separate page. The title, author(s), abstract, and (space permitting) beginning of the paper itself should all be on the first page. The title, author(s), and author affiliations should be centered (center-justified) on the first page. The title should be of font size 16 and bolded, the author names should be of font size 12 and bolded, and the author affiliation should be of font size 12 (regular font, neither italic nor bolded).

2. An abstract is required. The abstract should be a brief summary of the work described in the paper. It should state the computer codes, computational techniques, and applications discussed in the paper (as applicable) and should otherwise be usable by technical abstracting and indexing services. The word "Abstract" has to be placed at the left margin of the paper, and should be bolded and italic. It also should be followed by a hyphen (—) with the main text of the abstract starting on the same line.

3. All section titles have to be centered and all the title letters should be written in caps. The section titles need to be numbered using roman numbering (I. II. ….)

4. Either British English or American English spellings may be used, provided that each word is spelled consistently throughout the paper.

5. Internal consistency of references format should be maintained. As a guideline for authors, we recommend that references be given using numerical numbering in the body of the paper (with numerical listing of all references at the end of the paper). The first letter of the authors' first name should be listed followed by a period, which in turn, followed by the authors' complete last name. Use a coma (,) to separate between the authors' names. Titles of papers or articles should be in quotation marks (" "), followed by the title of journal, which should be in italic font. The journal volume (vol.), issue number (no.), page numbering (pp.), month and year of publication should come after the journal title in the sequence listed here.

6. Internal consistency shall also be maintained for other elements of style, such as equation numbering. As a guideline for authors who have no other preference, we suggest that equation numbers be placed in parentheses at the right column margin.

7. The intent and meaning of all text must be clear. For authors who are not masters of the English language, the ACES Editorial Staff will provide assistance with grammar (subject to clarity of intent and meaning). However, this may delay the scheduled publication date.

8. Unused space should be minimized. Sections and subsections should not normally begin on a new page.

ACES reserves the right to edit any uploaded material, however, this is not generally done. It is the author(s) responsibility to provide acceptable camera-ready pdf files. Incompatible or incomplete pdf files will not be processed for publication, and authors will be requested to re-upload a revised acceptable version.

COPYRIGHTS AND RELEASES

Each primary author must sign a copyright form and obtain a release from his/her organization vesting the copyright with ACES. Copyright forms are available at ACES, web site (http://aces.ee.olemiss.edu). To shorten the review process time, the executed copyright form should be forwarded to the Editor-in-Chief immediately after the completion of the upload (electronic submission) process. Both the author and his/her organization are allowed to use the copyrighted material freely for their own private purposes.

Permission is granted to quote short passages and reproduce figures and tables from and ACES Journal issue provided the source is cited. Copies of ACES Journal articles may be made in accordance with usage permitted by Sections 107 or 108 of the U.S. Copyright Law. This consent does not extend to other kinds of copying, such as for general distribution, for advertising or promotional purposes, for creating new collective works, or for resale. The reproduction of multiple copies and the use of articles or extracts for commercial purposes require the consent of the author and specific permission from ACES. Institutional members are allowed to copy any ACES Journal issue for their internal distribution only.

PUBLICATION CHARGES

All authors are allowed for 8 printed pages per paper without charge. Mandatory page charges of $75 a page apply to all pages in excess of 8 printed pages. Authors are entitled to one, free of charge, copy of the journal issue in which their paper was published. Additional reprints are available for a nominal fee by submitting a request to the managing editor or ACES Secretary.

Authors are subject to fill out a one page over-page charge form and submit it online along with the copyright form before publication of their manuscript.

ACES Journal is abstracted in INSPEC, in Engineering Index, DTIC, Science Citation Index Expanded, the Research Alert, and to Current Contents/Engineering, Computing & Technology.